Gas-consuming triphasic gas-liquid-liquid reactions in segmented slug flow

Zur Erlangung des akademischen Grades eines

Dr.-Ing.

von der Fakultät Bio- und Chemieingenieurwesen
der Technischen Universität Dortmund

genehmigte Dissertation

vorgelegt von

M.Sc. Niclas Baron von Vietinghoff-Scheel

aus

Speyer

Tag der mündlichen Prüfung: 20.03.2023

1. Gutachter: Prof. Dr. David W. Agar

2. Gutachter: Prof. Dr. Norbert Kockmann

Dortmund 2023

Abstract

The chemical industry in Europe is transforming. Diversifying raw materials, an increased circular economy and a growing market of specialty chemicals require flexible and fast process development. Small-scale continuous reactors can contribute to these requirements.

In particular, triphasic gas-liquid-liquid slug flows can perform complex multiphase systems at a laboratory scale. This work investigates strategies to counteract a gas shortage in gas-consuming reactions in such capillaries. On the one hand, gas permeation through the polymer capillary is investigated, and its influence on an existing slug flow is studied. On the other hand, individual gas bubbles are integrated into the slug flow using valves and an electrolysis cell. Both methods preserve the advantageous slug flow - however, they have advantages and disadvantages depending on the reaction applied. Moreover, they can be used in a scale-up of capillary reactors, contrary to established methods.

For success in scale-up, inexpensive and robust sensors are necessary in addition to gas-feeding methods. For this purpose, non-invasive optoelectric sensors are developed for triphasic slug flows, which can detect the flow (velocity, phase ratios, segment lengths), but also determine local concentrations. Both light refraction and light absorption are exploited. Concentration sensors are used to study the homogeneously catalyzed hydrogenation of a dye to a colorless form. A change in hydrodynamic parameters had only minor effects compared to chemical parameters. However, the reaction was significantly intensified compared to a stirred tank reactor.

Finally, selective fat hydrogenation in a triphasic slug flow is investigated. A suitable solvent selection can counteract unfavorable solid formation. The monounsaturated fatty acid could be selectively obtained from sunflower oil with a high content of polyunsaturated fatty acids.

Kurzzusammenfassung

Die chemische Industrie in Europa steht vor einem Wandel, eine Diversifizierung der Rohstoffe, eine vermehrte Kreiswirtschaft und ein wachsender Anteil an Spezialchemikalien erfordern eine flexible und schnelle Prozessentwicklung. Kleinskalige kontinuierliche Reaktoren können dazu beitragen.

Insbesondere dreiphasige gas-flüssig-flüssig Pfropfenströmungen können komplexe Mehrphasensysteme im Labormaßstab gut abbilden. Diese Arbeit untersucht Strategien, wie in gaskonsumierenden Reaktionen in solchen Kapillarreaktoren einem Mangel an Reaktionsgas entgegengewirkt werden kann. Zum einen wird die Gaspermeation durch die Polymerkapillare untersucht und deren Einfluss auf eine bestehende Pfropfenströmung untersucht. Zum anderen wird gezielt mit Ventilen und einer Elektrolysezelle einzelne Gasblasen in die Pfropfenströmung integriert. Beiden Methoden erhalten die vorteilhafte Pfropfenströmung - sie haben allerdings Vor- und Nachteile je nach angewandter Reaktion. Sie lassen sich beide, entgegen etablierter Verfahren, in einer Maßstabsvergrößerung der Kapillarreaktoren verwenden.

Für das Gelingen einer Maßstabsvergrößerung sind neben Gasnachspeisungsmethoden, günstige und robuste Sensoren notwendig. Dafür werden für die dreiphasigen Pfropfenströmungen nicht-invasive optoelektrische Sensoren entwickelt, die sowohl die Strömung (Geschwindigkeit, Phasenverhältnisse, Segmentlängen) detektieren, aber auch lokale Konzentrationen bestimmen können. Dabei werden sowohl die Lichtbrechung, als auch Lichtabsorption ausgenutzt. Konzentrationssensoren werden verwendet, um eine homogenkatalysierte Hydrierung eines Farbstoffs zu einer farblosen Form zu untersuchen. Eine Veränderung der hydrodynamischen Parameter hatte im Vergleich zu chemischen Parametern nur geringfügige Einflüsse. Allerdings konnte die Reaktion im Vergleich zu einem Rührkesselreaktor stark intensiviert werden.

Abschließend wird die selektive Fetthydrierung in einer dreiphasigen Pfropfenströmung untersucht. Einer ungünstigen Feststoffablagerung kann durch eine geeignete Lösungsmittelwahl entgegengewirkt werden. Ausgehend von Sonnenblumenöl mit einem hohen Anteil an mehrfach ungesättigten Fettsäuren konnte selektiv die einfach ungesättigte Fettsäure umgesetzt werden.

Acknowledgment

The presented work was performed during my employment at the Chair of Reaction Engineering (CVT) between September 2018 and February 2022. I would like to thank numerous people without whom this work would not have been possible.

First of all, I would like to thank my supervisor and first reviewer Prof. Dr. David W. Agar for the opportunity to do my research under his chair and for his supervision. I especially appreciate his global view without forgetting the details.

I am also happy to have found the examination committee with Prof. Dr. Norbert Kockmann as the second reviewer and Prof. Dr. Hannsjörg Freund as examiner and chairman and I would like to thank them for their interest in the work. Furthermore, I would like to thank TU Dortmund University and the Faculty BCI for their facilities, especially the scientific workshops, which have contributed significantly to the functional experimental setup.

As part of the "last generation" of the chair CVT, I enjoyed the time during my doctoral studies thanks to all my colleagues. The collegial and supportive environment helped me to constantly have fun and enjoy my work. Also, the support of the non-scientific staff was essential for the success of the experimental work.

The numerous students who completed their theses and internships under my supervision were one of the main contributors to my work, and thanks to them, I was able to fill my work with a lot of life and data. I appreciate that you have worked with me with great enthusiasm and energy.

I had the chance to spend time abroad in Toulouse (France) at the Laboratoire de Chimie Agro-industrielle (LCA) of the Institut National Polytechnique (INP) thanks to a mobility grant (PROCOPE) from the French Embassy in Berlin. Despite strong COVID-19 restrictions at the end of 2020, I received strong support from the director and supervisor Sophie Thiebaud-Roux, and my further supervisor Pascale de Caro. Thanks to my office colleague Clarissa Detomi, I always felt welcome there and was delighted by the interest in my topic.

The combination of the triphasic capillary reactor and homogeneous catalysis would not be possible without the support provided by Thomas Seidensticker and the Chair of Industrial Chemistry (TC) in the form of discussions and ligand donations. I am also pleased to continue my research at the TC.

Finally, I would like to thank my friends and family for their support. In particular, I would like to mention my flatmates and my girlfriend Leonie, who made my everyday life brighter.

Table of Contents

List of Figures

List of Tables

Nomenclature

Symbols

Symbol	Unit	Meaning
A	m^2	Area
a	m/s^2	Acceleration
a	variable	Constant
b	variable	Constant
C	variable	Constant
Ca	-	Capillary number
CP	-	Coalescence performance
d	m	Diameter
E	Pa	Elastic modulus
F	N	Force
FP	-	Feeding performance
h	m	Wall film thickness
I	A	Electrical current
K_{OW}	-	1-octanol-water partition coefficients
K_P	-	Proportional gain
L,l	m	Length
m	kg	Mass
N	-	Amount
n	-	Refractive index
p	Pa	Pressure
$\tilde{P}$	-	Relative pressure deviation
q	m^3/s	Permeation flux
R	$J/(K \cdot mol)$	Ideal gas constant
R,r	m	Radius or radial direction
Re	-	Reynolds number
s	m	Capillary wall thickness or distance
t	s	Time
T	K or °C	Temperature
U,u	m/s	Velocity
V	m^3	Volume
v	m/s	Velocity
$\dot{V}$	m^3/s	Volume flow rate
x	m	Coordinate
z	m	Axial coordinate
z	-	Charge number of ion
α	1/K	Coefficient of thermal expansion
α	rad	Angle
Δ,δ	-	difference
ϵ	-	Expansion
ε	$(cm^3 \cdot mm)/(cm^2 \cdot kPa \cdot s)$	Permeation coefficient
η	mPas	Dynamic viscosity
θ	rad	Contact angle

ρ	kg/m³	Density
σ	Pa	Stress
σ	N/m	Surface/interfacial tension
τ	Pa	Shear stress
τ	s	Residence time
υ	-	Poisson's ratio

Indices

Index	Meaning
active	Active
aq	Aqueous
bubble	Bubble
c	Critical
cap	Capillary
cont	Continuous
cs	Cross section
delay	Delay
end	End, outlet
Fr	Friction
g	Gas
gas	Gas
H	Hydrostatic
I	Inertia
i	Counting variable
i	Inside, internal
IF	Interface
in, inlet	Input, inlet
j	Time step or material variable
L	Liquid or lateral
liq	Liquid
max	Maximal
o	Outside, outer
off	Off
open	Open
pi	Pressure
set	Setpoint
slug, SL	Slug or continuous phase
ss	Steady-state
t	Tangential
T	Temperature
tot	Total
unit, uc	Unit cell
x	Position
z	Axial direction

Abbreviations

Abbreviation	Meaning
µPIV	Micro-particle image velocimetry
0D	Zero dimensional
2D	Two dimensional
3D	Three dimensional
B	Vessel, tank
BTB	Bromothymol blue
C^4D	Capacitive coupled contactless conductivity detection
CFD	Computational fluid dynamics
CSTR	Continuous stirred tank reactor
CV	Crystal violet
FAME	Fatty acid methyl esters
FEP	Fluorinated ethylene propylene
FI	Flow indicator
Hex	Hexanol
ID	Inner diameter
K	Coaxial slug generator
LED	Light-emitting diode
MFC	Mass flow controller
MOSFET	Metal–oxide semiconductor field effect transistor
MTBE	Methyl tertiary-butyl ether
NIR	Near-infrared (spectrum)
OD	Outer diameter
P	Pump
PBS	Ponceau BS
PFA	Perfluoroalkoxy alkanes
PFR	Plug flow reactor
PI	Pressure Indicator
PIC	Pressure indicator and controller
PLA	Polylactic acid
PMMA	Poly(methyl methacrylate)
PTFE	Polytetrafluoroethylene
QI	Quality indicator: Sample taking or senor location
R	Reactor element (1-4)
Rh(TPPTS) or Ru(TPPTS)	Simplified form of homogeneous Rh or Ru – Ligand complex
SB3	Solvent Black 3
SD	Secure digital
SIII	Sudan III
TI	Temperature indicator
TIC	Temperature indicator and controller
TMSH	Trimethyl sulfonium hydroxide
TPM	Triphenylmethane (dye)
TPPTS	3,3',3''-phosphanetriyltris(benzenesulfonic acid) trisodium
UV-Vis	Ultra violet and visible (light)

1 Introduction and motivation

The chemical industry is facing major challenges that could significantly impact the future of individual sectors and sites. Probably the greatest challenge in the coming years is the path to sustainable and climate-neutral production without losing international competitiveness. Reducing and eliminating carbon dioxide emissions are not the exclusive focus of this challenge. The industry also has to deal with the increasing water shortage, for example, or the greater involvement of a viable circular economy. Especially the latter is elementary for one of the largest and best-selling product groups of polymers. Furthermore, polymer waste pollutes almost all ecosystems globally due to poor recycling strategies, which reflects manufacturers' responsibility. *(1)*

While on the other hand, the use of fossil raw materials should be reduced. Both contribute to the diversification of raw materials, such as renewable raw materials or reusing (polymer) waste. These considerations are not the only ones forcing the chemical industry to rethink its raw material procurement. Increasing global tensions are questioning the reliable availability of crude oil and natural gas. On the other hand, other global manufacturers are not forced to rethink politically and do not have to fear raw material procurement. *(2)*

European locations, in particular, are under increased pressure. Many European governments and the European Union intend to become pioneers in climate neutrality, reflected in stricter regulations, especially in emissions regulations, in a global comparison. On the other hand, there are only limited resources of fossil raw materials in Europe, which leads to dependencies on other countries. Recent conflicts with one of Europe's largest natural gas suppliers show that a reliable supply of raw materials cannot be guaranteed. Other global locations have no or fewer political restrictions to face in the medium term and have access to local sources of raw materials. Therefore, new approaches and technologies are essential to maintain the competitiveness of European locations in the long term. *(1–3)*

The change and diversification of raw material sources require high flexibility in production plants. In addition, the dynamic market for specialty chemicals is growing faster than basic chemicals, which also requires high flexibility in the process development. As a result, new processes planned for years and designed to run for decades are presumably losing importance in the future. In order to manage this necessary flexibility and fast adaptability both in production and development, novel technologies become relevant. *(3–5)*

An additional aspect of the transformation to renewable feedstocks is that natural materials usually have a higher oxygen content (except, e.g., fats and oils) than fossil raw materials resulting in a higher polarity. Consequently, to convert these polar feedstocks into nonpolar products or integrate them into existing processes, an increase in the importance of multiphase fluidic systems can be expected in the future. This further increases the complexity of new processes in development due to multiphase systems. Micro-process engineering offers a solution for combining high flexibility and complex multiphase systems.

Microstructured reactors can be utilized for process development, especially with low material and time requirements. In addition, due to small volumes, reactions can be investigated quickly and safely, even at high temperatures and pressures *(6)*. Gomollón-Bel identifies microstructured flow chemistry as one of the ten key technologies for a more sustainable chemical industry *(7)*.

In the following, the segmented slug flow, advantageous in multiphase microreactors, is first introduced, and a focus is set on triphasic gas-liquid-liquid systems in particular. Subsequently, the importance and possibilities of scaling up such reactors are highlighted, and strategies are discussed for achieving a small-production scale with such reactors. Then, the importance and accompanying problems of gas-consuming reactions in microreactors are briefly discussed. Finally, resulting research questions are formulated, which are discussed within the scope of this thesis.

1.1 Bi- and triphasic slug flow in microcapillaries

The slug flow regime (also called segmented flow or Taylor flow) has been intensively studied for biphasic (gas-liquid and liquid-liquid) systems in the last decades *(8–12)*. In particular, the hydrodynamics and transport processes of gas-liquid and liquid-liquid systems have been investigated *(13, 14)*. If slug flow is used in micro capillaries (≤1 mm), processes can be intensified by high surface-to-volume ratios, small transport pathways, but also by the characteristic internal Taylor eddies *(15)*. The main focus is on enhanced heat and mass transfer processes *(9, 16)*. In addition, slug flow in microcapillaries represents a continuous multiphase reactor on a laboratory scale, allowing reactions and other unit operations with a plug flow reactor (PFR)-like residence time behavior to be investigated at low cost without the requirement of large pilot plants *(11)*. In particular, the low back-mixing within the reactor makes this type of reactor attractive for reaction systems with consecutive reactions, which are favored in a continuous stirred-tank reactor (CSTR) by the back-mixing prevailing therein. Continuous slug flow microreactors are thus attracting attention due to their potential for increasing selectivities and space-time yields *(6, 17–19)*.

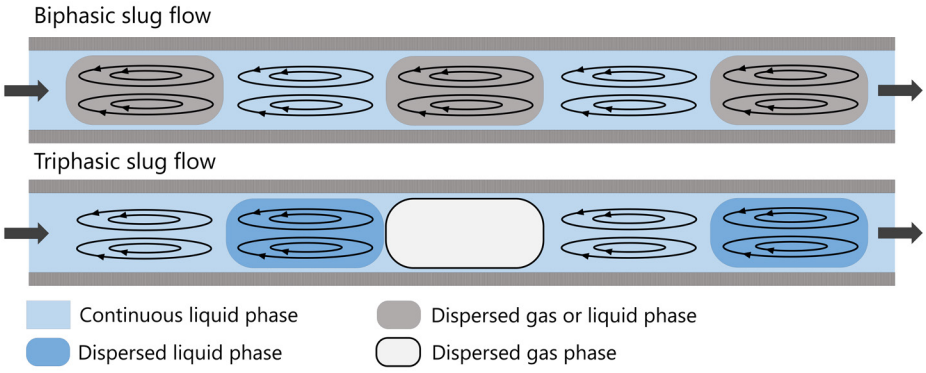

Figure 1.1. Biphasic slug flow on the top with a continuous slug and a dispersed bubble, which can be either gas or liquid. Triphasic slug flow on the bottom. Internal circulations in each phase are indicated. Each phase may be indicated as a slug.

Slug flows occur in gas-liquid or liquid-liquid systems in small flow channels (tubular or rectangular), where the involved phases regularly alternate, forming a certain symmetry in the flow pattern (see Figure 1.1). The phase with the better wetting properties to the capillaries forms the continuous phase. The continuous phase often forms a wall film on which the longish, dispersed phase flows along. Due to its regular and specific form, the interfacial surface area and the surface-to-volume ratio are both large and well-defined, representing a benefit compared to other multiphase reactors, such as bubble columns with a statistical bubble distribution *(20)*. In reactions, most transport limitations can be overcome by intensification; therefore, a slug flow reactor can serve as an asymptote in optimizing large-scale processes.

In sum, slug flows offer a substantial process intensification and are also very flexible in their input streams and may be used for rapid process development.

In catalytic gas-liquid reactions, the challenge remains in which phase the catalyst is dissolved. Heterogeneous catalysts have so far had only limited success. Fix-bed reactors can be implemented in microscales, but with a gas-liquid flow, contrary to the slug flow, only a stochastic distribution of surfaces can be achieved *(21)*. Catalysts can also be embedded on the microcapillary wall, for example, in zeolites *(22–24)*. Some cases show deactivation even after short operating times of <1 day though *(25, 26)*. A catalyst suspension in a liquid phase is also conceivable *(27–30)*. The remaining issue, in this case, is the subsequent separation and recycling of very fine solid particles and preserving a homogeneous suspension along the capillary. For liquid-liquid systems, it was also considered that a surface treatment to increase the affinity for one of the phases could not wholly keep the suspension in one phase. A simple separation of the catalyst is desirable in terms of recyclability.

Adding a second functional liquid phase can satisfy the requirement for a catalyst phase. Nanoparticles or homogeneous transition metal catalysts are dissolved in this extra liquid phase, while the reactants and products are present in the other liquid phase *(31–37)*. Subsequently, the liquid catalyst phase can be separated and recycled. This means a more complex multiphase system with three phases for gas-liquid reactions. A transfer of such gas-liquid-liquid systems into slug flows represents an attractive solution for this type of multiphase reaction since mass transfer resistances are reduced, and the separation and recycling of the catalyst phase are ensured.

Triphasic gas-liquid-liquid slug flows have therefore received attention in recent years *(16, 28, 38–43)*. One essential requirement of the triphasic slug flow is the reliable generation and stability of this flow regime. Some works in literature created a reproducible and stable triphasic flow with T- or Y-junctions in series, but the operating range in slug lengths and phase ratios remained small *(39, 42)*. In most cases, the inserted gas phase was significantly smaller than the other two phases, which is particularly disadvantageous for gas-consuming reactions, as this is a major limitation on the amount of substance provided. However, with the use of adjustable coaxial mixers, this operating range could be significantly increased *(43, 44)*. Nevertheless, structured analysis of reactions in this triphasic system has been performed only on a small scale *(34)*.

In addition to a different functional phase, a triphasic flow also has advantages in terms of flow stability. Hellmann showed for a hexanol-water system that in a biphasic liquid-liquid flow, a slug flow could only be generated at small capillary numbers (up to 0.2); at higher volume flows, an unfavorable annular flow occurred more frequently. When the same system was investigated in a triphasic flow (additional phase: nitrogen), a slug flow could be obtained at significantly higher volume flows (capillary number >0.7). A transition to a different flow pattern could not be observed so far. *(45)*

Furthermore, Hellmann observed that during slug generation, the dispersed phases (gas and liquid) initially formed wall films of different thicknesses (analogous to biphasic flows) and exhibited different velocities. Once the faster slug caught up with the slower slug, the faster slug's velocity and wall film adapted to the slower slug. In the systems studied by Hellmann, the gas phase was always the slower phase. Thus in residence time measurements, the residence time distribution of gas-liquid-liquid flows approximated that of gas-liquid flows and revealed significantly less back-mixing than liquid-liquid slug flows. *(45)*

By developing theoretical equations for pressure drop and measuring the mass transfer between the liquid phases, Hellmann has comprehensively studied the triphasic slug flow in terms of hydrodynamics *(45)*.

Based on these findings, analyzing the triphasic slug flow with respect to further applications is beneficial. In particular, the higher stability of the triphasic flow compared to the biphasic flow could allow a scale-up of these capillary reactors. In this way, the slug flow with all its advantageous properties could be brought from the lab scale to a small production scale, which could flexibly cover the demand for specialty chemicals, for example. Furthermore, catalytic gas-liquid reactions in triphasic flows are attractive because the necessary catalyst can be immobilized in the additional liquid phase, and recycling by phase separation is easily feasible.

1.2 Strategies to scale up slug flow reactors

The capacity of the capillary reactor remains a challenge. With just a few milli- or microliters per minute in a single capillary, the throughput is inadequate for most production scale plants, even for small specialty chemicals scales. In order to preserve the favorable properties of microreactors at scale-up, the microscale structures are essential. However, a conventional scale-up of characteristic sizes like the capillary diameter usually involves the loss of the small transport ways and concerning multiphase flows, or the advantageous slug flows cannot be generated or maintained. For these reasons, a conventional scale-up of these microreactors is not desirable. Nevertheless, to generate larger product volumes, other strategies are being pursued. Timothy Noël's group distinguishes between three alternative methods that can be used for scaling-up microstructured reactors. All methods attempt to increase the total volume flow rate introduced. This can be accomplished by using a large number of parallel capillaries (numbering-up) or by using longer or wider capillaries (sizing-up) (see Figure 1.2). *(46)*

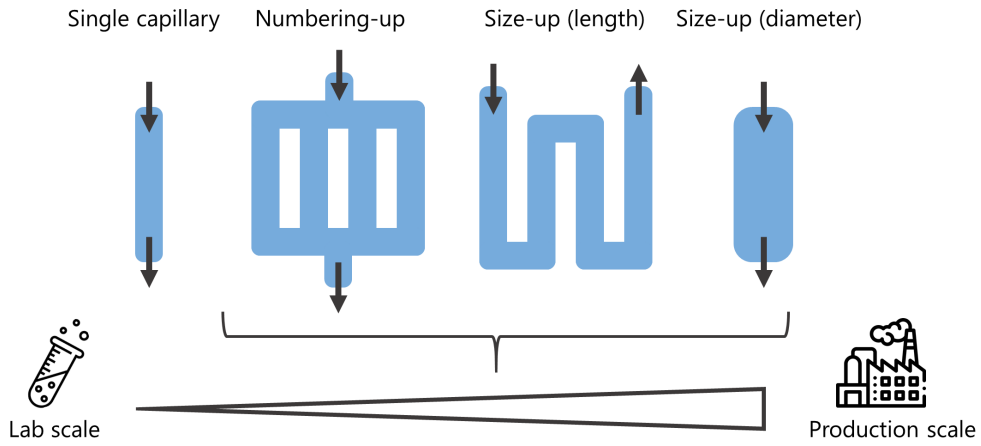

Figure 1.2. Strategies for transferring capillary reactors from a single capillary (lab scale) to a production scale, which is the sum of the individual methods. Figure adapted from *(46)*.

A numbering-up is a parallelization of single capillaries together with distribution units for each phase. Distribution units are preferred to decrease the number of pumps necessary and thus the costs. For single-phase systems, the distributor design has already been optimized to minimize the maldistribution of the volumetric flow rates and, thus, harmonize the conditions inside each capillary *(47–50)*. By modifying only the design, the systematic maldistribution of the volumetric flow rate for more than 100 parallelized channels can be reduced to around 5% *(49)*. Multiphase systems aggravate this non-uniformity. Based on the maldistribution for the single-phase systems, different slug/bubble lengths and phase ratios arise in individual channels, leading to different pressure drops due to the extent of the phase interfaces in each channel, which increases the maldistribution further. Even by changing the design of the distributor for the biphasic flow by increasing the pressure drop within the manifold, a maldistribution could not be eliminated *(51)*. Nevertheless, it has been demonstrated that the inhomogeneities of biphasic liquid-liquid flow in a numbering-up can be suppressed by feedback control of the volumetric flow rate and slug lengths in each channel using a temperature-regulated pressure drop element and a step-motor driven coaxial slug generator *(52)*. This technique necessitates actuators and sensors for each channel in the numbered-up system.

This technique is based on the temperature-dependent viscosity and, thus, the respective pressure loss of a single phase in one channel. Multiple phases within these control elements would lead to high variations and a more complex control task. Therefore, if a gas-liquid-liquid flow should be realized in a numbering-up, one strategy could be to generate a liquid-liquid flow according to Arsenjuk et al.'s approach and inject gas bubbles directly into the existing segments *(52)*.

A size-up of a single capillary in length with simultaneous flow rate increase results in harsher conditions. For example, the higher velocities increase the Reynolds number and the wall film thickness in slug flows. If the capillary diameter remains constant, the size-up in length results in a high pressure drop along the capillary *(53)*. Depending on the reaction network and the pressure dependency, this can be advantageous but also disadvantageous. In any case, the high pressures require more expensive equipment. However, low-viscosity solvents or larger

capillary diameters can counteract the high pressure drop. Biphasic slug flows, moreover, can only be accelerated to a specific limit since they would otherwise switch to the more unfavorable annular flow. The triphasic flow, however, can enable this scale-up method due to its stability at high velocities.

Size-up in diameter, however, is only possible to a limited extent, as previously discussed, since the small scales are necessary to provide the small transport paths and the advantageous flow pattern. The larger transport paths, however, could be counteracted with stronger mixing at higher velocities. Hence, the preservation of the slug flow is essential. The exact limits depend on the system. Some examples in the literature show a stable slug flow up to a 3.2 mm capillary diameter (tubular) *(31)*.

For a scale-up, it is helpful to extend the limits of a single capillary (length and diameter) - which should be easier in a triphasic flow - and then perform a numbing-up.

In any case, effective and inexpensive sensors that can track flow conditions and reactions non-invasively are necessary to make a scale-up of capillary reactors economically attractive.

1.3 Gas-consuming reactions in capillary reactors

Although the hydrodynamics of slug flows are already well characterized, actual applications in these reactor types entail additional challenges. Therefore, this thesis focuses on catalytic gas-consuming reactions, which follow the simplified reaction equation (Eq. 1.1) below.

$$A_{liq} + B_{gas} \xrightarrow{[cat]} C_{liq} \tag{1.1}$$

Examples of such reactions are hydrogenations, oxidations, or hydroformylations. If such reactions are applied in a capillary reactor with slug flows, a rapid shrinkage of the gas phase can be observed *(54)*. This effect is due to the significant density differences between gases and liquids. In a slug flow with pure liquid reactant A in one phase and a gas phase of an equal volume of B, the conversion is strongly limited by the low molar quantity of the gas component. In order to compensate this shortage, various solutions can be considered.

A dilution of the liquid reactant A to a stoichiometric equivalence of A and B leads to a downstream purification separating product C from an excess solvent. On the other hand, increasing the volume fraction of the gas phase to a stoichiometric equivalence to the liquid substrate minimizes the capillary reactor's throughput and space-time yield substantially. In addition, large gas bubbles tend to disintegrate within slug flows, so no defined flow pattern can be generated *(45)*.

Another strategy is to feed the gas phase through a membrane into the capillary. For example, the oxidation of a single-phase flow has been successfully performed with high conversions *(55)*. In addition, commercially available tube-in-tube reactors, which can feed gas into a capillary with high permeability, have been used for single-phase gas-consuming reactions *(56–58)*. Anyhow, in multiphase systems, it is possible for a high gas feeding rate that tiny gas bubbles form at the capillary wall. It is so far unknown if these influence the existing slug flow.

Adding reaction gas into the reactor along the capillary with Y- or T-junctions is also a suitable option. However, awaiting the complete disappearance of the gas bubble in the triphasic flow leaves two phases remaining. If gas is injected again, it is necessary to ensure that the segments of the respective phases are not destroyed; otherwise, the advantageous properties of the slug flow cannot be kept. A gas supply through Y- or T-junctions is, therefore, unsuitable. Even the coaxial slug generators cannot provide a solution since the triphasic flow is created by surrounding the existing biphasic slug flow with the continuous (liquid) phase. A targeted single gas bubble injection would be required for this purpose.

In terms of scale-up, gas-consuming reactions are challenging. In a numbering-up, which suffers from minimal variations in residence time and phase ratios, the reaction rates of individual capillaries may vary slightly. In a capillary with slightly better conditions, the gas is rapidly consumed, leading to volume contraction and increasing residence time, which can result in more consecutive reactions. Whereas in a capillary with slightly worse conditions, less gas is consumed, and thus the residence time and conversion become smaller. This effect increases the inhomogeneities in the numbering-up. In gas-producing reactions, on the other hand, the opposite occurs so that reaction progress balances the residence times.

Therefore, a size-up in length is an alternative solution for gas-consuming triphasic reactions. However, if the size-up is combined with the requirement of gas feeding, no concepts are available for slug flows. Due to their fragile materials, tube-in-tube reactors are limited to a maximum length of 4 m and only small diameters (max. 1 mm). Hence, they are only suitable for small-scale studies. Furthermore, the influence of gas permeation on a multiphase flow is unknown.

This work uses a water-soluble homogeneous transition metal catalyst for gas-consuming reactions to avoid additional challenges arising from heterogeneous catalysts. For this purpose, an established rhodium complex with three 3,3',3''-phosphanetriyltris(benzenesulfonic acid) trisodium ligands (TPPTS) is used, which can be applied in hydrogenations besides its main application of hydroformylations. The resulting catalyst complex for simplification is titled Rh(TPPTS) *(59–64)*.

1.4 Resulting objectives in triphasic slug flow

Overall, a triphasic gas-liquid-liquid slug flow in capillaries seems profitable for multiphase reactions. In addition to the benefit of another functional phase, triphasic flow can be advantageous in the scale-up of slug flows. Since it has been shown that a triphasic flow preserves the advantageous slug pattern even at high volumetric flows, the size-up in length approach can be applied. However, this approach cannot be implemented for biphasic flows due to the transition to other less advantageous flow patterns (e.g., annular flow). For gas-consuming reactions, the question remains to which extent reaction gas could be fed in long capillaries to make the reaction most efficient.

Therefore, the following research questions arise, which will be answered in the corresponding main chapters of this thesis.

- *General:* What is the setup to establish a stable and reproducible triphasic slug flow and operate it under reaction conditions? Start-up: How long does it take to reach a steady state? How can a capillary reactor's residence time be estimated based on temperature profiles and gas expansion?
  In Chapter 2, the slug flow is first considered theoretically to provide a basis for the setup's geometries and procedures (especially the start-up). Then, the fundamental setup is briefly discussed, on which all following chapters are based. Specific additional equipment is presented in the respective chapters.
- *Gas introduction via permeation.* Is a gas feed via permeation feasible for long capillaries analogous to tube-in-tube reactors with fluorinated ethylene propylene (FEP) capillaries? How does permeation affect the flow pattern over long distances?
  In Chapter 3, it is shown that at long capillaries and elevated temperatures, reaction gas permeates out of polymer capillaries. Furthermore, it is demonstrated that permeation can be either suppressed or used to feed gas through the capillary wall. This way, gas can also be fed along long capillaries for gas-consuming reactions.
- *Gas introduction via electrolysis or valves.* Can single gas bubbles be integrated into an existing multiphase slug flow? Which gas injection method is appropriate for which application?
  Chapter 4 uses miniaturized solenoid valves and electrolytic cells to inject gas bubbles into an existing slug flow. It is investigated whether filling existing gas bubbles or generating new ones is preferable. Finally, selection criteria for gas feeding methods for capillary flows are given.
- *Slug flow detection.* Can triphasic flows be detected at high volumetric flow rates to determine local velocities and phase ratios?
  Chapter 5 investigates low-cost optical sensors for the non-invasive detection of triphasic capillary flow. A focus is set on exploiting light refraction in the detection and mathematical processing to enable robust detection of flow velocity and phase ratios.
- *Concentration detection in slug flows.* In addition to refraction, can optical sensors exploit the light absorption of reactants or products to detect local concentrations non-invasively?
  In Chapter 6, the sensors from Chapter 5 are extended to enable the detection of concentrations of dye molecules. These sensors are then used to observe the hydrogenation of the dye Sudan III to a colorless product.
- *Selective hydrogenation of vegetable oil.* Which additional challenges may arise from reactions? For example, is it possible to work in oxygen-free conditions? Can gas feeding counteract the lack of gas resulting from gas-consuming reactions?
  In Chapter 7, the selective hydrogenation of polyunsaturated vegetable oils is used as an example to reveal challenges of the long triphasic capillary reactor. Furthermore, hydrogen is fed into the capillary via permeation to increase the hydrogenation conversion.

Apart from Chapter 2, which provides a basis for all chapters, each chapter is independent and introduces the respective topic. In addition, cross-references are used to indicate connection points.

2 Theoretical study of slug flow and resulting setup

DEVELOPMENT OF A COMPRESSIBLE AND UNSTEADY UNIT CELL MODEL FOR START-UP AND OPERATION IMPROVEMENT IN THE EXPERIMENTAL SETUP

ABSTRACT

For triphasic slug flows in long capillaries, the influence of gas expansion becomes more relevant and could lead in interaction with the inertial force to dynamic variations. Therefore, a unit cell model is presented that includes expansion and inertia. For example, the start-up process can be considered, and favorable operating conditions can be identified. With axial velocity profiles in a steady state, mean residence times can be estimated, which are shortened by gas expansion and in hot reaction zones. In addition, a pressurized oil bath can counteract the radial expansion of polymer capillaries at high temperatures and pressures. Finally, the insights obtained from theoretical considerations are included in a principle setup, which provides a basis for further chapters.

This chapter is structured as follows:

- Motivation and state of the art
- Theoretical study of start-up and steady state of multiphase flow in capillaries
- Influence of capillary expansion
- Setup of a long triphasic capillary reactor
- Summary and conclusion

2.1 Motivation and state of the art

For implementing multiphase processes and reactions in capillary reactors with slug flow, predicting the resulting conditions for selecting the capillary (inner diameter, length) is helpful. Especially the pressure at the beginning of the capillary is relevant, which results from the pressure drop and the end pressure of the capillary. This influences the required equipment and the processes, for example, the gas-liquid mass transport, which depends on the local pressure. Besides complex computational fluid dynamics (CFD) simulations *(65–68)*, the simplified fast-track one-dimensional unit cell model was often used in the past. Here, the slug flow is divided into unit cells consisting of one segment of each phase. Within this cell, the pressure drop is determined based on experimental data and theoretical considerations. A summation of the pressure losses of all unit cells then gives the total pressure loss and, thus, also the capillary inlet pressure. The unit cell models are based on a theoretical consideration of liquid flows in a monolithic reactor loaded with particles by G. Wallis *(69)*. Several studies use this approach to develop pressure loss models for biphasic or triphasic slug flows. The main distinction is between flows with or without the wetting phase forming a wall film enclosing the disperse phase*. (16, 70–75)*

However, multiphase flows in long capillaries containing gases make the consideration more complex. Due to the long distances, the pressure drop is in a magnitude where an expansion of the gas segments may influence the local velocity. If there are also different temperatures along the capillary, this expansion of the gases may have an additional impact. Consequently, an axial velocity profile develops, which, on the one hand, influences the local pressure drop and, on the other hand, reduces the residence time within the capillary. Furthermore, due to the expansion, the flow experiences local acceleration so that inertial forces of the liquid phase could become relevant (in current models, inertia is neglected).

Thus, if the existing unit cell models are extended to include the expansion of gas segments and inertial forces, a mean residence time can be determined, contributing to the selection of a capillary length. Furthermore, if this model is considered non-stationary, the dynamic start-up behavior can be investigated, and it can be proven if unstable states could occur.

Therefore, a simplified model is created in the following that considers the gas expansion, the inertial forces of the liquid phases, and time dependence. Based on the results, the geometries of the capillary reactor used in this work are determined, and the start-up process is optimized. Subsequently, the basic setup for the following chapters is briefly presented. Only tubular capillaries are considered since they are commercially available in large quantities at low cost.

2.2 Theoretical study of start-up and steady state of multiphase flow in capillaries

An unsteady compressible unit cell model for multiphase slug flows in long capillaries is developed in the following. The model should achieve the following goals:

- Determine the influence of volume expansion or inertia force
- Dynamic behavior during the start-up process and unsteady states
- Influence of reactor length, diameter, viscosity, and pressure at the outlet
- Calculation of axial velocity profiles for estimation of mean residence times
- Influence of an axial temperature profile

With these insights, a capillary reactor can be designed and operated more efficiently.

2.2.1 Unit cell model for unsteady and compressible capillary flow

First, a unit cell consisting of a compressible gas segment and a combined liquid phase is considered. Then, within a short time δt, the gas and liquid phases are considered separately. While evaluating the liquid phase results in the actual velocity, the respective pressure is calculated from the gas phase.

In order to describe the complex multiphase problem, some assumptions are made; the most important are listed below:

- The flow is considered a block flow without a wall film.
- For gas-liquid-liquid flows, both liquid phases are combined into one, resulting in averaged properties (density, dynamic viscosity).
- The gas is compressible, but the mass is neglected. On the other hand, the liquid is incompressible, and the mass is considered.
- The inlet unit cell always has the same geometry and volume flow. Only the pressure is variable. This means that the liquid segment (incompressible) always has the same geometries (length, volume).

With all assumptions made (complete list in Appendix A), the force balance in the axial direction around the liquid phase is reduced to the pressure forces F_{pi} at the phase interfaces to the gas segments, the friction force F_{Fr} and the inertia force F_I (Figure 2.1).

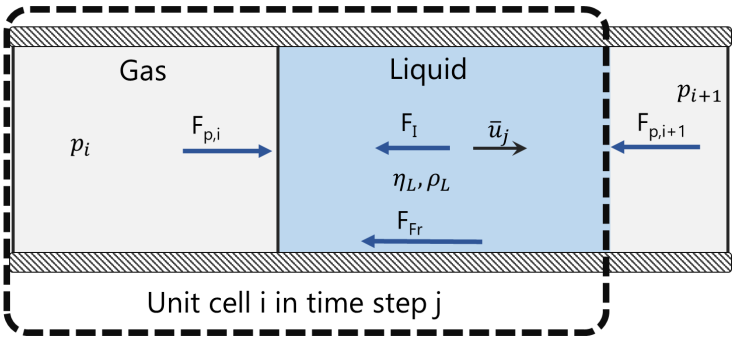

Figure 2.1. Force balance at the liquid phase in the simplified unit cell model. The forces involved (pressure, inertia, and friction) are each marked with blue arrows. i=unit cell identification starting with 1 at the capillary inlet. j=time step.

The frictional force F_{Fr} results from the product of the shear stress τ and the lateral surface A_L. The shear stress can be expressed for Newtonian fluids over the radial derivative of the axial velocity profile $u_{z,i}(r)$ of unit cell i at the capillary wall (r=R) and the dynamic viscosity of the fluid η_L (Eq. 2.1). *(76)*

$$F_{Fr} = \tau \cdot A_L = -\eta_L \frac{\partial u_{z,i}(r)}{\partial r}\bigg|_{r=R} \cdot A_L \tag{2.1}$$

The velocity profile $u_{z,i}(r)$ is assumed to be parabolic as in the derivation of the Hagen-Poiseuille law *(77)*. Even if this is not true at the interfaces, other models using Hagen-Poiseuille to describe the friction fraction in slug flows showed good agreement with experimental data *(16, 70, 71)*. By integrating over the cross-sectional area A_{cs}, the mean velocity ū can be used to describe the derivative of the velocity at the capillary wall (Eq. 2.2).

$$\frac{\partial u_{z,i}(r)}{\partial r}\bigg|_{r=R} = -4\bar{u} \cdot \frac{1}{R} \tag{2.2}$$

As a result, the friction force can be calculated as follows.

$$F_{Fr} = 8\eta_L \cdot \bar{u}_j \cdot \pi \cdot L_L \tag{2.3}$$

The pressure forces result from the product of the cross-sectional area A_{cs} and the respective pressures p_i at the phase interface (Eq. 2.4).

$$F_{pi} = p_i \cdot A_{CS} \tag{2.4}$$

The inertial force F_I is calculated by the acceleration a_j of the liquid segment in time step j and the mass of the liquid segment m_L, which can be determined by the density ρ_L and the volume V_L of the liquid segment (Eq. 2.5).

$$F_I = m_L \cdot a_j = \rho_L \cdot V_L \cdot a_j \tag{2.5}$$

The forces described can be correlated in a balance of forces (Eq. 2.6).

$$F_{pi} = F_I + F_{Fr} + F_{pi+1} \tag{2.6}$$

The average velocity $\bar{u}_j$ for the respective time step j can be determined via the velocity of the fluid from the previous time step (j-1) and the acceleration a_j with the time difference δt between the two time steps (Eq. 2.7).

$$\bar{u}_j = \bar{u}_{j-1} + a_j \cdot \delta t \tag{2.7}$$

If the forces (Eq. 2.3-2.5) are inserted into the force balance (Eq. 2.6) and additionally equation 2.7 is rearranged to the acceleration a_j and also inserted into equation 2.6, equation 2.8 results for the mean velocity of the liquid segment $\bar{u}_j$.

$$\bar{u}_j = \frac{\bar{u}_{j-1} + \frac{\delta t}{m_L} A_{cs} \Delta p}{1 + 4 \frac{\delta t}{m_L} \eta_L \frac{A_L}{R}} \tag{2.8}$$

Except for the pressure drop Δp, all necessary values are known from the substance system or the capillaries' geometry. For the pressure drop Δp, the pressure of the gas segment upstream and downstream of the liquid segment must be calculated. For this purpose, the volume change of the compressible gas segment within the time step δt is required. The length of the gas segment may be changed within one time step due to the different velocities of the surrounding liquid segments (Figure 2.2).

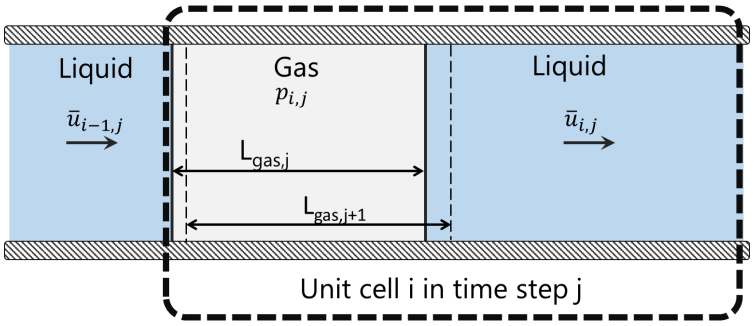

Figure 2.2. Change of the gas volume within one time step due to different velocities of the liquid segments. The vertical dashed lines indicate the shift of the phase interface after a time step.

The new resulting gas volume $V_{g,j}$ of time step j is obtained from the length of the gas segment from the previous time step $L_{g,j-1}$ and the respective mean velocities $\bar{u}_{i,j-1}$ of the previous (i-1) and subsequent (i) liquid segments from the previous time step (j-1). The velocities are each multiplied by the time interval δt to determine the distance displaced and the cross-sectional area A_{CS} to determine the corresponding volume (Eq. 2.9).

$$V_{g,j} = L_{g,j} \cdot A_{cs} = \left(L_{g,j-1} + \left(\bar{u}_{i,j-1} - \bar{u}_{i-1,j-1}\right)\delta t\right) \cdot A_{cs} \tag{2.9}$$

The resulting new pressure $p_{g,j}$ from the volume change is calculated according to the ideal gas law and the pressure and volume of the gas segment from the previous time step (j-1) (Eq. 2.10).

$$p_{g,j} = p_{g,j-1} \frac{V_{g,j-1}}{V_{g,j}} \tag{2.10}$$

Using the main equations for the mean velocity of the liquid phase (Eq. 2.8) and the pressure of the gas segment (Eq. 2.10), several unit cells can be linked together, and consequently, it is possible to simulate slug flows in long capillaries. Furthermore, with appropriate initial conditions, the pressure and velocity of each unit cell can be determined at any time.

Since the flow can only pass within a given capillary length, boundary conditions are required for the inlet and outlet of the capillaries.

Since it is assumed that each newly inserted unit cell has the same geometry and enters the capillary at the same velocity, a constant velocity is initially assumed until the complete unit cell has entered the capillary. Thus, a new unit cell is added to the system when the first unit cell at the beginning of the capillary has passed the distance of an initial unit cell. The newly inserted unit cell is considered independently with the previously mentioned equations in the following time steps. The new unit cell is assigned to the initial velocity $\bar{u}_{in}$ resulting from the incoming volume flow $\dot{V}$ and the capillary cross-section A_{CS}. Then, the pressure of the gas segment $p_{1,j}$ is estimated by the sum of the pressure of the previous unit cell $p_{2,j}$ and the pressure drop of the liquid phase according to the Hagen-Poiseuille equation (Appendix A, Eq. A.2).

At the capillary outlet, the liquid segment is trimmed according to the distance passed in the previous time interval and considered in calculating the mean velocity. A given end pressure p_{end} is used as the reference pressure. Once the liquid segment has completely left the capillary, the pressure of the remaining gas segment is set to the end pressure. As soon as it has also left the capillary, the exiting unit cell is no longer considered, and the liquid segment of the following cell is trimmed.

Since the start-up process is to be represented, all unit cells in the capillary at time t=0 are considered to be resting ($\bar{u}=0$) and with equalized pressure ($p(z)=p_{end}$). The number of unit cells in the capillary can be chosen freely so that both a completely filled capillary and an empty capillary can be examined during the start-up process. For the empty capillary, a minimum number of three unit cells is used for programming reasons.

2.2.2 Influence of volume expansion and inertia in start-up

The derived model is now used to evaluate the influence of gas expansion and inertial force on the start-up process. For this purpose, the time pressure profile at the inlet of the capillaries and the velocity profile at the last unit cell in a 20 m long capillary with an inner diameter of 1 mm were considered as an example. The profiles were calculated on the one hand as described in 2.2.1, taking into account the inertia force and, on the other hand, without inertia force (for details, see Appendix A).

Figure 2.3 shows the pressure profiles at the inlet of the capillary over time. A substantial pressure increase can be observed at the beginning for both cases. However, the increase is linear and slower for the empty capillary (left) than for the filled capillary (right). In contrast, the filled capillary (right) builds up a higher pressure more quickly since more liquid segments are being moved, and thus the frictional forces to be overcome are greater. After a maximum, the pressure drops to a small local minimum and converges to a steady state.

The influence of the inertia force appears very small at first sight. The maximum absolute deviation of both models is 407 Pa in the studied case, which appears within the first 0.1 s. In the following time, the deviation decreases to $\ll 1$ Pa. The deviation in the filled capillary is, on average, five times higher.

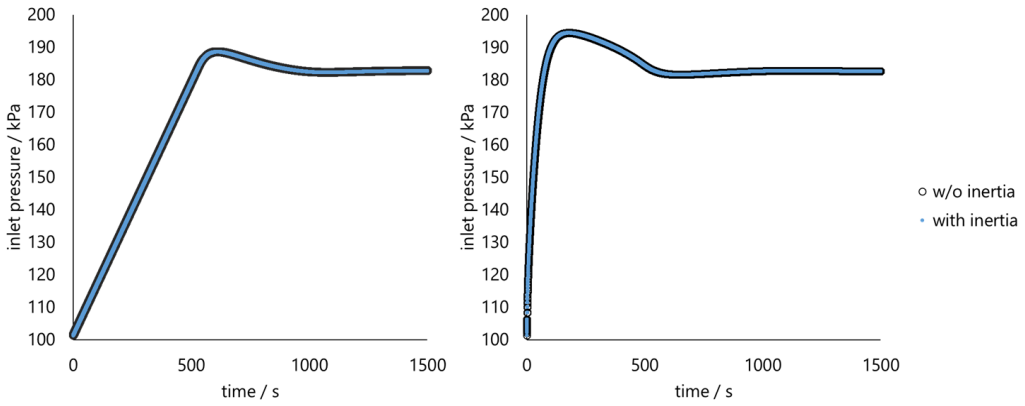

Figure 2.3. Inlet pressure during the start-up process using models with and without inertia. Left: initially empty capillary. Right: initially completely filled capillary. 20 m capillary length, 1 mm inner diameter, L_{gas}=0.5 mm, L_{liq}=1mm, $\dot{V}_{tot}$=1.8 mL/min, p_{end}=1.013 bar, ρ_{liq}=800 kg/m³, $\bar{\eta}_{liq}$=5 mPas, δt=0.0125 ms.

In the first 75 ms of the start-up process of the empty capillary, a fading oscillation in the initial pressure and the velocity of the last unit cell can be observed (Figure 2.4). These oscillations are due to the inertia of the initially resting liquid segments. These oscillations are not observed in the model without inertial force, but both values converge after about 50 ms. Therefore, these small-scale oscillations are not relevant for estimating the start-up behavior in the time range from minutes to hours.

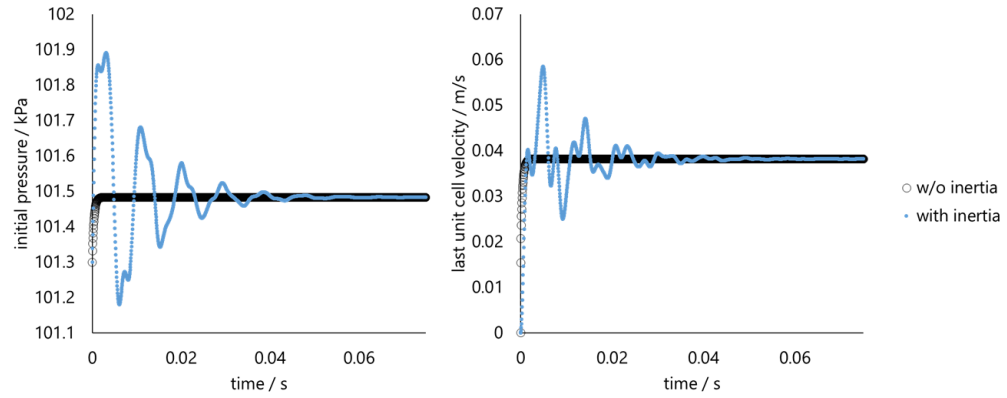

Figure 2.4. Influence of liquid phase inertia on the inlet pressure (left) and velocity of the last unit cell (right) during the first 75 ms of a start-up process in an empty capillary. 20 m capillary length, 1 mm inner diameter, L_{gas}=0.5 mm, L_{liq}=1mm, $\dot{V}_{tot}$=1.8 mL/min, p_{end}=1.013 bar, ρ_{liq}=800 kg/m³, $\bar{\eta}_{liq}$=5 mPas, δt=0.0125 ms.

However, despite the more straightforward formula for the mean velocity in the model without inertia (see Appendix A), smaller time intervals must be selected (approx. one-tenth) to avoid negative volumes caused by different velocities of two subsequent liquid cells. This is because even if the influence of the inertial force is minimal, it dampens the velocity on a small time scale, and therefore negative volumes occur less. It is, therefore, advisable to include inertia in the model, despite its small influence, as this allows the simulation to run faster and more robustly. Therefore, inertia is included in all of the following considerations.

2.2.3 Dynamic behavior during the start-up process and unsteady states

As observed in Figure 2.3, the filled capillary reaches a steady state faster in the start-up process since it is not necessary to wait for the capillary to fill. However, a higher pressure maximum is formed during the start-up of the filled capillaries. The higher pressure increases the molar amount of gas in the unit cell entering the capillary compared to the previous ones (since the introduced gas bubble length is assumed to be constant). This higher amount of substance provides a more significant potential to expand and therefore accelerates the flow. This can be seen by a temporally shifted peak in the velocity (Figure 2.5). This plotting can be used to estimate when a steady state is reached to start measurements, for example.

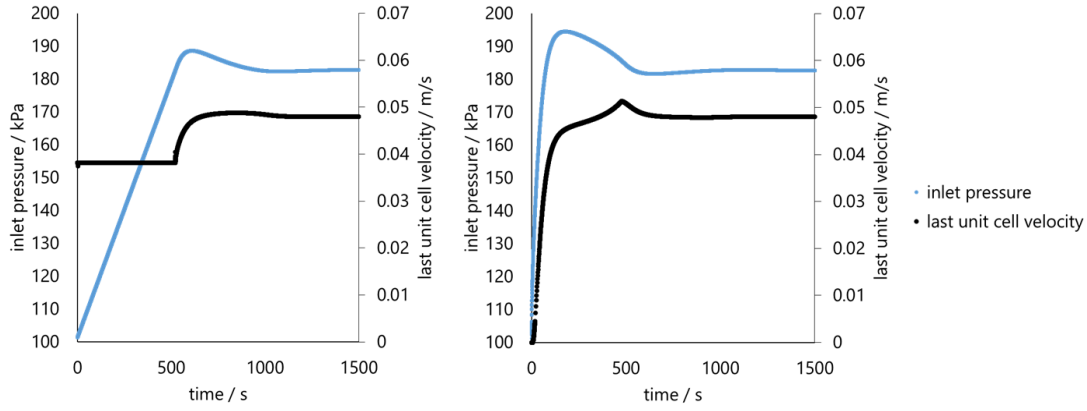

Figure 2.5. Inlet pressure and velocity of the last unit cell during the start-up process. Left: initially empty capillary. Right: initially completely filled capillary. 20 m capillary length, 1 mm inner diameter, L_{gas}=0.5 mm, L_{liq}=1mm, $\dot{V}_{tot}$=1.8 mL/min, p_{end}=1.013 bar, ρ_{liq}=800 kg/m³, $\bar{\eta}_{liq}$=5 mPas, δt=0.0125 ms.

In real applications, however, the rapid pressure increase can lead to fluctuations. The gas is usually fed into the system via mass flow controllers (MFC), which are connected to the slug generation via tubes or pipes. If the pressure at the start of the capillaries changes, the pressure in the supply system needs to be built up or released first. With small volume flows and large volumes in the supply pipe system, adjusting to a new pressure requires a certain time. The gas supply system, therefore, reacts slowly to pressure changes. This can be counteracted by keeping the volume of the gas supply as small as possible. Nevertheless, large pressure fluctuations in the capillary represent an increased risk of unstable conditions in the real process. Therefore, in this theoretical consideration, it is desirable to reduce rapid pressure variations. Therefore, a start-up process of a multiphase capillary with an empty capillary is more advantageous, even if a compromise must be made with the time to reach a steady state. It has the additional advantage of keeping the capillary empty at rest. For example, a fluid at rest may interact with the capillary wall (e.g., water absorption) and change the wetting behavior, or catalysts may deposit.

The pressure and velocity profiles are similar to the shapes shown in Figure 2.5 for all other parameters, such as capillary length, volume flow rate, and viscosity. However, the position and height of the maximum values differ. Therefore, to improve the evaluation of the influence of different parameters for the maximum pressure increase, the relative deviation $\widetilde{P}$ of the maximum pressure (p_{max}) from the final steady-state pressure (p_{ss}) according to Eq. 2.11 is

used for different parameters in the following. The pressure at the capillary outlet p_{end} is subtracted to evaluate the absolute pressure change.

$$\tilde{P} = \frac{p_{max} - p_{end}}{p_{ss} - p_{end}} \tag{2.11}$$

Figure 2.6 (left) shows the initial pressure profiles for different lengths. The longer the capillary, the more unit cells it contains, and the greater the pressure and the pressure peak. If the respective maximum is related to the pressure at a steady state according to Eq. 2.11, it becomes apparent that the maximum is relatively more significant with increasing capillary length (Figure 2.6, right). For example, the maximum pressure for a 125 m capillary is about 30% higher than the steady state pressure, while for a 40 m capillary, it is only 20%. In the start-up of an empty capillary, the relative pressure deviation is always lower (about half), which proves that this start-up is more advantageous.

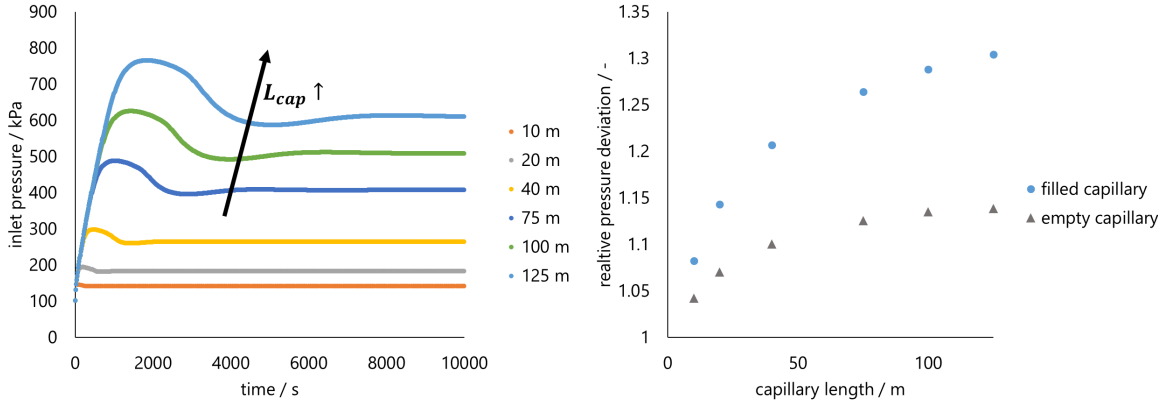

Figure 2.6. Left: Time-depending pressure profile at the inlet of the capillary for a start-up of a filled capillary at different capillary lengths. Right: Relative pressure deviation of filled and empty capillaries during start-up for different capillary lengths. 1 mm inner diameter, L_{gas}=0.5 mm, L_{liq}=1mm, $\dot{V}_{tot}$=1.8 mL/min, p_{end}=1.013 bar, ρ_{liq}=800 kg/m³, $\bar{\eta}_{liq}$=5 mPas, δt=0.0125 ms.

A change in viscosity and inlet flow rate results in similar plots and are not discussed in detail here. However, the corresponding graphs can be found in Appendix A.

In contrast, increased pressure at the outlet of the capillary p_{end} has a stabilizing effect (see Figure 2.7). The pressure peaks are significantly lower at higher outlet pressures. Although the pressure difference between the inlet and outlet are almost identical regardless of the outlet pressure, higher reference pressures mitigate the expansion of the gas and, thus, the pressure peak. For example, if a slug flow has a pressure drop of 1 bar along the capillary, the gas volume would double according to Eq. 2.10 at an outlet pressure of 1 bar but would only increase by 10% at an outlet pressure of 10 bar. Thus, if a process in a long capillary is independent of the pressure, it is advisable to choose an elevated pressure. However, a compromise between equipment and stability must be made.

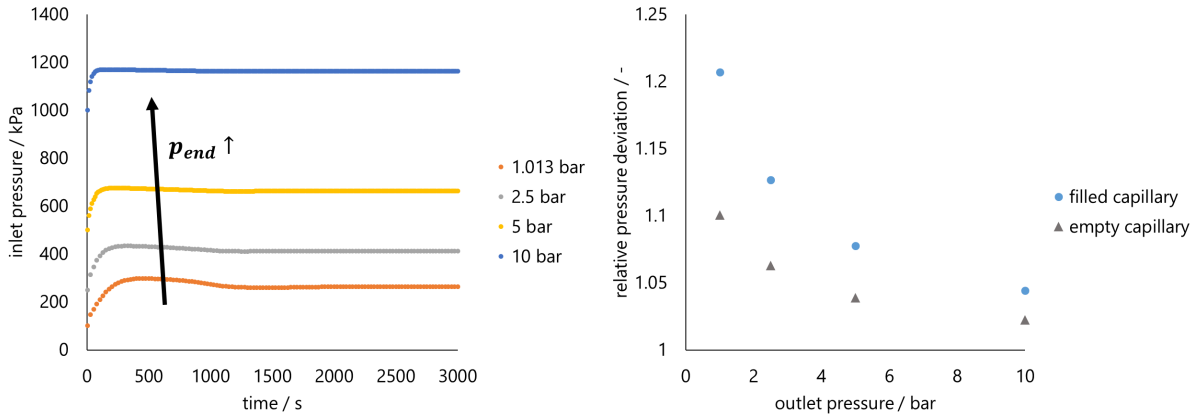

Figure 2.7. Left: Time-depending pressure profile at the inlet of the capillary for a start-up of a filled capillary at different outlet pressures. Right: Relative pressure deviation of filled and empty capillaries during start-up for different outlet pressures. 40 m capillary length, 1 mm inner diameter, L_{gas}=0.5 mm, L_{liq}=1mm, $\dot{V}_{tot}$=1.8 mL/min, ρ_{liq}=800 kg/m³, $\bar{\eta}_{liq}$=5 mPas, δt=0.0125 ms.

A differentiated analysis of the inner diameter is complicated since a variation is accompanied by changing the volume flow or the average velocity and, thus, the residence time. However, reducing the volume flow is not desirable in considering scale-up. Therefore, in Figure 2.8, the flow rate and the capillary length were kept constant while the inner diameter was varied. A decrease in diameter leads to a drastic increase in pressure. If the same residence time is desired, the thinner capillary would need to be lengthened, increasing the pressure dramatically. A large capillary diameter would therefore be advantageous. However, with larger diameters, the advantageous intense mixing of the slug flow is diminished, or the flow pattern may not be formed.

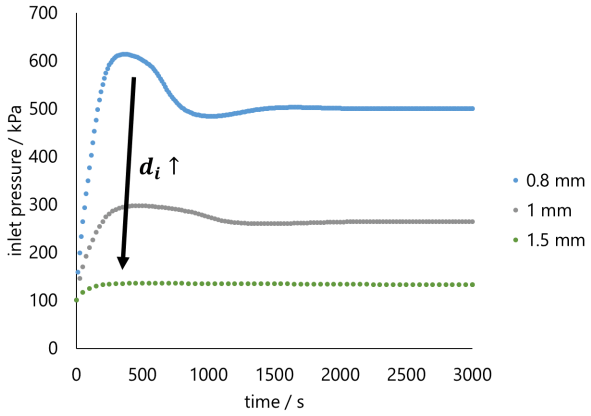

Figure 2.8. Time-depending pressure profile at the inlet of the capillary for a start-up of a filled capillary with different inner diameters. 40 m capillary length, L_{gas}=0.5 mm, L_{liq}=1mm, $\dot{V}_{tot}$=1.8 mL/min, p_{end}=1.013 bar, ρ_{liq}=800 kg/m³, $\bar{\eta}_{liq}$=5 mPas, δt=0.0125 ms.

Therefore, a compromise between process intensification, volume flow, and pressure must be made to choose the capillary. Whether and to what extent a slug flow is stable even with capillary diameters >1 mm depends on the substance system. Khan et al., for example, have considered substance systems that form a stable slug flow even in tubes with an inner diameter of 3.2 mm (*31*). Since the set-up developed here is designed to be as flexible as possible for numerous applications, an inner diameter of 1 mm is chosen for all the following

considerations. However, if a specific system should be scaled up, it is reasonable to increase first the diameter to a point where the desired slug flow is stable. Then, a reduction of the intensive contact could be counteracted in a second step by increasing the volume flow and the capillary length.

2.2.4 Temperature influence on axial velocity and pressure

The model considered previously observes the flow at a constant temperature. However, in real applications, it is more likely that the slug flow is generated at room temperature and then led into a hot reaction zone. Because of the small dimensions, the temperature change can be assumed to be instantaneous, but the temperature critically affects the flow conditions. In the model shown previously, an increase in temperature causes additional expansion of the gas segment. In the liquid segment, the viscosity, in particular, decreases at higher temperatures, which reduces the frictional force and, thus, the pressure drop.

To address these effects, two hot zones ($T_1 > T_0$) are implemented along the capillaries, according to Figure 2.9. The interruption between the zones represents a possible sampling point.

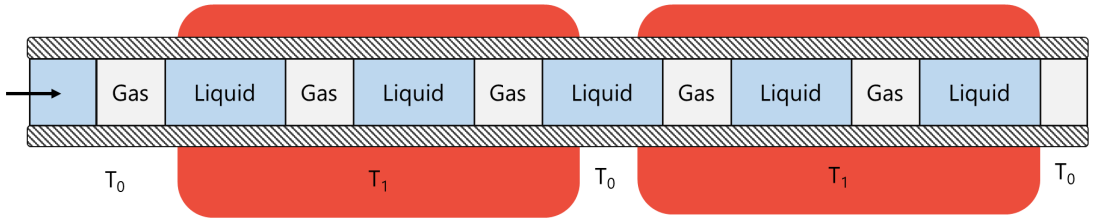

Figure 2.9. Schematic illustration of a gas-liquid block flow with two heated zones at T_1, whereas the rest of the capillary is at T_0.

To consider the temperature profile in the unit cell model, Eq. 2.10 is modified to describe the pressure in the gas bubble. Once a gas segment has wholly entered the hot zone, the pressure $p_{g,j}$ for that time step j is calculated according to Eq. 2.12.

$$p_{g,j} = p_{g,j-1} \frac{V_{g,j-1}}{V_{g,j}} \cdot \frac{T_1}{T_0} \tag{2.12}$$

The volume $V_{g,j}$ calculated in this time step also considers the expansion of the volume from the previous time step $V_{g,j-1}$ corresponding to Eq. 2.13 (analogous to Eq. 2.9).

$$V_{g,j} = V_{g,j-1} \cdot \frac{T_1}{T_0} + \left((\bar{u}_{i,j-1} - \bar{u}_{i-1,j-1}) \delta t \right) \cdot A_{cs} \tag{2.13}$$

For the transition from the hot zone to a cold zone, the temperatures are used correspondingly vice versa.

For the velocity of the liquid segment, Eq. 2.8 remains valid. However, the dynamic viscosity is adjusted according to the temperature. For the following calculations, a substance system

consisting of a 1:1 mixture of 1-hexanol and water is used as an example; the temperature-dependent viscosities can be found in Appendix A.

The influence of the temperature profile applied in this manner will be discussed using an example. According to Figure 2.9, two hot zones (T_1=100 °C, first zone: 4-18 m, second zone: 22-38 m) are integrated along a 40 m long capillary. The remaining cold sections each have a temperature of T_0=25 °C.

In Figure 2.10, the time pressure profile of the start-up of an empty capillary is shown on the left. Different from before, the region in front of the maximum is no longer continuously linear. The different slopes result from the local viscosity change and, thus, the pressure losses. A change in the slope represents the entry of the first unit cell in a different temperature range. The axial pressure and velocity profiles in a steady state are shown on the right. The temperature sections are also reflected in the axial pressure profile slopes. These pressure profiles could help collect samples, using counterpressure to allow the flow to exit slowly at any axial location.

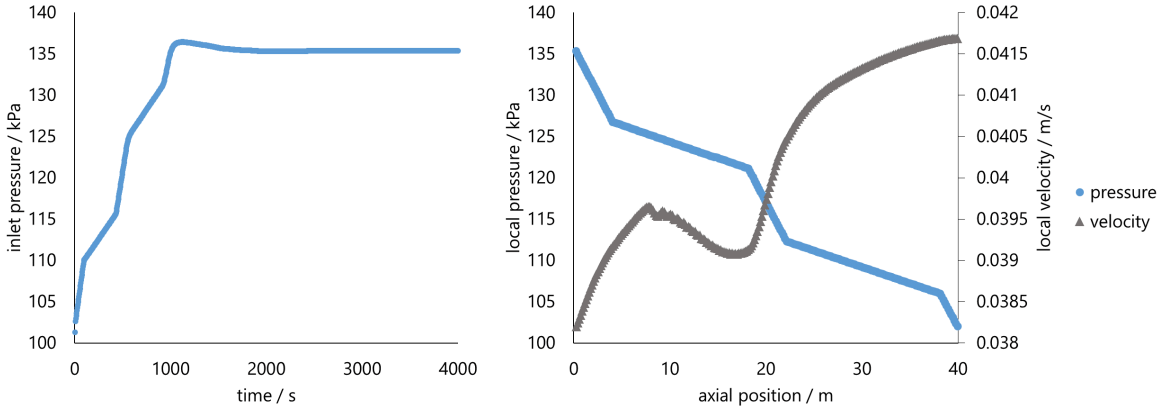

Figure 2.10. Left: Time-depending pressure profile at the inlet of the capillary for a start-up of an empty capillary. Right: Axial pressure and velocity profiles in steady state. Temperature profile applied with two hot zones (T_1=100 °C, first zone: 4-18 m, second zone: 22-38 m), all other sections with T_0=25 °C. 40 m capillary length, 1 mm inner diameter, L_{gas}=0.5 mm, L_{liq}=1mm, $\dot{V}_{tot}$=1.8 mL/min, ρ_{liq}=800 kg/m³, δt=0.0125 ms, viscosity variable according to Appendix A.

The hot zone causes the local velocity to increase first, decrease before entering the cold zone and increase again afterward. The temperature profile thus influences the local velocity, and minima or maxima of the velocity could occur. The axial velocity profile can, in turn, be used to calculate the mean residence time in the capillary.

2.2.5 Axial velocity profiles for mean residence times

When a reaction is transferred from a batch reactor to a capillary, known reaction times are transferred to a residence time in the capillary to define the length and volume flow. For this purpose, the average residence time $\bar{\tau}$, the incoming volume flow $\dot{V}_{tot}$ and the capillary geometry A_{CS} and L_{cap} are often estimated according to Eq. 2.14.

$$\bar{\tau} = \frac{A_{CS} \cdot L_{cap}}{\dot{V}_{tot}} = \frac{L_{cap}}{\bar{u}_{in}} \tag{2.14}$$

Due to the previously discussed volume expansion, the flow accelerates (also in a steady state), so the actual mean residence time is lower than Eq. 2.14.

Instead of the incoming velocity $\bar{u}_{in}$, an average axial velocity $\bar{U}$ can be used via integration (Eq. 2.15). The axial velocity profiles from the unit cell model can be used for the integration.

$$\bar{U} = \frac{1}{L_{cap}} \int_0^{L_{cap}} \bar{u}_z \, dz = \frac{1}{L_{cap}} \sum_{i=1}^{N} \bar{u}_{z,i} \Delta z_i \tag{2.15}$$

Since the local velocity $\bar{u}_{z,i}$ is known for each unit cell i within its axial boundaries Δz_i, the integral can be transformed into a summation for the total number of unit cells N.

Taking the axial velocity profiles in Figure 2.11 as an example, the mean residence time can be calculated taking into account the flow acceleration. While the velocity almost doubles for the viscous medium (10 mPas), the velocity increases slightly for the low-viscosity liquid (0.5 mPas). The stronger acceleration is caused by a higher frictional force of the more viscous fluid and, thus, the higher inlet pressure, which relaxes along the capillary.

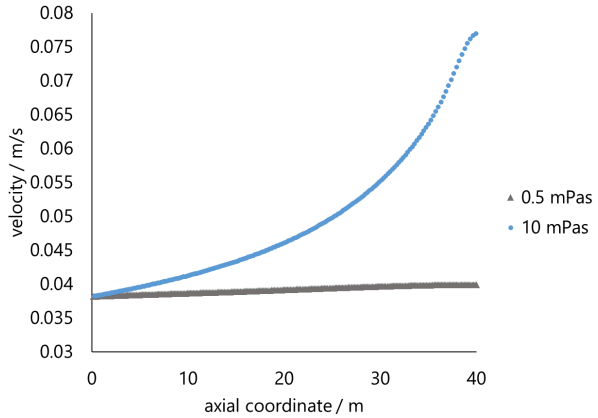

Figure 2.11. Stationary axial velocity profiles for 0.5 mPas and 10 mPas dynamic viscosity of the liquid phase. 40 m capillary length, 1 mm inner diameter, L_{gas}=0.5 mm, L_{liq}=1mm, $\dot{V}_{tot}$=1.8 mL/min, p_{end}=1.013 bar, ρ_{liq}=800 kg/m³, δt=0.0125 ms.

Table 2.1 shows the resulting theoretical mean residence times based on these axial velocity profiles and the deviations from the residence time assuming no volume expansion. For a thin fluid, the relative deviation of the residence time change with a 25 s difference is only 2.4%

smaller than the residence time without expansion. With a dynamic viscosity of 10 mPas, the residence time is reduced by 240 s and thus by 22.9%. If a residence time in the capillary without expansion would be assumed, a transfer of a reaction from the batch into the capillary would be accompanied by a significantly shorter reaction time and complicate a comparison. With the calculation of the axial velocity profiles, the length of the capillaries can be better estimated to achieve the desired residence time.

Table 2.1. Calculated mean residence times (Eq. 2.14 and 2.15) for different axial velocity profiles resulting in different viscosities and temperature profiles. 0.5 mPas and 10 mPas correspond to the axial profiles shown in Figure 2.11. The temperature profile corresponds to the axial velocity profile of Figure 2.10 (right). In 40 m capillaries with $\dot{V}_{tot}$=1.8 mL/min.

	mean residence time / s	**relative change**
no expansion	1047	0.0%
0.5 mPas	1022	-2.4%
10 mPas	807	-22.9%
temperature profile	996	-4.8%

Gas is often consumed in gas-liquid reactions, which can decrease the molar amount of gas in the gas segment. The gas bubble may be consumed entirely depending on the reaction kinetics and selected concentrations. This would have the opposite effect. The residence time would increase, which is especially disadvantageous for undesired consecutive reactions. However, the unit cell model can also integrate sources and sinks for the gas. If the reaction kinetics are known, the shrinkage of the gas bubble can be taken into account. However, a source can also be considered, for example, in gas-consuming reactions or gas permeation through the capillary wall (Chapter 3). The more data available, the more accurate the prediction of the mean residence time.

2.3 Influence of capillary expansion

Pressure differences between the inside and outside of a capillary lead to stress on the material, causing it to deform. Increased temperatures also lower the E-modulus (often called Young's modulus) and cause the material to expand by mechanical inflation. Both of these can cause the inner diameter to change along the capillary. Whether elastic deformation may affect the flow, the elastic expansion and its effect on the volume is estimated for some cases.

For this purpose, the radial expansion ϵ_r of a rotation-symmetric tube is considered according to Hooke's law, neglecting axial stresses. The radial shift Δr_x at any radial location x of the capillary wall can be calculated using the E-modulus E, the stresses in the tangential (σ_{tt}) and radial (σ_{rr}) directions, and the Poisson's ratio υ. In case of temperature change, the additional expansion of the material can be expressed with the coefficient of thermal expansion α_T and the temperature differential ΔT (Eq. 2.16). *(78)*

$$\epsilon_r \approx \frac{\Delta r_x}{r_x} = \frac{1}{E}(\sigma_{tt} - \upsilon \cdot \sigma_{rr}) + \alpha_T \cdot \Delta T \tag{2.16}$$

The differential equation (Eq. 2.17) expresses the stresses σ_{rr} and σ_{tt} *(79)*.

$$\frac{d\sigma_{rr}}{dr} + \frac{\sigma_{rr} - \sigma_{tt}}{r} = 0 \tag{2.17}$$

The following equations (Eq. 2.18 and 2.19) solve the differential equation with unknown constants C_1 and C_2 *(79)*.

$$\sigma_{rr} = C_1 + \frac{C_2}{r^2} \tag{2.18}$$

$$\sigma_{tt} = C_1 - \frac{C_2}{r^2} \tag{2.19}$$

Based on exposure to an applied internal pressure p_i, the following boundary conditions are obtained at the inner wall coordinate r_i and the outer wall coordinate r_o (Eq. 2.20 and 2.21).

$$\sigma_{rr}(r = r_i) = -p_i \tag{2.20}$$

$$\sigma_{rr}(r = r_o) = 0 \tag{2.21}$$

From Eq. 2.16 and the aforementioned boundary conditions, the radial displacement Δr_x of any coordinate x in the wall material is given by Eq. 2.22.

$$\Delta r_x = \frac{r_x}{E} \cdot \frac{p_i \cdot {r_i}^2}{{r_o}^2 - {r_i}^2} \left(\frac{{r_i}^2}{{r_o}^2} (1 + \upsilon) + 1 - \upsilon \right) + r_x \cdot \alpha_T \cdot \Delta T \tag{2.22}$$

For the displacement of the inner radius Δr_i relevant here, the radius r_x can be substituted with r_i accordingly.

Table 2.2 lists the used material data at 23 °C and 100 °C. 23 °C is used as the reference point for expansion.

Table 2.2. Physical and thermal properties of FEP. The E-modulus at 100 °C was estimated using the E-modulus of FEP at room temperature and the temperature dependence of polytetrafluoroethylene PTFE.

Temperature	**23 °C**	**100 °C**	**Sources**
E-Modulus / GPa	0.7	0.3	*(80, 81)*
Poisson's ratio / -	0.36	0.48	*(80)*
Coefficient of thermal expansion / 1/K	0.001 (temperature independent)		*(82)*

Based on the change of the inner radius, a relative change of the inner volume with respect to the original capillary with a 1 mm inner diameter and a wall thickness of 293.75 µm is calculated.

Table 2.3 shows the relative volume change of a 1 mm inner diameter FEP capillary for different pressures and temperatures. At the reference temperature (no change in E-modulus, Poisson's ratio, thermal expansion) of 23 °C, the relative deviation for pressures up to 10 barg is negligible (<1%). The influence is more considerable at high pressures and temperatures of

100 °C. For example, at a pressure of 50 barg and increased temperature, the volume of the capillary changes by more than 11%. In an application scenario, if a reaction needs to be operated at 50 bar and the capillary is passed from room temperature to a heating zone, the local volume in the hot zone will change by more than 7%. This may impact the pressure profile, so the elasticity and thermal expansion of the capillary should be considered for such harsh conditions. However, this volume change would have a damping effect on the pressure maxima in the start-up process.

Table 2.3. Change of inner radius and relative change of the capillary volume as a function of temperature and pressure. All values in percent reflect the relative volume change, whereas all other values are temperature or pressure. The capillary volume change is calculated by the ratio of the cross-sectional areas with and without capillary inflation.

	inner radius change / µm		Capillary volume change / -	
Pressure / barg	23 °C	100 °C	23 °C	100 °C
1	0.19	4.32	0.08%	1.73%
5	0.96	6.18	0.38%	2.49%
10	1.92	8.52	0.77%	3.43%
20	3.83	13.19	1.54%	5.34%
50	9.58	27.20	3.86%	11.15%

Still, it is questionable whether such harsh conditions can be implemented in a FEP capillary. The heat deflection stability of FEP decreases sharply at high temperatures. While FEP is still stable up to 181 bar at 51 °C, at 70 °C, it is only stable up to 45 bar, and at 150 °C, only to 18 bar *(82, 83)*. When this stability limit is exceeded, the material deforms irreversibly, and material failure can occur. If a polymer capillary is to be operated at high temperatures and pressures, it is, therefore, advisable to counteract this in the heated zone with increased external pressure. For example, the capillary can be led into a heated pressurized oil bath to reduce the pressure difference and, thus, the stress on the material, especially at high temperatures.

2.4 Setup of a long triphasic capillary reactor

The general setup is presented in this chapter, which will be used as a basis in the following chapters. Modifications will be mentioned in the relevant sections. The previous theoretical considerations result in an inner capillary diameter of 1 mm, based upon which the rest of the setup is designed.

The capillary reactor for a triphasic gas-liquid-liquid slug flow should be able to be run with heated zones and under pressure, which according to Chapter 2.3, requires an external backpressure in the heating zone. Furthermore, it should be possible to take samples along the capillary. The length of the capillary should be as flexible as possible.

The capillary reactor consists of up to 40 m long FEP capillary (1 mm ID, 1/16" OD), which on the one hand, is well wetting for hydrophobic solvents like hexanol, and on the other hand, it is optically transparent. Since polymers tend to permeate gas at high temperatures and pressure differences (see Chapter 3) and to avoid stress in the material (see Chapter 2.3), the

capillary is placed in a pressurized oil bath. This prevents the permeation of reaction gas outside the capillary and the permeation of atmospheric oxygen into the capillary, which could deactivate a catalyst (Chapters 6.5 and 7.3). The oil bath is in a steel housing that can be electrically heated from the outside (HAT 22, Horst, Lorsch, Germany), which is insulated from the environment with mineral wool. The performance of the heater can be found in Appendix C.

Since the steel housing is also to permeate gases into the capillary, the internal volume is kept as small as possible to avoid large hold-ups of explosive or toxic gases. In addition, the steel is austenitic stainless steel (V4A) to prevent hydrogen embrittlement. An external gas supply can provide gases or pressurize the oil bath. The steel housing is divided into four individual elements that are stacked together. Each element can contain up to 20 m of a capillary. Depending on the requirements, several elements can be used to increase the capillary length. However, each element can also be filled with a different medium, e.g., different reaction gases, which can be used at other axial locations. Thus, the highest possible flexibility is achieved with this setup. Figure 2.12 shows the closed steel housing with all four elements on the left and a single open element with an internal capillary on the right. Each element (R1-R4) has an input and output and is equipped with a temperature sensor (TI). A technical drawing of one reactor element can be found in Appendix B.

Figure 2.12. Left: Main capillary reactor. This steel housing is electrically heated and represents the reaction zone. The steel housing is divided into four individual elements that are stacked together. A single element with an inner capillary is shown on the right.

For the following chapters, two elements were equipped with 5 m capillaries each and the other two with 10 m and 20 m. Thus, a maximum reaction zone of 40 m is possible with this configuration. In between those elements, the capillary can be led out, and sensors can be connected, or samples can be taken through a valve (indicated with QI in the flow sheet, Figure 2.13). In these sections, between the elements, the flow patterns can be observed and recorded with a camera (DFK37BUX, Imagingsource, Bremen, Germany).

A small vessel (B2) is set with nitrogen to the reactor's pressure at the sampling point for taking samples. The pressure is estimated using the axial pressure profiles obtained with the unit cell model (Chapter 2.2) or the measured pressure at the capillary's inlet and the outlet, measured with pressure indicators (PI1, PI2, D9A-05, AirCom, Ratingen, Germany). If several samples are to be taken between the reactor elements, the sample at the capillary end is taken

first to maintain the flow in the remaining capillary. Subsequently, the respective previous sampling point is to be used.

The syringe pumps P1 and P2 (SyrDos2, Hitec-Zang, Herzogenrath, Germany) provide a continuous volume flow of the liquid phases, while the flow sensors (FI1, FI2, SLI-2000, Sensirion, Chicago, IL, USA) additionally observe these liquid flow rates. A mass flow controller (FIC1, F-200CV, Bronkhorst, Kamen, Germany), in turn, provides hydrogen. The gas lines are kept as small as possible to minimize fluctuations due to compression and expansion. In addition, backpressure valves (CV-3000, Idex H&s, Oak Harbor, WA, USA) are installed downstream of the pumps and the mass flow controller to stabilize the system.

The slug flow is generated using two mechanically adjustable coaxial mixers *(43, 44)*. A biphasic slug flow consisting of the aqueous phase and gas is generated in the first slug generator (K1), which is subsequently surrounded by a concentric flow of the better-wetting liquid phase in the second mixer (K2) (details in Appendix B). In this way, a well-defined triphasic slug flow can be formed. Furthermore, due to the adjustability of the internal capillary in the first slug generator, the segment length of the gas phase can be set independently of the geometry, volume flow, and phase ratios; all other segment lengths then result from the volume flow ratios; this provides high flexibility. A stepper motor on the adjustable capillary allows control of the resulting slug flow geometries. However, manual adjustment is sufficient in most cases. For better stability of a biphasic gas-water flow, the capillary between K1 and K2 can be soaked in 15 w% nitric acid for about one day to increase the wetting of water on the capillary.

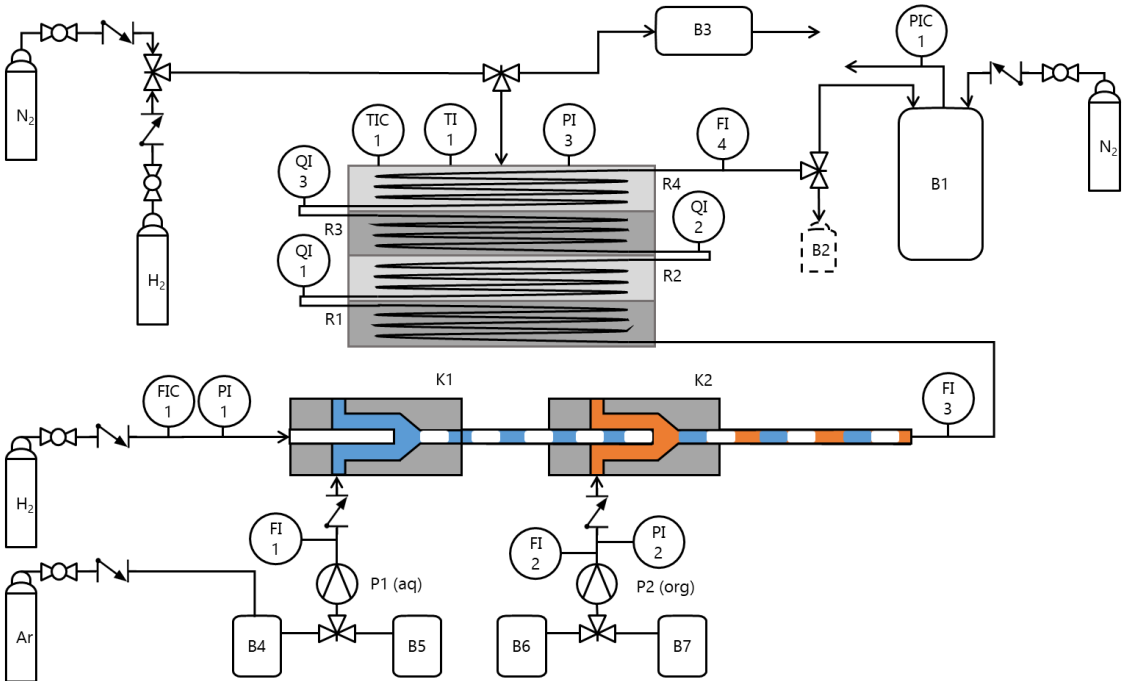

Figure 2.13. Schematic flow sheet of the capillary reactor. Bottom: Slug flow generation with coaxial mixers. Middle: Temperature-controlled capillary in pressurized oil bath with outlets to sensors/sampling locations. Top, right: Collection vessel. PI: Pressure indicator, TI: Temperature indicator, FI: Flow indicator, QI: sampling port/camera observation, TIC: Temperature indicator and controller, PIC: Pressure indicator and controller.

Velocities and segment lengths are measured 30 cm after the second slug generator and at the end of the reactor with an optical sensor, which is developed in Chapter 5. At the end of the capillary, the reaction mixture is collected in a steel vessel (B1). This is supplied with a continuous flow of nitrogen to prevent an explosive atmosphere. This nitrogen flow can be used with a pressure control valve (PIC1, C5I, Bronkhorst, Kamen, Germany) at the outlet of the steel vessel to control the capillary's end pressure. Reactions with higher pressures are, therefore, possible in this setup.

The syringe pumps can each convey from two vessels, which can be selected with a three-way valve. Pump P2, for example, can choose between a rinsing medium and a substrate (B6, B7), while pump P1 for aqueous media can choose between water and the aqueous catalyst solution (B4, B5). This way, the slug flow can be initiated without reaction, and the start of a reaction can be clearly defined. In addition, this prevents the waste of expensive catalysts. The vessel for the catalyst solution B4 can be pressurized with up to 1.5 barg argon to create an inert atmosphere. The resulting flow sheet of the setup is shown in Figure 2.13. The generated process data are read out with a data acquisition (modbus TCP 750-891, wago, Minden, Germany) and processed and stored in LabView (LabView 2020, National Instruments, Austin, TX, USA).

The resulting setup is shown in Figure 2.14. It is divided into four sections, each fulfilling a task. The yellow main section contains, among other equipment, the two slug generators at the bottom left and the main reactor at the bottom right, which is covered with rock wool. Here, samples are taken, and the required pressures are provided. On the other hand, the syringe pumps and vessels for solvents and substrates can be found below in the blue section. Electronics and data acquisition are located in the red section, whereas a computer for operation and storage is located above in the green section.

Figure 2.14. Setup of triphasic gas-liquid-liquid slug flow reactor with four main sections. Yellow: Main reactor and slug generation. Blue: Syringe pumps and tanks for solvents and reactants. Red: Electronics and data acquisition. Green: Operating computer.

In order to generate the multiphase (reaction) system, water (deionized) and 1-hexanol (in the following only hexanol, Alfa Aesar, Ward Hill, MA, USA, 99%) were used as immiscible liquids in all experiments conducted unless otherwise specified. The gas phase was either nitrogen (Messer, Bad Solden, Germany, 99.999%) or hydrogen (Messer, Bad Solden, Germany, 99.999%). To better visualize the different phases in some experiments, hexanol was dyed with Sudan III (Roth, Karlsruhe, Germany, 88%) and water with blue ink (Pelikan 4001 blue, Pelika, Hannover, Germany). Due to the good wettability of hexanol on FEP, hexanol forms the continuous phase, whereas hydrogen and the aqueous phase each form a dispersed phase.

A detailed start-up and shut-down process and a list of equipment and chemicals can be found in Appendix B.

The Reynolds and Capillary numbers describe the flow characteristics in the capillary reactor, whereas the Reynolds number Re_i represents the ratio between inertial and viscous forces for phase i (Eq. 2.23). The Capillary number Ca_i describes the relationship between viscous forces and surface tension between two phases (Eq. 2.24). It is determined for each dispersed phase. It refers to the phase interface with the continuous phase (hexanol).

$$Re_i = \frac{\rho_i \cdot d \cdot u_i}{\eta_i} \tag{2.23}$$

$$Ca_i = \frac{\eta_{cont} \cdot u_i}{\gamma_{i,cont}} \tag{2.24}$$

2.5 Summary and conclusion

This chapter first considers theoretically the challenges associated with transferring a triphasic slug flow into long capillaries with hot reaction zones and under pressure. For this purpose, a unit cell model is derived that is able to calculate the time-dependent pressure profiles taking into account the gas compressibility and the inertia of the liquid segments. Only a minor influence of the inertial force was determined, which is only visible in small time intervals of 100 ms. Over long periods (minutes to hours), the influence is not significant. Nevertheless, the mathematical consideration of the inertia improves the stability of the modeling and leads to a reduction in the calculation time.

Next, the model was used to simulate the start-up behavior of empty and filled capillaries. Although filled capillaries theoretically reach a steady state more quickly, they exhibit a significantly larger pressure maximum, which can lead to increased instability in real applications. The pressure peak relative to the steady-state pressure is about twice as high as in a start-up of an empty capillary. Therefore, a start-up process with empty capillaries is more advantageous. The model can also be used to calculate axial velocity profiles, which can be used to calculate the mean residence time, taking into account the acceleration of the flow due to gas expansion.

In addition, the capillary's expansion was estimated, and if there are limits to the stability of the capillary. Since the capillary can deform irreversibly under the combination of high pressures and temperatures, it is recommended to operate the capillaries in hot reaction zones in an environment with increased external pressure.

Based on the previous theoretical considerations, a setup was developed which allows a flexible and stable operation of a triphasic slug flow in long capillaries. This principle setup represents the basis for the investigations in the following chapters. For example, in Chapter 2, it can be used to supply gas by permeation into the capillary to counteract gas shortage in gas-consuming reactions.

3 Gas feeding via permeation

GAS INTRODUCTION BY PERMEATION INTO LONG POLYMER CAPILLARY REACTORS WITH SLUG FLOW

ABSTRACT

Due to the density differences between gases and liquids, the conversion in gas-liquid reactions in slug flows is often limited by the gas supply. In order to operate at reasonable liquid reactant concentrations, it is thus necessary to introduce additional gas along the capillary to make such microreactors competitive with alternative gas-liquid reactor types. This chapter investigates the permeation of the reacting gas into an existing gas-liquid slug flow in fluorinated ethylene propylene (FEP) capillaries. The amount of gas introduced can be estimated with permeation coefficients given in the literature. Moreover, existing gas bubbles serve as reservoirs for the permeating gas, maintaining the advantageous slug flow pattern, while slug flows without previously introduced gas bubbles are negatively affected. Using FEP capillaries describe a sizing-up technic of already existing tube-in-tube reactors, allowing higher volumetric throughput at the same residence times.

The chapter is based on the publication:

von Vietinghoff, N.; Immken, A.; Seidensticker, T.; de Caro, P.; Thiebaud-Roux, S.; Agar, D. W. Gas introduction by permeation into long fluorinated ethylene propylene capillaries with slug flow. *Chem. Eng. Technol.* **2023**. DOI: 10.1002/ceat.202200557. (accepted and prepublished)

Adopted in many parts, extended and modified.

This chapter is structured as follows:

- Motivation and state of the art
- Materials and methods
- Gas loss due to gas permeation at high temperatures
- Theoretical estimation of permeation flux
- Permeation in a liquid-liquid flow
- Permeation in an existing gas-liquid-liquid flow
- Summary and conclusion

3.1 Motivation and state of the art

Capillary microreactors are often polymer-based, such as polytetrafluoroethylene (PTFE), fluorinated ethylene propylene (FEP), or perfluoroalkoxy alkanes (PFA), which are commonly used due to their chemical resistance, mechanical robustness, transparency, wettability characteristics and convenient handling *(84)*. One physical property of these polymers is their permeability to gas provided concentration differences are present over the capillary walls. In the permeation process, the gas first dissolves in the (non-porous) polymer and then diffuses through the wall. The resulting diffusion depends on the temperature, the pressure difference, the surface area, and the thickness of the polymer barrier *(85–88)*. Such permeation flows through these polymers are usually negligible and often considered a leakage, if at all. However, at higher temperatures and for large surface areas offered by capillaries, mass flows due to permeation are sufficiently large to influence reactions occurring within the capillary.

In reaction systems involving gases, various issues related to gas permeation may arise: (a) gas-sensitive components are present in the system, (b) the reaction consumes gas; (c) the reaction generates gas.

In (a), gas-sensitive components might include, for example, oxidation-sensitive reactants, products, and ligands. In homogeneous catalysis, for instance, ligands are often phosphorus-based, which suffer losses in activity and catalyst lifetime upon contact with just a few ppm of oxygen *(89)*. In polymer-based microreactors, this may arise via oxygen permeation from the outer atmosphere into the capillary.

Since the gas-consuming reactions in case (b) are often performed at elevated temperatures, the reaction gas may diffuse out of the capillary and, thus, no longer be available for the reaction. In this instance, permeation from the inside of the capillary to the outside should also be eliminated. A further complication becomes apparent when the dissolved liquid reactant's concentration is increased to raise space-time yield. Due to the significant density difference between gases and liquids, the gaseous reactant is quickly exhausted, and the reaction thus ceases. In such cases, permeation might even be used to advantage by supplying the otherwise limiting reaction gas externally along the capillary.

If gas is produced (c), it can influence both the residence time and the stability of the flow regime along the capillary. Therefore, when large volumes of gas are produced, removing it along the capillary is beneficial, although gas-generating reactions can also exert a self-regulating influence on flow uniformity in parallel capillary systems.

In conclusion, the following challenges with gas-dependent reactions in capillary reactors have to be surmounted if polymer-based capillaries are to be utilized: either the prevention of gas permeation from inside or outside and the deliberate feeding or removal of individual gaseous components along the capillary. In particular, should it prove possible to manipulate the feed and removal of gases in a controlled manner, the permeation through polymer capillaries might be advantageous since local reaction conditions can be elegantly adjusted.

In the literature, such concepts are also referred to as tube-in-tube reactors, which commonly employ highly specialized polymers, such as Teflon AF 2400, exhibiting very high permeation

coefficients *(56–58, 90–92)*. In this reactor concept, reaction gases are usually fed externally over a limited distance of 0.5-4 m from an outer concentric gas-bearing tube through the internal capillary wall into the usually single-phase liquid reaction medium within, or vice-versa. This approach offers excellent mass transport behavior for gas-liquid reactions (also in comparison to slug flow). In addition to permeation into and out of liquid flows, utilizing a uniform slug flow pattern in the inner capillary can provide further benefits. First, due to segmentation, back-mixing is much lower than in single-phase laminar flow. Secondly, additional functionalities can be assigned to the various phases. For example, a different liquid phase can extract products or heterogenize a catalyst. Loewe et al. successfully introduced a second liquid phase and utilized liquid permeation through the capillary wall *(93)*. Gas-liquid reactions that require significantly longer capillaries due to slower kinetics or the volumetric flow rates desired are also of interest. It has not yet been investigated how far gas bubble formation - either in gas-producing reactions or in external gas permeation - affects the flow behavior and whether this influence can be predicted.

In addition, conventional materials with lower permeation coefficients, such as FEP or PTFE, can be employed for long capillaries since the gas flow per area is not required to be as large as for short specialized capillaries using Teflon AF 2400. If permeation is suitable with FEP and PTFE, a resulting tube-in-tube reactor could be operated at much higher volumetric throughputs. This may represent a sizing-up approach compared with the Teflon AF 2400 capillaries, which are currently limited to a length of 4 m.

Demello et al. demonstrated the syntheses of ascaridole from α-terpinene with singlet oxygen by using oxygen permeation in a single liquid flow through a FEP microcapillary film, which consists of multiple parallel microcapillaries *(94)*. Demello et al. observed a substantial increase in the reaction rate by increasing the partial pressure of oxygen outside the microcapillary film. The results prove that the permeation of gases is feasible even for FEP capillaries, despite the low permeation coefficients, and it is beneficial for reactions. Furthermore, the results indicate a dependence of the permeation flux on the partial pressure, which can be actively used to control the reaction performance.

For short residence time reactions like the aerobic dimerization of desmethoxycarpacine, Felpin et al. demonstrated that slug flow is more favorable compared to a tube-in-tube reactor for yield and reaction times under otherwise similar conditions *(95)*. In this case, the slug flow showed better results due to the favorable PFR-like flow pattern; hence, there is no indication of mass flow limitations. This indicates, in any case (mass transport limitation or not), that a combination of slug flow and wall permeation is promising, also on the background of gas shortage.

Only a few examples in which permeation was used to feed reaction gas in slug flow reactors have been presented in the literature. Khan et al. demonstrated a feed of CO in a <1 m capillary in an existing liquid-liquid slug flow to provide constant flow conditions using a poly(dimethylsiloxane) membrane. In this study, no gas bubble formation was observed as a consequence of the parameters and the short capillary distance *(96)*. Önal and Claus hydrogenated prenal to prenol with a homogenous Ru(TPPTS) catalyst (in the second liquid phase) and investigated various reactor designs and the influence of their operating

parameters on the reaction using such an arrangement. Initially, Önal and Claus observed low conversion in a gas-liquid-liquid slug flow compared to batch reactors, which was caused by a lack of hydrogen *(34).* By imposing an external hydrogen pressure on the PTFE capillary used, permeation was exploited to overcome this hydrogen deficit. However, the gas flow into the capillary via permeation was too low under the conditions selected (temperature, pressure differences, residence times, and capillary lengths) *(54)*. Huvaere and Kouridaki investigated the oxygen content introduced via a tube-in-tube reactor as a part of their work on oxidations in photocatalytic flow reactors *(97)*. After the permeation section, a backpressure regulator was used to drastically reduce the pressure, resulting in outgassing the dissolved oxygen forming 2-3 cm long and regularly occurring gas segments. A camera observed these gas segments to determine the introduced amount of gas. The results show a dependency of the introduced oxygen on the temperature, residence time, and solvent. Although, in this case, the regular gas bubble formation was triggered by a strong local decrease in pressure, the influence of gas permeation on the stability of an existing slug flow without such a trigger is so far unknown.

Hence, on paper, combining the advantageous regime of slug flow with gas supply via permeation along the capillary would seem to open up an elegant technique of process intensification. It would be possible to run various complex multiphase and multi-gas reactions at a laboratory scale in an effectively PFR-behaved continuous reactor.

Slug flow with gas addition through permeation is investigated in the following. First, gas permeation fluxes into long FEP capillaries (30-40 m) containing slug flow are determined, and the gas bubble formation's influence on the flow's stability is examined. Both temperature and pressure differences between the inside and outside of the capillary are utilized as appropriate control parameters, and their effect is compared with theoretical predictions. In addition, it will be briefly discussed how unwanted gas permeation, e.g., of oxygen from the surroundings into the capillary, can be suppressed.

3.2 Materials and methods

For measuring and evaluating gas permeation in FEP capillaries, the setup from Chapter 2 with either 30 or 40 m FEP capillary is used. The flow is generated with a continuous phase (hexanol) and a dispersed phase (water). For the triphasic flows, hydrogen or nitrogen is used as the gas phase. For all experiments performed, the volume flow per phase is 0.6 mL/min, which results in all experiments in Reynolds numbers of ≤45 and Capillary numbers of ≤0.009. For facile volume measurement, all experiments were performed with the end of the capillary open to the atmosphere (p_{end}=1 atm). In addition, the measurements were performed after reaching a steady state (pressure and temperature constant). The ambient gas is provided in the heated steel vessel around the capillary at constant pressure in all reactor modules.

To determine the volumetric permeation flow, a pneumatic trough (Figure 3.1) is used to collect gas over liquid at the end of the capillary. The data presented is based on triplicate measurements of 5 min gas collection each and shown with error bars in the later diagrams.

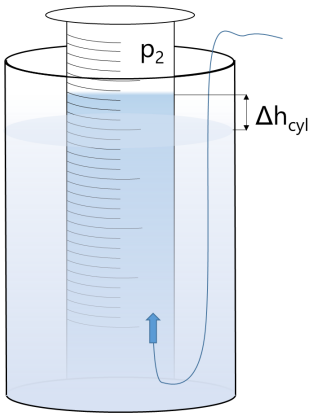

Figure 3.1. Pneumatic trough to measure the outflowing gas at the end of the capillary.

For the gas-liquid-liquid flows, the volume of the introduced gas at the inlet of the capillary is subtracted under the consideration of the ideal gas law and the resulting gas expansion due to the pressure drop as well as the hydrostatic pressure in the pneumatic trough (Eq. 3.1).

$$\dot{V}_{perm} = \frac{V_{gas,meas}}{t_{meas}} - \dot{V}_{gas,in} \frac{p_{in}}{p_{atm} - \rho_{fluid} g \Delta h_{cyl}} \tag{3.1}$$

The comparison with theoretical values considers the measured pressure drop according to Eq. 3.2 in Chapter 3.4. The axial pressure profile is assumed linear, based on calculations of biphasic and triphasic pressure drop models with the present system *(45, 71)*.

3.3 Gas loss due to gas permeation at high temperatures

To confirm that reaction gas can permeate out of a pressurized capillary, a 30 m long FEP capillary was coiled around a heated steel tube, and a non-reactive gas-liquid-liquid slug flow (hexanol, water, hydrogen) was passed through the capillary at various temperatures and pressures. At room temperature and inlet capillary pressure of 7 bar, no visible changes in the flow pattern were observed, whereas, at 80 °C, all gas bubbles disappeared after about half the capillary length. In addition, the capillary was immersed in an oil bath under the same conditions to render permeation visible. In this setup, the gas bubbles also disappeared, and simultaneously, the formation of tiny gas bubbles at the outer capillary wall was observed. After these bubbles disengaged, a gas sensor identified them as hydrogen. Figure 3.2 shows the capillary immersed in the oil bath with slug flow and gas bubbles forming outside the capillary.

Thus, it could be experimentally confirmed that gas permeation in FEP capillaries at high pressures and temperatures becomes significant and that the entire reaction gas may diffuse out of the capillary and is no longer available for the reaction.

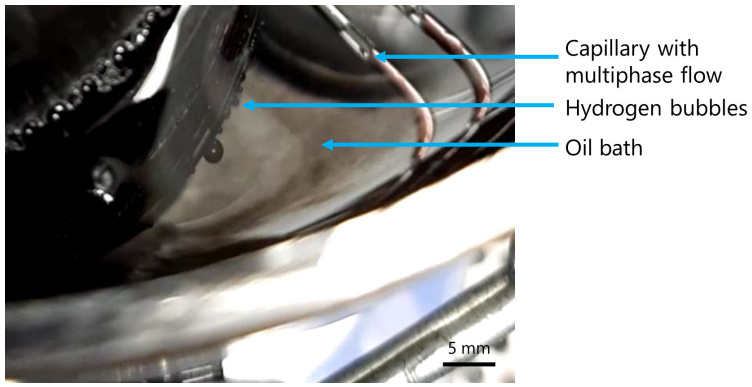

Figure 3.2. Capillary with a gas-liquid-liquid slug flow (hexanol, water, hydrogen) in an oil bath illustrating bubble formation on the outer wall of the capillaries. Every couple of seconds a gas bubble rose to the oil bath surface. T=80 °C, p_{cap}=7 bar.

However, if the oil bath is exposed to a higher pressure than inside the capillary, no gas bubbles will form since this would imply mass transfer against the driving force as soon as a gas bubble would form in the higher-pressured oil bath. A small mass flow of gas inside the oil bath cannot be suppressed due to gas solubility in the oil *(98)* – however, this mass transfer should be negligible after reaching an equilibrium state. When the capillary reactor is placed in a pressurized oil bath, as described in Chapter 2, gas permeation out of the capillary was thus suppressed under previously discussed conditions and at higher temperatures and pressures.

This setup also hinders the permeation flow of unwanted atmospheric gases into the capillary. Absolute higher pressure in the capillary alone is insufficient to enable (for example) oxygen-free operation because the permeation flow results from the concentration (e.g., partial pressure) difference. The environment surrounding the capillary thus has to be oxygen-free, which can be ensured by using the oil bath. The pressurized oil bath thus suppresses both permeation from the inside to the outside and vice versa, and it serves as a heat transfer medium.

As discussed, gas permeation can also be used to actively feed gas into the capillary in analogy to the tube-in-a-tube reactors. In this case, pure reaction gas is used as the surrounding medium instead of the previously used oil bath. The following will examine whether FEP capillaries are suitable for such concepts since their permeation coefficients are significantly lower than those of the highly specialized polymers used in tube-in-a-tube reactors. In addition to quantifying the permeation fluxes at different temperatures and pressures, the influence of gas permeation on an existing multiphase slug flow is also investigated. First, it is discussed how the permeation flux is estimated using permeation coefficients from the literature. These calculated theoretical values are then used as a reference to evaluate the measured permeation fluxes.

3.4 Estimation of permeation flux

Permeation coefficients for various temperatures, pressures, widely available polymers, and common gases can be found in the existing literature *(87)*. However, these values have been determined over much smaller surface areas and extended periods under otherwise ideal conditions (i.e., no further liquid flow). Comparing such data with the following experimental data should ascertain if such permeation coefficients could be used to predict the gaseous flux through a long capillary with slug flow. A prediction of this sort would be very valuable for estimations in combination with future applications and for designing the experimental equipment.

The permeation flux q_i of component i through a polymer material j with a surface area A and a wall thickness s and the partial pressure difference of Δp_i can be described with Eq. 3.2 (*85*).

$$q_i = \varepsilon_{i,j}(T) \cdot \frac{A}{s} \cdot \Delta p_i \tag{3.2}$$

The permeation coefficient $\varepsilon_{i,j}$ depends on the polymer and the (gaseous) component and is also a function of temperature T. The permeability increases at higher temperatures since the solubility and diffusion of the gaseous component in the polymer are raised. For cylindrical geometries of the polymer, such as a capillary, the surface area A differs on the inside and outside, respectively. In this case, Eq. 3.2 can also be used by calculating the surface area either with the arithmetic or logarithmic mean.

Under the perspective of a sizing-up strategy, FEP capillaries were of particular interest since they are widely employed in flow chemistry due to their chemical resistance, facile handling, and optical transparency. Therefore, with the data presented in *(87)*, temperature-dependent functions for hydrogen, nitrogen, oxygen, and ammonia have been derived (Table 3.1), which were subsequently used to interpolate the value of the permeation coefficient for a given temperature T.

Table 3.1. Permeation coefficients for various gases through FEP depending on the temperature (in Kelvin). Data used to derive these equations can be found in *(87)*.

Component i	**Permeation coefficient / (cm³·mm)/(cm²·kPa·s)**
H_2	$\varepsilon_{H_2,FEP} = 2.12 \cdot 10^{-4} \cdot exp(-3.12 \cdot 10^3/T)$
N_2	$\varepsilon_{N_2,FEP} = 1.51 \cdot 10^{-3} \cdot exp(-3.93 \cdot 10^3/T)$
O_2	$\varepsilon_{O_2,FEP} = 1.19 \cdot 10^{-02} \cdot exp(-4.78 \cdot 10^3/T)$
NH_3	$\varepsilon_{NH_3,FEP} = 1.25 \cdot 10^{-03} \cdot exp(-4.14 \cdot 10^3/T)$

3.5 Permeation in a liquid-liquid flow

First, the gas permeation of nitrogen into an existing liquid-liquid slug flow was quantified, and the stability of the flow was evaluated. If the flow retains a stable and regular form, a liquid-liquid flow would be preferable to an initially gas-liquid-liquid slug flow, as this would simplify slug generation. The influence of the temperature and the pressure difference was investigated.

The volumetric permeation flow is plotted against temperature at various external pressures in Figure 3.3. The experimentally determined volumetric flow rates (points) were each averaged from three data points and increased with rising external pressure and temperature. This behavior is well predicted by the theoretically calculated curves (dashed lines), even though the permeation data presented in the literature was established under more ideal conditions, and the FEP properties may vary depending on the supplier (different ratios of ethylene/propylene and/or degree of crystallinity).

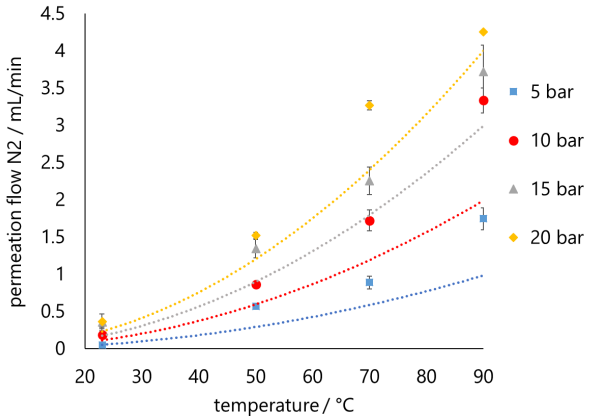

Figure 3.3. Permeation flow rates of nitrogen versus temperature for different external pressures into a liquid-liquid slug flow. The same colors are used for the experimental (points) and the corresponding theoretical values (dotted lines). FEP capillary, ID: 1 mm, OD: 1/16" (1.5875 mm), length: 40 m.

Although the total gas permeation measured through the capillary is in an acceptable range compared to the theoretically estimated values, the liquid-liquid slug flow pattern is negatively affected. Figure 3.4 (right) shows the flow patterns in the capillary at different distances downstream. While isolated small bubbles can be observed after 10 m, irregular larger gas agglomerates (about one larger gas slug agglomerate with several single gas bubbles per m of the capillary) can be observed at the end of the capillary. The formation of these irregular long agglomerates destroys the previously uniform liquid-liquid slug flow. Conversely, a setup without permeation (Figure 3.4, left) showed a stable liquid-liquid flow along the whole capillary. The instabilities thus result from the permeation and bubble formation.

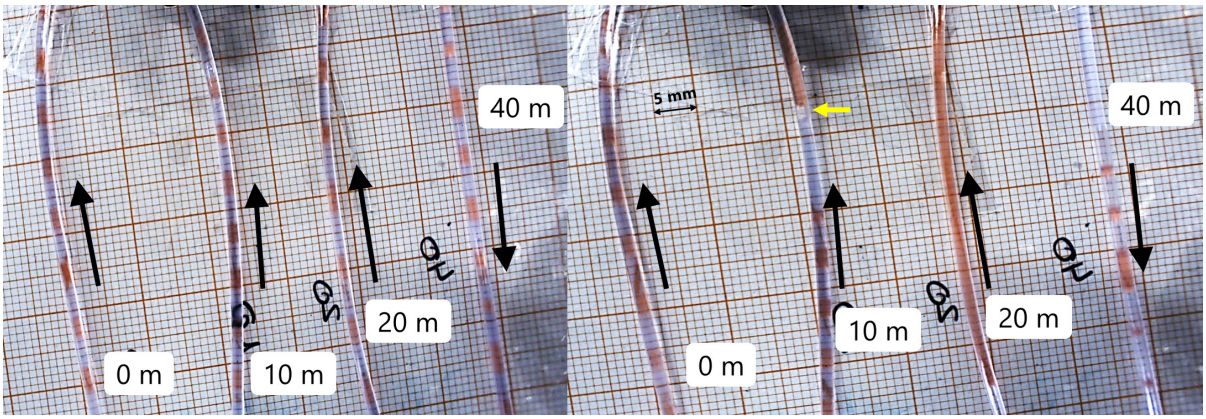

Figure 3.4. Flow patterns of a liquid-liquid slug flow with nitrogen permeation after 0, 10, 20, and 40 m. Left: No permeation, Right: With nitrogen permeation. After 10 m, the first single gas bubbles are visible (indicated by the yellow arrow). Subsequently, the flow loses its regular structure. Red phase: hexanol, blue phase: water. Clear phase: nitrogen. The black arrows indicate the flow direction of the respective capillary section. Permeation conditions: T=50 °C, Δp=5 bar.

Phenomenologically, the dissolved gas concentration in the liquid solvents increases until saturation is reached, after which a small gas bubble is formed. Further dissolved gas molecules have two possibilities: forming another bubble or affiliating with an existing bubble. Energetically, the latter option is more favorable since no additional high surface energy is required to form a new phase interface. Thus, it is more likely that existing bubbles will be filled with the permeated dissolved gas rather than that new bubbles will be formed. Very long gas segments can then, in turn, break down into smaller gas bubbles due to shear forces. Thus, gas agglomerates are formed as several single gas segments that appear to coalesce in the flow.

The irregular gas bubble formation in the liquid-liquid slug flow could be counteracted by creating a regular gas-liquid-liquid slug flow at the capillary inlet. In this case, the permeating gas would fill the existing gas bubbles and maintain the original flow pattern of the slug flow. However, conceptually, this only becomes relevant if more gas is required by the reaction than the existing gas bubble can provide. Also, combining pre-supplied gas-liquid slug flow with additional gas permeation is feasible for biphasic gas-liquid reactions. In this instance, the advantageous fluid mechanics of the slug flow (uniform residence time distribution and intense mixing) are utilized, and the gas supply is ensured simultaneously. A schematic set-up presenting the permeation in a gas-liquid-liquid flow is shown in Figure 3.5.

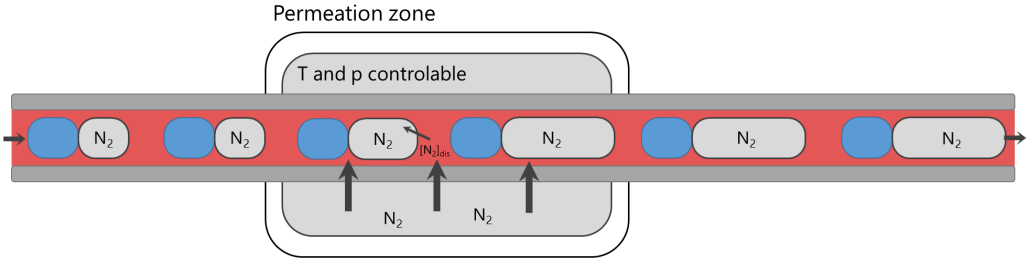

Figure 3.5. Schematic illustration of the setup of controlled nitrogen permeation in an existing gas-liquid-liquid slug flow. The nitrogen is dissolved in the polymer and diffuses into the capillary, then expanding the gas bubbles.

3.6 Permeation in an existing gas-liquid-liquid flow

The flow's behavior and the nitrogen's permeation flux into an existing gas-liquid-liquid slug flow were investigated based on the previous discussions. Two temperature levels (23 °C and 50 °C) were studied. The quantity of permeation fluxes was similar to those of the biphasic liquid-liquid flow and comparable to the theoretical values calculated. A continuous and stable triphasic flow pattern could be observed. The gas bubbles entering grew in size along the capillary to form long segments. In the process, all the gas bubbles in the inlet became uniformly larger, and the slug flow, with its advantageous flow pattern, was maintained along the entire length of the capillary.

Hydrogen was used instead of nitrogen as the permeating gas to increase the permeation flux since, as a smaller molecule, it exhibits a higher permeation coefficient. In addition, hydrogen is also of particular interest as a reaction gas for real applications (i.e., hydrogenations). In Figure 3.6, hydrogen permeation in a 40 m capillary is shown versus the temperature at different pressure differences. As expected, the permeation rates for hydrogen are significantly higher than those for nitrogen. However, a more significant deviation can be observed from the theoretically estimated values. Presumably, these differences result from the different conditions of the measurements and the different compositions of FEP in each production batch. Nevertheless, the theoretical permeation coefficients predict the gas flow in the right magnitude, sufficient for a rough estimation. Anyhow, measuring the permeation fluxes for each new capillary installed is advisable for the exact operating conditions.

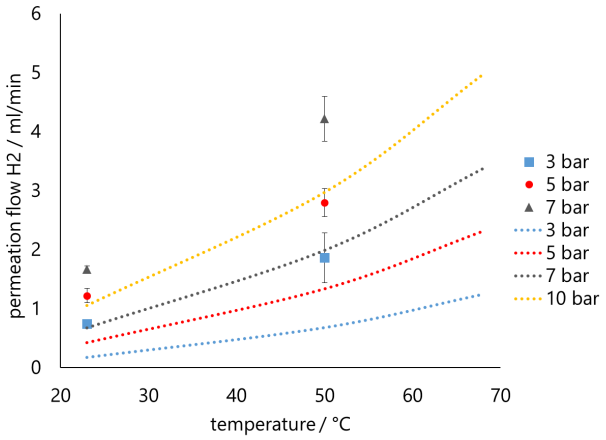

Figure 3.6. Permeation hydrogen flow rates versus temperature for different external pressures into a gas-liquid-liquid slug flow. The same colors are used for the experimental (points) and the corresponding theoretical values (dotted line). FEP capillary, ID: 1 mm, OD: 1/16", length: 40 m.

Figure 3.7 depicts the flow pattern at three locations along the capillary (at 0 m, 15 m, 35 m) in a triphasic slug flow with additional hydrogen gas permeation at two different temperatures (23 °C and 50 °C) and a pressure difference of 5 bar. In both cases, it can be seen that despite the significant increase in the size of the gas bubbles, the liquid segments remain unaffected. However, for very high permeation fluxes (at 50 °C), it can be observed that the liquid segments become separated by a gas segment. This is unfavorable for systems with required liquid-liquid mass transfer since, in this case, a liquid-liquid interface is no longer available. In

actual applications, the permeation flow should therefore be adjusted to ensure that only a comparable amount of gas consumed by the reaction is fed.

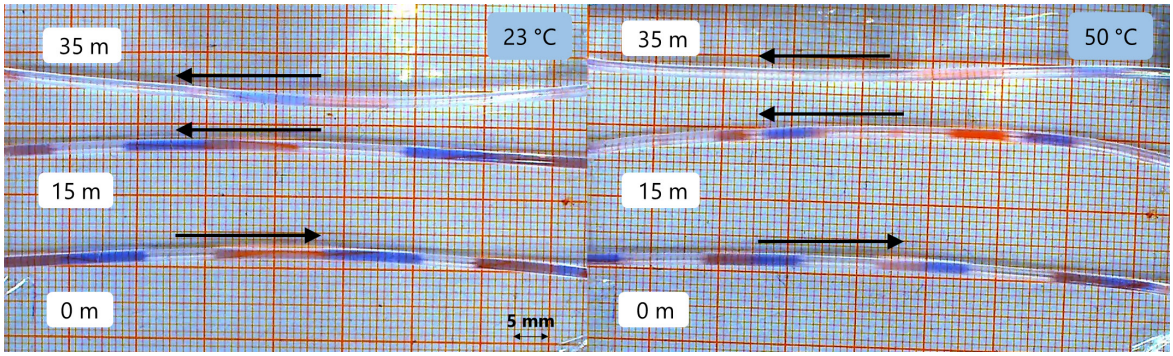

Figure 3.7. Flow patterns of a gas-liquid-liquid slug flow with hydrogen permeation after 0, 15, and 35 m. Red phase: hexanol, blue phase: water, and clear phase: hydrogen. The black arrows indicate the flow direction of the respective capillary section. Left: Permeation conditions: T=23 °C, Δp=5 bar; Right: Permeation conditions: T=50 °C, Δp=5 bar. On the right, the liquid phases become separated completely by gas.

The permeation of gases into slug flows presented is a suitable method for feeding reaction gases but exhibits certain limitations. The temperature of the capillary is usually dictated by reaction kinetics and is not a degree of freedom that can be exploited to manipulate permeation. Nevertheless, the pressure difference between the inside and the outside of the capillary can be adjusted as an operating parameter since it does not directly affect the reaction pressure. However, the permeation flux is often insufficient, especially at low temperatures, even for large pressure differences. Whether or not the permeation is sufficient to supply enough reaction gas can be reliably predicted using theoretical estimation before selecting this method.

Another limitation is the mechanical and deflection stability of polymer capillaries at high temperatures and pressure differences. If the reaction temperature and pressure difference are excessive, the polymer softens due to the temperature, and the external pressure might deform the capillary (see Chapter 2.3). This is especially the case when a large amount of reaction gas is required locally, i.e., when a rapid reaction occurs. In this case, it is recommended to use polymers with exceptionally high permeation coefficients to reduce the required pressure difference. Instead of conventional polymers such as FEP and PTFE, highly functional polymers such as Teflon AF 2400 (used in tube-in-tube reactors) can be used in such instances. The capillary material should thus be selected according to the reaction and the required gas flow rate. For example, if large volumetric flow rates with moderate residence times in a capillary are desired for a particular application, this will result in long capillaries with a large surface area so that polymers such as FEP and PTFE would be entirely adequate for the purpose.

If permeation is used for degassing or removing gases, a short distance for degassing is often preferred, for example, if reaction gas has to be removed to suppress consecutive reactions. Accordingly, polymers with high permeation coefficients are most appropriate. Conversely, in gas-producing reactions in which the benefits of a slug flow are paramount, polymers with low permeation coefficients are more advantageous over a long distance.

3.7 Summary and conclusion

Gas permeation is suitable with conventional polymer materials such as FEP to feed gases into capillary flows. The measured gas flows are in the same magnitude as a theoretical estimation. For precise gas flows, the permeation coefficient should be measured for each new set-up. Alternatively, the pressure in the surrounding vessel can be kept variable, and the desired permeation flow from the surrounding vessel into the capillary can be adjusted via the inlet flow of the gas into the vessel by using a mass flow controller. Nevertheless, the pressure should be monitored to prevent a deforming of the capillary under high mechanical stress.

It was found that a slug flow with regular gas bubbles entering a capillary is advantageous since, in this case, the existing gas bubbles are uniformly filled, whereas the flow pattern without gas bubbles was affected by random gas bubble formation, thus losing the advantageous properties of the slug flow. The positive influence of permeation on reactions was already demonstrated several times in tube-in-tube reactors *(56, 57, 91)*. For long FEP reactors, the benefit of introducing gas with this method is demonstrated with the hydrogenation of vegetable oil in Chapter 7.5.

The technique presented can thus be applied to gas-limited multiphase gas-consuming reactions to the operation of a slug flow in capillaries without the trade-off of lower conversions. Furthermore, since gas permeation can be exploited in both directions (into or out of the capillary), it offers a wide range of further reaction options. For example, (consecutive) reactions can be regulated locally. In a tandem-catalyzed reaction system, for instance, hydrogenation could be performed selectively, excess hydrogen could be removed, and another reaction gas could be introduced for a subsequent reaction.

Compared to existing tube-in-tube reactors, which are limited in length, the presented system describes a sizing-up (increasing volumetric flow and capillary length). This enables reactions with slow kinetics and increases the capacity of such permeation-capillary systems.

However, permeation as a gas feed method has its limitations. Since it depends crucially on pressure and temperature, it is not suitable for all applications. For reactions that only occur selectively at low temperatures, the permeation flux may be too low to satisfy the gas demand due to the exponential dependence on the temperature. At elevated temperatures and with a high gas demand, required pressure differences may, in turn, cause deformation of the capillary. On the other hand, due to their harsh conditions, some reactions can only be operated in flow using metal capillaries, where permeation is excluded as a gas-feeding method *(99)*. For such applications, other gas injection methods are needed, which, ideally, do not affect the advantageous flow conditions such as permeation. Therefore, in the following chapter, the direct injection of single gas bubbles into an existing slug flow is developed and investigated. Observing the flow beforehand allows this gas bubble to be introduced into the continuous phase without destroying the existing slug flow. In Chapter 4.9, a discussion with selection criteria for the different gas-feeding methods can be found.

4 Single gas bubble injection

INTERMEDIATE GAS FEED IN SLUG FLOW CAPILLARY REACTORS WITH SOLENOID VALVE AND ELECTROLYSIS

ABSTRACT

In gas-consuming reactions, the gas bubbles shrink and may even disappear, limiting the conversions and throughputs of capillary reactor systems. A single bubble injection was developed to overcome such shortcomings. In order to maintain the well-defined slug flow characteristics, it is necessary to introduce the gas rapidly and precisely in small amounts of <10 µL. This allows to preserve the well-defined alternating triphasic slug flow. A miniaturized electrolysis cell and a solenoid valve are thus devised and implemented as an intermediate gas feed. Feeding new gas bubbles into an existing liquid-liquid slug flow had a success rate of up to 99%, whereas refilling an existing gas bubble is often limited by a lack of coalescence. Here, only at low volumetric flow rates, 70% of the gas bubbles were refilled by coalescence. A combination of an electrolytic cell with gas separation by a membrane and a solenoid valve can feed hydrogen bubbles into a capillary even at 10 bar.

The chapter is based on the publication:

Vietinghoff, N.; Hellmann, D.; Priebe, J.; Agar, D. W. Intermediate Gas Feed in Bi- or Triphasic Gas–Liquid(–Liquid) Segmented Slug Flow Capillary Reactors. *Symmetry* **2020**, 12 (12), 2092. DOI: 10.3390/sym12122092.

Adopted in many parts, extended and modified.

This chapter is structured as follows:

- Motivation and state of the art
- Materials and methods
- Operating concept for the single bubble injection in slug flows
- Solenoid valve for gas injection
- Electrolysis cell for gas injection
- Intermediate gas feeding in an existing biphasic slug flow
- Electrolysis with membrane and combination with solenoid valve
- Feedback control for the injected gas droplet length
- Selection criteria for gas feeding methods
- Summary and conclusion

4.1 Motivation and state of the art

The previously discussed permeation is an elegant method for feeding gases into slug flows as long as the application's reaction temperatures and residence times are sufficiently high. For example, if a reaction requires low temperatures to be particularly selective, the permeation flux drops significantly and cannot be compensated with pressure without deforming the capillary. On the other hand, particularly fast reactions with undesired consecutive reactions may require only a short residence time in the capillary, which means that the contact time with the permeation area is not sufficiently high. Therefore, gas permeation in FEP capillaries is insufficient for such reactions, and other gas-feeding methods are needed.

The controlled intermediate gas feed is a suitable option. New gas is introduced into the microcapillary in a targeted manner to replace either an entirely consumed gas bubble or refill a shrunken gas bubble. This forms a new alternating triphasic slug flow. Injecting into the continuous phase is useful to preserve the existing slug flow. In order to ensure that the time of injection is accurate, it is necessary to observe and characterize the slug flow at the injection point. A further observation point after the intermediate gas injection allows, on the one hand, an evaluation of whether the gas bubble has affected the flow and, on the other hand, a feedback control of the length of the injected bubble. Figure 4.1 shows, schematically, this method of intermediate gas feeding.

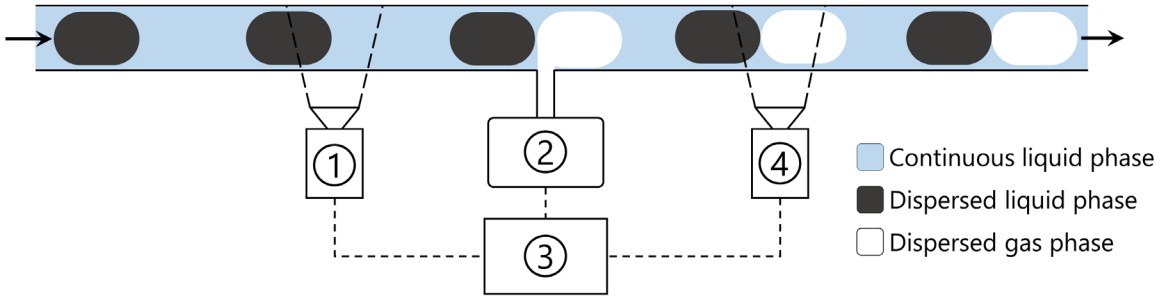

Figure 4.1. Schematic illustration of an intermediate gas feeding into an existing liquid-liquid biphasic slug flow. (1): Observation and characterization of the slug flow before injection, (2): gas injection, (3): control unit, and (4): observation and characterization of the slug flow after injection.

Various apparatuses can be utilized for the intermediate gas feed. For example, a solenoid valve or a piezo element could open at an appropriate time and inject the desired gas volume into the capillary. Jiang et al. showed that a pneumatic valve could control the gas bubble length by changing the opening frequency for a gas-liquid slug flow generation in T-junctions *(100)*. In comparison, Zhang et al. used a pulsating gas intake to control the gas bubble lengths *(101)*.

Another possibility is using an electrolysis cell, which can feed defined volumes by controlling the electrical current. Hellmann developed water electrolysis cells to generate a biphasic gas-liquid slug flow. Here, an electrolysis cell was directly connected to a single-phase liquid flow with a T-junction and was operated with a non-pulsating electrical current. In particular, Hellman investigated different free gas volumes of the electrolysis cells and its influence on

the resulting gas-liquid flow. In a steady state, the gas production was constant and could be well controlled according to Faraday's law with the electrical current. *(45)*

This turns electrolysis into an elegant, demand-controlled gas supply for micro-process technology. However, the free gas volume in the electrolysis cell significantly influences the start-up and shut-down behavior. The larger the volume of the electrolysis cell, the slower the system response. For a direct gas feed, it is therefore desirable to have a small free gas volume as possible, as this allows individual gas bubbles to be fed into an existing flow in a more targeted. The electrolysis cell with the smallest gas volume (~0.2 mL) showed almost instantaneous behavior. The resulting slug length in the capillary followed the correlations of Garstecki *(102)*, which predicts the segment lengths of a gas-liquid flow as a function of the incoming volume flows and the geometry of a T-junction for slug generation.

This chapter investigates the method of gas-bubble injection in capillary reactors with multiphase slug flows. For this purpose, the possible operations are first developed theoretically, followed by an experimental investigation of gas injection.

First, a low-grade solenoid valve is used to determine the effect of upstream pressure on the bubble length injected in a single liquid flow. Then, the 0.2 mL electrolysis cell of Hellmann is used to show the prediction of the injected bubble length influenced by the electrical current, the pulsation time, and the velocity of the single liquid flow *(45)*. Based on this, the electrolysis cell is used to inject gas bubbles into a liquid-liquid slug flow and to refill gas bubbles in a gas-liquid slug flow.

Since this electrolysis cell of Hellmann can only feed a mixture of oxygen and hydrogen into a capillary at near ambient pressure, a pressure-stable electrolysis cell with gas separation is then developed. This is used together with a high-performance solenoid valve to feed single gas bubbles into a slug flow at up to 10 bar.

The operating concept of intermediate gas feeding and the relevant formulae are presented in the following. Then, the ability to control the solenoid valve and the electrolysis cell for intermediate gas feeding is evaluated. Thereby gas is first fed into a single-phase flow. Afterward, the intermediate gas feeding is demonstrated with an electrolysis cell in a liquid-liquid and a gas-liquid slug flow. Finally, it is verified that it is possible to provide a closed-loop control for the length of the injected gas bubble.

4.2 Materials and methods

The supply of the flow (single-phase or biphasic) is provided according to Chapter 2.4. For a biphasic flow, only one coaxial mixer is used. Hexanol and water are used as liquids. The gas injection positions are located 50 cm behind the slug generators.

In the initial gas injection experiments into a single-phase flow, only the resulting flow with the injected gas bubbles 20 cm after the injection is evaluated with a camera (DFK37BUX, Imagingsource, Bremen, Germany). For feeding into an existing slug flow, an optical sensor (TCUT1300×01, Vishay, Malvern, PA, USA, see Chapter 5) is used 10 cm upstream of the feed location, and its signal is processed with an Arduino microcontroller board (Arduino Uno Rev

3 SMD, Arduino LLC, Chiasso, Switzerland). The microcontroller board also controls the solenoid valve and the electrolysis cell. The setup for the solenoid valve and the electrolytic cell is presented below.

Solenoid valve

The solenoid valve (ATS-V4, Wittko, Riedenburg, Germany) is attached directly into a T-junction to keep the free gas volume as small as possible and thus minimize compression effects. The T-junction is made of poly(methyl methacrylate) (PMMA), whereby all channels have a diameter of 1 mm. A metal–oxide semiconductor field effect transistor (MOSFET) is used to control the solenoid valve electrically. The solenoid valve is supplied with nitrogen from a pressure vessel controlled with a pressure regulator (R414003373, Aventics, Laatzen, Germany). The schematic setup of the intermediate gas feeding via the solenoid valve is shown in Figure 4.2.

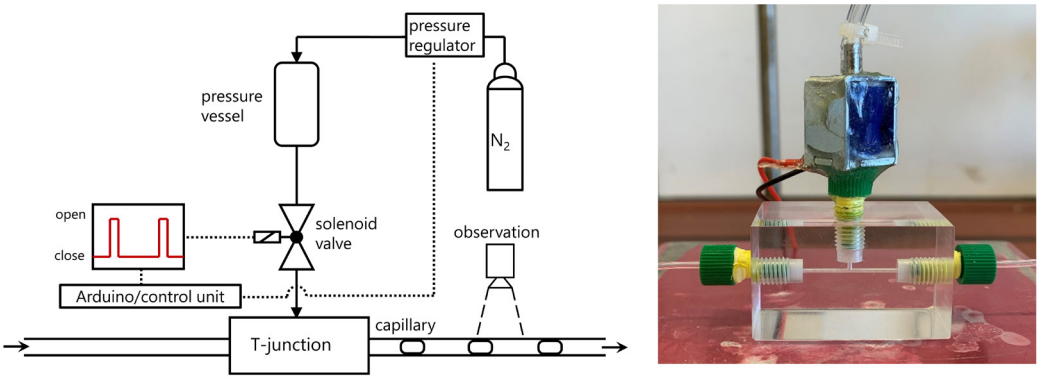

Figure 4.2. Left: Schematic setup of the intermediate gas feeding with a solenoid valve and control communication Right: Experimental setup of T-junction with included solenoid valve.

A high-performance solenoid valve (VA204-715 12 V, Staiger, Erligheim, Germany), which can be operated at high switching rates and pressures up to 10 bar, is used to combine the gas valve and electrolysis (Chapter 4.8). The corresponding setup can be found there.

Electrolysis cells

Electrolysis exploits gas generation directly at the location of gas injection. Only water electrolysis is used, which produces oxygen at the anode and hydrogen at the cathode from water in an alkaline solution, according to Eq. 4.1-4.3 *(103)*.

Cathode (reduction): $$4\,H_2O + 4\,e^- \rightarrow 2\,H_2 + 4\,OH^-$$ (4.1)

Anode (oxidation): $$4\,OH^- \rightarrow O_2 + 2\,H_2O + 4\,e^-$$ (4.2)

Overall reaction: $$2\,H_2O \rightarrow 2\,H_2 + O_2$$ (4.3)

Two electrolysis cells were used to apply electrolysis as a gas-feeding method. The first is the electrolysis cell of Hellmann, which operates without gas separation and only at atmospheric

conditions. In comparison, a more advanced cell that is pressure stable, is able to separate gases and has a bigger liquid holdup. *(45)*

The electrolysis cell of Hellman showed already good performance in non-pulsing operation, but no separation of the gases is possible *(45)*. The electrolyte used was a 1 molar potassium hydroxide solution.

Since the amount of gas produced is minimal, the mixture of hydrogen and oxygen does not cause safety issues. The gas outlet is connected to a T-junction (1 mm each channel) within the assembly. The cell has internal dimensions of 15.5 mm height, 3 mm width, and 5 mm depth. Nickel electrodes are attached directly to the PMMA chamber walls. The cell volume is approximately 0.23 mL. The gas volume during operation is between 0.005 and 0.02 mL, depending on the liquid level. With one electrolyte filling, up to 120 mL of gas can be produced, sufficient for investigating intermediate gas feeding. This cell is shown in Figure 4.3.

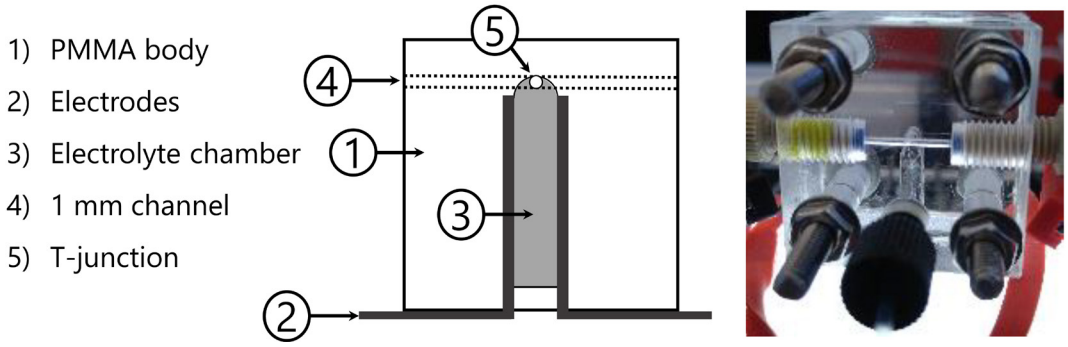

Figure 4.3. Schematic illustration and photograph of the electrolysis cell by Hellmann *(45)*. Electrolysis cell with minimal free gas volume. No membrane is used, and a mixture of hydrogen and oxygen is produced, introduced with a T-junction in the capillary. Middle: Schematic illustration. Right: Photo of the electrolysis cell.

The second electrolytic cell uses a Nafion membrane (NM 115, Quintech, Göppingen, Germany), which acts as a separator between the electrodes, ensuring the separation of hydrogen and oxygen during water electrolysis *(104)*. Since the hydrogen is to be fed into the capillary (e.g., for hydrogenation reactions) via a T-junction, the free volume on the cathode side (hydrogen-producing) is kept as low as possible (~0.66 mL). The holdup for the potassium hydroxide is located on the anode side (oxygen-producing). There is also an outlet for the produced oxygen, and a supply of an additional electrolyte solution is possible.

The electrodes are separated exclusively by the proton-conducting Nafion membrane. This allows, at least theoretically, a liquid-free cathode side so that only hydrogen is present at the outlet to the capillary (if the liquid hold-up is exclusively on the anode side). The electrodes are made of stainless steel (V4A), with the anode additionally gold-plated to prevent corrosion. The electrolytic cell is pressure-tight up to 20 bar. The carriers of the electrodes are made of stainless steel (V4A) and separated by a PMMA ring. The carriers act as electrical conductors and additionally serve for heat removal.

Figure 4.4 shows the exploded assembly drawing of the pressure-stable electrolytic cell with gas separation. Technical drawings of the individual components and information on the gold-plating of the anode can be found in Appendix D.

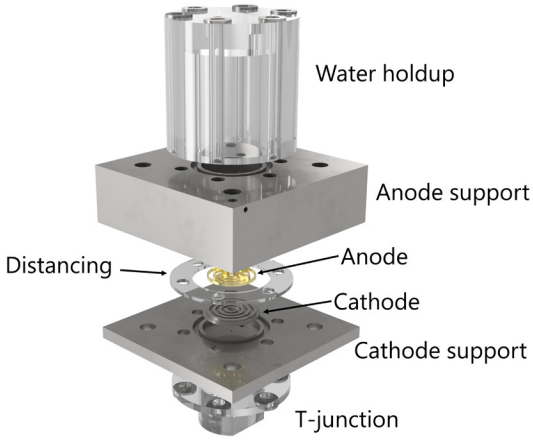

Figure 4.4. Exploded assembly drawing of the pressure-stable electrolysis. Hydrogen is formed at the cathode and can be fed into a capillary via the T-junction. Oxygen is produced on the anode side.

The electrolysis was supplied by a current source (LPS 301, Amrel, Pasadena, CA, USA). This source can either be controlled by a transistor at a given electrical current or by an external control unit (fabricated by the workshops of the TU Dortmund University). The external control unit regulates the current and the times supplying electricity. A serial interface is used for communication with the Arduino board. The setup of the intermediate gas feeding via an electrolysis cell is shown in Figure 4.5. For feedback control, a second transmissive sensor is placed after the injection.

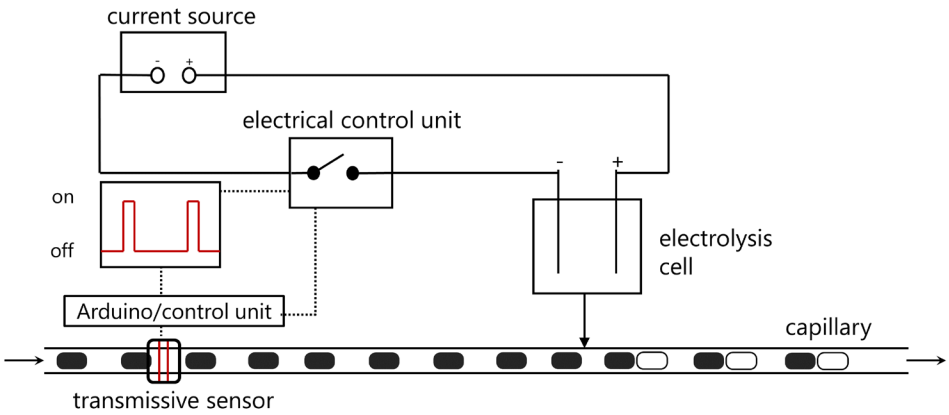

Figure 4.5. Schematic setup of the intermediate gas feeding via an electrolysis cell and control communication between the transmissive sensor before the gas injection in a biphasic slug flow and the electrolysis cell.

4.3 Operating concept for the single bubble injection in slug flows

This chapter outlines the general principles for the design and operation of intermediate gas feeding into a capillary with multiphase flows, which are the fundament for the following chapters. Intermediate gas feeding aims to integrate a gas bubble of a given length into an existing slug flow. $L_{gas,set}$ describes the desired gas bubble length in the capillary. In principle, two possibilities are conceivable.

In a gas-liquid(-liquid) slug flow, an existing but shrunken gas bubble is filled up to reach $L_{gas,set}$. If the gas bubble is completely dissolved at the location of intermediate gas feeding, a new gas bubble must be injected into the remaining liquid-liquid flow. Either a gas bubble has to be refilled, or a new one has to be generated. The bubble's length, not its volume, represents the desired value since it is easier to determine with standard measuring methods and may influence the hydrodynamics. Accordingly, the length of the gas bubble ΔL_{gas} to be injected is defined as follows, depending on the flow pattern.

$$\Delta L_{gas} = \begin{cases} L_{gas,set} - L_{gas,actual} \geq 0 & , gas - liq(-liq) \\ L_{gas,set} & , liq - liq \end{cases} \tag{4.4}$$

For a successful adjustment of the desired value $L_{gas,set}$, both the correct injection time and the necessary gas volume must be controlled, depending on the current length of the bubble to be filled.

First, the control of the injection timing is discussed, using the example of gas-liquid-liquid flow with already depleted gas bubbles. Then, with the help of the slug flow characterization in front of the intermediate gas feeding (Figure 4.1), the actual flow velocity and the lengths of each phase can be determined. One of the essential requirements of intermediate gas feeding is not to disturb the existing dispersed (liquid) phases. Therefore, feeding into the continuous phase is desired.

The duration of the continuous phase flowing past the feeding location depends on the flow velocity and length. Therefore, the length of a continuous phase L_{slug} and the subsequent bubble lengths $L_{bubble,gas}$, and $L_{bubble,liq}$ are considered one unit, L_{unit}. After the phase triplet is detected as a unit, a new, shortened distance s*, to the injection location is obtained. This distance depends on the phase lengths, which can vary depending on the operation of the capillary reactor. By dividing s* by the slug velocity v_{slug}, the time t_{delay} can be determined (Eq. 4.5), which must be awaited to inject gas into the observed phase triplet. By slight variations of t_{delay}, the injection can be changed so that the gas is injected in the slug or the front or rear of the gas bubble.

$$t_{delay} = \frac{s^*}{v_{slug}} \tag{4.5}$$

Figure 4.6 shows the procedure and the determination of the time delay. A unit cell's length and velocity measurement starts once the phase triplet's continuous phase reaches the sensor. The length measurement of L_{unit} is finished by passing the last disperse phase (here liquid) at the sensor, the new distance s*, and thus the required time delay t_{delay} can be calculated. After waiting for the calculated time, the gas is injected in the last step.

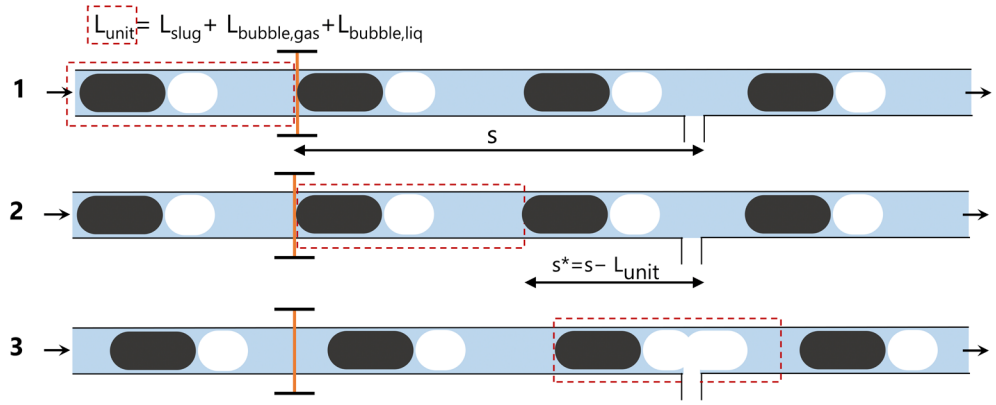

Figure 4.6. Illustration of the necessary steps to determine the operating parameters required for the control variables and the feeding after a time delay (t_{delay}). (1) Starting measuring slug velocity v_{slug}, and unit cell length L_{unit}. (2) Calculation of the new distance to the location of gas feeding. (3) Gas injection to the unit cell.

The other variable that needs to be controlled for the intermediate gas feeding is the injected gas bubble length ΔL_{gas}. Again, depending on the type of intermediate gas feeding used, the actuators and, thus, the control variables can change. Therefore, for both of the intermediate gas feeding options (solenoid valve and electrolysis cell), it is discussed how the released gas volume can be controlled.

For the solenoid valve, it is assumed that the gas is fed from a vessel with a constant pressure p_1 in a subcritical state into the capillary with a pressure p_2. It is also assumed that the diameter of the inlet of the T-junction is the smallest cross-section A_{inlet}. In that case, V_{gas} is only fed into the capillary during a defined opening time of the solenoid valve t_{open}. The following simplified relationship (Eq. 4.6) based on the Bernoulli and continuity equations can be used.

$$V_{gas} = A_{inlet} \cdot t_{open} \cdot \sqrt{\frac{2(p_1 - p_2)}{\rho_{gas}}} \tag{4.6}$$

The capillary pressure p_2 and the inlet cross-section A_{inlet} cannot be changed during operation and are, therefore, unsuitable for actively controlling the gas volume. However, with the opening time t_{open} and the inlet pressure p_1, two variables are available to modify the gas volume injected.

Faraday's law determines, by contrast, the amount of gas produced in the electrolytic cell. Assuming that the ideal gas law is valid, the gas volume V_{gas} can be calculated as follows (Eq. 4.7), given the temperature T and the capillary pressure p_2.

$$V_{gas} = t_{active} \cdot I \cdot \frac{R \cdot T}{z \cdot F \cdot p_2} \tag{4.7}$$

In this case, two possible control variables are also available, the active time t_{active}, in which the electricity is supplied (comparable with t_{open} of the solenoid valve), and the electrical current I (comparable with p_2).

In both cases, a few requirements regarding times t_{open} and t_{active} are needed. This time should be sufficiently short and easily variable within this range, so the gas is only injected when the slug (or the gas bubble in case of refilling) passes by. A reference time for phase segments between 3 and 8 mm and velocities of 15–30 mm/s is about 20–75 ms. In addition, the distance between the individual feedings must also be appropriately short so that a gas bubble can be injected into each unit cell. The injection frequency should be 1-5 Hz according to the abovementioned conditions.

The front and rear of a dispersed bubble are also referred to as caps. The shape of the caps varies depending on interfacial tension, viscosity, and velocity *(105)*. This makes it difficult to predict the exact bubble length as a function of volume. Nevertheless, the gas volume V_{gas} is used to infer the injected bubble's length. Two basic geometries represent the possible extrema: a cylinder with respective flat caps and a cylinder with perfect hemispheres. Since the actual bubble length should presumably be located between these two extrema, the detected bubble lengths are compared with the two estimated lengths in the subsequent chapters. The formation of a wall film also reduces the diameter of the bubble from the inner diameter of the capillary d by the wall-film thickness h. The wall film thickness can be calculated using existing models *(106, 107)*. ΔL_{gas} can thus be calculated from the gas volume for the two cases, as follows (Eq. 4.8).

$$\Delta L_{gas} = \begin{cases} \dfrac{4 \cdot V_{gas}}{\pi \cdot (d-h)^2} & for\ flat\ cap \\ \dfrac{4 \cdot V_{gas}}{\pi \cdot (d-h)^2} + \dfrac{1}{3}(d-h) & for\ hemispherical\ cap \end{cases} \tag{4.8}$$

4.4 Solenoid valve for gas injection in single-phase flow

The gas feeding with the solenoid valve was first examined in a single-phase (water) flow. It was found that the solenoid valve used only partially fulfilled the requirements for gas injection. The minimum opening time t_{open} seemed to be limited by the time needed to close the solenoid valve. This is probably due to the mechanical closing of the valve by a spring. An exact minimum opening time could not be experimentally determined. A variation of the opening time within the reference time (20–75 ms) did not result in a variation in the bubble length. The feed frequency was also limited for the solenoid valve since it overheated above a frequency of 1 Hz and no longer operated reliably. The solenoid valve used, therefore, did not meet the requirements for opening time and feed frequency. Nevertheless, the influence of the inlet pressure p_1 was investigated. The opening time was assumed to be constant and unknown, and gas was fed into the flow with a feeding frequency of 1 Hz.

Figure 4.7 shows the resulting biphasic flow at different pressures. Δp represents the difference between the capillary pressure p_2 and the upstream pressure of the solenoid valve p_1. A substantial increase in the bubble length can be observed as a function of the pressure difference. If the lengths at 40 and 50 mbar pressure difference are compared, the gas bubble increases by more than twice the length, which does not correlate with the theoretical

considerations from Eq. (4.6) with a square root relationship. This can be attributed to two causes. First, there is the unknown opening time of the valve, and second, the accuracy of the inlet pressure by the pressure regulator is insufficient for these pressure ranges, which can lead to deviations from the set pressures. Nevertheless, pressure seems to be the crucial factor in gas injection, which requires an exact adjustment of the pressure difference for an actual application.

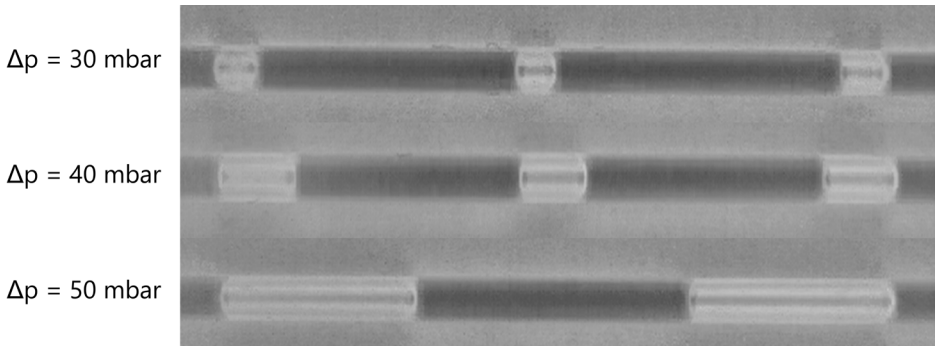

Figure 4.7. Bubble injection into a single-phase (water) flow via a solenoid valve, under variation of the pressure difference. Feeding frequency: 1 Hz.

Even if a dependence between pressure difference and injected bubble lengths were shown, this solenoid valve is unsuitable for intermediate gas feeding. This is mainly due to an inaccurate adjustment of the opening time and a slow feeding frequency.

In Chapter 4.8, therefore, a high-performance solenoid valve is used whose opening times can be set much more precisely. In addition, since the upstream pressure strongly influences the released gas volume, the electrolysis cell with a membrane is used to regulate precisely the upstream pressure.

4.5 Electrolysis cell for gas injection in single-phase flow

In the following, Hellmann's electrolysis cell is used to introduce gas bubbles into a single-phase liquid capillary flow. First, the limits of the operating conditions (maximum gas bubble length, maximum flow rate) are determined. For this purpose, influences such as the volume flow of the liquid phase, the electrical current, and the pulsation time of the electrolysis cell are considered individually. According to Faraday's law, the electrical current and pulsation time directly influence the amount of gas produced.

4.5.1 Volumetric flow variation of the continuous phase

The electrolysis cell was supplied with electricity via a transistor with a controlled rectangular signal to set the active time of the electrolysis t_{active}. The time between the pulsations, in which no electricity is supplied, is marked as t_{off} and set to 300 ms. Figure 4.8 shows the feeding of bubbles with a length of 2 mm in a range from 0.25 to 1 mL/min volumetric flow rate of the continuous phase. The length remains constant despite increasing volumetric flow. The low standard deviations indicate that the bubble lengths are generated precisely and regularly.

However, the bubbles become unstable at flow rates higher than 1.25 mL/min, whereby the gas volume produced in one pulsation is divided into a larger and a smaller bubble. This is caused by the T-junction and the resulting maximum possible bubble length due to the inlet diameter and ratio of the volumetric flows (see Garstecki and Fuerstmann) *(102)*. Therefore, when selecting the T-junction for gas feed, a sufficiently large inlet diameter for the gas phase has to be selected to produce regular bubbles, even at high volume flow rates.

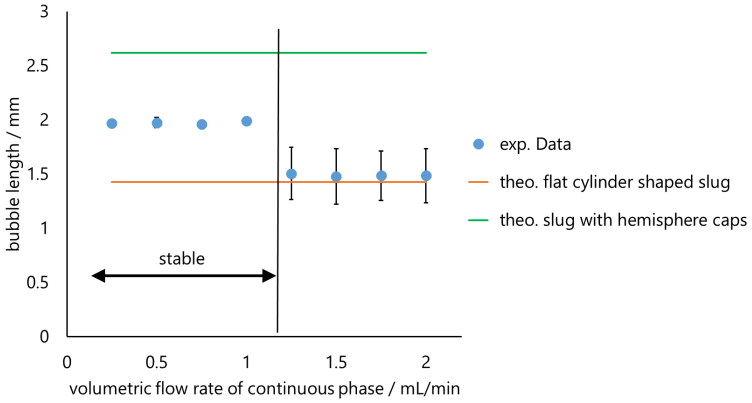

Figure 4.8. Dependence of bubble length with varying volumetric flow of the continuous phase. For volumetric flows from 0.25 to 2 mL/min, at t_{active}=40 ms, t_{off}=300 ms, and I=150 mA.

In addition, the experimentally determined bubble length is compared with two theoretical bubble geometries (see Eq. (4.8) flat/hemispherical caps). The actual length is between these two extrema, as illustrated in Figure 4.9. The two extrema show a deviation of about 0.5 mm, whereby the cylinder volume predicts a smaller bubble length, and the variant with additional hemispheres predicts longer bubbles. This shows that, with Faraday's Law (Eq. 4.5), the actual bubble lengths can be estimated approximatively.

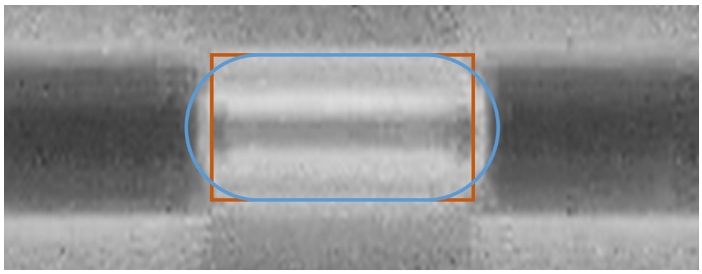

Figure 4.9. Comparison of the approximation methods with an actual bubble. Length of the actual bubble: 3.5 mm. Brown: approximation with cylindrical volume and flat caps. Blue: approximation of the bubble caps with perfect hemispheres.

4.5.2 Variation of the active time of electrolysis

To examine the influence of t_{active}, a range of 10 to 120 ms was analyzed at intervals of 10 ms. Figure 4.10 indicates that stable bubble lengths are obtained with values of t_{active} between 30 and 80 ms. Values below 30 ms show a constant length of about 1.5 mm; however, a reduction in length would be expected. This is because a bubble was not released every electrical pulsation, so the gas accumulates over several pulsations until it is released. The maximum

bubble length at 80 ms is 3.5 mm, which, as discussed before, is due to the limitation of the bubble generation at the T-junction. At higher electrical currents I and smaller values of t_{active}, and thus a higher volumetric flow of the gas, larger gas bubbles could be achieved.

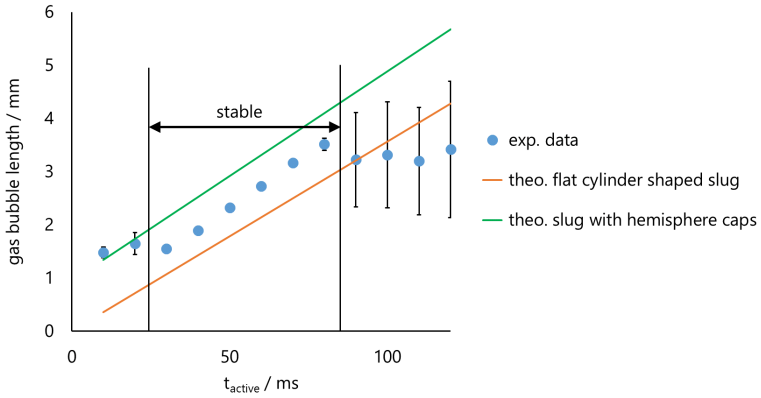

Figure 4.10. Dependence of the bubble length with the variation of the t_{active}. For a period of gas production from 10 to 120 ms, t_{active}=40 ms, t_{off}=300 ms, V_{cont}=0.5 mL/min, I=150 mA.

4.5.3 Variation of the electrical current

Figure 4.11 illustrates the variation of the electrical current I in a range from 25 to 350 mA. From a value of 100 mA, stable bubble lengths are generated. Below 100 mA, the gas volume per pulsation is too small to produce a bubble with each electrical pulsation. A flattening profile of the bubble length with increasing electrical current is noticeable. As from 250 mA, the bubble length no longer follows a linear trend. Probably, the selected electrical current cannot be reached entirely due to a too short t_{active}, caused by the current control unit used here. However, this effect can be minimized with other controllable power sources. By increasing t_{active}, this effect can also be minimized.

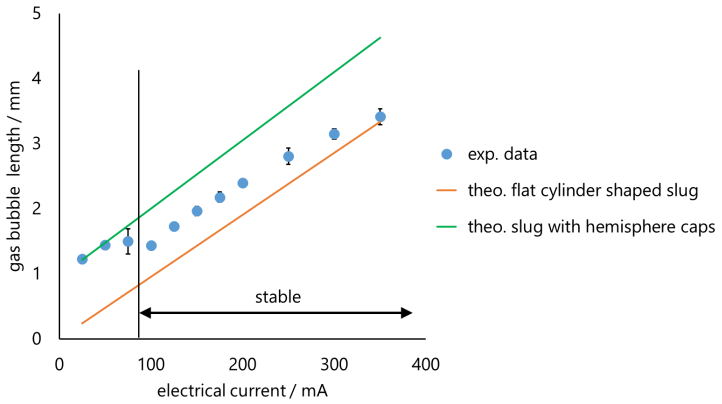

Figure 4.11. Dependence of the bubble length with varying electrical currents. For electrical currents from 25 to 350 mA; t_{active}=40 ms; V_{cont}=0.5 mL/min.

Thus, the electrolysis cell represents a suitable gas source for micro-process engineering, characterized by a volumetric flow rate with minimal fluctuations. In addition, the desired gas volume can be controlled effectively by the electrical current and the time supplying electricity

(t_{active}). Thus, electrolysis is also suitable for the controlled injection of gas bubbles into an existing multiphase flow in capillaries.

4.6 Intermediate gas feeding in an existing biphasic slug flow

The electrolysis cell by Hellmann (no membrane) examined in the following is used to inject an existing slug flow. First, gas bubbles are injected into an existing liquid-liquid slug flow, forming a regular triphasic flow. The feeding performance FP is used to evaluate this procedure, which describes the quotient between the successfully fed and stable gas bubbles and the liquid-liquid slug doublet passing within the same time, and thus the maximum possible number of bubbles to be injected (Eq. 4.9). Two hundred possible feeds are used as a reference.

$$FP = \frac{amount\ of\ actual\ fed\ and\ stable\ gas\ bubbles}{amount\ of\ maximal\ possible\ gas\ feedings} \tag{4.9}$$

Furthermore, gas is fed into a gas-liquid slug flow to fill the existing gas bubble. The objective is a coalescence of the injected gas with the existing gas bubble. The coalescence performance CP is used for evaluation, which describes the quotient between the number of injected and fully coalesced bubbles and the number of injections. For this purpose, 100 injections are used as the data basis.

$$CP = \frac{amount\ of\ coalated\ gas\ bubble}{amount\ of\ gas\ feedings} \tag{4.10}$$

Only the equations presented in Chapter 4.3 are used to determine the exact time of gas injection (Eq. 4.5) and to predict the amount of gas produced by using Faraday's law (Eq. 4.7). A feedback control is not applied yet.

4.6.1 Intermediate gas feeding in an existing liquid–liquid slug flow

The intermediate gas feeding into the liquid-liquid flow is first evaluated with a phase ratio of 1:1, whereby the gas is constantly injected into the continuous slug. Then, the total volumetric flow V_{tot} is varied with constant lengths of both liquid phases. Subsequently, at a constant volumetric flow, the lengths of the two liquid phases are varied. Finally, larger gas bubbles than the continuous phase are fed into the biphasic flow.

Gas bubbles are fed into a liquid-liquid slug flow with a length of the liquid disperse phase of 6.7 mm and a length of the continuous phase of 5.8 mm. The total volume flow is varied in the range of 0.25 to 1 mL/min. In addition, the set-point length of the gas bubble to be introduced is set to 2 mm, using an active time t_{active} of 40 ms, together with a resulting electrical current of 208 mA.

During the start-up, it is observed that the electrolysis cell requires a few pulsations (<5) to generate the necessary pressure for bubble formation and to release it in the continuous

phase. However, this effect is neglected when evaluating the feeding performance FP. Table 4.1 shows the feeding successes at different volumetric flows.

Table 4.1. Feeding performance of gas bubbles into an existing biphasic liquid-liquid slug flow at different total volumetric flows. Length of the liquid bubble=6.7 mm, length of the continuous slug=5.8 mm, length of the injected gas bubbles=2 mm, t_{active}=40 ms, and I=208 mA.

Volumetric flow/mL/min	Amount of successful feedings/-	Amount of resulting stable triphasic flow/-	Feeding performance (FP/%)
0.25	200	195	97.5
0.5	200	198	99
0.75	200	197	98.5
1	200	164	82.4

For a range of 0.25 to 0.75 mL/min, the feeding performance is at least 97.5%. At 1 mL/min, however, the feeding performance is only 82.4%. The two observed releasing mechanisms can explain this difference during gas injection (depicted in Figure 4.12). At higher volumetric flows, the gas bubble is often detached by the liquid bubble, and thus the produced gas quantity of one pulsation is often divided into two bubbles. The existing liquid bubble is also separated, and the stability of the slug flow is disrupted.

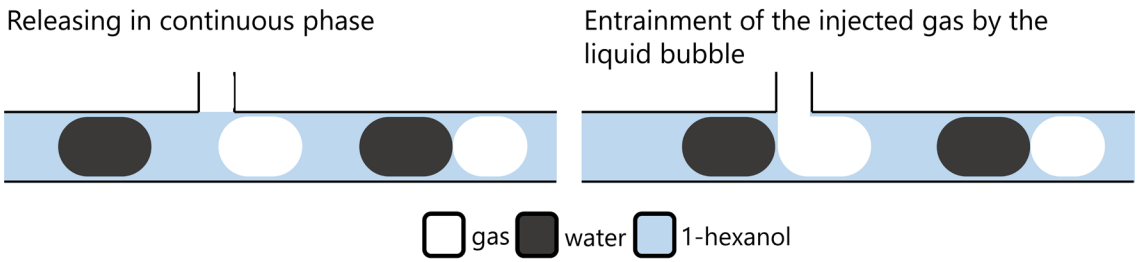

Figure 4.12. Two release mechanisms for the gas injection. Left: release in the continuous phase. Right: the fed gas bubble is attached at the T-junction outlet until the dispersed liquid bubble entrains it.

In these experiments, gas was always injected into the middle of the continuous phase. In order to have a comparable feeding performance at higher volume flows, the gas can either be injected further in front of the continuous phase or the injection can be accelerated by lowering the t_{active} and increasing the electrical current I. Figure 4.13 shows the resulting triphasic flow after a successful feeding at a total volume flow of 0.5 mL/min.

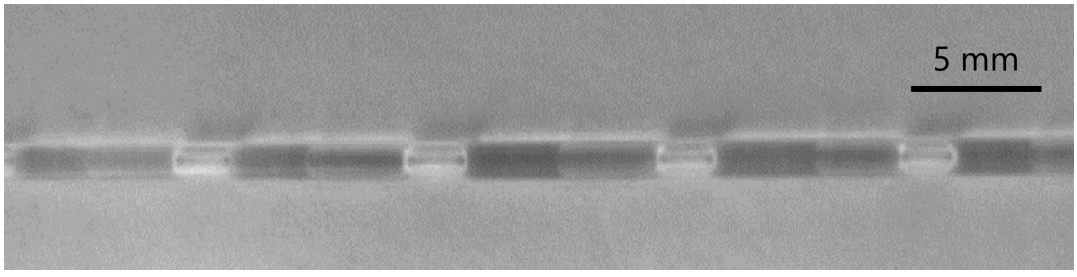

Figure 4.13. Resulting triphasic flow after successful intermediate gas feeding. V_{tot}=0.5 mL/min. Length of the liquid bubble: 3.1 mm. Length of the continuous slug: 3.5 mm. Length of the injected gas bubbles: 2 mm.

Such bubble detachment occurs when the injection time of the generated bubble is greater than the time for the bubble to be detached in the continuous phase. This detachment time

is influenced by the flow velocity and by the length of the continuous phase. In contrast to 0.5 and 0.75 mL/min, at 1 mL/min, it is crucial into which part of the continuous phase the bubble is injected. The time delay t_{delay} could be varied so that the gas bubble is released in the front of the continuous phase. Another approach is to reduce t_{active} to lower the releasing time. Simultaneously, the electrical current should be increased to ensure the same bubble lengths.

At 0.25 mL/min, it is also observed that the gas bubble is detached from the following water bubble. However, no early detachment occurs. In this case, the pressure force exerted by the continuous phase is not high enough to release the bubble due to its low velocity. Therefore, the gas bubble remains at the outlet of the T-junction until the next water bubble constricts and detaches it. The release time is thus shorter than the break-off time. Anyhow, this does not influence the flow pattern or feeding performance.

A manual variation of t_{delay} can also be used to analyze the effect if the gas is regularly fed into the center of the liquid droplet. It was observed that a regular triphasic flow is nonetheless formed. The front part of the divided water droplet is faster than the gas bubble due to a smaller wall film and catches up with the preceding water droplet, so both droplets coalesce into one segment as large as the previously non-divided droplet (see Figure 4.14).

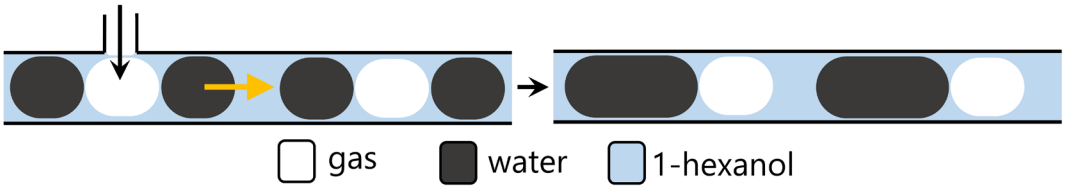

Figure 4.14. Schematic illustration of intermediate gas feeding into the water droplet with subsequent coalescence of the divided water droplets.

From these observations, it can be concluded that, despite the imprecise selection of t_{delay}, the slug flow is disturbed only locally for a short time and that, subsequently, the flow pattern can still be preserved. However, this effect can only be observed for a small t_{active}.

The segment lengths of the existing liquid-liquid slug flow were reduced in the following, decreasing the time for injecting gas in the continuous phase.

Table 4.2 shows the feeding performance with different segment lengths in the liquid-liquid slug flow. It can be concluded that intermediate gas feeding is applicable even to the smallest examined length of the continuous slug of 2.2 mm. However, the feeding performance is about 20% lower at these lengths. At these lengths, the effect of early detachment is more significant since the detachment time is shortened due to the reduced phase lengths.

Table 4.2. Injection of gas bubbles into an existing biphasic liquid-liquid slug flow at different total volume flows. V_{tot}=0.5 mL/min, length of the injected gas bubble 2 mm; t_{active}=40 ms; I=208 mA.

Length of water bubble / mm	Length of continuous slug / mm	Feeding performance (FP) / %
4.5	4.1	99
3.5	3.1	97
3.1	2.2	81

This observation, together with the results at different volumetric flows, indicates that the residence time of the continuous phase at the injection location limits the feeding.

Furthermore, this residence time depends on the flow velocity and the length of the continuous phase.

Since the single gas bubble injection is intended to counteract the low gas availability in the reactor, it is reasonable to introduce as much gas as possible. Therefore, large gas bubbles were fed into a liquid-liquid slug flow with small phase lengths. The liquid droplets had a length of 2.9 mm, and the length of the continuous slug was 2.7 mm. 5 and 7 mm gas bubbles were fed into this flow.

From Table 4.3, it can be deduced that an injection of a gas bubble, which is 2.5 times longer than the continuous slug, generates a regular triphasic flow in 88% of cases. In contrast, the shorter 5 mm long gas bubble shows only a 2.5% improvement. The short continuous slugs and the high active electrolysis time t_{active} can explain the deviation of 10% from the maximum feeding performance. The resulting large amount of gas, fed into the capillary quickly, causes a pulsation of the flow. Increasing the electrical current and shortening t_{active} intensifies this effect.

Table 4.3. Injection of gas bubbles into an existing biphasic liquid–liquid slug flow. Length of the liquid bubble: 2.9 mm. Length of the continuous slug: 2.7 mm. V_{tot}=0.5 mL/min.

Length of injected gas bubble/mm	I/mA	t_{active}/ms	Feeding performance FP/%
5	260	80	90.5
7	350	80	88

With such a quick injection into a 10 m capillary, the pulsations could be observed directly after the injection. However, these pulsations were eliminated entirely at the end of the capillary. Due to compression and expansion, the gas bubbles along the capillary have a damping and stabilizing effect, so the pulsations only occur locally and barely influence the overall flow. Figure 4.15 shows the resulting triphasic flow directly after injecting 7 mm gas bubbles.

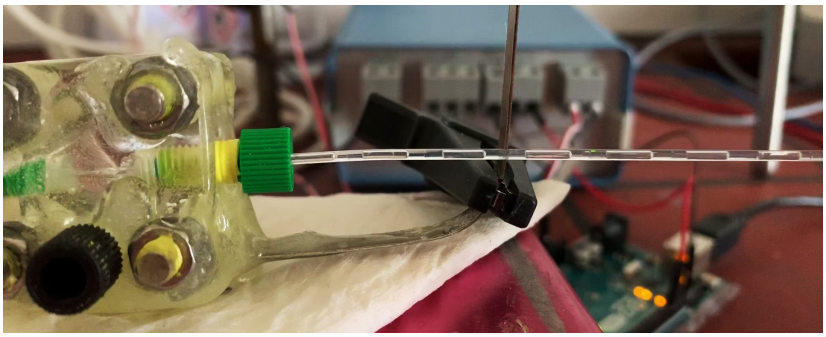

Figure 4.15. Triphasic slug flow after intermediate gas feeding with long gas bubbles (7 mm). Length of liquid droplet: 2.9 mm. Length of continuous slug: 2.7 mm. V_{tot}=0.5 mL/min.

4.6.2 Intermediate gas feeding into an existing gas-liquid slug flow

Refilling a gas bubble with new reactive gas can also be an attractive option, as, in this case, it is not necessary to await the total consumption of the existing bubble. Refilling may also be necessary if parts of the gas bubble contain inert components, so the entire gas bubble cannot

disappear. Therefore, gas was injected into an existing gas-liquid slug flow, and it was observed whether the existing gas bubble and the injected gas would merge.

Two influencing factors were examined: the influence of the total volumetric flow of the incoming biphasic flow and the location of the feeding. In principle, several locations are possible for the injection; the options illustrated in Figure 4.16 were examined.

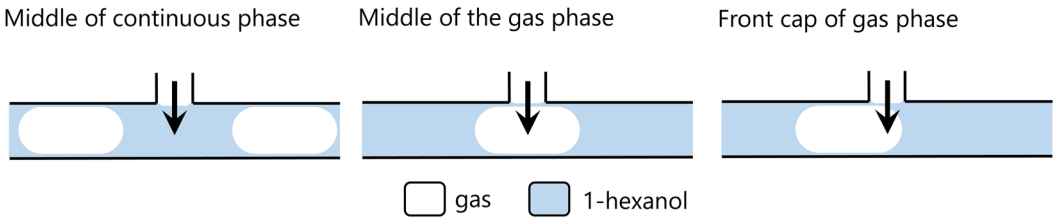

Figure 4.16. Three possible locations for injecting gas bubbles with the aim of refilling them. Left: Injection in the middle of the continuous phase. Middle: Injection in the middle of the gas phase. Right: Injection in the front cap of the gas phase.

The main advantage of feeding at the position of the gas bubble is that the two gas phases are forced to contact, and thus coalescence is more probable. Therefore, a distinction is made between feeding at the front cap and the middle of the gas bubble. If injection into the continuous phase is sufficient to unite both bubbles, this option is the simplest since this requires less precision in calculating t_{delay}. In order to feed at the different locations, the calculated t_{delay} was adjusted accordingly.

Table 4.4 presents the three alternatives' coalescence performances using two total volume flows. The injection into the continuous phase shows no coalescence. This is because the produced bubbles moved with the same velocity as the original bubbles. Therefore, injecting the gas into the continuous phase is insufficient if the gas bubble is to be refilled. On the other hand, feeding directly into the gas phase has partly led to coalescence. At lower volume flows (0.5 mL/min), the coalescence performance is 60–70%. At higher total volume flows (1 mL/min), the coalescence success is less than 10%. Qualitatively, coalescence is favored when filling the gas bubbles at a lower volume flow. Conversely, this implies that the increased forces in the capillary resulting from higher velocities are less favorable for coalescence. Furthermore, feeding into the cap is identified as a slightly more suitable option. Since coalescence depends on many factors, such as the interfacial tension, the viscosity of the continuous phase, and the geometry of the phase interfaces, the bubble refilling must be evaluated separately for each system.

Table 4.4. Coalescence performance of the intermediate gas feeding into the continuous phase, into the middle, and into the front cap of the gas phase. For a gas-liquid slug flows with a gas phase length of 7.3 mm and a continuous phase length of 6 mm. Gas injections: 100. ΔL_{gas}=2 mm; t_{active}=40 ms; and I=208 mA.

Volumetric flow V_{tot} / mL/min	**Injection in continuous slug CP/%**	**Injection in the middle of gas bubble CP/%**	**Injection in the front of gas bubble CP/%**
0.5	0	60	70
1	0	9	8

4.7 Electrolysis with membrane and solenoid valve

The previous experiments were repeated with a different electrolysis cell. This differs in that a membrane is used, and the gases produced are supplied separately. The electrolysis cell with gas separation membrane showed comparable reproducible results for a short duration (~10 min). However, a correspondingly higher electrical current was required to achieve the same volumes since oxygen was not fed into the capillary. Also, higher electrical currents were required for the same volumes at higher operating pressures since more mass per volume is present according to the ideal gas law.

After the operating time of about 10 min, the performance collapsed, and gas was injected into the capillary irregularly. After shutting down the electrolysis and disassembling it, a liquid was found on the cathode side, which had wetted the feed tube to the capillary. This liquid prevented the produced gas from entering the capillary directly, and the gas entered the capillary after a few pulsations.

The pH value of the liquid indicated that it originated from the water hold-up of the electrolysis cell on the anode side. The Nafion membrane is not entirely water-sealed and allows small amounts of liquid to diffuse. In the typical application of water electrolysis, this is not critical, but in the case of gas feeding into capillaries, this leads to instability. Furthermore, an additional hydrophobic gas diffusion layer (E20H GDL, Quintech, Göppingen, Germany) between the Nafion membrane and the cathode could not prevent the liquid transfer. The electrolysis cell in this form is, therefore, not suitable for continuous operation as a gas injection method. Nevertheless, together with a high-performance solenoid valve, it can be an elegant form of intermediate gas injection.

In Chapter 4.4, it was shown that a solenoid valve requires very accurate upstream pressure to inject small volumes into a capillary. However, the electrolysis cell can provide gases (with membrane, i.e., hydrogen) very accurately and quickly. Thus, if the electrolysis produces gas and feedback control pressure in a small pressure vessel (B8) upstream of a solenoid valve, the liquid leakage in the membrane is less relevant because the free gas volume in the vessel is sufficiently large.

By measuring the difference between the capillary and vessel pressure (PI4, PI5, DRMOD-I2C-PD0B5, B+B Thermo-Technik, Donaueschingen, Germany), a precise and small pressure difference can be built up, which can be used by the solenoid valve to inject defined gas volumes into the capillary. This combination of electrolysis and solenoid valve is particularly elegant since the pressure control is highly fine-tunable, and at the same time, this setup does not require any external gas cylinders. This setup is controlled by a microcontroller (Teensy 4.1, pjrc, Sherwood, OR, USA) and can be operated autonomously by a set point and operation mode input via a touch screen. The setup is shown schematically in Figure 4.17.

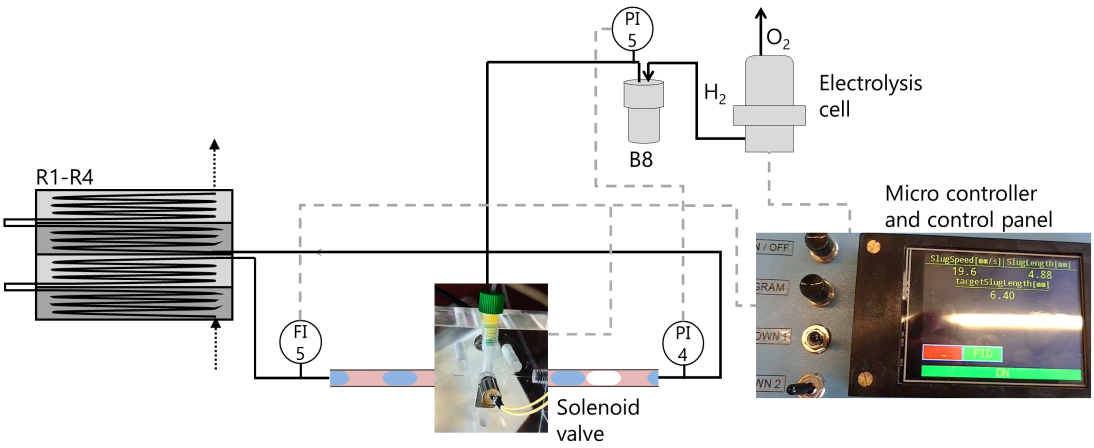

Figure 4.17. Schematic single gas bubble injection setup via solenoid valve in an existing liquid-liquid slug flow. Grey dashed lines: Communication lines. FI5: optical sensor from Chapter 5.

In Appendix D, the resulting gas bubble lengths for different opening times of the solenoid valve at constant upstream pressure can be found. According to Eq. 4.6, a linear relationship between the opening time and the gas volume could be determined with an accuracy of >99%.

4.8 Feedback control for the injected gas droplet length

It was already demonstrated that the control of the timing of the injection and the amount of gas released based on theoretical calculation led to satisfactory results of single bubble injection. Nevertheless, feedback control can be applied to optimize the feeding further. With the detection of the slug flow, the target values t_{delay} and ΔL_{gas} can be adjusted by closed-loop control. Therefore, only the case of the newly injected gas bubbles in a liquid-liquid flow is examined for the electrolysis cell without a membrane (Chapter 4.5). Figure 4.18 shows several undesired cases that might occur during intermediate gas feeding. Cases (1) and (2) represent an incorrect injection time and thus a false t_{dealy}. Cases (3) and (4) represent a deviation from the target value ΔL_{gas}.

Due to different physical properties, the liquid and gaseous bubbles form wall films of different thicknesses. Therefore, bubbles with a larger wall film are faster and catch up with the slower bubble of the other phase *(45).* Due to this effect, no adjustment of t_{delay} is required in case (1). However, if the bubble detaches too early, t_{delay} can be lowered to inject the gas bubble at the front of the continuous phase. In case (2), the existing liquid droplet is destroyed by a delayed injection. As shown in Chapter 4.6.1, this does not necessarily have to be disadvantageous, as the divided liquid droplets can unite into one single drop. In this case, however, early detachment is more likely than injection into the continuous phase. Therefore, t_{delay} must be lowered, so the gas is fed into the continuous phase.

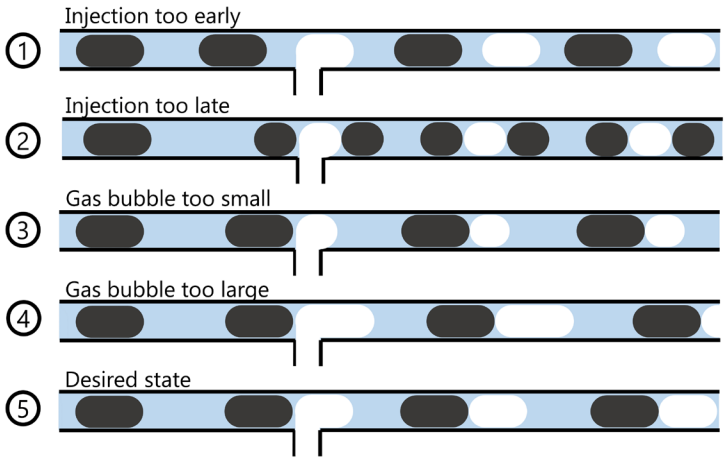

Figure 4.18. Four cases in which a control of the manipulated variables for intermediate gas feeding is beneficial. (1): The gas injection was performed too late. (2): The injection was performed too early. (3): The injected gas bubble is too small. (4): The injected gas bubble is too large. In (5) the desired state is shown.

Cases (3) and (4) describe either a too short or a too long injected gas bubble. The control of the setpoint ΔL_{gas} can be performed by the two actuating variables t_{active} and I. Reasonable initial values of both control variables should be carried out using the Faraday law suitable for ΔL_{gas}. In particular, t_{active} is the limiting variable since the time of feeding depends on the duration of the continuous slug passing. A good reference for t_{active} corresponds to about 30-80% of the residence time of the continuous phase at the feeding location. Based on t_{active} determined in this way, a starting value for electrical current I can be calculated using the Faraday law (see Eq. (4.7)). For active control, it is recommended to use the actuating variable of electrical current I since this can usually be set more precisely. However, if the flow is pulsating strongly due to large electrical currents, it is also advisable to increase t_{active}. It is helpful to define limits for the ratio between t_{active} and the electrical current depending on the capillary pressure. However, t_{active} is limited by the residence time of the continuous phase.

A P-controller was used to control the electrical current to demonstrate bubble-length regulation. Figure 4.19 depicts the progression of the injected droplet length after feeding. After approximately 20 gas bubbles, a maximum error of 2% is reached.

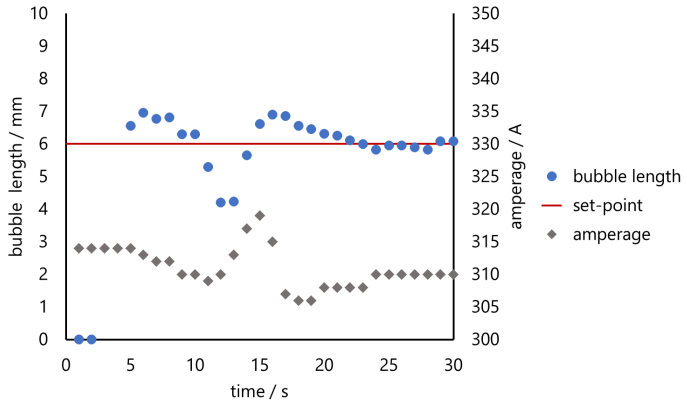

Figure 4.19. Time course of the controlled gas-bubble length injected with a P-controller. The electrical current was controlled, and one measuring point corresponds to one gas bubble. Proportional gain for P-controller: K_P=0.75, and t_{active}=80 ms.

4.9 Selection criteria for gas feeding methods

In the following, methods for feeding gas into slug flows are compared, and the merits and shortcomings of the respective methods are discussed. Tube-in-tube reactors and directed gas bubble injection by electrolysis or microvalves are considered. Donor reactions such as transfer hydrogenations are also briefly discussed as a conceptually distinct technique.

Gas permeation in tube-in-tube configuration (Chapter 3) is an elegant method, as it can feed gas into the capillary but also reduces mass transfer resistances *(56)*. However, commercially available tube-in-tube reactors with Teflon AF2400 are only suitable for short residence times or low volume flow rates, as they are limited to 4 m with the current state of the art. Other polymers, such as FEP or PTFE, are much cheaper and available in long capillaries. Due to their lower permeation coefficients, they require large exchange areas but thus allow a size-up of the length and volume flow. Low temperatures, however, minimize the gas flow.

The single gas bubble injection (Chapter 4) can introduce precise volumes into the capillary and is also suitable for low-temperature applications for which gas permeation is unsuitable. However, the equipment required is considerably more complex in comparison, especially if larger volumes of gas have to be fed - i.e., if several injection points are necessary. Therefore, this method is particularly interesting if gas permeation cannot be utilized due to incompatible reaction conditions (e.g., low temperatures) or if an exact gas volume is to be introduced into the capillary. This technique is also possible for steel capillaries as long as the optical sensors are replaced with contactless conductivity sensors *(108)*.

A conceptual alternative for triphasic capillary slug flow reactions could also entail a chemical modification to the system. For example, donor reactions (e.g., transfer hydrogenations see Appendix E) can be used to avoid the need for any reaction gas *(109–111)*. This reduces the equipment required enormously, although other case-specific challenges may arise, such as subsequent separation problems or shifts in selectivity.

For each application, it is essential to select the most suitable method for gas feeding individually and to choose the most appropriate setup. The advantages and disadvantages of the methods described above are summarized in Table 4.5.

Table 4.5. Comparison of different techniques for meeting reaction gas demands in multiphase capillary reactors.

	Temperature	**Kinetics**	**Set-up complexity**	**Costs**
Permeation with low permeation coefficient (FEP; PTFE, PFA)	Moderate temperatures are necessary. At high temperatures, plastic deformation is possible	Favorable for moderate/slow kinetics or high throughputs	moderate	moderate
Permeation with high permeation coefficient (Teflon AF 2400)		Favorable for (very) rapid kinetics	moderate	high
Single gas bubble injection (electrolysis, valve)	All temperatures	independent	very high	very high
Transfer reaction	Depends on chemistry	Depend on chemistry	low	Depend on reactants, but due to less equipment probably low

4.10 Summary and conclusion

Single gas bubble injection into multiphase slug flows was investigated. Parameters influencing the injection volumes when using valves and electrolysis cells were determined theoretically first, which were thereafter verified in practice.

For this purpose, a low-performance solenoid valve, a water electrolysis cell without gas separation, and the combination of a high-performance solenoid valve and a pressure-resistant electrolysis cell with gas separation were designed and studied. Slight variations (10 mbar) in the upstream pressure significantly influenced the feeding volume with a low-performance solenoid valve. As a result, precise upstream pressure control and an exact valve are necessary to implement solenoid valves successfully.

In comparison, the electrolysis cell without a membrane results in very accurate and reproducible gas bubble injection by controlling the power source. In addition, the Faraday Law can be used to predict the released gas volume. Feeding into an existing biphasic liquid-liquid flow with this electrolysis cell led to 99% success. In comparison, refilling existing gas bubbles in a gas-liquid flow was less successful because the gas bubbles rarely coalesce. Based on these results, it is preferable to await a gas-consuming reaction until the gas bubble has reacted completely and then introduce a new gas bubble.

Based on the presented equations, control is sufficient for most applications with the measured feeding performances. Nevertheless, individual actuating variables can be regulated by detecting the slug flow after the feeding. In some cases, this may be relevant for the injected gas bubble length since its shape is dictated by the individual system (interfacial forces, viscosities, velocity).

The electrolysis cell with gas separation alone could only perform well in short durations. Due to the small volume required on the cathode side and minimal water diffusion through the membrane, the permeating water clogged the inlet tube to the capillary and led to strong fluctuations in the gas bubble feed. Nevertheless, this electrolytic cell could control the upstream pressure of a high-performance solenoid valve, creating a setup that could precisely and consistently inject hydrogen bubbles into existing slug flows up to 10 bar. Moreover, this setup was automated with a microcontroller and a touchscreen interface, allowing a stand-alone application.

In the case of water electrolysis, the reaction gases, hydrogen and oxygen, separated by a membrane, can be used as reacting gas. Both gases are relevant for many gas–liquid reaction systems (i.e., hydrogenations, oxidations). In principle, other reaction gases, such as halogens and carbon monoxide, are also conceivable *(112, 113)*.

Finally, selection criteria for various gas injection methods into slug flows were given. Besides single gas bubble injection, permeation (Chapter 3) and chemical alternatives were discussed. One advantage of single gas injection is that it enables flexible utilization in steel capillaries with contactless conductivity sensors *(108)*.

The optical sensors, which have already been applied for control in this chapter, are analyzed in the following chapter concerning the influence of light refraction, the capillary position towards the detector and a mathematical processing proposed, which allows stable and fast slug detection.

5 Non-invasive triphasic flow sensor

PHOTOELECTRIC SENSOR FOR FAST AND LOW-PRICED DETERMINATION OF BI- AND TRIPHASIC SLUG FLOW PARAMETERS

ABSTRACT

Critical aspects of the well-studied slug flow, such as bubble generation and pump control, can be automated, providing a robust sensor for the reliable determination of velocity, segment lengths, and phase ratio(s) is available. A fast and low-priced sensor is presented, based on two optical transmission sensors detecting flow characteristics non-invasively together with a microcontroller. The resulting signal is mainly due to the refraction of the bubble-specific geometries, as shown by a simulation of light beams. The high performance of the processing procedure, utilizing the derivative of the signal, is demonstrated for a bi- and triphasic slug flow. The error of <5% is entirely reasonable for the purpose envisaged. The sensor presented is very fast, robust, and inexpensive, thus enhancing the attractiveness of scale-up approaches for capillary reactors in industrial applications.

The chapter is based on the publication:

Vietinghoff, N.; Lungrin, W.; Schulzke, R.; Tilly, J.; Agar, D. W. Photoelectric Sensor for Fast and Low-Priced Determination of Bi- and Triphasic Segmented Slug Flow Parameters. *Sensors* **2020**, 20 (23). DOI: 10.3390/s20236948.

Adopted in many parts, extended and modified.

This chapter is structured as follows:

- Motivation and state of the art
- Materials and methods
- Influence of vertical capillary position
- Mathematical data processing
- Distance between transmissive sensors
- Experimental validation
- Summary and conclusion

5.1 Motivation and state of the art

Although it has been demonstrated that a scale-up of capillary reactors (numbering or size-up) is feasible, the slug flows in capillaries have to provide an affordable option for multiphase systems in the chemical industry. Thus low-priced and robust actuators and sensors are essential if capillary reactors are to be an attractive, practical solution. In addition, precise and fast sensors are also essential for single bubble injection (Chapter 4). However, invasive sensor systems, such as a hot-wire anemometer, are fundamentally unsuitable since they can affect and disrupt the advantageous flow pattern. Further work thus needs to be focused on non-invasive sensors for monitoring velocities, phase ratios, and slug or bubble lengths.

First, Figure 5.1 depicts the variables to be controlled in a slug flow. It should be noted that the dispersed bubbles are enclosed by the better wall-wetting continuous phase, which usually forms a thin wall film. The continuous phase is also considered a slug, the length of which can be measured. The wall film must nevertheless be considered if a volumetric flow rate is to be determined from the velocity. For this purpose, existing models for the thickness of the wall film can be applied to calculate the volumetric flow rate, which is useful, for example, if a pump is to be controlled *(106, 107, 114)*.

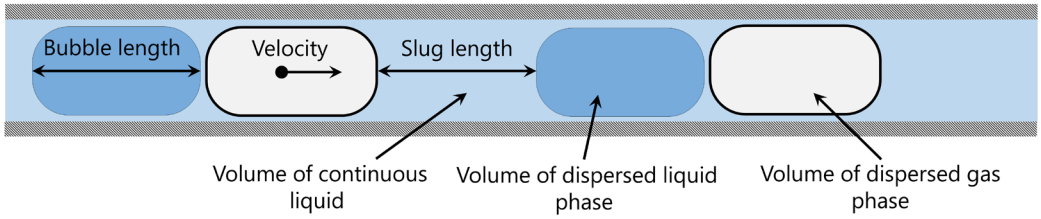

Figure 5.1. Schematic of a triphasic slug flow with two liquid and one gaseous component. The phase ratios can be determined either by a ratio of the slug and bubble lengths or, more appropriately, by the ratio of the phase volumes. The volumetric flow rate can be calculated using the velocity and the cross-sectional area together with the wall-film thickness. The slug/bubble lengths and velocity are thus required to control volumetric flow rate and phase ratio. The velocity is defined as a mean velocity from the cross-sectional area and assumed to be constant for all phases within a fully developed slug flow.

Multiple strategies had already been implemented to determine characteristic parameters from the slug flow. Tracking the slug flow with a high-speed camera is one possibility. High resolution of both the image and the time, together with adequate image processing, yield in slug/bubble lengths, phase ratios, velocity, and bubble shape. The raw image data is usually converted to a binary gray-scale facsimile, which permits the various phases to be distinguished. The number of pixels enables one to deduce the slug and bubble lengths. The velocity may be calculated with the subsequent snapshot and the frame rate *(115)*. This method determines precise values for the acquired data. However, since high-resolution images and high frame rates are needed, the expensive camera required is an inappropriate sensor system for industrial scale-up tasks. Flow characterization by micro-particle image velocimetry (µPIV) could also be used to ascertain the data required and enable visualization of internal slug flow patterns *(116)*. This technique is similarly too expensive for the purposes intended. Both camera tracking and µPIV utilize time-dependent two-dimensional (2D) images, thus increasing the complexity of data processing. These techniques are primarily

suitable for obtaining detailed insights into laboratory-scale equipment flow and calibrating other sensors.

On the other hand, time-dependent zero-dimensional (0D) sensor systems offer a viable alternative. 0D sensors monitor only a single location along the capillary, which all the phases of interest flow past. Two major 0D tracking systems have been investigated for slug flows based on either variation in electrical (conductivity) or optical behavior (i.e., transmissive sensors: absorption, refraction) for each phase involved.

The measuring principle of 0D sensors is illustrated in Figure 5.2. The sensors must be able to distinguish between the passing phases. For velocity and length measurements, two sensors are required. The quotient of the distance between the sensors ΔL and the time difference $t_\Delta=t_1-t_0$, which a specified characteristic point of the flow (e.g., a bubble cap) requires to flow from the first sensor to the second, yields the slug velocity as (Eq. 5.1):

$$u_{SL} = \frac{\Delta L}{t_\Delta} \tag{5.1}$$

Using the slug velocity u_{SL}, the segment length l_i can also be calculated. This is obtained by multiplying the time $t_{Pi}=t_2-t_0$ required by one segment to pass one of the sensors (Eq. 5.2).

$$l_i = u_{SL} \cdot t_{Pi} \tag{5.2}$$

With this method, the length of each phase can be determined. The phase ratios can be evaluated by using the ratios of the lengths for the individual phases.

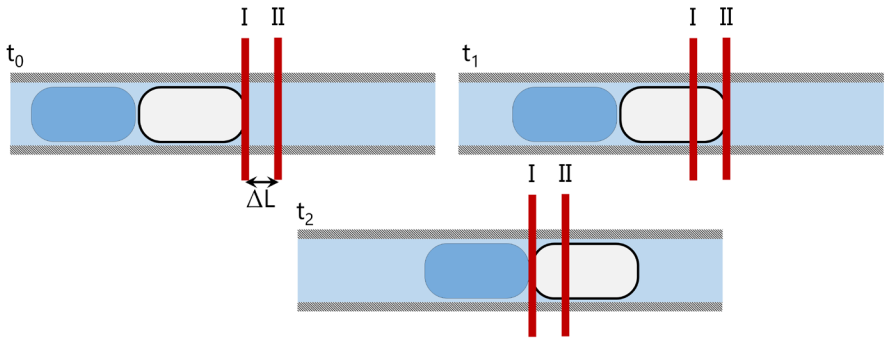

Figure 5.2. Principle of a 0D segment length and velocity sensor. In this case, the length and velocity of the first white bubble are measured. At t_0, the front cap of the bubble passes by the first sensor I. At t_1, the same feature passes sensor II. Finally, at time t_2, the rear cap of the bubble passes sensor I. With the help of the time differences, the velocity and bubble length of this bubble can be calculated by the equations given.

Conductivity sensors, like the commercially available capacitive coupled contactless conductivity detection (C^4D) sensor, employ a contactless measurement of the medium conductivity in a capillary with two external electrodes *(108, 117, 118)*. This measurement method is particularly elegant since it can also be utilized for non-transparent capillaries and is well-suited for biphasic systems *(118)*. A disadvantage, however, is that at least one of the phases (usually an aqueous phase) must have good conductivity *(108, 118)*. For example, this method can only hardly measure a liquid-gas slug flow with a non-conducting oil as a liquid phase. In a triphasic gas-liquid-liquid flow, which generally only has one conductive phase,

only information on the conductive phase can be captured. Therefore, measurement via contactless conductivity sensors is suitable for some biphasic systems but not generally applicable.

Photoelectric sensors represent an even more straightforward measurement technique, comprising one light emitter and one photodetector. The emitted light is transmitted through the capillary, and the flow is to be evaluated. Due to substance-specific light refraction, reflection or absorption, different light intensities are detected. Based on the resultant temporal light intensity change, individual phases can be clearly assigned to certain detection levels. The velocity and segment lengths can be calculated using two photoelectric sensors for a biphasic slug flow *(52, 119, 120)*. Mithran and Venkatesan configured one transmissive sensor horizontally and another vertically to acquire additional information about the wall-film thickness *(119)*. Harvie and de Mello ascribed the primary influence on the signals to light refraction and reflection, which, in turn, depended on the substance-specific refractive indices and the geometry of the phase interfaces *(120)*. Thus, the phases can be detected independently of their conductivity, and, in theory, the differentiation between the three phases is also possible. Harvie and de Mello employed centered positions for the detectors when setting up their sensor. Changes in this position could lead to an optimization of the resulting signal in light refraction because, in a centered location behind the capillary, the light beams are focused, which renders a differentiation of the phases more complicated, depending on the substances comprising the system. A smaller photodetector can also lead to a higher sensitivity of the capillary position with respect to the photodetector. Commercial "forked" photoelectric sensors (i.e., TCUT1300X01, Visahy) are particularly appealing because they are photodetectors having an edge length of 0.3 mm and the distance between emitter and detector of 3 mm, which is well suited for micro-capillaries *(121)*.

The approach of using dual transmissive sensors as a sensor system for slug flow appears to be one of the most effective and economical ways to detect slug-flow characteristics. In light of recent research on triphasic slug flows, this Chapter extends the sensor system from biphasic to encompass triphasic flows *(16, 38, 43)*. In this context, the influence of capillary position is examined since an improvement in phase discrimination is expected based on light refraction. A forked photoelectric sensor will be used for this purpose. Since two transmissive sensors are required to determine the velocity and the slug length, the degree of freedom with respect to the distance between the transmissive sensors is also discussed. In order to compensate for slight variations of the signal level (e.g., due to a change in the refractive index as a result of reaction), a data evaluation method is presented, which operates independently of the signal level and automates the acquisition of the required parameters.

In order to make the optical 0D sensor considered a feasible alternative for cost-effective application to an industrial multiphase capillary reactor, it is first investigated how the raw signal from the sensor can be reproducibly adjusted and improved. The resulting data are then interpreted by simulated beam paths through the capillary. Next, the data processing is explained, and a robust and rapid technique for this step is presented. Subsequently, the distance between the two sensors required is discussed, which directly influences the velocity calculation. Finally, the velocities and lengths determined by the sensor developed are evaluated according to their accuracy.

5.2 Materials and methods

The optical sensor used, a transmissive optical sensor equipped with two channels (TCUT1300X01, Vishay, Malvern, PA, USA), has a forked arrangement incorporating one emitter (emitted wavelength: 940 nm, detector: 0.3 mm width, 0.3 mm height; aperture: 0.3 mm width, 1 mm height) and two detectors (phototransistors). Detailed dimensions and specifications can be found in its technical specifications *(121)*. Two optical sensors are firmly soldered onto a circuit board and are placed 30 cm after the triphasic slug generation. In Figure 5.3, the experimental setup is presented schematically, and the transmissive sensors are shown from the top view. A high-speed camera (DMK 23G618, Imagingsource, Bremen, Germany) is installed just behind the optical sensor, which is used to validate the data measured with the optical sensor.

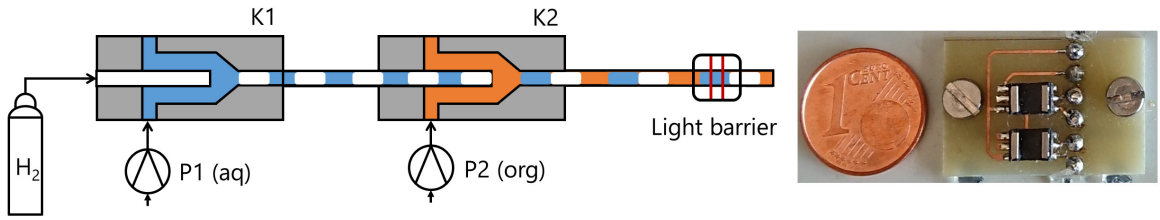

Figure 5.3. Left: Schematic simplified setup to generate the triphasic slug flow with detection of the flow with a transmissive sensor. Right: Circuit board with two transmissive sensors.

A capillary holder was fabricated, allowing the capillary position to adjust evenly and in small steps to change the capillary's height reproducibly. In Figure 5.4 (a+b), the capillary holder is presented schematically, and in (c), a photo of the three-dimensional (3D) printed holder made of polylactic acid (PLA) is shown. A recess is provided inside the capillary holder; the dimensions are selected so that the transmissive sensor circuit board can be embedded in the capillary holder. At the lowest position, it rests on the circuit board. A small top plate is attached on the top of the transmissive sensor unit, which prevents the screw from protruding between the emitter and the detector. The capillary holder contains a hole for fixing the capillary. This hole is placed so that at the lowest position, the capillary is located at the sensor's bottom. For a detailed analysis of capillary position, a capillary holder and a step motor (d) adjusting the screws was constructed, allowing an automated and uniform positioning of the capillary.

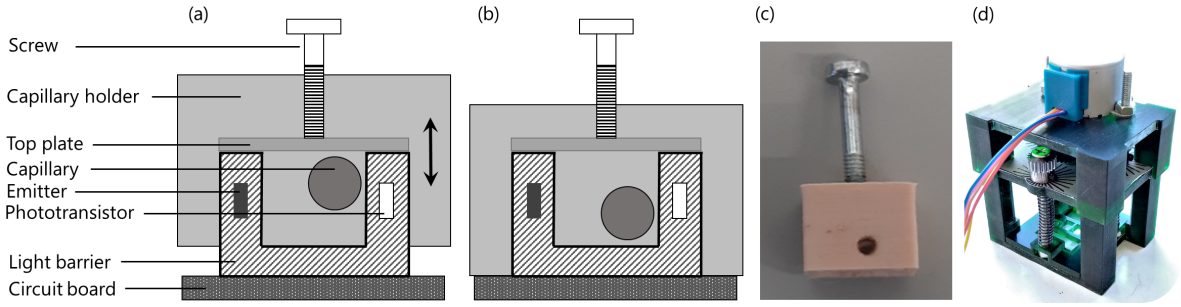

Figure 5.4. Schematic drawing and photos of the capillary holders. By pressing the screw against the stationary top plate, the holder (including the capillary) can be lowered and raised relative to the transmissive sensor. (a)

Capillary in highest position; (b) capillary in lowest position; (c) 3D-printed capillary holder with screw; (d) capillary holder combined with step motor.

The function of the prototype constructed in this way is that by screwing in the adjusting screw, the construction - including the fixed capillary - is pushed up evenly via the plate on the transmissive sensor housing. The screw is connected to the holder with a nut attached to it. In addition, the capillary holder shields the transmissive sensor from external light.

With this capillary holder, the vertical position can be adjusted by a screw with a pitch of 0.5 mm, which thus varies the capillary height by 0.125 mm per quarter rotation. Hence, the influence of the vertical capillary position on the signal quality can be investigated systematically.

The optical sensor is connected to a microcontroller board (teensy 4.1, pjrc, Sherwood, OR, USA), where the signals of the transmissive sensors are digitalized with a 12-bit resolution. The data evaluation to determine the velocity and lengths is also performed on the microcontroller board (see Chapter 5.4). The resulting data can either be stored on a micro secure digital (SD) card or transferred serially to a personal computer.

MatLab (2020a, MathWorks, Natick, MA, USA) was used to simulate the light beam paths (see Chapter 3.3). Firstly, the angle of incidence was determined at which a light beam impinges upon a phase interface. For simplification, it was assumed that depending on the angle of incidence and the refractive indices of the substances involved, the light beam is either completely refracted or reflected.

Table 5.1. Refractive indices of the substances considered, with air being considered to have the same refractive index as nitrogen.

Substance	Aggregation state	Refractive index / -	Sources
nitrogen/air	gaseous	1.003	*(122)*
water	liquid	1.333	*(122)*
hexanol	liquid	1.416	*(122)*
Fluorinated ethylene propylene (FEP)	solid	1.344	*(123)*

Of the materials used (FEP, hexanol, water, nitrogen, air), nitrogen and air show the most significant difference to the other substances in their refractive indices (see Table 5.1). Based on this and Fresnel's formulae, total reflection is only assumed if the incoming light beam from an optically denser medium (hexanol, water, FEP) passes into one of the optically less dense phases (nitrogen, air) *(124)*. Total internal reflection only occurs if the angle of incidence exceeds a critical value. The critical angle α_c depends on the ratio of the refractive indices and is determined by the following relationship (Eq. 5.3, where $n_2 < n_1$ applies).

$$\alpha_c = arcsin\left(\frac{n_2}{n_1}\right) \tag{5.3}$$

If the ratio of the refractive indices is greater than 1, the proportion of reflected light is low, according to Fresnel, and only becomes relevant at angles close to 90°. For this reason, only the refraction of light is taken into account when light passes from an optically less dense medium (nitrogen, air) to an optically denser one (hexanol, water, FEP).

If the light is refracted, Snellius' law of refraction (Eq. 5.4) is used to calculate the exit angle *(125)* :

$$\frac{sin(\alpha_i)}{sin(\alpha_j)} = \frac{n_j}{n_i} \tag{5.4}$$

Parallel light rays hitting the capillary are considered. A parallel light beam alignment can be assumed since the light source is relatively far away from the capillary, and no other light sources are present. The following dimensions of the capillary are assumed: 1/16" OD, 1 mm ID, FEP. In the capillary, either a pure hexanol phase is observed or a discrete bubble (nitrogen or water), separated from the inner wall film of hexanol. The wall film thickness of the considered system is determined with the help of the model proposed by Aussillous and Quéré to be 90 µm *(106)*. The whole system of capillary, wall film, and bubble is assumed to exhibit rotational symmetry.

5.3 Influence of vertical capillary position

Since the optical detector is considerably smaller than the capillary diameter, a detailed analysis of its position to the capillary concerning the form of the signal is possible. This degree of freedom allows manipulating the signal to optimize the data processing for more accurate measurements.

First, the height of a capillary containing a single phase is adjusted, and the resulting voltage is observed. The dispersed phases were positioned in the transmissive sensor by stopping a slug flow to consider the wall film. The capillary was then moved evenly from the lowest to the upper position by using the capillary holder with a stepper motor. The capillary is located at the lowest position on the bottom of the transmissive sensor. Figure 5.5 shows the resulting voltage of the transmissive sensor at different heights. Suppose the capillary is centered (~550 µm) in front of the detector. In that case, the signals for the liquid phases are 5 V and thus at the detection limit and significantly higher than the baseline signal (emitter to the detector without capillary) of 4 V. If the capillary is displaced vertically away from the detector, the resulting signal drops sharply. Proceeding from the centered position of the capillary, this drop is symmetrical for the upward and downward displacement. Nitrogen also exhibits a maximum signal for the centered capillary but does not attain the upper detection limit.

Optical considerations alone can explain this observation. It is assumed that the refraction of light is the decisive issue dictating the signal. Thus, the signal only depends on the system geometry, the light's wavelength, and the media's refractive indices.

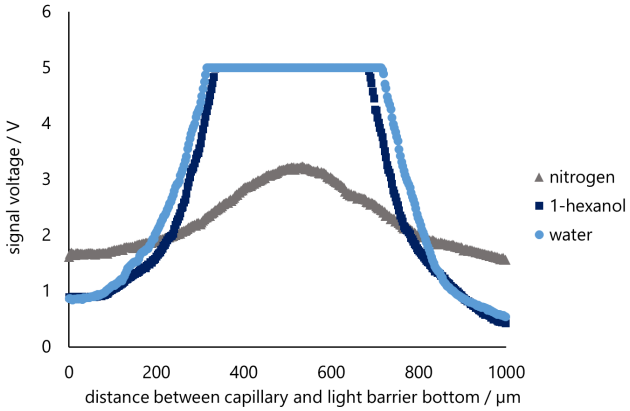

Figure 5.5. Measured voltage from phototransistor for a single-phase hexanol-filled capillary and water or nitrogen bubble with uniform capillary vertical displacement using a step motor.

Simulations of light beams through the capillary lead to light refraction, shown in Figure 5.6. The simulated beam paths through hexanol and water (Figure 5.6 A+B) show a focus of the light in the center of the capillary. This explains why the recorded voltage (see Figure 5.5) is higher than the baseline signal of the transmissive sensor without the capillary. This can explain the sharp drop at 300 and 750 µm because the rays are deflected and are not reaching these regions. The drop can occur earlier in the case of hexanol, which can be attributed to a stronger focus. In the gas phase (Figure 5.6 C), no light focusing but a slight divergence can be identified. In addition, some light rays are reflected at the interface between the wall film (hexanol) and nitrogen due to the large angle of incidence. This explains the low signals compared to the liquid phases. The higher signal in the center of the capillary results from the light focusing of the rays, which only pass through the capillary (FEP) and do not enter the gas phase.

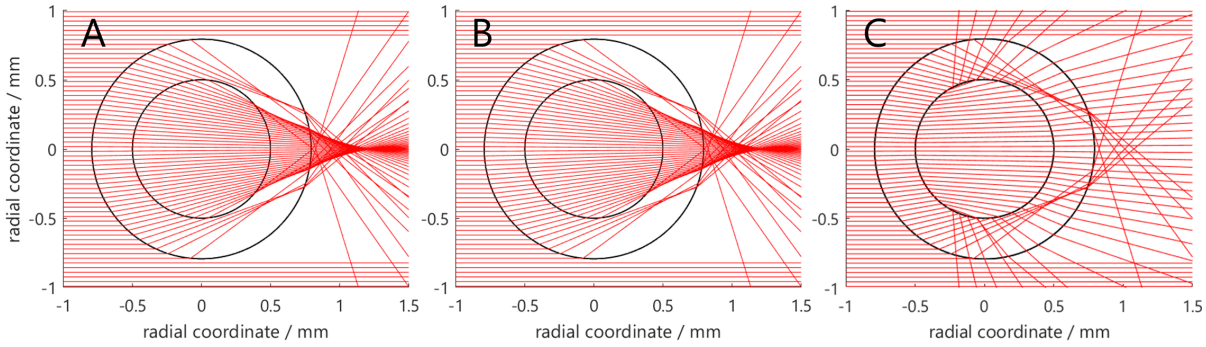

Figure 5.6. Simulated light refraction through capillary in vertical cross-sectional view. External medium: air, capillary: FEP, wall film: hexanol (not visible due to its low thickness), internal medium: hexanol (no wall film, A), water (B), nitrogen (C). The phototransistor can be assumed to be located approximately at 1 mm axial coordinate.

Since a significant influence of the position of the capillary vis-à-vis the detector had already been observed in a resting slug flow, dynamic signals for different capillary positions were also recorded for a triphasic flow. In Figure 5.7, the signals for a triphasic flow are shown. The gas phase was chosen to be particularly long in order to be able to assign it unambiguously to a particular voltage plateau. Furthermore, it was observed that the gas phase is followed first by

a water bubble and then the continuous phase of hexanol, which also facilitates the identification of the liquid phases from the signal.

The effect of the light being focused can be observed in the case of the centered position of the capillary and, thus, the amplitude of the resulting signal (see Figure 5.7, capillary position at 525 µm). This effect is nevertheless unsuitable for an evaluation since it is no longer possible to discriminate between the two liquid phases. An exception is the nitrogen bubble, which has a low signal at most heights and, thus, a low transmission. If the deflections in the vertical cross-section of the capillary with a nitrogen bubble are considered (Figure 5.6 C), the divergence and reflections lead to no focusing and a low voltage. Since this effect depends only partially on the capillary position, the signal for the gas phase is consistently at a low level.

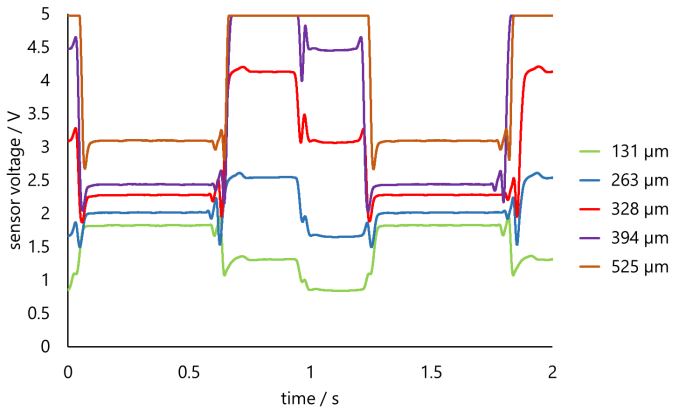

Figure 5.7. Measured voltages at different positions of the capillary relative to the phototransistor. The height is the distance between the lowest capillary position in the transmissive sensor and its actual position. Shown are positions from the bottom to an approx. centered position at 525 µm. Plateaus: nitrogen (0.1-0.6 s and 1.3-1.8 s), water (0.6-1.0 s and from 1.8 s), hexanol (up to 0.1 s and 1.0-1.3 s). The length of the plateaus show slight deviations due to deviations in bubble and slug length. Raw signal is processed with a moving average filter (see Chapter 5.4).

All three phases may be distinguished if the capillary moves away from the centered position (~550 µm). Such a signal makes it possible to distinguish between the individual phases clearly. Moreover, each phase present can be assigned to a given signal plateau. The signal at position (328 µm) is particularly suitable due to the significant differences in amplitude.

Symmetry can be observed if the capillary position is moved in the other direction (Figure 5.8). The signal depends only on the distance to the centered position and not the direction. For example, the signals at 328 µm and 788 µm are almost identical due to a similar distance to the centered position.

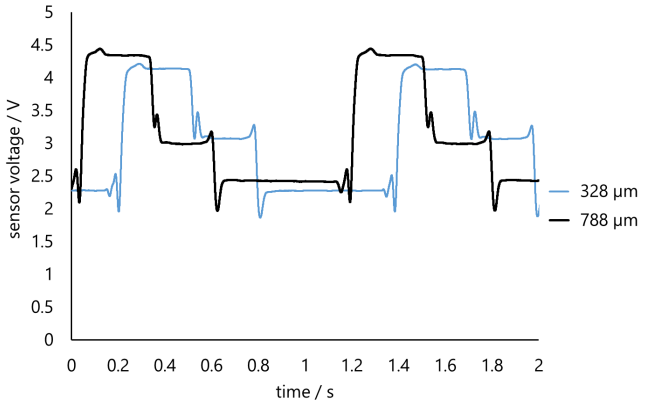

Figure 5.8. Measured voltages at two positions of the capillary relative to the phototransistor. The height is the distance between the lowest capillary position in the transmissive sensor and its actual position. Shown are positions with the approximatively same distance to the centered position. Plateaus: nitrogen (~2.3-2.5 V), hexanol (~3.0-3.2 V), water (~4.2-4.4 V). The signals were shifted with respect to time for a better comparison. Raw signal is processed with a moving average filter (see Chapter 5.4).

At the respective ends of the phase plateaus, minima and maxima are also visible in the signal. This shape can also be explained by light refraction. Figure 5.9 shows the beam path in the horizontal cross-section of a capillary with bubbles. Although only hemispheres were assumed as bubble caps here, which does not entirely reflect reality, the effects of light refraction are nevertheless well-represented *(65)*. A slight deflection of the rays can be observed at the cap of the water bubble (A). The deflection at the bubble cap creates a minimum since less transmission can be measured at this point. In this case, the light focuses to the right of the cap, which explains the signal's maxima. In the case of the nitrogen bubble (B), light deflection is more decisive due to the more significant difference in refraction, and the effect is correspondingly greater. These phenomena and the alignment of the individual segments result in the transition zones between the phase plateaus. In this case, the exact shape depends on the substance-specific refractive indices and the geometric shapes. The shape of the bubble cap may differ depending on the constituent substances and the flow velocities.

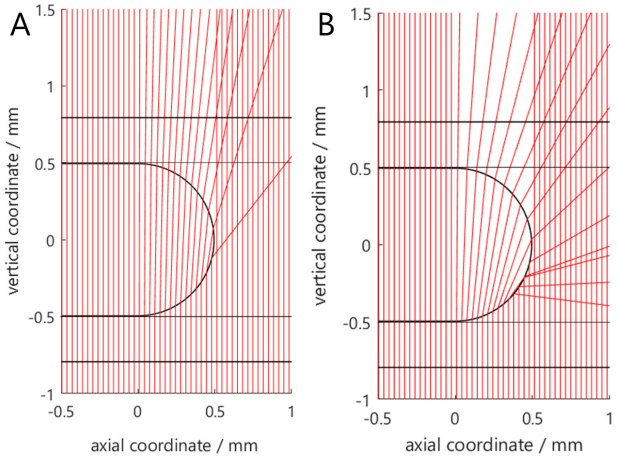

Figure 5.9. Simulated light refraction through capillary in horizontal cross-sectional view. External medium: air, capillary: FEP, wall film: hexanol (not visible due to its low thickness), continuous medium: hexanol, dispersed phases: water (A), and nitrogen (B). The phototransistor can be assumed to be located at approximately the 1 mm radial coordinate.

The distinct plateau heights result from the different light beam deflections, which can also be seen in the vertical cross-sections. Since absorption by the substances involved can be considered low (see UV-Vis spectra, Appendix F), the resulting signals are predominated based on the different refractive indices, the geometry, and the capillary position to the detector.

With the capillary holder and the positioning relative to the detector, the signal can be adjusted so that all phases can be clearly distinguished. Using these signals, the data evaluation described in the following can be used to determine the flow velocity, segment lengths, and phase ratios.

5.4 Mathematical data processing

With the fine-tuning of the signal via the capillary height, the improved signal can now be used to calculate the slug velocity. The simplest method is to set limits between the signal plateaus, which can be related to the respective phases. The signal section is assigned to a particular phase if the limit values are exceeded or not attained. Thus the signal of a biphasic flow can be transformed into a binary square-wave signal and the signal of the triphasic flow correspondingly into a ternary square-wave signal. With the square-wave signals, the flow velocity and segment lengths can be determined from a distance between two transmissive sensors. If this method is used, the signal height of the respective phase plateaus is required to define the limits. This is illustrated in Figure 5.10 using the signal at the centered position (Figure 5.7, 525 µm), which presents the differentiation between gas and liquid, as in a biphasic flow. The limit value can, for instance, be the average value of the two plateaus. A high measuring frequency and measurement noise can lead to a limit value being exceeded several times within a short period. A filter is, therefore, used to smooth the measured signal. In this particular case, a moving average filter was used. The number of averaged values is set depending on the measuring frequency. At a measuring frequency of 9600 Hz, for example, the last 128 values (approximately 13.3 ms) are averaged.

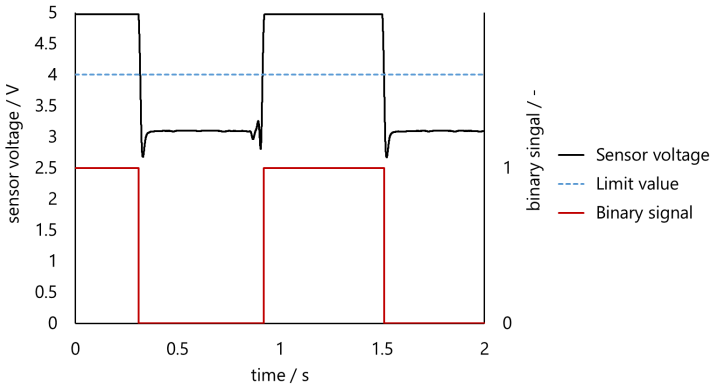

Figure 5.10. Transmissive sensor voltage (filtered with moving average) and its corresponding binary signal at 525 µm. The high plateau can be assigned to the liquid phases and the low plateau to nitrogen. The limit value was chosen to be 4 V.

However, this technique demands that the plateau heights remain constant. As soon as these change, with other media, for instance, a calibration to establish the new plateau heights is necessary. As shown above, slight differences in the capillary height relative to the detector can significantly affect the signal amplitude. Since it has been shown that the refractive index significantly influences the signal, a change in the refractive index may also necessitate new calibration. If the refractive index changes axially within the capillary due to reaction, extraction, or temperature variation, processing with a limit value may not be possible. These factors often fluctuate dynamically and can change according to the mode of operation. New limits must also be defined for each new system of media. Thus the evaluation of the signal may be suitable in some cases, but it is not as flexible to be generally applicable. In order to eliminate this lack of robustness, an alternative evaluation method is presented, which can account for variations in the plateau height without recalibration.

If the first time derivative of the smoothed signal is considered, the phase plateaus are located approximately on the x-axis. However, the flanks represent a clear boundary between the plateaus. The flank describes the transition between the two phase plateaus, generally characterized by a steep gradient. The derivative is, therefore, independent of the plateau height, and the phase differentiation can be performed exclusively based on the flanks. Therefore, a calibration based on the plateau height is no longer necessary. For the calculation of the slug velocity, the time t_Δ is needed, which one segment needs to pass from the first to the second transmissive sensor. Therefore, a characteristic point in the recorded signal must be identified. In the latter validation, it is shown that with the measurement accuracy for the velocity, it is sufficient to use the transition between the plateau and the following flank. Therefore, the plateau and the flank must be distinguished in the data. Figure 5.11 depicts the derivative of a signal for a triphasic flow.

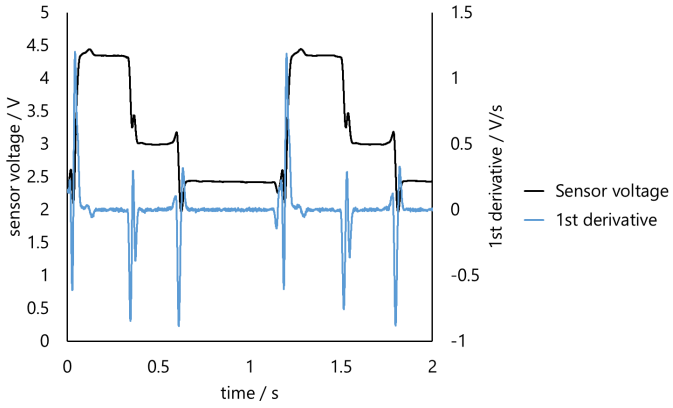

Figure 5.11. Transmissive sensor voltage (filtered with moving average) and its first derivative for a triphasic slug flow at a position of 788 µm. The plateaus can be assigned to the phases as follows: water, 1-hexanol, and nitrogen in the direction shown from left to right; the nitrogen plateau is the longest.

For the segment length, the exact time of the beginning and end of the cap is needed. It can be assumed that a bubble cap creates a minimum in the signal due to the divergence of the light beams (Chapter 5.3, Figure 5.9). Indeed, one minimum can be observed in the signal between a bubble and the continuous slug. Two minima can be observed at the transition between nitrogen and water because a thin layer of the continuous phase (hexanol) separates

both phases, so two bubble caps (for water and nitrogen) arise at this point. The time between the two minima surrounding a plateau is utilized to obtain the time t_{Pi} needed for the phase length calculation (Eq. 5.2). The minima can be derived from the first derivative. However, the derived segment length has to be evaluated for a new substance system since the cap shape may change. In this case, other characteristic points in the signal may also be used to obtain an appropriate segment length value.

Segment lengths and velocities can thus be unequivocally determined. However, the precondition for the clear identification of the phases involved remains. In a triphasic flow, therefore, triphasic plateaus must still be identifiable. For this purpose, the direction of the slope can be used. If the average slope direction (positive, negative) is determined for the flanks, only two sequences of slope direction of the flanks are possible: positive (I), positive (II), negative, or vice versa. By an initial observation, the phases can be assigned to the transitions of the slope directions of the previous flank. For example, in Figure 5.11, the assignment is as follows: nitrogen (negative (II) → positive), water (positive → negative (I)), and hexanol (negative (I)→ negative (II)). As long as the segment sequence along the capillary does not change, no further calibration is necessary. The data evaluation is, therefore, more robust than the calculation via the limiting values. Figure 5.12 summarizes the mathematical approach to determine the velocity and phase segment length.

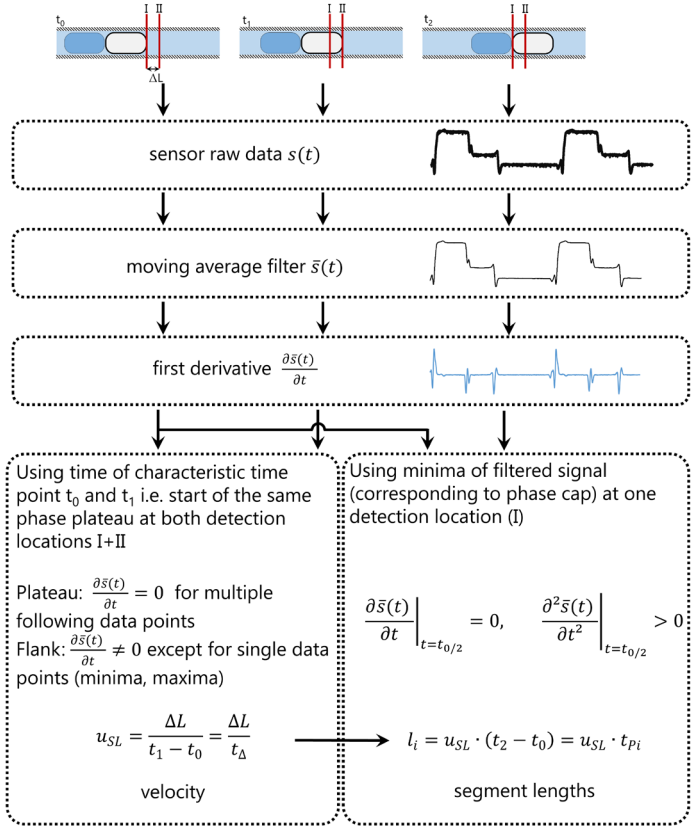

Figure 5.12. Mathematical approach to determine the velocity in a fully developed slug flow and the length of each phase segment. The velocity is determined by the characteristic time, a new phase plateau is beginning using the first derivative of the filtered signal. The minimum points surrounding the corresponding phase plateau are utilized for calculating all segment lengths.

5.5 Distance between transmissive sensors

The distance between the photoelectric sensors is an essential factor influencing the method's accuracy. If this distance is too short, even the smallest fluctuations in the flow velocity can cause a significant measurement error. If the distance is too large, it must be ensured that the segments can be tracked correctly since several unit cells may be located between both sensors. For this reason, several distances between the transmissive sensors were chosen, and the resulting velocities were compared with camera recordings. The smallest distance is 0.8 mm, determined by the dimensions of the dual transmissive sensor. With a second transmissive sensor, greater gaps can be realized. When the spacing between the transmissive sensors is larger than a unit cell, a third transmissive sensor is used. The second sensor stays at the minimum distance (0.8 mm) from the first to capture an approximate velocity. With the known distance to a third sensor, the time can be estimated when the observed segment will enter the third sensor so that a segment can be followed over several millimeters. Thus, the distances between the first and last sensors of 0.8-23 mm are compared. Whereas the distance of 0.8 mm does not use an additional sensor.

Figure 5.13 illustrates the measured velocities at different flow rates and transmissive sensor distances. Beginning with the smallest distance of 0.8 mm, a deviation from the actual value can be seen, and they also exhibit a large standard deviation. With low measuring frequencies, this could be attributed to the inaccuracy in the time parameter. However, with the measurement frequency of 9.6 kHz used here, this error can be assumed to be small. Slight fluctuations in the flow velocity lead to deviations. These are caused, for example, by slug generation or by fluctuations in the gas inlet flow. If other pumps, such as micro-gear or peristaltic pumps, are utilized, these can create additional disturbances.

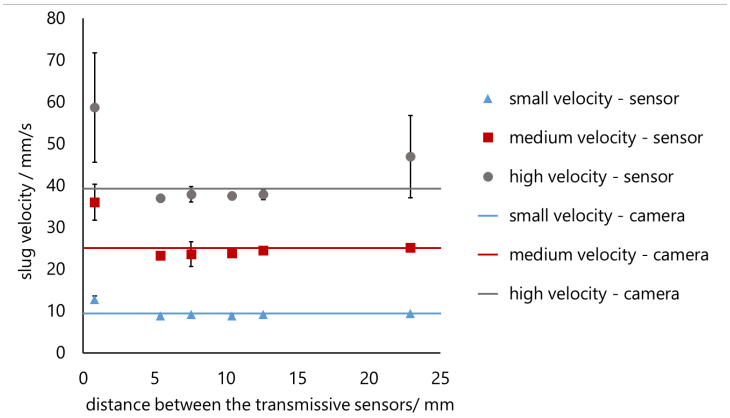

Figure 5.13. Comparison of measured velocities in a biphasic slug-flow (water, hexanol) for different distances between the two essential transmissive sensors. The velocities are compared with data from the high-speed camera.

The transmissive sensor distances between 5 and 12.5 mm show a good agreement with the actual flow velocities at all overall volumetric flow rates. A significant deviation can also be detected for the largest distance of 23 mm at high flow rates. This is because the velocity estimation of the first two transmissive sensors with a small gap between them is not sufficiently precise to predict the segment entrance in the third sensor.

The accuracy of the photoelectric sensor separation is essential for precise velocity determination. For example, if the distance used for calculation has an error of 5%, the velocity will, according to Eq. 5.1, deviate from its actual value by 5%. For a spacing of 5 mm, 5% corresponds to a deviation of 250 µm, a distance that is difficult to measure. Calibration of the distance is recommended to minimize this error. The difference between the measured velocities (transmissive sensor) to the actual ones (camera) can be minimized by varying the distance used in the calculation. In order to define the distance, it is recommended to solder both transmissive sensors on a single circuit board.

5.6 Experimental validation

Since the accuracy of the measurement method plays a major role in effectively implementing feedback control, the measures devised are combined. The capillary is fixed at such a height within the capillary holder that all three phases can be easily distinguished (525 µm). The data evaluation via the time derivative of the measuring signal allows a robust determination of velocity and length. The distance between the transmissive sensors was chosen to be 6.5 mm. It is narrow enough to identify the phase segment easily and wide enough to decrease the deviation at minimal distances. Under these conditions, the velocities and lengths from the transmissive sensors are compared with those of the camera images.

Figure 5.14 shows parity diagrams for velocities and lengths. The measured values deviate from the actual values by a maximum of 5%, which is in the same range as the C^{4}D sensor systems, but the new method is additionally applicable to arbitrary triphasic and non-conductive slug-flows.

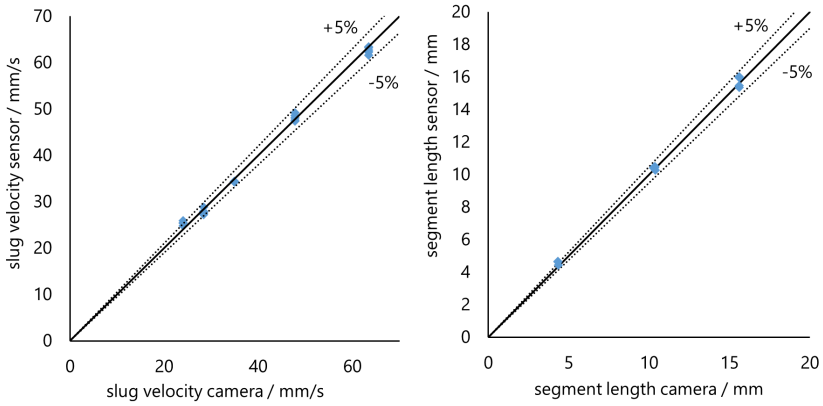

Figure 5.14. Parity diagrams to compare the performance of the transmissive sensor with the evaluation method presented to camera-determined values. Left: Slug velocity. Right: Segment length. Blue points: Measured data.

5.7 Summary and conclusion

The optoelectric sensor and the evaluation presented are a convincing alternative to the traditional 2D measuring methods, which have to handle much more data. A flexible capillary positioning allows even a triphasic flow to be monitored with high accuracy. By combining the optoelectronic sensor with data evaluation on a microcontroller board, the characteristic values of the slug flow, the lengths, and velocities can be determined reliably and quickly with sufficient precision (<5% error). This non-invasive sensor can therefore be easily integrated into a feedback control. To increase the sensor's sensitivity and create an even more significant difference between the phase plateaus, a more sensitive detector could be utilized, allowing voltages above 5 V. This would lead to a continuous symmetric function with a maximum for each phase at the centered capillary position. Anyhow, the most sensitive position is probably not in a centered position, considering the three-dimensional light refraction at the bubble caps.

The transmissive sensor may get to its limitations in some applications, for instance, when reactions or extractions exhibit rapid dynamics or considerable variations in refractive indices, when substances have very close or identical optical properties, and for systems that strongly absorb light.

The evaluation method utilizing the first derivative of the sensor signals can cope with most of the variations encountered in the refractive indices since the phase plateau height is not considered in the evaluation process. However, the technique becomes unsuitable for a considerable change in the refractive index, where the signal plateaus can no longer be assigned to a given phase through the slope direction. Other independent methods to identify the individual phases are required in such cases. For example, the gas phase, with its usually low refractive index leading to constant plateau height or two local minima of the signal indicating two successive dispersed bubbles, could be used for orientation purposes in interpreting the multiphase structure.

In terms of cost, the optoelectric sensor is very cheap with a price of <1 $. The use of microcontroller boards allows the simultaneous evaluation of several sensors with a single board, or, as another option, they can be integrated directly into a control system. New channels can be added flexibly to this system as required in a numbering-up. A hierarchical control system, for example, is ideal for this purpose, in which the reactor conditions can be defined at a central location, but the control and sensor systems are implemented locally for individual capillaries or capillary bundles. Outsourcing these sensor evaluations has the advantage that the sensors do not significantly occupy the computing power of the main control unit (e.g., a personal computer).

The sensor devised can be used for various control tasks, for example, the control of slug or bubble lengths and volume flow rates already mentioned. Moreover, if the actuators for such systems can also be implemented at a low cost, an industrial application of parallelized capillary reactors becomes a realistic, high-performance design strategy.

In this chapter, the wavelength was chosen so that the substances absorb only small parts of the light, and thus the signal form is dictated by light refraction. However, the wavelength can also be selected so that one or more phases absorb light; thus, an even stronger differentiation of the phases becomes possible. This can be helpful if the refractive indices of the individual phases are very close to one another. Light absorption in certain substances does thus not exclude this sensor. The absorption of a specific wavelength can also be used to evaluate the concentrations of individual substances. For example, non-invasive residence time measurements or local conversions can be determined. Therefore, Chapter 6 develops an optoelectronic sensor that exploits a dye's absorption to non-invasively measure the dye's local conversion with a decolorization reaction in a capillary.

6 Non-invasive conversion tracking

EXPERIMENTAL STUDY OF HYDRODYNAMIC INFLUENCES IN A TRIPHASIC GAS-LIQUID-LIQUID SLUG FLOW WITH A DYE HYDROGENATION

ABSTRACT

A non-invasive concentration sensor is developed to track the hydrogenation of a dye in a triphasic slug flow. After identifying suitable dyes that turn colorless during hydrogenation, optical sensors based on light absorption in the UV-Vis spectrum are developed and used for conversion tracking. A homogeneous catalyzed hydrogenation of the azo dye Sudan III is then used to investigate the influence of hydrodynamic operating variables in multiphase slug flows, such as the flow velocity or phase segment lengths. Changing the segment length and velocity did not significantly increase the conversion. Furthermore, it is shown that the slug flow per se greatly minimizes mass transport limitations of the triphasic reaction compared to a stirred tank reactor. Nevertheless, within the slug flow regime, kinetics seem to be limiting, and changes in hydrodynamic parameters show only a small effect. However, catalyst deposits can be detected on the capillary wall, indicating a loss of the active catalyst species. Possibly a small permeation flow of oxygen might be responsible.

This chapter is structured as follows:

- Motivation and state of the art
- Materials and methods
- Selection of a suitable dye
- Development of a non-invasive online sensor
- Catalyst deposition in the capillary reactor
- Investigation of hydrodynamic influences in a slug flow
- Summary and conclusion

6.1 Motivation and state of the art

For applying a multiphase reaction in triphasic slug flows capillary reactors, chemically relevant operating conditions such as the reaction temperature, pressure, and solvent selection influence the reaction. Nevertheless, the hydrodynamic operating conditions of this particular reactor type are also relevant. In particular, the flow velocity, residence time, segment lengths, and phase ratios are relevant. Each of these affects the internal Taylor eddies intensity and thus the transport processes in the reactor. Therefore, the influence of these hydrodynamic parameters is studied in this chapter. In this context, the hydrodynamic influences are widely considered independent of the chemical influences. The findings obtained could then be transferred to other more complex reaction systems.

This results in some requirements for the reaction system. Thus, a gas-liquid reaction should be utilized, which has little influence on the hydrodynamics (e.g., substantial shrinkage of the gas phase in gas-consuming reactions). Furthermore, from a chemical perspective, the reaction system should be relatively simple, i.e., it should have few or no side or consecutive reactions and be well analyzable - ideally with a non-invasive online sensor.

A functional reaction system is, for example, the hydrogenation of conjugated dye molecules (e.g., azo or triphenylmethane (TPM) dyes). By hydrogenating a double bond of the molecule, the conjugated π-electron system is interrupted, and the molecule loses its chromaticity. By analyzing the light absorption in visible light using ultraviolet-visible light spectroscopy (UV-Vis), the concentration and, thus, the conversion can be deduced. This principle of decoloration has previously been used, for example, to determine the degradation of wastewater or to study the activity of newly developed catalysts *(126–129)*. By using optically transparent FEP capillaries, it is even possible to perform non-invasive concentration measurements at multiple locations in the capillary. Another advantage of dyes is the small concentrations required, which already induce intense coloration. At the same time, small concentrations mean only a minor consumption of hydrogen and thus approximately constant hydrodynamic conditions (no shrinkage of the gas phase, no change in viscosity/density).

Such dye hydrogenations have not yet been applied in a capillary, but color reactions have been used to determine mass transport phenomena. Krieger et al., for example, used the color change of indigo carmine from yellow over red to blue to determine the mass transport of oxygen in a gas-liquid flow. In addition, they tracked a flow segment along the capillary with a moving camera *(130, 131)*. Dietrich et al., in turn, used resazurin to likewise measure oxygen transport in gas-liquid capillary flows with a camera setup *(132)*. For liquid-liquid mass transfer, in turn, Hellmann was already using dye sensors in triphasic flows *(45)*.

Theoretically, it is also possible to track the color change using an optical 0D sensor (see Chapter 5), which, in addition to the refractive indices, sensitively exploits the wavelength of the color change to receive additional information on the light absorption. Höving et al. have recently developed such a 0D sensor for biphasic flows, which, among other applications, could also determine the local concentration of dyes *(133)*. So that implementation seems to be feasible for hydrogenation reactions in triphasic flow.

Therefore, a suitable dye, soluble in hexanol, for a triphasic gas-liquid-liquid reaction will be identified first in Chapter 6.3. Then, a water-soluble homogeneous catalyst is used in the second liquid phase, with hydrogen in the gas phase, a triphasic reaction system is present. Then, based on this dye, a non-invasive online sensor will be developed, which measures the dye's concentration and, thus, the reaction's conversion in Chapter 6.4. After the characterization of this sensor, the deposition of the homogenous catalyst in the capillary is discussed (Chapter 6.5), and finally, the mentioned hydrodynamic influences in the triphasic slug flow will be investigated (Chapter 6.6).

Finally, an additional comparison will be made between the performance of the microcapillary reactor and the same reaction in a discontinuous stirred tank reactor to prove if the slug flow improves the reaction. Figure 6.1 shows a schematic setup with two optical sensors and a triphasic slug flow. The continuous phase contains the dye to be hydrogenated, and a homogeneous catalyst is dissolved in the second liquid phase.

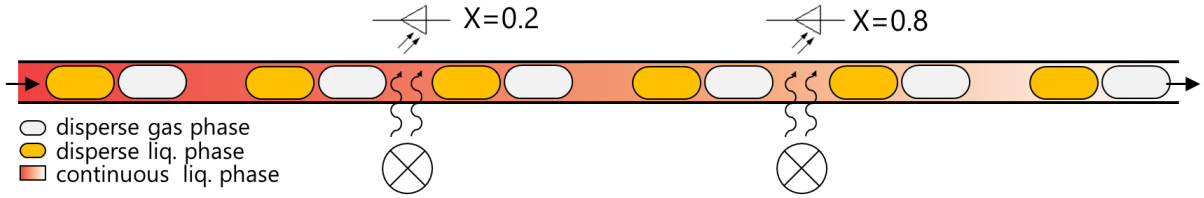

Figure 6.1. Schematic setup of the investigated system with two optical sensors measuring online the local concentration of a coloring dye and calculated exemplary the conversion to 0.2 and 0.8. The red dye is dissolved in the continuous liquid phase, whereas the second liquid (dispersed) phase contains a catalyst, and hydrogen forms an additional dispersed phase.

6.2 Materials and methods

To select a suitable reactant (see Chapter 6.3), the two azo dyes Solvent Black 3 (Kremer Pigments, Aichstetten, Germany, >99.99%) and Sudan III (Roth, Karlsruhe, Germany, 88%), as well as the TPM dyes bromothymol blue (Merck, Damrstadt, Germany, ACS, Reag. PhEur) and crystal violet (Merck, Darmstadt, Germany, ACS, Reag. PhEur) are used. The structural formulas can be found in Figure 6.2. The dyes are completely dissolved in hexanol by stirring. The highest concentration is initially chosen to measure the UV-Vis spectra below the highest extinction value (3) without dilution. For a later comparison between the reaction with two liquid phases and one liquid phase, the dye Ponceau BS (Thermo Fischer Scientific, Waltham, MA, USA, >85%) is used. This dye has the same molecular structure as Sudan III but is water-soluble due to two additional sulfone groups.

A water-soluble variant of the Wilkinson catalyst is used as the homogeneous transition metal catalyst. In addition to the active rhodium center, water-soluble 3,3′,3′′-phosphanetriyltris(benzenesulfonic acid) trisodium salt (TPPTS) ligands are used (structure is also shown in Figure 6.2). For this purpose, the rhodium precursor chloro-(1,5-cyclooctadiene)-rhodium(I) dimer (abcr, Karlsruhe, Germany, 98%), and the TPPTS ligands (oxea, saturated aqueous solution) are dissolved in degassed water under an argon atmosphere (Argon, Messer, Bad Solden, Germany, 99.996%). This involves treating the

solution in an ultrasonic bath for at least one hour until no solid is visible. A rhodium concentration of 0.3 mmol/L and a molar rhodium-to-ligand ratio of 1:5 are used in all experiments presented. For the experiments in the capillary reactor, the catalyst is preformed directly in vessel B4 of the setup. This can be connected to the syringe pump under an argon atmosphere without further contamination (see Chapter 2.4). The catalyst was prepared on the same day as the experiment was conducted.

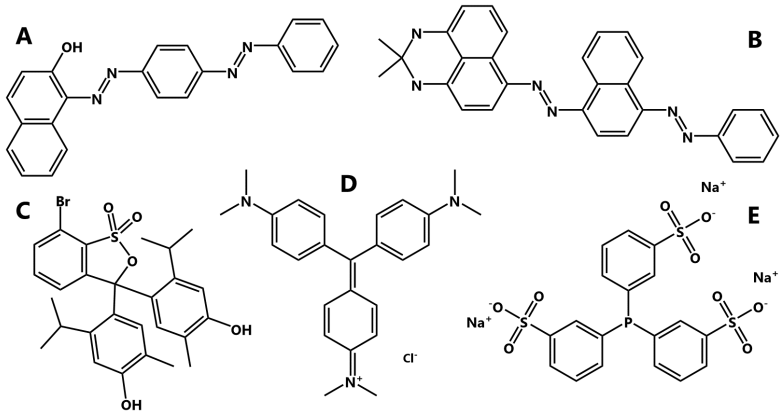

Figure 6.2. Structural formulas of the dyes studied and the catalyst ligand TPPTS. A: Sudan III, B: Solvent Black 3, C: Bromothymol blue, D: Crystal violet, E: TPPTS

For analysis, an UV-Vis spectrometer (Genesys 10 UV, Thermo Electron, Langensbold, Germany) was used in addition to the online sensor developed in Chapter 6.4. Air was used as the reference medium for recording extinction coefficients.

For selecting the dye (Chapter 6.3), a stirred tank reactor (approx. 200 mL, Parr 4560, Parr Instruments, Frankfurt, Germany) is used. In all other experiments, the capillary reactor with the setup from Chapter 2.4 is used.

The stirred tank reactor is placed in a heating jacket, operated with water, and tempered via a thermostat (F25, Julabo, Seelbach, Germany). Stirring is performed with a four-blade stirrer at 712 rpm, positioned approximately on the liquid-liquid interface at rest. Since the catalyst is sensitive to oxygen, it must be ensured that no oxygen is present in the reactor vessel. For this purpose, the reactor is evacuated several times and purged with nitrogen and argon. The liquid phases can then be fed into the reactor from the outside through a vacuum. Hydrogen is then introduced at the desired pressure. The reactor is initially filled with 100 mL of liquid, and hydrogen is continuously added so that the pressure remains constant. Samples can be taken from the reactor interior through a capillary tube. The drawn samples are cooled in ice and gassed with helium so that any hydrogen still dissolved can be stripped from the liquid phases to stop the reaction as quickly as possible.

The design and components used for the sensor developed later are described in Chapter 6.4.

The flow velocity changes due to gas expansion by different temperatures. Therefore, the average velocity from the inlet and outlet is used to determine the Reynolds and Capillary numbers. In the experiments performed, the Ca number was between 0.003 and 0.018, and the Reynolds number was between 0.69 and 122.1, so non-turbulent flows can be assumed. The unit cell length introduced (all phase segments together) L_{uc} is measured at the inlet and

is noted for each experiment. The necessary physical properties and their temperature dependence were taken from the literature *(134, 135)*.

6.3 Selection of a suitable dye

In order to develop a suitable inexpensive, fast online concentration sensor, a suitable reaction system is required. Hydrogenation of a conjugated dye molecule is to be considered. The hydrogenation breaks the conjugated double-bond system of the dye, which causes the dye to lose its color in the visible light spectrum. Using Sudan III as an example, the assumed primary reaction is shown in Figure 6.3. The product structure or product mixture is irrelevant as long as these species are colorless. In sum, the overall intensity of the dye decreases over the reaction time. The remaining light absorption in the dye-specific wavelength range can then be used to infer the concentration. Therefore, a set of requirements is defined for an appropriate dye selection, and a pre-selection of azo and TPM dyes is evaluated for suitability.

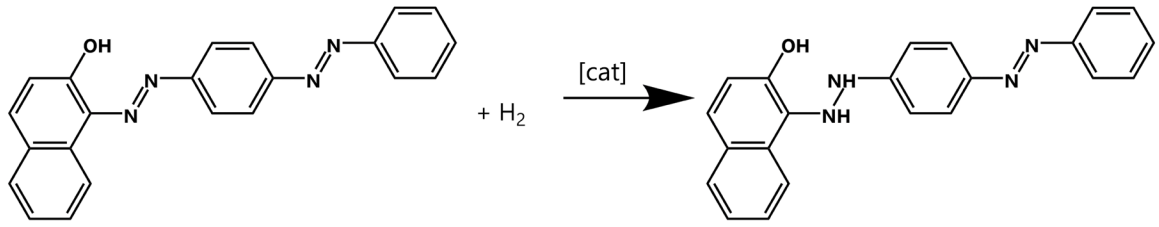

Figure 6.3. The suggested primary reaction of Sudan III with hydrogen to a colorless species. Several other hydrogenation locations are possible. The left azo bond has a high electron density due to mesomeric effects and is preferentially hydrogenated. Hydrogenation of other sites should also lead to a colorless species.

Hexanol and water are chosen as solvents for the dye and the homogeneous catalyst since triphasic systems with these substances, including a gas phase, have already resulted in stable and reproducible slug flows in optically transparent FEP capillaries *(16, 43)*. However, other substance systems are not principally excluded. Therefore, only azo and triphenylmethane dyes are considered, which should be mainly soluble in the organic phase. Due to long carbon chains and aromatic structures, this condition is fulfilled by most of these dyes.

The dye sought should therefore be well soluble in hexanol and practically insoluble in water for easy and accurate conversion monitoring. In addition, a distinct and intense peak must be visible in the UV-Vis spectrum in a wavelength range where is no overlap with other spectra, such as those of the solvents or the catalyst. The wavelength of the maximum absorbance and, thus, of the maximum sensitivity should be within a range that can be easily accessed with electronic components and a few auxiliary devices. The light absorption should show a strong dependence on the concentration to detect even small changes in concentration accurately.

During the hydrogenation, the dye should undergo uniform decolorization so that the concentration of the dye can be inferred from the light absorption. In addition, no hypsochromic or bathochromic shift should occur. This means that even during hydrogenation, the maximum absorbance always appears at the same wavelength, and no

shift in the UV-Vis spectrum occurs. If this were not the case, a sensor that is exclusively sensitive to a small wavelength range could not be calibrated.

Based on literature values for solubilities or 1-octanol-water partition coefficients (K_{OW}), a preselection of dyes was made which have good solubility in organic solvents but poor solubility in water (the K_{OW} coefficient is suitable since the molecular structure of 1-octanol is close to the used solvent 1-hexanol). Therefore, the TPM dyes bromothymol blue (BTB) and crystal violet (CV), as well as the azo dyes Solvent Black 3 (SB3) and Sudan III (SIII), are investigated in the following.

In order to evaluate the dyes in terms of their light absorption and possible mass transfer to the aqueous phase, the dyes dissolved in hexanol were mixed intensively with water in a two-phase system. UV-Vis spectra of both phases were then recorded so that the change in spectra could be observed compared to the pure phases before mixing. If the spectra of the respective phases do not change during the contact time, it can be assumed that no cross-mixing occurs. In parallel, the spectra of the hexanol phase are measured at different dye concentrations to assess whether a subsequent calibration of absorbance to dye concentration is possible. After validation of the dyes concerning mass transfer and calibratability, the remaining dyes are initially hydrogenated in a discontinuous stirred tank reactor to determine whether shifts in the spectra occur due to the reaction.

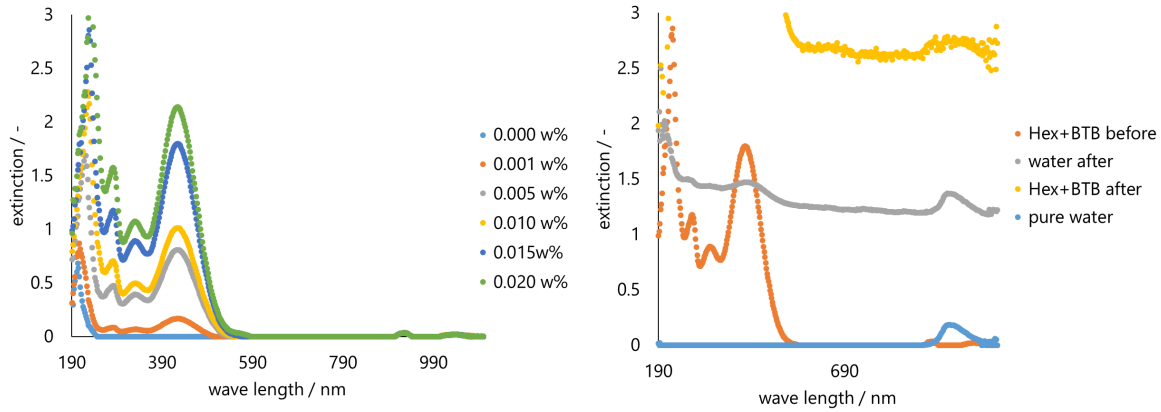

Figure 6.4. Left: UV-Vis spectra of bromothymol blue (BTB) dissolved at different concentrations in hexanol. Right: UV-Vis spectra of bromothymol blue in hexanol and water before and after intensive mixing of both phases.

Bromothymol blue (Figure 6.4 left) shows a good dependence between concentration and absorbance at a wavelength of about 430 nm when dissolved in pure hexanol. In contact with water, the spectra of both phases before and after mixing are strongly shifted and show significant light absorption over the whole UV-Vis range. However, with strong turbidity, a white-yellowish sediment is formed in the organic phase shortly after initial stirring. The turbidity disappears after a few days, but the sediment remains. The aqueous phase is also turbid. Turbidity is represented in the spectrum by a vertical shift of the entire spectrum. The shift is visible in Figure 6.4 (right), which shows the spectra before and after mixing. The substantial shift in the spectrum of the organic phase after mixing is particularly prominent. Here, the main peak of the dye is no longer detectable.

Furthermore, the small peaks in the aqueous phase at the wavelengths of the dye peaks indicate that small amounts of the dye transfer into the aqueous phase. The sediment formation is probably due to bromothymol blue containing nonpolar (isopropyl) and polar (such as -SO_3, -OH) groups. Intense contact between water and hexanol was created by stirring. The dye may act as a surfactant, forming micelles with water in hexanol, which becomes visible as turbidity and sediment. For these reasons, bromothymol blue is unsuitable for microcapillary reactor utilization. These turbidities and sediment formation do not occur with the other three dyes shown in Figure 6.5.

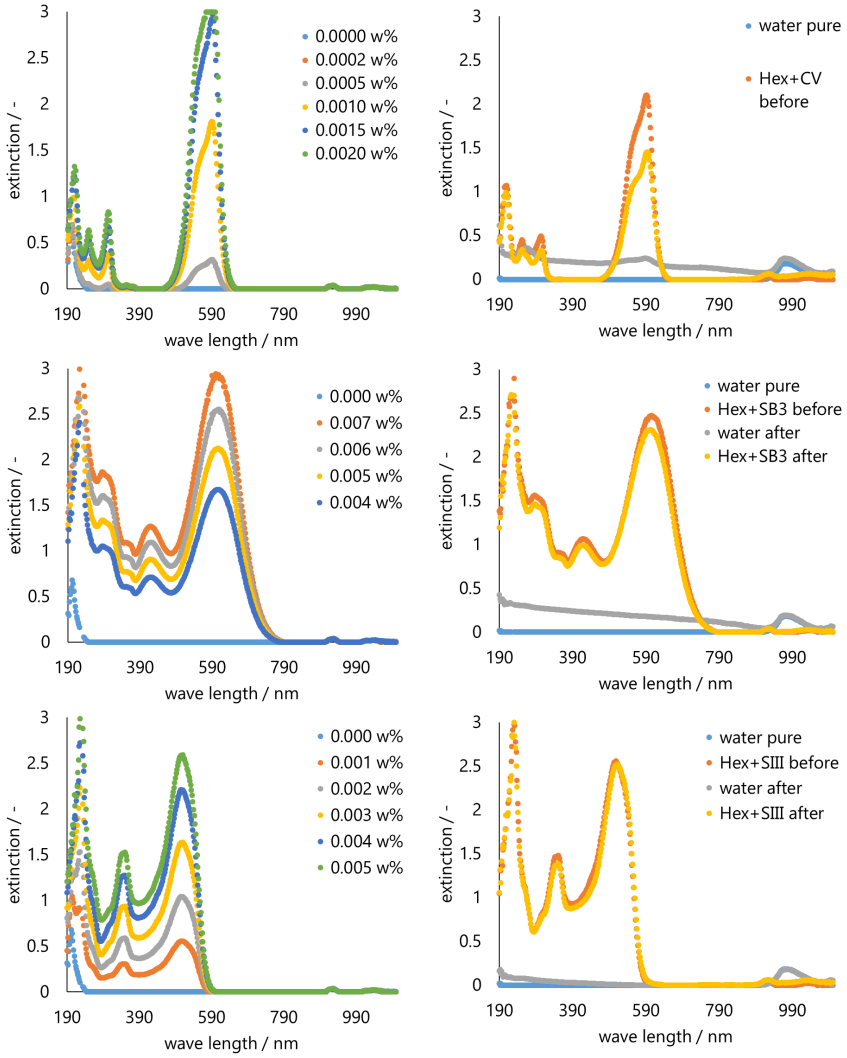

Figure 6.5. Left column: UV-Vis spectra of various dyes dissolved at different concentrations in hexanol. Right column: UV-Vis spectra of various dyes in hexanol and water before and after intensive mixing of both phases. Top: crystal violet. Middle: Solvent black 3. Bottom: Sudan III.

For crystal violet, Solvent black 3, and Sudan III, the dependence between absorbance and concentration of the dye in hexanol is fulfilled (Figure 6.5 left). Crystal violet, in particular, seems suitable for comparison since here, the spectrum's main peak (approx. 590 nm) is clearly separated from the other peaks. However, if the spectra of hexanol and water are considered after mixing, crystal violet is unsuitable due to the concentration of the dye in the hexanol

phase is reduced, and turbidity occurs in the aqueous phase. In the case of Solvent black 3, only slight shifts of both phases can be seen in comparison. Nevertheless, here the extinction decreases from approx. 2.45 to 2.30 during the mass transfer experiment. Comparing this with the samples of Sudan III, only a minor change in the spectra can be observed. Therefore, Sudan III can fulfill the conditions of concentration detectability, solubility, small cross-mixing and is selected as the only dye for further investigation.

For this purpose, the hydrogenation of dissolved Sudan III in hexanol with an aqueous catalyst phase (Rh(TPPTS)) with hydrogen in the gas phase was studied in a discontinuous batch reactor. Figure 6.6 shows the spectra of the hexanol phase after different reaction times. Here, a time depending decrease in absorbance can be observed. The main peak (approx. 510 nm) nearly reaches an absorbance near 0 after two hours, which is advantageous for later calibration and concentration measurements. In addition, it can be seen that there is no horizontal shift of the UV-Vis spectrum due to the reaction. A hypsochromic or bathochromic shift can therefore be excluded.

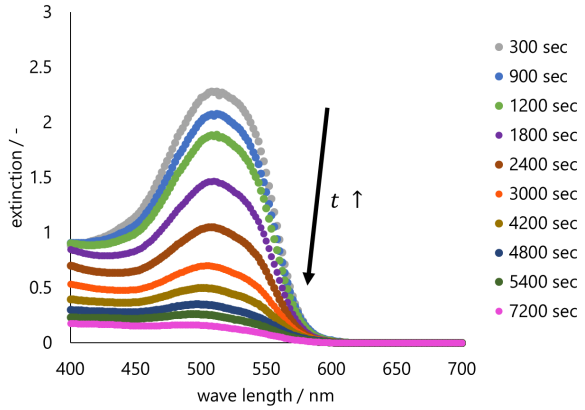

Figure 6.6. UV-Vis spectra of the hexanol/Sudan III-phase after different reaction times in homogeneous hydrogenation in a discontinuous stirred tank reactor. T=55 °C, p_{H2}=3 bara, phase ratio aqueous/organic=1. Hydrogen pressure hold constant during the reaction.

Figure 6.7 shows samples of a comparable reaction after the different reaction times. The reaction sequence from a bright red to an almost colorless and transparent hexanol phase can be observed with a bare eye.

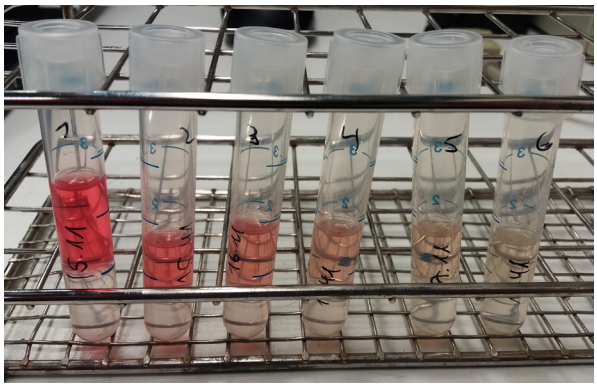

Figure 6.7. Example of hydrogenation samples of Sudan III dissolved in hexanol at different reaction times. 30 min between the samples.

Since Sudan III fulfills all the above conditions, a non-invasive online sensor for transparent capillary reactors based on concentration-dependent light absorption is developed.

6.4 Development of a non-invasive online sensor

An optical flow sensor is designed for non-invasive conversion monitoring of Sudan III hydrogenation in the reactor. A light source with a confined wavelength range emits light through the optically transparent FEP capillary. A light detector detects the remaining light intensity on the other side of the capillary. Depending on the local concentration of the dye, more or less light is absorbed, so the measured light intensity at the photodetector can infer the concentration and, thus, the conversion. Compared to the sensor from Chapter 5, a wide (wider than the capillary diameter) light source and photodetector are used to reduce the light refraction effects.

The main peak of the UV-Vis spectrum for the selected dye Sudan III is around a maximum of 510 nm, which corresponds to turquoise light (Figure 6.8). Unfortunately, only a few light sources specifically include this wavelength range. Therefore, a cold-white light-emitting diode (LED) is used as a light source together with a filter.

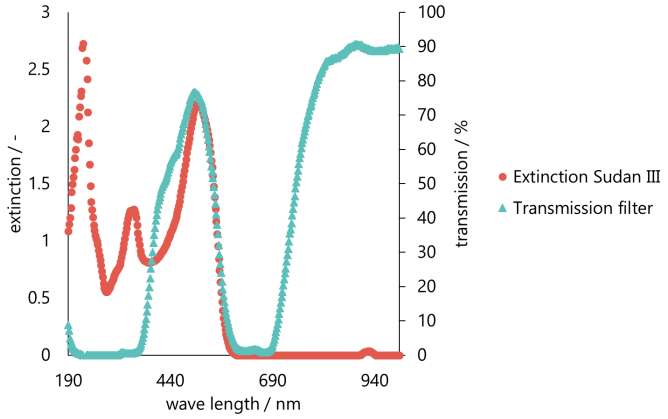

Figure 6.8. Comparison between the extinction of Sudan III (0.004 w%) and the transmission spectrum from the selected filter film (Peacock Blue, Lee Filters, Hampshire, UK).

The filter used is a turquoise foil (Peacock blue, Lee filters, Hampshire, UK) whose light transmission was analyzed with a transmission spectrum. Figure 6.8 shows the light extinction of Sudan III and the light transmission from the filter foil. The transmission gap and the main peak of dye absorption are in the same wavelength range. However, the filter foil has a large transmission greater than 750 nm. However, cold-white light-emitting diodes (LED) generally do not emit light above a wavelength above 690 nm *(136)*. Therefore, an absorption measurement of the dye is possible with a cold-white LED (LED-5 white 18 cd, Thomsen, Greifenstein-Nenderoth, Germany) and the filter foil considered here. A phototransistor (BPY 62, Osram, München, Germany) is chosen as the light detector, which can sensitively detect light in a wavelength range of 400-1100 nm.

These components are firmly soldered on a circuit board and installed in a housing. The capillary is placed through this housing and fixed at the inputs and outputs. This is to prevent the capillary from slipping and, thus, the sensor system from being susceptible to mechanical interference. In addition, the housing shields the capillary and detector from external light. The filter foil is inserted into an inlet between the LED and the 2 mm wide circular aperture. The other required resistors and the power supply are installed on another external circuit board. The voltages recorded by the phototransistor are recorded via a microcontroller (Teensy 4.1, pjrc, Sherwood, OR, USA) and then evaluated on a computer. With this setup, measurement frequencies of up to 25 kHz are possible; the measured signal is between 0 and 1.2 V. The sensor is shown in Figure 6.9.

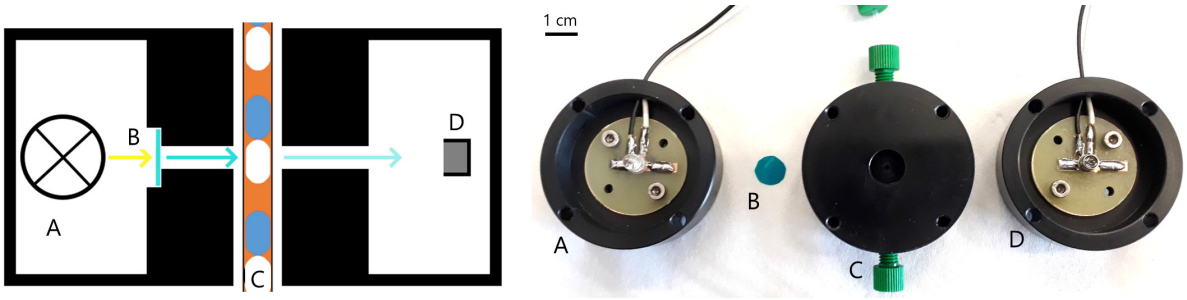

Figure 6.9. Non-invasive sensor for detection of Sudan III concentrations in triphasic slug flow. Left: Schematic setup. Right: Disassembled sensor. A: LED/light source, B: Light filter, C: Capillary holder, D: Phototransistor.

Figure 6.10 shows the raw signal of the sensor from a triphasic flow. Plateaus can be identified in the filtered signal (moving average), which can each be assigned to a phase. The height of the plateau of the Sudan III phase depends on the dye concentration. Since only the dye phase is of interest, the signal plateaus are distinguished from each other with a MatLab script (MatLab 2020a, Mathworks, Natick, MA, USA), and only the dye plateaus are further processed. Especially with small segment lengths and large volume flows, high measurement frequencies are necessary to process these plateaus sufficiently. Therefore, measurement frequencies of 1-10 kHz were used in the experiments presented here.

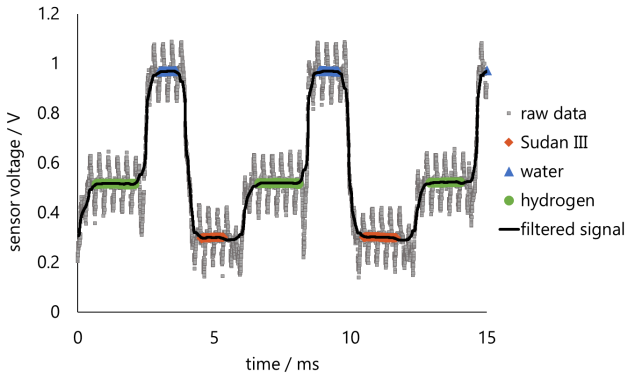

Figure 6.10. Resulting signal of a triphasic slug flow detected by the online sensor. The raw data are filtered with a moving average. The resulting plateaus of the signal can be assigned to the respective phases.

A calibration curve (Figure 6.11) can be used to calculate the concentration of the Sudan III phase at the sensor's location. Analogous to the Lambert-Beer law, the measured voltages can be calibrated with an exponential function of the type b·exp(a), where a and b are constants, respectively. The dashed line represents a fit of all measuring points, whereas the solid line was calculated only with the first and last measuring points. The difference between the two calibration curves is only a few percent. Therefore, it is sufficient to perform a calibration with only two measuring points since this also represents the other measuring points with sufficient accuracy. Thus, the sensor can be calibrated regularly more efficiently with only two measuring points. No difference was found whether the flow during calibration is single-phase or multiphase.

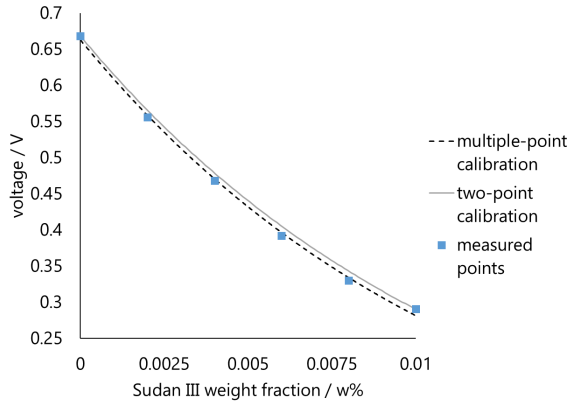

Figure 6.11. Measured voltages for different concentrations of dye phase in the non-invasive online sensor and possible calibration curves obtained with either six or only two measurement points using an exponential approach (b·exp(a)).

Due to the simple and inexpensive setup, several sensors can be installed and evaluated. In this setup, five sensors are used (after 0 m, 5.8 m, 9.5 m, 20.1 m, and 40.8 m) to determine a local concentration profile.

In order to verify the significance of the developed sensors, the hydrogenation is carried out at two different temperatures in the capillary reactor. In the process, the voltage of the sensors is recorded for approximately ten minutes after reaching a steady state. Additionally, samples were taken along the reactor and measured in the UV-Vis spectrometer.

Figure 6.12 shows the local conversion at 40 °C and 55 °C. Conversions were determined by concentration measurement using either optical sensors or a UV-Vis spectrometer. At 55 °C, both measurement methods show similar conversions. However, except for the measuring point after 5.8 m, both conversions differ by a couple of percent. At 40 °C, on the other hand, the conversions measured by the UV-Vis spectrometer always show higher conversions than the optical online sensors. The latter may be because the physically taken sample can still react with the dissolved hydrogen after the sampling and before degassing with helium, allowing more dye to react.

In contrast, the optical sensor avoids this measurement delay. However, slight turbidity of the liquid phases can occur due to, for example, the dissolved hydrogen, which increases the

absorption and can cause the measured concentration to differ upwards. As a result, the conversion for the optical sensor is correspondingly lower.

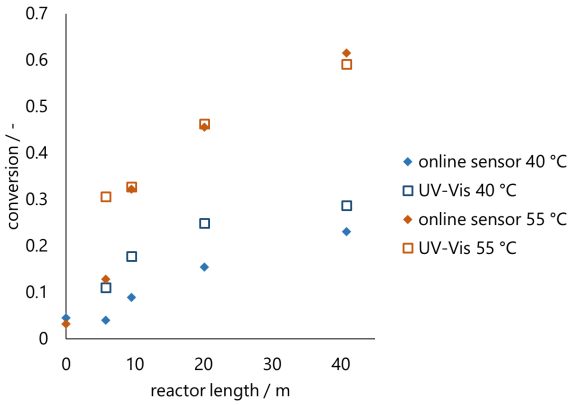

Figure 6.12. Comparison of the measured conversions via UV-Vis spectrometry or online optical sensors at 40 °C and 55 °C in the capillary reactor. $\dot{V}_{tot}$=1.8 mL/min, phase ratio 1:1:1 (org:aq:gas), p_{end}=1 atm, Δp(40 °C)=1.14 bar, Δp(55 °C)=0.98 bar, L_{uc}(40 °C)=15.3 mm, L_{uc}(55 °C)=17.5 mm.

Overall, the sensors show accuracy, which allows tracking the conversion sufficiently. Nevertheless, the conversions are additionally determined at the end of the reactor by UV-Vis in each subsequent experiment.

6.5 Catalyst deposition in the capillary reactor

The Rh(TPPTS) catalyst is sensitive to oxygen, and contact can lead to deactivation and precipitation of small rhodium particles. It has already been demonstrated in Chapter 3 that the permeation of gases through the capillary wall can occur. Hence the hot reaction zone in the setup is oxygen-free. However, the zones at room temperature are not protected against oxygen. The theoretical oxygen permeation at room temperature in FEP capillaries is less than 0.08 mL/h per meter (calculated with the equation in table 3.1 in Chapter 3). Whether oxygen permeation affects the catalyst in the capillary is discussed below.

A distinct catalyst deposit can be identified in the capillary between the two slug generators. After several hours of operation of the capillary reactor, a continuous silver-grey shimmering layer becomes visible on the inner capillary wall (Figure 6.13).

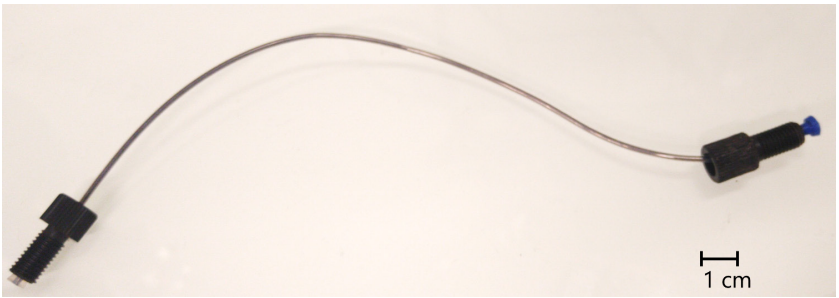

Figure 6.13. Disassembled capillary after an operation with Rh(TPPTS) between the slug generators. A biphasic slug flow containing hydrogen and the aqueous catalyst flowed through the capillary for several hours.

A biphasic slug flow of the aqueous catalyst solution and hydrogen passes through this intermediate section while the aqueous phase is wetting. In the short capillary, atmospheric oxygen permeates through the capillary wall and comes into direct contact with the catalyst on the inner wall. This leads to the precipitation of some rhodium, which is visible via accumulation in the silver-grey shimmering layer. Presumably, an interaction of oxidation of the phosphorus ligand and simultaneous reduction of the rhodium by the hydrogen is causing the deposition.

However, no capillary coating is visible in the remaining capillary. After the second slug generator in the triphasic flow, the aqueous phase is dispersedly surrounded by the hexanol phase. Direct contact with the capillary wall is, therefore, not possible. In addition, the oxygen solubility in hexanol (at room temperature) is about five times higher than in water, which further protects the catalyst phase from oxygen *(137)*.

Since only part of the catalyst is deactivated in this way due to the short distance, a reaction in the main part of the capillary reactor is still possible. The capillary section with the non-transparent layer should be changed occasionally to keep the visibility of the biphasic slug flow.

Nevertheless, small amounts of catalyst could deposit on the capillary wall of the triphasic flow. For this purpose, a long-term recording of the reaction performance, including the start-up and shut-down process, is carried out with the developed concentration sensor. This will help to determine whether such deposits occur and whether these affect the results of the individual experiments.

Figure 6.14 shows the dynamic conversion of Sudan III in the capillary. First, a triphasic slug flow was started up under reaction conditions without a catalyst. At 0 min, the catalyst was then added to the system. Up to about 50 min, the conversion of Sudan III increases until it reaches a plateau. This ramp-in time is mainly due to mixing in the syringe pump, feed lines, and, in particular, the slug generator. Due to the design of the coaxial mixer, there are many dead zones in the surrounding phase, resulting in a wider residence time distribution.

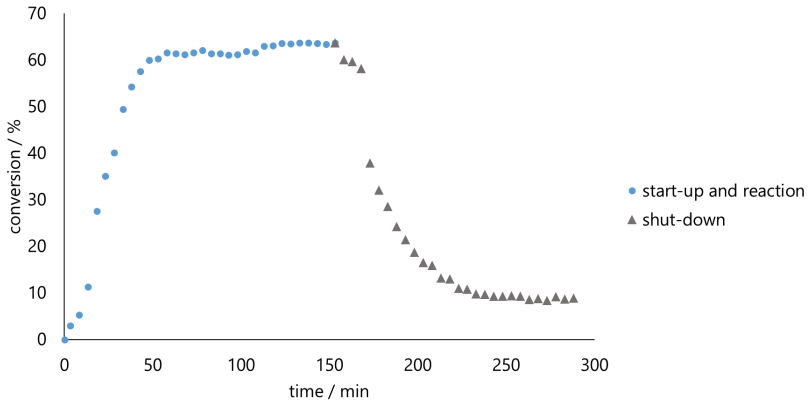

Figure 6.14. Conversion of Sudan III in triphasic slug flow during start-up (blue) and shut-down (grey) at the end of the capillary (40 m). Each point is a mean value of a period of 5 min. At 0 min, the catalyst was added in a stable triphasic flow. At 153 min, the catalyst solution was switched to water. T=55 °C, $\dot{V}_{tot}$=1.8 mL/min, p_{end}=1 atm.

The height of the plateau increases slightly at 110 min, possibly due to catalyst deposition. Therefore, starting at 153 min, the catalyst solution was replaced with water, thereby stopping the reaction. Up to 230 min, the conversion decreases and then remains at about 9% constant until the end of the recording.

The residual conversion indicates that the catalyst remains in the capillary. A comparison of the UV-Vis spectra of the mother solution with a sample in the end plateau region confirms the remaining conversion of about 5% (and thus slightly lower than the sensor measurement).

The capillary (only the triphasic region) was rinsed for about 60 min with a single-phase isopropanol flow (4.8 mL/min) to flush out the catalyst. Subsequently, the triphasic flow was started without a catalyst, and another sample at the capillary outlet was analyzed by UV-Vis spectroscopy. This procedure reduced the conversion to 2%. Deposition of the catalyst on the capillary wall is, therefore, likely.

For a reaction, this initially seems advantageous but makes a direct comparison of different parameters difficult. Therefore, after one day of the experiment, the capillary was rinsed for several hours with isopropanol. However, a basic conversion (without a catalyst) was always retained. In order to nevertheless make qualitative conclusions about the influence of different hydrodynamic operating conditions, the following measures were taken for analysis: First, when calibrating the sensors with a triphasic flow (without catalyst), a sample was taken at the beginning and at the end of the reactor, which was analyzed in UV-Vis.

Furthermore, the experiments of one degree of freedom (e.g., the velocity) are recorded dynamically as "step response". This means that after reaching a steady state, the degree of freedom is changed spontaneously (e.g., the velocity is doubled). In this case, the dynamic behavior of the concentration is observed until a new steady state is reached. In this manner, qualitative conclusions can be obtained regarding the influence of one degree of freedom within a series of experiments, but conclusions outside of a series of experiments are only possible to a limited extent.

6.6 Investigation of hydrodynamic influences in a slug flow

In this chapter, the hydrogenation of the selected dye is applied in the triphasic slug flow capillary reactor and analyzed using the developed sensors. The same chemical conditions (pressure, temperature, catalyst concentration) are invariably applied, and only the hydrodynamic conditions are changed to investigate their specific influence. Temperature and pressure are selected to achieve a conversion of 40-80%. So the influences of the different operating variables can thus be visualized. The reactor is therefore operated at 55 °C and atmospheric pressure at the capillary outlet. Due to different flow conditions (e.g., smaller/larger segments), the pressure drop varies over the entire capillary and is, therefore, additionally indicated for each experiment.

The reactor-specific hydrodynamic parameters investigated in the following are the total volumetric flow rate, the unit cell length (sum of continuous and dispersed phases length), and the phase ratio. All of these parameters can be changed and adjusted independently.

However, the precise adjustment of the segment length is challenging and may vary slightly within a series of experiments.

By changing the velocity in the reactor, a higher mixing and more intense contact of the phases is expected. The higher the velocity, the more intensive the phase-internal mixing and also the mass transfer between the phases. However, the residence time in the reactor also changes with the velocity.

Figure 6.15 on the left shows the conversion curves at 1.8 and 3 mL/min total flow rates at equal phase ratios (1:1:1). In this case, the smaller volume flow has higher conversions at the same reactor lengths than the high volume flow. However, the residence time in the reactor is considerably shorter for the higher flow rate.

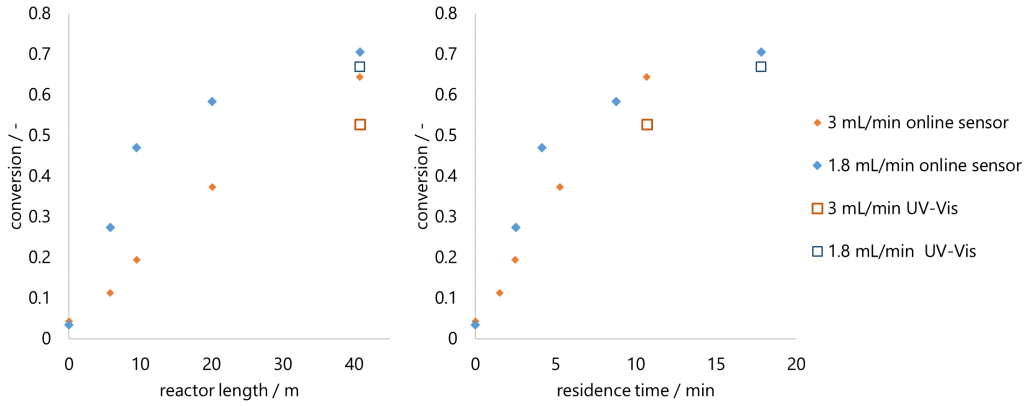

Figure 6.15. Comparison of conversions measured via UV-Vis spectrometry or online optical sensors at $\dot{V}_{tot}$=1.8 mL/min hexanol and $\dot{V}_{tot}$=3 mL/min hexanol in the capillary reactor. T=55 °C, p_{end}=1 atm, phase ratio 1:1:1 (org:aq:gas), Δp(0.6 mL/min)=0.99 bar, Δp(1 mL/min)=1.67 bar, L_{uc}(0.6 mL/min)=17.3 mm, L_{uc}(1 mL/min)=15.8 mm.

If the conversions are plotted versus the residence time in the reactor (Figure 6.15 right), the conversions converge. Thus, approximately the same conversions are achieved for the same residence time. This indicates that higher volume flow rates do not significantly improve mixing and, thus, mass transport and that the reaction is dictated by reaction kinetics. The mass transfer may be already improved by the slug flow sufficiently that further increases in mixing do not lead to any improvement. However, the higher volumetric flow rate also introduces more reactants per time into the reactor.

This means more product can be obtained by increasing the volumetric flow rate and lengthening the capillary, representing a size-up in length. However, with a longer capillary and simultaneous higher volumetric flow, the pressure at the beginning of the capillary is correspondingly higher, which could lead to undesirable side reactions.

The unit cell length was changed to investigate the influence of dye hydrogenation at the same phase ratio and volume flow rate. Two unit cell lengths were examined with 8 mm and 26 mm at the reactor inlet. The resulting conversions are shown in Figure 6.16. The measured conversions of the shorter unit cells are slightly higher than those of the long unit cells. Despite the large change in unit cells, no significant effect on conversion was detected. Similar to the variation of the volume flow, this leads to the conclusion that the existing slug flow per se

leads to an improvement of the mass transfer and that the change of individual parameters (such as the unit cell length) barely causes an additional positive effect within the possible range.

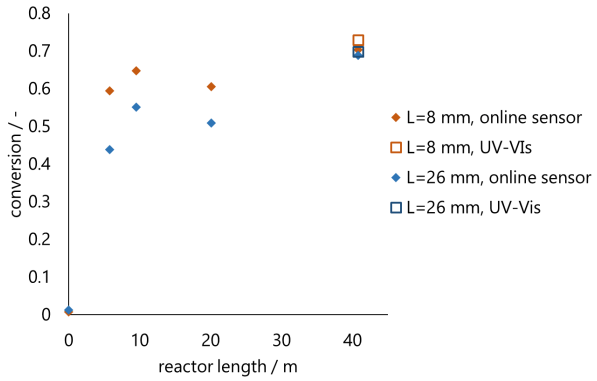

Figure 6.16. Comparison of conversions measured via UV-Vis spectrometry or online optical sensors at different phase lengths: L_{uc}=26 mm and L_{uc}=8 mm in the capillary reactor, respectively. T=55 °C, $\dot{V}_{tot}$=1.8 mL/min, phase ratio 1:1:1 (org:aq:gas), p_{end}=1 atm, Δp(26 mm)=0.83 bar, Δp(8 mm)=1.20 bar.

The third parameter investigated is the phase ratio. Here, one of the three phases was introduced into the capillary at three times the volume flow rate compared to the other phases involved. The lengths of the individual segments were adjusted so that the unit cell length was approximately equal in each experiment. In addition, the total volume flow rate was kept constant. Figure 6.17 shows the local conversions at different phase ratios. Within this series of experiments (one experimental day with dynamic change of parameters), the experiment with a tripled hexanol phase (3:1:1) was performed twice, once at the beginning of the experimental day (a) and at the end (b). So, the impact of catalyst deposition within an experiment without intermediate rinsing could be estimated. Between the first experiment 3:1:1a, and the last experiment 3:1:1b, a slight general increase in conversion was observed, caused by the temporal deposition of the catalyst on the capillary wall (see Chapter 6.5). However, the change in conversion due to this effect is small compared to the measured change in conversion at other phase ratios. Thus, the significant changes in conversion measured are related to the changing conditions in the capillary and not to the time-dependent catalyst deposition. The conversions were also confirmed in replicate experiments with a different sequence of experiments.

The slug flow with a tripled aqueous catalyst phase (1:3:1) shows significantly higher conversions than the other experiments. At 20 m, a conversion of 102% is measured by the online sensor; the deviation from 100% is attributable to the measurement inaccuracy. Compared to the tripled hexanol phase experiment (3:1:1), the conversion at the outlet is about 50% higher. The increase in conversion might be due to the improvement of mass transfer with a more extensive aqueous phase. Since the segment length of the dispersed aqueous phase is increased and thus more mass transport could occur over the larger wall film area (with the hexanol phase). This assumption is supported by theoretical studies, which suggest that the principal part of mass transfer occurs via the wall film *(65)*. However, this is

unlikely since this effect would also occur if all phases were elongated. Much more likely in this case is the change in chemical conditions.

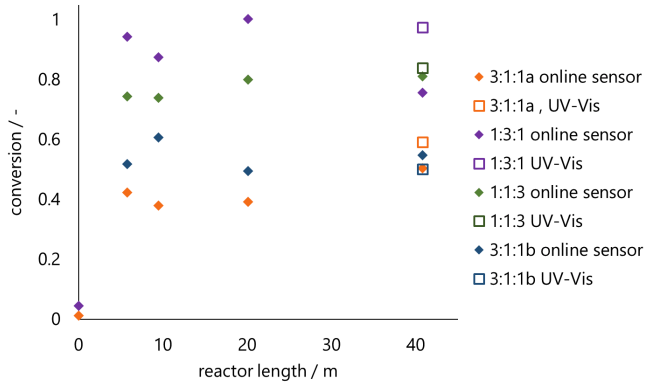

Figure 6.17. Comparison of conversions measured via UV-Vis spectrometry or online optical sensors at different phase ratios. $\dot{V}_{tot}$=1.8 mL/min, T=55 °C, p_{end}=1 atm. 3:1:1a/b: large hexanol phase (Δp(a)=1.26 bar, Δp(b)=1.27 bar, L_{uc}(a)=14.2 mm, L_{uc}(b)=13.1 mm) 1:1:3: large aqueous phase (Δp=0.98 bar, L_{uc}=12 mm) and 1:1:3 large gas phase Δp=0.80 bar, L_{uc}=11.5 mm).

With an enlarged aqueous phase, the total amount of catalyst (at constant concentration) also increases compared to the reactant. With the tripled hexanol phase experiment, there is, in turn, also more reactant per catalyst molecule. These changed chemical conditions appear to have a much more significant impact than the hydrodynamic change. The high catalyst availability in the 1:3:1 experiment increases the conversion enormously (~50%), even at short reactor lengths. With an excess of hydrogen (1:1:3), the conversion is about the same as in the previous experiments with the same phase ratio (1:1:1). Due to the small concentrations of the dye, hydrogen is already in excess even with the same phase ratio, hence further excess of hydrogen does not significantly affect the conversion.

However, these results show that the change in hydrodynamic conditions has nearly no influence on the reaction. Whereas chemical influences (temperature, phase ratios) have a much more significant influence. This indicates no major mass transfer problem in the slug flow for this system. This can be attributed to the fact that the mixing and surfaces between the phases in the capillary reactor are sufficient, so possible mass transport resistances are already minimized. By comparing the capillary reactor with a batch reactor, it can be indicated whether the capillary reactor's flow conditions influence the reaction.

Since the solubility of the dye or catalyst in the respective other liquid phase is very low compared to the solubility of hydrogen in water or hexanol, it is assumed that the reaction occurs mainly at or near the liquid-liquid phase interface.

Mass transfer limitation of the reaction due to the transport of Sudan III to the catalyst is therefore probable. Therefore, as an additional comparison, a similar reaction system in a stirred tank reactor is considered, which has only a liquid phase. Since changing the solvent of the catalyst phase could strongly influence the reaction system, an alternative is a water-soluble dye, which is still comparable to the molecular structure of Sudan III. Therefore, the dye Ponceau BS (also Acid Red 73) was used. It has the same basic molecular structure as

Sudan III, and due to two sulfonate groups, Ponceau BS (PBS) is well-soluble in water (see Figure 6.18 left). If the UV-Vis spectra (Figure 6.18 right) of PBS and Sudan III are considered, both exhibit a comparable characteristic spectrum. This indicates that the added sulfonate groups have little influence on the electron distribution within the molecule (e.g., due to mesomeric or inductive effects). Therefore, it is likely that PBS is hydrogenated similarly to Sudan III, except that in this reaction system, the reactant and catalyst are in the same phase. The sulfonate groups might inhibit only the coordination of PBS to the catalyst more than in Sudan III.

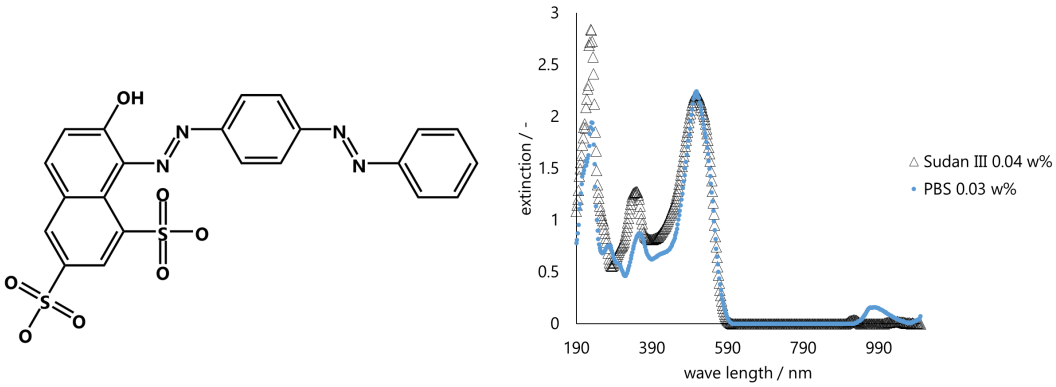

Figure 6.18. Left: Chemical structure of Ponceau BS, Right: Comparison of the UV-Vis spectra of Sudan III and Ponceau BS.

This reaction system with only one liquid phase can be used for comparison to evaluate if the capillary reactor overcomes the presumed liquid-liquid mass transfer limitation. Figure 6.19 shows the conversion versus reaction time of the respective reactors and reaction systems. The measured conversion is plotted versus the time in stirred tank reactor or the residence time in the capillary reactor since both correspond to the reaction time.

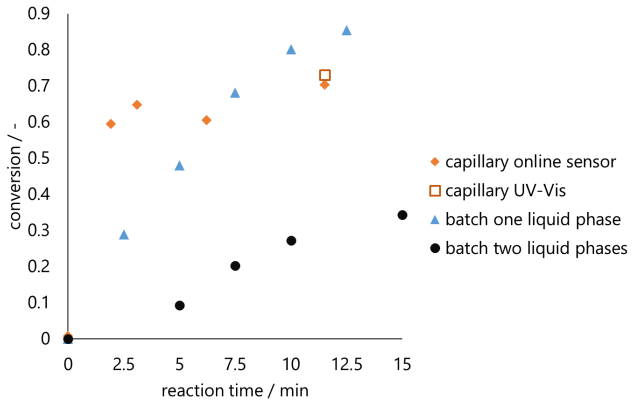

Figure 6.19. Comparison of conversion over time between capillary reactor (two liquid phases) and stirred tank reactor (one and two liquid phases, respectively). T=55°C, p_{H2}(batch)=1 bara, $p_{capillary,end}$=1 atm, $\Delta p_{capillary}$=0.96 bar. Results for capillary taken from variation in segment length (8 mm).

As expected, the batch reaction with only one liquid phase is significantly faster than that with two liquid phases. Therefore, mass transfer between the two liquid phases appears to influence significantly.

The capillary reactor, in turn, already shows a high conversion after a short residence time, which increases only slightly in the further course. Within the first 5 min, the conversion is always higher than in the reaction with only one phase in the batch reactor. The stagnation of the conversion is possibly due to the deactivation of the catalyst in the FEP capillary (see Chapter 6.5). The initial high conversion in the capillary reactor can also be attributed to the pressure gradient in the capillary. While the pressure in the stirred tank reactor remains constant over time (1 bara), the capillary reactor has a higher pressure (1.98 bara) at the beginning of the reactor. This higher pressure accelerates the kinetics of the reaction and, thus, the conversion. This effect can additionally explain the higher conversions of the capillary reactor.

Based on the results, it can be assumed that the capillary reactor can overcome the mass transfer resistances from the considered batch system and is mainly limited by kinetics. Changes in hydrodynamic conditions result in only minor improvements to the system.

6.7 Summary and conclusion

A reaction system was first found to investigate how hydrodynamic operating variables, such as flow velocity or segment lengths, affect a reaction in a triphasic slug flow. Hydrogenation of Sudan III with a homogeneous transition metal catalyst Rh(TPPTS) forms a triphasic reaction system and is also suitable because the reaction barely affects the hydrodynamics of the slug flow (constant density, viscosity, no strong gas consumption).

The red dye loses its color due to the breakage of the conjugated double-bond system. Based on the light absorption, the reaction progress can be determined optically. In addition to the entire UV-Vis spectra, the concentration can also be measured at a specific wavelength. Due to this property, a non-invasive concentration sensor was developed based on the optical sensors from Chapter 5 to track the decolorization of Sudan III. Instead of a small light source, a large LED with a dye-sensitive wavelength was used to measure the light absorption beside the light refraction. These non-invasive online sensors allow tracking of the reaction conversion at several locations in the capillary reactor.

The reaction system was then used to investigate various slug flow-specific operating variables. When the volume flow rate was changed, it was found that the conversions measured were similar for the same residence time. This indicates that a higher volume flow rate and resulting increased mixing do not directly improve the reaction. Also, a variation in the segment lengths did not significantly affect the conversion, indicating that the slug flow reaction is not dominated by mass transfer. However, the slug flow significantly minimizes mass transfer limitation compared to a stirred tank reactor.

Apparently, the mass transfer intensification in the slug flow is probably already sufficient, and changes in the hydrodynamic conditions only slightly improve the reaction. This may be

advantageous for the apparatus used. Instead of using more complex adjustable slug generators, for example, a T-junction and a static coaxial mixer can be used instead.

Significant conversion changes were observed when the phase ratios were changed (up to 50%). However, these significant changes are less due to hydrodynamic changes than chemical changes. With a different phase ratio, the ratio of the reactant's substance to the catalyst changes simultaneously.

Overall, it was shown that in the triphasic reaction system, existing mass transfer limitations are minimized in a slug flow. However, the intensification in this flow regime is already so significant that changing other hydrodynamic variables did not lead to any significant improvement. Chemical changes, in turn, had significantly greater influences on the reaction.

However, deposits and deactivations of the catalyst were detected in the capillary, which a small permeation flux of oxygen might cause. These deposits lead to a basal conversion in the capillary, which can be reduced by intensive rinsing with isopropanol. However, the deactivation of the catalyst is so small that the reactions can still be performed. Therefore, although reactions can be performed in the setup with an oxygen-sensitive system, the catalyst deposition and deactivation make the experiments hardly reproducible and thus unsuitable for comparison.

The measurement principle could also be extended to relevant processes by using, i.e., the near-infrared (NIR) spectrum instead of the UV-Vis spectrum and identifying product-specific wavelengths. For example, for a single-phase capillary flow, Richard et al. tracked a transesterification of triglycerides with ethanol with a NIR spectrometer connected to the transparent capillary with fiberglass *(138, 139)*. For multiphase systems, only the relevant phase needs to be filtered, as shown in the Sudan III hydrogenation. With such a setup, reaction kinetics can be directly determined from axial concentration profiles.

Nevertheless, in Chapter 7, the catalyst system is kept, and sunflower oil is hydrogenated. Then, the influences of solids formation are considered, and the permeation from Chapter 3 is applied for gas feeding to overcome the gas shortage.

7 Homogeneously catalyzed hydrogenation of vegetable oil

EXPERIMENTAL STUDY OF FLOW STABILITY AND SOLID FORMATION IN A TRIPHASIC GAS-LIQUID-LIQUID SLUG FLOW WITH HYDROGENATION OF VEGETABLE OIL

ABSTRACT

The homogeneously catalyzed hydrogenation of vegetable oils is transferred to the triphasic capillary reactor. First, the stability of the flow is investigated, and a periodically oscillating state occurs where the flow comes to a standstill at the capillary outlet and then accelerates rapidly. Furthermore, the deposition of solids in the capillary is considered, and its negative influences are evaluated. Subsequently, fat hydrogenation is studied. A substantial decrease in C18:2 fatty acid is observed in all cases, but isomerization reactions cannot be suppressed. A replication experiment with the same catalyst batch a few days after the first experiment shows a sharp decrease in the conversion and, thus, in the catalyst's activity. Finally, fat hydrogenation with permeation was performed. Compared to a reaction without additional permeation under the same conditions, about 70% more C18:2 is converted in the experiment with permeation.

This chapter is structured as follows:

- Motivation and state of the art
- Materials and methods
- Flow stability and catalyst deposition
- Selective hydrogenation in a triphasic slug flow
- Selective hydrogenation in a triphasic slug flow with permeation
- Summary and conclusion

7.1 Motivation and state of the art

Due to the low concentration of the dye molecule, the dye hydrogenation of Sudan III has almost no influence on the triphasic capillary flow due to, e.g., large gas consumption or change in viscosity. While this is advantageous for a model system to discover better individual influences, relevant applications often involve significant influences on the system.

Reactions involving, for example, a strong gas consumption and a strong increase in viscosity or even solids formation have a dynamic influence on the system's pressure drop and, thus, possibly on the stability of the slug flow. Such a reaction is, for example, the hydrogenation of unsaturated vegetable oils or the equivalent fatty acid methyl esters. According to the reaction equation in Figure 7.1, the double bonds of the fatty acids are saturated with hydrogen, causing them to become more viscous or even form a solid. At room temperature, unreacted vegetable oil is usually liquid, while the fully hydrogenated product (with saturated fatty acids) forms a solid wax *(140)*.

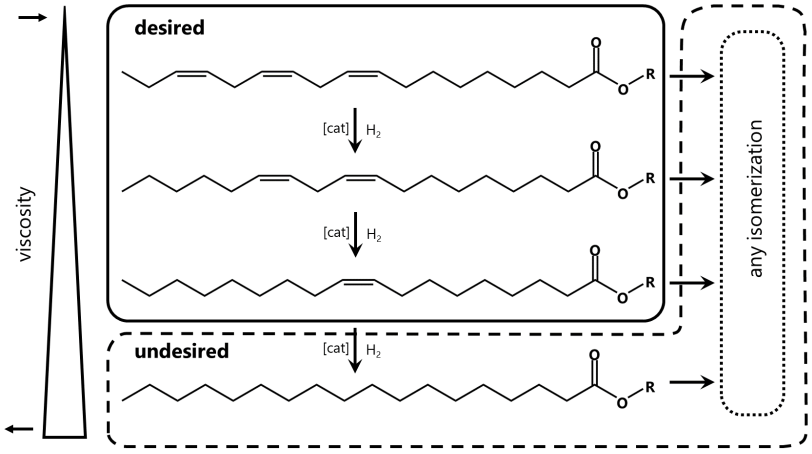

Figure 7.1. Reaction equation of fatty acid esters with 18 carbon atoms. The desired monounsaturated fatty acid is formed by catalytic hydrogenation. In contrast, the consecutive reaction to the saturated fatty acid and isomers is undesired. With R=H: Fatty acid, R=CH_3: Methyl esters, or R=triglyceride: ester with glycerin, simultaneously esterified with two other fatty acids.

In fat hydrogenation, selective hydrogenation towards monounsaturated fatty acids is often desirable. For food applications, properties such as melting point and low sensitivity to oxidation are necessary, e.g., for deep-frying fat. Also, saturated fats are associated with adverse effects on consumer health *(141, 142)*. In chemical utilization, mostly only the methyl esters of the triglycerides are used, which are obtained by transesterification with methanol *(143)*. These methyl esters are mainly used as biodiesel. However, several other chemical utilizations of fats and fatty acids via modifications to a double bond are conceivable, for example, via dimerization, addition, or cleavage, such as oxidative cleavage *(144, 145)*. For these subsequent steps to be as selective as possible, a very high proportion of monounsaturated fatty acids is elementary. Therefore, selective hydrogenation to the monounsaturated fatty acid is crucial for chemical use and is often called a tool for standardizing fatty acid raw materials *(146)*. This also includes the suppression of isomerization to *trans*-unsaturation *(147)*. Furthermore, for the transformation process of the chemical

industry to a larger amount of renewable feedstocks, the selective hydrogenation of fats and their derivatives could become decisive.

The hydrogenation of fats is a well-known process, which in its early days was carried out with heterogeneous catalysts such as nickel. In these processes, the temperature was used to control selectivity *(148)*. Later, palladium catalysts poisoned with lead (Lindlar catalyst) were used to achieve a higher selectivity *(149, 150).* Finally, in the 1970s, homogeneous palladium and chromium complexes were also used for selective hydrogenation *(151, 152)*.

In the current literature, rhodium and ruthenium catalysts are the main catalysts that are soluble in water with water-soluble ligands (like TPPTS) and thus separable from the product after the reaction. Primarily fatty acid methyl esters (FAME) of various oils such as soybean or sunflower are used as substrates since they are more attractive for chemical use and show faster reaction kinetics *(59–62, 153, 154)*.

However, the selectivities of fat hydrogenation may be controlled not only by the selection of the catalyst but additionally by the appropriate choice of reactor type. Especially for continuous operation, reactors with a plug flow behavior are suitable to suppress the undesired consecutive reaction to the saturated fatty acid. Winterbottom and Roukounakis demonstrated this effect by comparing a bubble column and fixed bed reactor for selective hydrogenation of soybean oil with a heterogeneous palladium catalyst. The fixed bed reactor exhibited a more ideal (plug flow) characteristic and achieved slightly higher selectivities to the monounsaturated fatty acid. *(155)*

The use of a slug flow for this reaction appears advantageous due to plug flow reactor-like characteristics and intensification of phase contact *(11)*. Albrand, therefore, used a gas-liquid slug flow in a monolith reactor with palladium immobilized on its wall. Unfortunately, the catalyst turned out to be disadvantageous since it deactivated after a short time *(25)*. The application of a homogeneous aqueous soluble catalyst, as previously described, would result in a triphasic gas-liquid-liquid slug flow, i.e., an organic oil-containing phase, an aqueous catalyst phase, and the hydrogen gas phase.

Therefore, the hydrogenation of sunflower oil with a homogeneous Rh(TPPTS) catalyst is analyzed in this chapter. Since the catalyst was not fully suitable for the capillary reactor (see Chapter 6.5), the focus is on the feasibility of transferring such a reaction into a polymer-based capillary. For example, the solid formation during hydrogenation is provoked to investigate the solids' influence and appearance (e.g., emulsion or at the capillary wall). For this purpose, a triglyceride (sunflower oil) is used instead of FAME due to its higher viscosity and since the hydrogenated forms have a higher melting point than FAMEs. In addition, the stability of the flow with viscous fluids is investigated. Subsequently, the reaction with and without permeation is discussed, and finally, the reaction’s feasibility in a capillary reactor is discussed.

7.2 Materials and Methods

The capillary reactor from Chapter 2 is used in two configurations to make a reaction with and without permeation possible. In addition, two samples can be taken at 20 and 40 m for Chapter 7.4. The substrate is 5w% sunflower oil (food grade, aro, Düsseldorf, Germany) in hexanol. The mixture is homogeneously mixed under constant stirring in storage tank B6. The homogeneous Rh(TPPTS) catalyst is prepared as in Section 6.2 and fed into the capillary under an argon atmosphere. The Rhodium concentration (0.3 mmol/L) and the Rhodium/ligand ratio (1:5) are not optimized and were based on literature *(60)*.

In the sunflower oil used, fatty acids with eighteen carbon atoms are particularly relevant, differing in the number and configuration of double bonds. For simplification, an abbreviated nomenclature of fatty acids is used for the following discussions in the form of CXX:Y. The XX indicates the number of carbon atoms, and the Y indicates the number of double bonds. For example, C18:1 is a fatty acid with 18 carbon atoms and one double bond. The configuration and position of the double bond can also be specified, e.g., C18:1 9-*cis*. In this case, the double bond is at the ninth carbon atom (counted from the carboxylic group/delta nomenclature) in *cis* configuration, i.e., oleic acid. The sum of all possible configurations is meant if no separate specification is given.

The fatty acid profile is determined by gas chromatography to monitor the reaction. Since triglycerides are challenging to analyze, the samples taken are first treated and transformed into their methyl esters.

After the reaction, the biphasic reaction sample is separated with a centrifuge into the fat-rich organic phase and the aqueous catalyst phase. All organic phases analyzed in this contribution contain 5w% sunflower oil in hexanol. For further processing, 200 µL of the fat-rich organic phase is mixed with 800 µL methyl tertiary-butyl ether (MTBE, Carl Roth, Karlsruhe, Germany, >99.5%). After 100 µL of this solution is mixed smoothly with 50 µL trimethyl sulfonium hydroxide (TMSH, tci chemicals, Eschborn, Germany, 0.2 mol/L in methanol) in order to convert the vegetable oil into its fatty acid methyl esters (FAME) via transesterification of triglycerides and methylation of free fatty acids contained in oil at atmospheric conditions for simplified analysis.

The fatty acid profile of the mixture is analyzed in gas chromatography (Agilent 8860, DB-FastFAME 90 m, 0.25 mm, 0.25 µm, Agilent, Santa Clara, CA, USA). Carrier gas: Helium. Detector: FID 260 °C. Injection volume: 0.1 µL. Split ratio: 30:1. Initial temperature: 75 °C. Temperature profile: a) rate: 40 °C/min, hold at 200 °C for 20 min; b) rate: 2 °C/min, hold at 208 °C for 1 min; c) rate: 8 °C/min, hold at 230 °C for 1 min. Total run time: 32.875 min.

Since the amount of palmitic acid (C16:0) does not change during the reaction, it is used as an internal standard.

7.3 Flow stability and solid formation

First, a triphasic flow was observed under reaction conditions but without a catalyst to evaluate the flow stability. For this purpose, a phase ratio of 1:1:1 (org:aq:gas, hexanol+5w% oil:water:hydrogen) was used at the inlet of the capillary.

An unstable flow condition was observed at some operating conditions (temperature, volume flow). For example, at 75 °C and a total flow rate of 1.8 mL/min (triphasic, same phase ratio), the flow stopped entirely at the capillary outlet while the pressure built up at the inlet.

This state was released when the pressure at the beginning of the capillary was sufficiently high that the flow was accelerated again, resulting in a very fast outflow velocity and a pressure decrease in the capillary. The rapid outflow continued until the inlet pressure was so low that the flow came to a standstill again at the outlet. This phenomenon occurred at periodic intervals of about ten minutes. The initial pressure in the capillary reflects the periodic cycle well (Figure 7.2). If a biphasic liquid-liquid flow is used with the same total volume flow, these fluctuations do not develop. However, slight irregularities can be seen in the pressure profile due to an irregular flow pattern at the high total volume flow. The biphasic slug flow is unstable compared to the triphasic flow at these velocities.

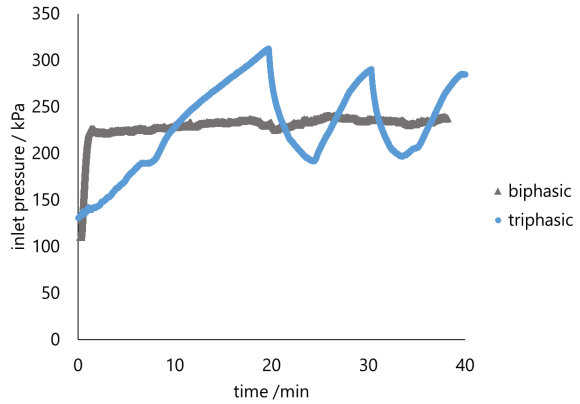

Figure 7.2. Inlet pressure of a start-up process of a biphasic (hexanol with oil, water, filled capillary) and a triphasic (hexanol+oil, water, hydrogen, empty capillary) slug flow into a 40 m capillary, 75 °C, $\dot{V}_{tot}$=1.8 mL/min, p_{end}=1 atm, Phase ratio 1:1 and 1:1:1 at the inlet.

The unit cell model from Chapter 2 could not reproduce this phenomenon that considered slug flow only, with the gas expansion and inertial forces. Since the periodic fluctuations appear only when a gas is used, it is likely that the periphery, such as the gas supply tubes, unstabilizes this system. The free gas volume between the MFC and the phase generator causes inertia in the system.

If the pressure in the capillary drops, the gas expands in the gas supply, so a higher gas volume fraction is released at the inlet of the capillary. This initially leads to an acceleration of the flow and a lower pressure drop since the phase fraction of the liquids (decisive for the pressure drop) in the entire capillary becomes smaller. However, once the gas in the supply tube is relaxed, the volume fraction of the gas at the capillary inlet decreases again. As a result, the flow slows down, and the pressure drop increases again. The free volume of the gas supply

must then pressurize again until the desired volume flow of the gas is released at the phase generator. Large free volumes in the gas supply lines, in particular, intensify this effect. Hence these supply lines were kept as short as possible in the setup (Chapter 2.4), and only tubes with 1 mm ID were used.

Nevertheless, some states exist in which the observed instabilities occur. However, increasing the incoming flow rate should reduce gas compression and expansion inertia. Therefore, the same system was studied with a higher total flow rate (2.4 and 3 mL/min), and the inlet pressures were recorded (Figure 7.3). In this case, the pressure initially overshoots when starting up in the empty capillary, which is consistent with the results of the unit cell model (Chapter 2.2), and then forms a constant pressure.

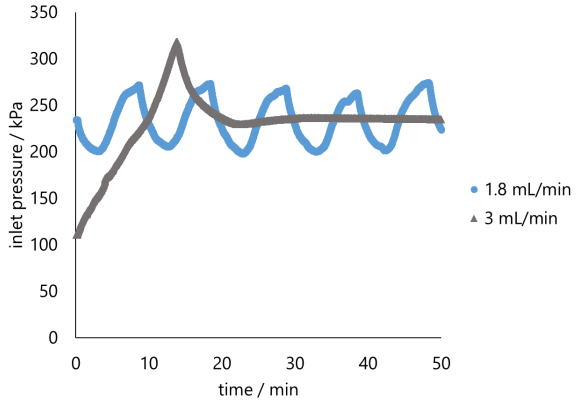

Figure 7.3. Inlet pressure of a triphasic (hexanol with oil, water, hydrogen) slug flow for a total volume flow rate of 1.8 mL/min (already started-up) and 3 mL/min (start-up in an empty capillary) in a 40 m capillary, 75 °C, p_{end}=1 atm, phase ratio 1:1:1 at the inlet.

The oscillations at 1.8 mL/min were independent of the previous state in the capillary. When the flow rate was reduced from a steady state at 3 mL/min to 1.8 mL/min, the identical periodic state as in Figure 7.2 was observed. Thus, a higher volume flow has a stabilizing effect on the triphasic slug flow.

The observed phenomenon was not detected at the same flow rate and capillary length at 55 °C for an almost identical system (organic phase: hexanol and dye, Chapter 6) or for lower total volume flow rates (1-1.2 mL/min). This indicates the formation of an oscillating system depending on the incoming volume flow and the total pressure drop (i.e., mainly the capillary length and the viscosity). If the viscosity is drastically reduced by a different solvent (e.g., MTBE instead of hexanol), this phenomenon is also not observed under otherwise identical conditions.

The operation conditions (temperature, volume flow, solvent) were always selected for all experiments in the following subchapters to reach a steady state.

Solid formation

The stable operating conditions previously determined can now be used for a reaction. For this purpose, the reaction conditions (T=75 °C, p_{end}=1 atm, $\dot{V}_{tot}$=3 mL/min, phase ratio 1:1:1) are selected so that a high conversion and a high content of saturated fats are produced. The complete hydrogenated fat is solid at room temperature and only partially soluble in hexanol. Thus, solid formation is provoked within the capillary.

The start-up of the flow is initially the same as shown in Figure 7.3 for 3 mL/min and reaches the same pressure level. After switching to the catalyst solution, the inlet pressure remains constant for the first few minutes (Figure 7.4). Over time, high-pressure peaks are developed, which spontaneously drop again. At the same time, solid formation is observed on the capillary wall at the exits of the heated reactor zone. The solid is barely visible as it forms a continuous slightly turbid film on the inside of the capillary. This indicates that the fats are hydrogenated in the hot zone but are still soluble in the heated hexanol. The solid deposits on the cold capillary wall as soon as the flow reaches a cold region. The fat film thus becomes thicker so that the pressure at the capillary inlet increases continuously. The fat clogs the capillary, so the pressure increases until the fat detaches and is carried with the flow.

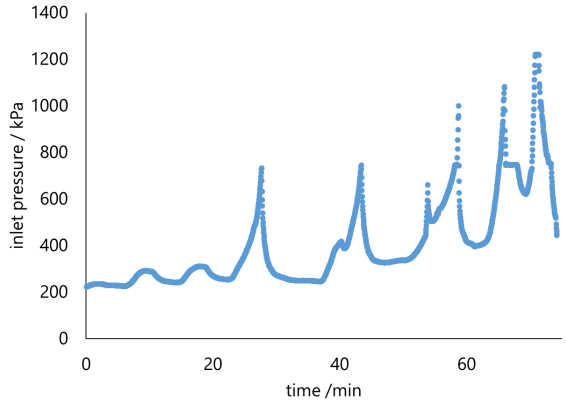

Figure 7.4. Inlet pressure of a triphasic (hexanol with 5 w% oil, water with Rh(TPPTS)), hydrogen) slug flow for a total volume flow rate of 3 mL/min (after start-up and switch to catalyst solution) in a 40 m capillary with solid formation, 75 °C, p_{end}=1 atm, phase ratio 1:1:1 at the inlet, $c_{Rh,aq}$=0.3 mmol/L, Rh:TPPTS=1:5.

The solids do not form an emulsion or suspension in the liquid phase and drastically affect the flow and stability due to the deposit formation. In addition, the high pressures, up to 12 bar in this case, could damage low-pressure components or equipment. The solid formation is, therefore, not recommended and should be avoided. However, solid formation is less relevant if the solid does not form agglomerates, like nanoparticle production.

An ether or ester can be used in fat hydrogenation, which dissolves fats well. For additional stability improvement, the low-viscosity methyl tertiary-butyl ether (MTBE) can be used, which is used in Chapters 7.4 and 7.5. With MTBE, no solids are formed at any time, and a stable triphasic slug flow is formed. MTBE is helpful since it is required as a solvent in the analysis and thus does not have to be added additionally.

7.4 Selective hydrogenation in a triphasic slug flow

Since the catalytic system is difficult to reproduce due to its sensitivity to oxygen and the uncertainty at which location the catalyst is present in which amount, a detailed comparative study of homogeneously catalyzed triphasic fat hydrogenation is not fruitful.

However, some results on fat hydrogenation are shown here, which support the results from Chapter 6. First, fat hydrogenation is compared at different residence times and volume flows, and the stability of the catalyst is tested after a few days stored under an argon atmosphere. Furthermore, in Chapter 7.5, fat hydrogenation with and without permeation is studied.

Figure 7.5 shows the molar composition of the fatty acids after the reaction. Here, equal volume flows represent one experiment each, showing samples at 20 and 40 m of the capillary. Thus, the sample at 20 m is about half the residence time than the sample at 40 m. During hydrogenation, the fraction of double unsaturated fatty acids decreases from about 60% down to 12% (1.5 mL/min, 40 m), and monounsaturated fatty acids and saturated fatty acids increase in accordance with the residence time. A high amount of isomerized products is also formed. Thus, the catalyst does not suppress the side reactions, but with a fraction of C18:1 fatty acids (sum of all configurations) of almost 60% compared to about 28% of the unreacted oil, a selectivity to monounsaturated fatty acids can still be observed.

The two experiments with the same mean residence time (~10.5 min: 1.5 mL/min at 20 m and 3 mL/min at 40 m) show an almost identical fatty acid profile. Thus, increasing the flow rate and lengthening the capillary at identical residence times barely affect this reaction system. This indicates that a scale-up in length is feasible in principle for this system.

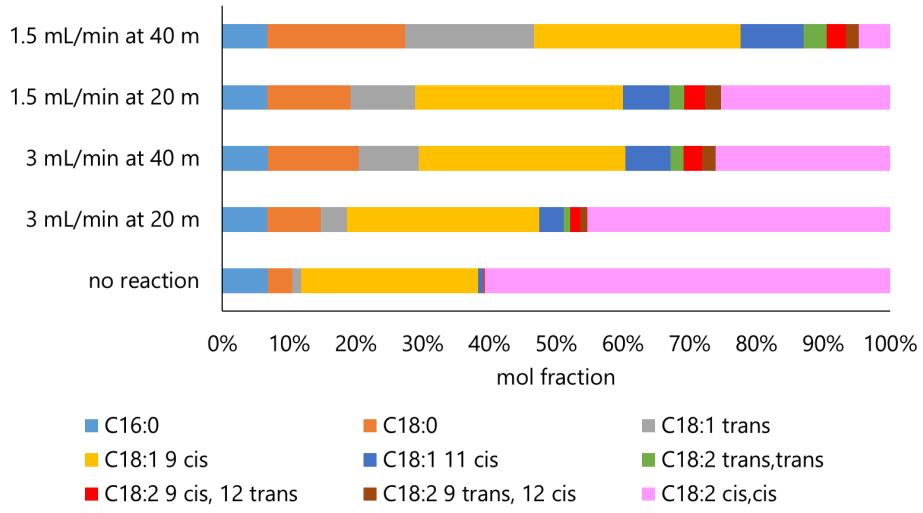

Figure 7.5. Fatty acid composition of sunflower oil in MTBE after hydrogenation in a capillary reactor at varying total volume flow rates and sample locations (20 or 40 m). T=100 °C, p_{end}=5.5 bara, phase ratio 1:1:1, $c_{Rh,aq}$=0.3 mmol/L, Rh:TPPTS=1:5.

The results shown in Figure 7.5 were all produced on one day with the same batch of catalyst. Since the catalyst was kept under an internal argon atmosphere in a pressurized environment, the following experiments verify if it retains its activity after storage, contrary to the

experimental procedure described in Chapter 6 (catalyst is prepared daily). For this purpose, the tests from Figure 7.5 were reproduced under identical conditions, using the same catalyst batch after it had been stored for four days.

The results of this reproduction are shown in Figure 7.6. Similar experiments show up to 20% lower conversion of the C18:2 *cis,cis* fatty acid compared to new catalyst. This indicates that the catalyst has lost its active species during storage. Remarkable is the different composition of the experiments at the same residence time (1.5 mL/min at 20 m and 3 mL/min at 40 m). The lower flow rate shows slightly higher conversions than the higher flow rate and a slightly higher fraction of *trans* fatty acids. Because of the smaller amount of active catalyst complex, more reactions could occur with a catalyst species deposited on the capillary wall. At a lower volumetric flow rate, these "wall species" can be better reached. This could also lead to slightly higher trans fractions, as this species could have a different selectivity.

In summary, storage of the homogeneous catalyst is undesirable and associated with a loss of activity.

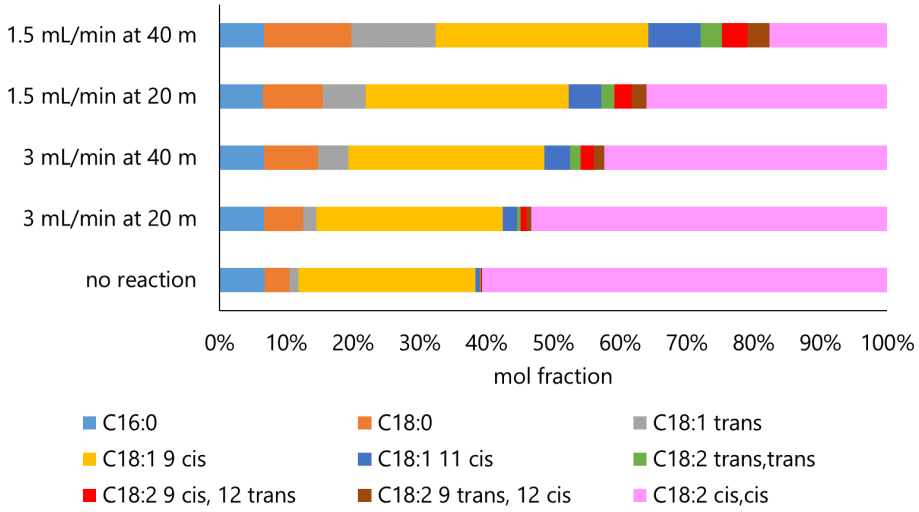

Figure 7.6. Fatty acid composition of sunflower oil in MTBE after hydrogenation in a capillary reactor at varying total volume flow rates and sample locations (20 or 40 m). T=100 °C, p_{end}=5.5 bara, phase ratio 1:1:1, $c_{Rh,aq}$=0.3 mmol/L, Rh:TPPTS=1:5. Catalyst was stored for four days under an argon atmosphere.

7.5 Selective hydrogenation with permeation

To demonstrate that gas permeation can effectively increase the conversion of gas-liquid reactions, a gas-consuming reaction with a limiting amount of gas was examined with and without permeation under otherwise identical conditions.

In this process, insufficient hydrogen was introduced at the beginning of the capillary in a gas-liquid-liquid slug flow (p_{end}=1 atm, phase ratio 3:3:1 org:aq:gas). Due to the initial hydrogen feed deficit, the conversion is theoretically limited to only 45% of the C18:2 fatty acids in the case without permeation. The permeation flow of hydrogen was regulated so that at least a full conversion was theoretically reachable. However, in the flow without permeation (capillary

surrounded by pressurized oil bath), a conversion of 24% of the C18:2 fatty acids was observed, while under the same conditions, including hydrogen permeation (Δp=3 bar), a conversion of 92% was obtained. The high fraction of C18:0 is remarkably indicating substantial reaction progress.

Due to permeation through the capillary wall, the hydrogen is already dissolved and does not have to overcome the gas-liquid phase interface. It has already been demonstrated that tube-in-tube reactors with Teflon AF2400 improve gas-liquid reactions with permeation often more intensively *(56, 90, 91)*. This significant increase in conversion shows that using gas permeation as an active method for supplying gas in FEP capillaries is a favorable operation mode.

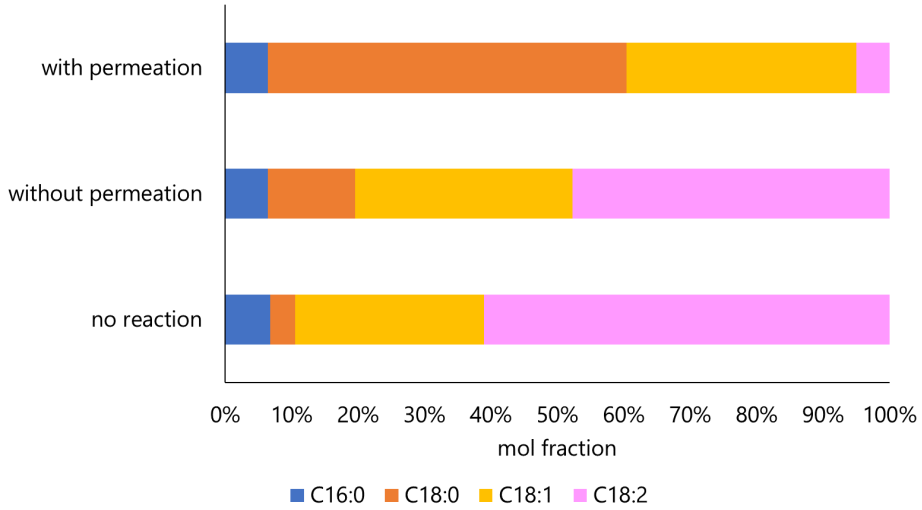

Figure 7.7. Fatty acid composition of sunflower oil after hydrogenation in a capillary reactor either with or without hydrogen permeation. Samples were taken at 40 m. p_{end}=1 atm, phase ratio 3:3:1 (org:aq:gas), $\dot{V}_{tot}$=1.4 mL/min, $c_{Rh,aq}$=0.3 mmol/L, Rh:TPPTS=1:5.

7.6 Summary and conclusion

The homogeneously catalyzed hydrogenation of vegetable oils was transferred to the triphasic capillary reactor. First, the stability of the flow was investigated, and a periodically oscillating state was observed where the flow came to a standstill at the capillary outlet and then accelerated rapidly. However, higher input volume flows, or lower viscosity could overcome this unstable condition.

In addition, the reaction provoked solid formation and observed whether it influenced the flow. Indeed, a layer of solids quickly formed on the capillary wall in colder areas. This deposit first led to complete clogging, causing a sharp increase in pressure until the clog was removed and a new deposit formed. Accordingly, the formation of solids led to strong instabilities, which could only be counteracted with a more suitable solvent.

Subsequently, fat hydrogenation under stable flow conditions was investigated. Two flow rates (1.5 mL/min and 3 mL/min) were investigated. A strong decrease in C18:2 fatty acid was observed in all cases, but isomerization reactions could not be suppressed. The comparison

of the samples of 1.5 mL/min at 20 m and 3 mL/min at 40 m, i.e., about the same residence time, is remarkable. The fatty acid profiles are almost in accordance, so a size-up in length without chemical sacrifice is also possible with this reaction. However, no additional improvement was observed from more intense mixing at high velocities, indicating that the reaction system is mainly limited by kinetics, as in the hydrogenation of Sudan III (Chapter 6). A replication experiment with the same catalyst batch (stored and an argon atmosphere) a few days after the first experiment showed a sharp decrease in the conversion and, thus, in the catalyst's activity.

Finally, fat hydrogenation with permeation was performed according to Chapter 3. A hydrogen deficit was induced, and whether the permeation was adequate to increase the conversion was investigated. Compared to a reaction without additional permeation under otherwise the same conditions, about 70% more C18:2 was converted in the experiment with permeation, and the high fraction of C18:0 also indicates substantial reaction progress. Therefore, permeation can also be effectively applied to FEP capillaries for gas feeding.

As discussed in Chapter 6.5, using the oxygen-sensitive Rh(TPPTS) catalyst in polymer-based capillaries is ineffective. A small permeation flow of oxygen deactivates the catalyst, leading to rhodium deposits on the capillary wall. Therefore, a detailed investigation and comparison with other concepts or catalyst systems are not helpful. However, the reaction can be carried out under oxygen exclusion in a setup with metal capillaries. Theoretically, significantly higher pressures and temperatures are also feasible, which could additionally accelerate the reaction. In single-phase reactions, such harsh conditions are already applied in metal capillaries *(99, 156)*. An alternative could also be using other catalysts that are not sensitive to oxygen.

8 Summary and outlook

This work investigated the challenges of gas-consuming reactions in triphasic slug flows, and solutions were developed. In addition, a prospective scale-up in terms of size-up in length has been considered.

First, the start-up process of a triphasic plug flow was investigated on a theoretical basis to consider the influence of gas expansion in long capillaries. A start-up in an empty capillary was advantageous compared to filled capillaries since lower pressure peaks occur, and the system is, therefore, more stable. The smaller the capillary diameter, the higher the pressures, so an inner diameter of 1 mm was selected for the experimental setup. Thus, the pressures were manageable even for long capillaries, and the advantageous slug flow could be preserved.

A setup similar to tube-in-tube reactors was used for feeding reaction gas, which feeds gas into the capillary by permeation. In this case, a FEP capillary was used instead of a highly permeable membrane material. The gas fluxes depend on the temperature and the pressure gradients but reach sufficient volume flows with long capillaries. Due to permeation, tiny gas bubbles are formed in a liquid-liquid slug flow over long distances, disintegrating the slug flow. If, on the other hand, a triphasic slug flow is present in the capillary, the existing gas bubbles are uniformly filled.

Since permeation depends on the reaction conditions (e.g., temperature and residence time), a single gas bubble injection was developed as an alternative. In this process, a slug flow is observed, and gas bubbles are injected into the continuous phase using electrolytic cells and solenoid valves. This method is very effective and flexible but costly compared to permeation.

In addition to gas feeding, there is a need for effective detection of local flow conditions and concentrations, especially in a scale-up of slug flows in numbering or size-up. Therefore, optical non-invasive sensors have been developed to detect triphasic slug flows robustly. For velocities and segment lengths, sensors with small dimensions were designed to take advantage of light refraction. For concentration measurements, larger sensors were used, which can track the change in concentration of a substrate by light absorption. These concentration sensors were used to study the hydrogenation of the dye Sudan III to a colorless species. Only hydrodynamic parameters of the slug flow were changed (volume flow, segment length), and their influence was investigated. The changes had only a minor influence on the reaction. However, a comparison with a batch reactor showed a significant increase in conversion. Therefore, the advantageous flow conditions of the slug flow probably minimize mass transport limitations that a change in the hydrodynamic parameter has only a minor influence.

Finally, the homogeneously catalyzed hydrogenation of sunflower oil was investigated to study the influences of solid formation. In this case, fat is deposited on the capillary wall until it is clogged, resulting in instabilities. A more suitable solvent, however, was able to prevent solids formation. Based on this reaction, permeation was also used to feed gas, resulting in a dramatic increase in conversion. Nevertheless, homogeneous catalysis with oxidation-

sensitive substances was evaluated as unsuitable for polymer capillaries since deactivation and deposition of the catalyst cannot be prevented, resulting in undefined states in the reactor.

Alternatively, these catalyst systems could be transferred to steel capillaries. However, this would lead to additional technical challenges. For example, detection could no longer be performed optically and must be carried out via contactless conductivity sensors *(108)*. For gas injection, either sections of polymer capillaries could be used for permeation, or single gas bubble injection could be implemented. However, steel capillaries also have advantages; for example, they can be operated at significantly higher temperatures and pressures *(99, 156)*. Steel capillaries are already established for single-phase systems, but multiphase operation and gas feeding with the corresponding sensors have not yet been demonstrated.

Polymer capillaries, however, remain attractive for many applications. For example, catalytic reactors with noble metal nanoparticles are of interest since they are stable to oxidation and can be treated like a homogeneous liquid *(35, 36, 96)*. Moreover, as long as they can be preserved in one liquid phase, they could be recycled by phase separation.

The triphasic slug flow is suitable for a size-up in length because it remains stable at high volume flow rates compared to a biphasic flow. However, the upper limits are unknown so far. Pulsation-free pumps that reach higher volume flow rates and high-speed cameras could be used for this purpose. Presumably, the wall film increases until a condition similar to an annular flow with an internal biphasic slug flow results. The thicker wall film probably negatively affects the residence time distribution and mixing intensity. Besides the size-up in length, triphasic slug flows can also be transferred to a numbering-up. If the approach of Arsenjuk et al. is adopted, in which the pressure loss of the inflowing liquid phases is adjusted by feedback control, the remaining gas phase could be added to the system by single gas bubble injection.

Adding and removing process gases by permeation open up many possibilities of combinations of multiple reaction steps within a single capillary. For example, in the case of fats, the first step could be selective hydrogenation, followed by removing excess gas and adding oxygen or ozone for oxidative cleavage in the second step *(144)*. In this case, the catalyst needs to be exchanged, or catalysts that are active for both reactions are needed. Another relevant process is the anthraquinone process, in which hydrogen peroxide is produced by the local or temporal separation of hydrogen and oxygen to avoid explosive mixtures *(157, 158)*.

In addition to reactions, other unit operations such as extractions, absorptions, or crystallizations can also be performed in capillaries *(14, 159–161)*. By combining these technologies, whole processes could be investigated and optimized on a laboratory scale. However, successfully linking unit operations often requires adding and removing individual phases. For the gas phase, some methods have been presented in this work. For the liquid phases, continuous phase separators are needed. Therefore, phase separators capable of separating a triphasic flow under atmospheric conditions have also been developed in this work (see Appendix G). In the literature, some phase separation concepts can already separate two liquid phases from each other *(162–167)*. Such networks would be valuable for process development because they are rapid and modular and thus can provide reliable experimental data.

9 References

1. Monnerjahn, M.; Otte, C.; Voell, B. "Wir stehen vor einem enormen Wandel": Die deutsche Chemiebranche steht im internationalen Wettbewerb gut da. Welche Märkte gewinnen an Bedeutung? Mit welchen Herausforderungen sieht sich die Branche konfrontiert? *Germany Trade&Invest* **2022** (accessed 2022-12-20).
2. IPCC, 2. Climate Change 2022: Impacts, Adaptation, and Vulnerability.: Contribution of Working Group II to the Sixth Assessment Report of the Intergovernmental Panel on Climate Change **2022**, 6. DOI: 10.1017/9781009325844.
3. Budde, F.; Ezekoye, O.; Hundertmark, T.; Klei, A.; Redenius, J. The state of the chemical industry—it is getting more complex: Three trends may change the future of the chemical industry. *McKinsey Insights* **2020** (accessed 2022-12-20).
4. American Chemistry Council. Mid-Year Outlook: A Good Year for US Chemistry Despite Risks to Growth Learn more at: https://www.americanchemistry.com/chemistry-in-america/news-trends/press-release/2022/mid-year-outlook-a-good-year-for-us-chemistry-despite-risks-to-growth. *American Chemistry Council Industry Statistics* **2022** (accessed 2022-12-20).
5. Cheng, H. N. Key Trends to Impact the Chemical Enterprise in the Near Future. *American Chemical Society Industry Matters* **2022** (accessed 2022-12-20).
6. Yue, J. Green process intensification using microreactor technology for the synthesis of biobased chemicals and fuels. *Chem Eng Process* **2022**, 109002. DOI: 10.1016/j.cep.2022.109002.
7. Gomollón-Bel, F. Ten Chemical Innovations That Will Change Our World: IUPAC identifies emerging technologies in Chemistry with potential to make our planet more sustainable. *Chemistry International* **2019**, *41* (2), 12–17. DOI: 10.1515/ci-2019-0203.
8. Hessel, V.; Angeli, P.; Gavriilidis, A.; Löwe, H. Gas−Liquid and Gas−Liquid−Solid Microstructured Reactors: Contacting Principles and Applications. *Ind. Eng. Chem. Res.* **2005**, *44* (25), 9750–9769. DOI: 10.1021/ie0503139.
9. Burns, J. R.; Ramshaw, C. The intensification of rapid reactions in multiphase systems using slug flow in capillaries. *Lab on a chip* **2001**, *1* (1), 10–15. DOI: 10.1039/b102818a.
10. Dummann, G.; Quittmann, U.; Gröschel, L.; Agar, D. W.; Wörz, O.; Morgenschweis, K. The capillary-microreactor: a new reactor concept for the intensification of heat and mass transfer in liquid–liquid reactions. *Catalysis Today* **2003**, *79-80*, 433–439. DOI: 10.1016/S0920-5861(03)00056-7.
11. Trachsel, F.; Günther, A.; Khan, S.; Jensen, K. F. Measurement of residence time distribution in microfluidic systems. *Chem. Eng. Sci.* **2005**, *60* (21), 5729–5737. DOI: 10.1016/j.ces.2005.04.039.
12. Li, D. Encyclopedia of microfluidics and nanofluidics **2008**. DOI: 10.1007/978-0-387-48998-8.

13. Sobieszuk, P.; Aubin, J.; Pohorecki, R. Hydrodynamics and Mass Transfer in Gas-Liquid Flows in Microreactors. *Chem. Eng. Technol.* **2012**, *35* (8), 1346–1358. DOI: 10.1002/ceat.201100643.
14. Schwarz, C. A.; Mendelawi, M.; Agar, D. W. Kreuz‐Gegenstrom‐Verschaltung zum Numbering‐up der Pfropfenströmung zu Extraktionszwecken. *Chem Ing Tech* **2022**, *94* (4), 594–598. DOI: 10.1002/cite.202100060.
15. Kashid, M. N.; Gerlach, I.; Goetz, S.; Franzke, J.; Acker, J. F.; Platte, F.; Agar, D. W.; Turek, S. Internal Circulation within the Liquid Slugs of a Liquid−Liquid Slug-Flow Capillary Microreactor. *Ind. Eng. Chem. Res.* **2005**, *44* (14), 5003–5010. DOI: 10.1021/ie0490536.
16. Hellmann, D.; Agar, D. W. Modeling of Slug Velocity and Pressure Drop in Gas‐Liquid‐Liquid Slug Flow. *Chem. Eng. Technol.* **2019**, *42* (10), 2138 – 2145. DOI: 10.1002/ceat.201900087.
17. Ibrahim, M. Y. S.; Abolhasani, M. Recyclable cooperative catalyst for accelerated hydroaminomethylation of hindered amines in a continuous segmented flow reactor. *Nat Commun* **2022**, *13* (1). DOI: 10.1038/s41467-022-30175-0.
18. Liu, P.; Ge, H.; Lu, Y.; Wang, Y.; Le Du; Zhu, J. Continuous synthesis of 2-tert-butyl phenol oxidation in gas-liquid segmented flow and its kinetic investigation. *Chem Eng Sci* **2022**, *248*, 117166. DOI: 10.1016/j.ces.2021.117166.
19. Peng, Z.; Wang, G.; Moghtaderi, B.; Doroodchi, E. A review of microreactors based on slurry Taylor (segmented) flow. *Chem Eng Sci* **2022**, *247*, 117040. DOI: 10.1016/j.ces.2021.117040.
20. Besagni, G.; Inzoli, F. Prediction of Bubble Size Distributions in Large-Scale Bubble Columns Using a Population Balance Model. *Computation* **2019**, *7* (1), 17. DOI: 10.3390/computation7010017.
21. Liu, X.; Ünal, B.; Jensen, K. F. Heterogeneous catalysis with continuous flow microreactors. *Catal. Sci. Technol.* **2012**, *2* (10), 2134. DOI: 10.1039/c2cy20260c.
22. Kiwi-Minsker, L.; Renken, A. Microstructured reactors for catalytic reactions. *Catalysis Today* **2005**, *110* (1-2), 2–14. DOI: 10.1016/j.cattod.2005.09.011.
23. Nijhuis, T.; Kreutzer, M.; Romijn, A.; Kapteijn, F.; Moulijn, J. Monolithic catalysts as efficient three-phase reactors. *Chem Eng Sci* **2001**, *56* (3), 823–829. DOI: 10.1016/S0009-2509(00)00294-3.
24. Kreutzer, M. T.; Du, P.; Heiszwolf, J. J.; Kapteijn, F.; Moulijn, J. A. Mass transfer characteristics of three-phase monolith reactors. *Chem Eng Sci* **2001**, *56* (21-22), 6015–6023. DOI: 10.1016/S0009-2509(01)00271-8.
25. Albrand, P. Développement d'un réacteur innovant de type monolithe pour l'hydrogénation sélective d'huile végétale, *Dissertation, Toulouse* **2020**.
26. Boger, T.; Zieverink, M. M. P.; Kreutzer, M. T.; Kapteijn, F.; Moulijn, J. A.; Addiego, W. P. Monolithic Catalysts as an Alternative to Slurry Systems: Hydrogenation of Edible *Oil. Ind. Eng. Chem. Res.* **2004**, *43* (10), 2337–2344. DOI: 10.1021/ie030809v.

27. Scheiff, F.; Neemann, F.; Tomasiak, S. J.; Agar, D. W. Suspensionskatalyse im Pfropfenströmungs-Mikroreaktor - experimentelle und numerische Stofftransportbewertung. *Chem Ing Tech* **2014**, *86* (4), 504–518. DOI: 10.1002/cite.201300131.
28. Liu, Y.; Chen, G.; Yue, J. Manipulation of gas-liquid-liquid systems in continuous flow microreactors for efficient reaction processes. *J Flow Chem* **2020**, *10* (1), 103–121. DOI: 10.1007/s41981-019-00062-9.
29. Ufer, A.; Sudhoff, D.; Mescher, A.; Agar, D. W. Suspension catalysis in a liquid–liquid capillary microreactor. *Chem. Eng. J.* **2011**, *167* (2-3), 468–474. DOI: 10.1016/j.cej.2010.09.088.
30. Ufer, A.; Mendorf, M.; Ghaini, A.; Agar, D. W. Liquid/Liquid Slug Flow Capillary Microreactor. *Chem. Eng. Technol.* **2011**, *34* (3), 353–360. DOI: 10.1002/ceat.201000334.
31. Karan, D.; Khan, S. A. Mesoscale triphasic flow reactors for metal catalyzed gas–liquid reactions. *React. Chem. Eng.* **2019**, *4* (7), 1331–1340. DOI: 10.1039/C9RE00150F.
32. Besenhard, M. O.; Pal, S.; Storozhuk, L.; Dawes, S.; Thanh, N. T. K.; Norfolk, L.; Staniland, S.; Gavriilidis, A. A versatile non-fouling multi-step flow reactor platform: demonstration for partial oxidation synthesis of iron oxide nanoparticles. *Lab on a chip* **2022**, *23* (1), 115–124. DOI: 10.1039/d2lc00892k.
33. Yap, S.; Yuan, Y.; Zheng, L.; Wong, W.; Yan, N.; Khan, S. Triphasic Segmented Flow Millireactors for Rapid Nanoparticle-Catalyzed Gas–Liquid Reactions — Hydrodynamic Studies and Reactor Modeling. *J Flow Chem* **2014**, *4* (4), 200–205. DOI: 10.1556/JFC-D-14-00031.
34. Önal, Y.; Lucas, M.; Claus, P. Application of a Capillary Microreactor for Selective Hydrogenation of α,β-Unsaturated Aldehydes in Aqueous Multiphase Catalysis. *Chem. Eng. Technol.* **2005**, *28* (9), 972–978. DOI: 10.1002/ceat.200500147.
35. Wong, W. K.; Yap, S. K.; Lim, Y. C.; Khan, S. A.; Pelletier, F.; Corbos, E. C. Robust, non-fouling liters-per-day flow synthesis of ultra-small catalytically active metal nanoparticles in a single-channel reactor. *React. Chem. Eng.* **2017**, *2* (5), 636–641. DOI: 10.1039/C7RE00072C.
36. Ravi Kumar, D. V.; Prasad, B.; Kulkarni, A. A. Segmented flow synthesis of Ag nanoparticles in spiral microreactor: Role of continuous and dispersed phase. *Chem. Eng. J.* **2012**, *192*, 357–368. DOI: 10.1016/j.cej.2012.02.084.
37. Guo, W.; Heeres, H. J.; Yue, J. Continuous synthesis of 5-hydroxymethylfurfural from glucose using a combination of AlCl3 and HCl as catalyst in a biphasic slug flow capillary microreactor. *Chem. Eng. J.* **2020**, *381*, 122754. DOI: 10.1016/j.cej.2019.122754.
38. Liu, Y.; Yue, J.; Zhao, S.; Yao, C.; Chen, G. Bubble splitting under gas-liquid-liquid three-phase flow in a double T-junction microchannel. *AIChE J.* **2018**, *64* (1), 376–388. DOI: 10.1002/aic.15920.

39. Widianto, A. Y.; Aubin, J.; Xuereb, C.; Poux, M. Gas-liquid-liquid reactions: Contacting mechanisms and effective process technologies. *Catal. Today* **2020**, *346*, 46–57. DOI: 10.1016/j.cattod.2019.02.064.
40. Yue, J.; Rebrov, E. V.; Schouten, J. C. Gas-liquid-liquid three-phase flow pattern and pressure drop in a microfluidic chip: similarities with gas-liquid/liquid-liquid flows. *Lab chip* **2014**, *14* (9), 1632–1649. DOI: 10.1039/c3lc51307f.
41. Cech, J.; Přibyl, M.; Snita, D. Three-phase slug flow in microchips can provide beneficial reaction conditions for enzyme liquid-liquid reactions. *Biomicrofluidics* **2013**, *7* (5), 54103. DOI: 10.1063/1.4821168.
42. Rajesh, V. M.; Buwa, V. V. Experimental characterization of gas–liquid–liquid flows in T-junction microchannels. *Chem. Eng. J.* **2012**, *207-208*, 832–844. DOI: 10.1016/j.cej.2012.07.082.
43. Hellmann, D.; Oliveira‐Goncalves, Í. de; Agar, D. W. Coaxial Flow Contactors as Alternative to Double T‐Contactors for Triphasic Slug Flow Generation. *Chem Ing Tech* **2020**, *92* (5), 532–539. DOI: 10.1002/cite.201900143.
44. Arsenjuk, L.; Asshoff, M.; Kleinheider, J.; Agar, D. W. A device for continuous and flexible adjustment of liquid-liquid slug size in micro-channels. *J Flow Chem* **2020**, *10* (2), 409–422. DOI: 10.1007/s41981-019-00064-7.
45. Hellmann, D. Fluiddynamik und Stofftransport der Gas-Flüssig-Flüssig-Pfropfenströmung in Mikrokanälen. *PhD thesis, Dortmund* **2021**. DOI: 10.17877/DE290R-22393.
46. Dong, Z.; Wen, Z.; Zhao, F.; Kuhn, S.; Noël, T. Scale-up of micro- and milli-reactors: An overview of strategies, design principles and applications. *Chem Eng Sci X* **2021**, *10,* 100097. DOI: 10.1016/j.cesx.2021.100097.
47. Commenge, J.-M.; Saber, M.; Falk, L. Methodology for multi-scale design of isothermal laminar flow networks. *Chem. Eng. J.* **2011**, *173* (2), 541–551. DOI: 10.1016/j.cej.2011.07.060.
48. Al-Rawashdeh, M.; Yue, F.; Patil, N. G.; Nijhuis, T. A.; Hessel, V.; Schouten, J. C.; Rebrov, E. V. Designing flow and temperature uniformities in parallel microchannels reactor. *AIChE J.* **2014**, *60* (5), 1941–1952. DOI: 10.1002/aic.14443.
49. Saber, M.; Commenge, J.-M.; Falk, L. Rapid design of channel multi-scale networks with minimum flow maldistribution. *Chem Eng Process* **2009**, *48* (3), 723–733. DOI: 10.1016/j.cep.2008.09.001.
50. Mendorf, M.; Nachtrodt, H.; Mescher, A.; Ghaini, A.; Agar, D. W. Design and Control Techniques for the Numbering-up of Capillary Microreactors with Uniform Multiphase Flow Distribution. *Ind. Eng. Chem. Res.* **2010**, *49* (21), 10908–10916. DOI: 10.1021/ie100473d.
51. Al-Rawashdeh, M.; Nijhuis, X.; Rebrov, E. V.; Hessel, V.; Schouten, J. C. Design methodology for barrier-based two phase flow distributor. *AIChE J.* **2012**, *58* (11), 3482–3493. DOI: 10.1002/aic.13750.

52. Arsenjuk, L.; Vietinghoff, N. von; Gladius, A. W.; Agar, D. W. Actively homogenizing fluid distribution and slug length of liquid-liquid segmented flow in parallelized microchannels. *Chem Eng Process* **2020**, *156*, 108061. DOI: 10.1016/j.cep.2020.108061.
53. Kockmann, N.; Gottsponer, M.; Roberge, D. M. Scale-up concept of single-channel microreactors from process development to industrial production. *Chem. Eng. J.* **2011**, *167* (2-3), 718–726. DOI: 10.1016/j.cej.2010.08.089.
54. Önal, Y. Reaktionstechnische Aspekte der wässrigen Mehrphasenkatalyse: Von Grundlagen-Untersuchungen über innovatives Reaktordesign bis zur kinetischen Modellierung, *Dissertation, Darmstadt* **2005**.
55. Klose, F. Operation modes of packed-bed membrane reactors in the catalytic oxidation of hydrocarbons. *Appl Catal A-Gen* **2004**, *257* (2), 193–199. DOI: 10.1016/j.apcata.2003.07.009.
56. Yang, L.; Jensen, K. F. Mass Transport and Reactions in the Tube-in-Tube Reactor. *Org. Process Res. Dev.* **2013**, *17* (6), 927–933. DOI: 10.1021/op400085a.
57. Brzozowski, M.; O'Brien, M.; Ley, S. V.; Polyzos, A. Flow Chemistry: Intelligent Processing of Gas–Liquid Transformations Using a Tube-in-Tube Reactor. *Acc. Chem. Res.* **2015**, *48* (2), 349–362. DOI: 10.1021/ar500359m.
58. Cranwell, P. B.; O'Brien, M.; Browne, D. L.; Koos, P.; Polyzos, A.; Peña-López, M.; Ley, S. V. Flow synthesis using gaseous ammonia in a Teflon AF-2400 tube-in-tube reactor: Paal–Knorr pyrrole formation and gas concentration measurement by inline flow titration. *Org. Biomol. Chem*. **2012**, *10* (30), 5774. DOI: 10.1039/c2ob25407g.
59. Bouriazos, A.; Mouratidis, K.; Psaroudakis, N.; Papadogianakis, G. Catalytic Conversions in Aqueous Media. Part 2. A Novel and Highly Efficient Biphasic Hydrogenation of Renewable Methyl Esters of Linseed and Sunflower Oils to High Quality Biodiesel Employing Rh/TPPTS Complexes. *Catal Lett* **2008**, *121* (1-2), 158–164. DOI: 10.1007/s10562-007-9314-3.
60. Milano-Brusco, J. S.; Schomäcker, R. Catalytic Hydrogenations in Microemulsion Systems with Rh-TPPTS: Partial Hydrogenation of Sunflower Oil. *Catal Lett* **2009**, *133* (3-4), 273–279. DOI: 10.1007/s10562-009-0187-5.
61. Nikolaou, N.; Papadopoulos, C. E.; Lazaridou, A.; Koutsoumba, A.; Bouriazos, A.; Papadogianakis, G. Partial hydrogenation of methyl esters of sunflower oil catalyzed by highly active rhodium sulfonated triphenylphosphite complexes. *Catal Commun* **2009**, *10* (5), 451–455. DOI: 10.1016/j.catcom.2008.10.026.
62. Vasiliou, C.; Bouriazos, A.; Tsichla, A.; Papadogianakis, G. Production of hydrogenated methyl esters of palm kernel and sunflower oils by employing rhodium and ruthenium catalytic complexes of hydrolysis stable monodentate sulfonated triphenylphosphite ligands. *Appl Catal B* **2014**, *158-159*, 373–381. DOI: 10.1016/j.apcatb.2014.04.046.
63. Zagajewski, M.; Dreimann, J.; Thönes, M.; Behr, A. Rhodium catalyzed hydroformylation of 1-dodecene using an advanced solvent system: Towards highly efficient catalyst recycling. *Chem Eng Process* **2016**, *99*, 115–123. DOI: 10.1016/j.cep.2015.06.014.
64. Behr, A.; Neubert, P. Applied homogeneous catalysis; *Wiley-VCH*, **2012**.

65. Heckmann, C.; Kurt, S. K.; Ehrhard, P.; Kockmann, N. Stofftransport in einer Flüssig/Flüssig-Pfropfenströmung im Mikrokapillarreaktor. *Chem Ing Tech* **2017**, *89* (12), 1642–1649. DOI: 10.1002/cite.201700030.
66. Harries, N.; Burns, J. R.; Barrow, D. A.; Ramshaw, C. A numerical model for segmented flow in a microreactor. *Int. J. Heat Mass Transf.* **2003**, *46* (17), 3313–3322. DOI: 10.1016/S0017-9310(03)00120-0.
67. Sontti, S. G.; Pallewar, P. G.; Ghosh, A. B.; Atta, A. Understanding the Influence of Rheological Properties of Shear - Thinning Liquids on Segmented Flow in Microchannel using CLSVOF Based CFD Model. *Can. J. Chem. Eng.* **2019**, *97* (5), 1208–1220. DOI: 10.1002/cjce.23391.
68. Yang, L.; Nieves-Remacha, M. J.; Jensen, K. F. Simulations and analysis of multiphase transport and reaction in segmented flow microreactors. *Chem Eng Sci* **2017**, *169*, 106–116. DOI: 10.1016/j.ces.2016.12.003.
69. Wallis, G. B. Macroscopic properties of a two-phase potential dispersion composed of identical unit cells. *Int. J. Multiph. Flow* **1992**, *18* (6), 989–1017. DOI: 10.1016/0301-9322(92)90072-O.
70. Kashid, M. N.; Agar, D. W. Hydrodynamics of liquid–liquid slug flow capillary microreactor: Flow regimes, slug size and pressure drop. *Chem Eng J* **2007**, *131* (1-3), 1–13. DOI: 10.1016/j.cej.2006.11.020.
71. Jovanović, J.; Zhou, W.; Rebrov, E. V.; Nijhuis, T. A.; Hessel, V.; Schouten, J. C. Liquid–liquid slug flow: Hydrodynamics and pressure drop. *Chem Eng Sci* **2011**, *66* (1), 42–54. DOI: 10.1016/j.ces.2010.09.040.
72. Ładosz, A.; Rigger, E.; Rudolf von Rohr, P. Pressure drop of three-phase liquid–liquid–gas slug flow in round microchannels. *Microfluid Nanofluid* **2016**, *20* (3). DOI: 10.1007/s10404-016-1712-7.
73. Rosa, E. S. Flow Structure In The Horizontal Slug Flow. *RETERM* **2004**, *3* (2), 151. DOI: 10.5380/reterm.v3i2.3536.
74. Soedarmo, A.; Fan, Y.; Pereyra, E.; Sarica, C. A unit cell model for gas-liquid pseudo-slug flow in pipes. *J Nat Gas Sci Eng* **2018**, *60*, 125–143. DOI: 10.1016/j.jngse.2018.10.006.
75. Méhault, C.; Vanoye, L.; Philippe, R.; Bellefon, C. de. Multiphase alternated slug flows: Conditions to avoid coalescence and characterization of mass transfer between droplets. *Chem Eng J* **2021**, *407*, 127215. DOI: 10.1016/j.cej.2020.127215.
76. Oertel, H. Prandtl - Führer durch die Strömungslehre: Grundlagen und Phänomene, 14. Auflage; *Springer Reference Technik; Springer Vieweg,* **2017**.
77. Sutera, S. P.; Skalak, R. The History of Poiseuille's Law. *Annu. Rev. Fluid Mech.* **1993**, *25* (1), 1–20. DOI: 10.1146/annurev.fl.25.010193.000245.
78. Mahnken, R. Lehrbuch der Technischen Mechanik - Elastostatik: Mit einer Einführung in Hybridstrukturen; *Springer Vieweg Berlin, Heidelberg*, **2015**.

79. Rill, G. Technische Mechanik 2 Lecture Notes on Applied Mechanics, Part 2: Vorlesungsskript (accessed 2023-01-02).
80. Matweb - Material Property Data. Properties of Chemoiurs 100 FEP Flourinated Ethylene Propylene. https://www.matweb.com/search/datasheet.aspx?matguid=3dbaaa8dbb114c57996acd6738a7efc1&ckck=1 (accessed 2023-01-02).
81. Mashkov, Y. K.; Egorova, V. A.; Chemisenko, O. V.; Maliy, O. V. The PTFE-nanocomposites mechanical properties for transport systems dynamic sealing devices elements. *J. Phys.: Conf. Ser.* **2017**, *858*, 12018. DOI: 10.1088/1742-6596/858/1/012018.
82. Reichelt Chemietechnik GmbH + Co. Technische Daten von Flourethylenpropylen. https://www.rct-online.de/de/RctGlossar/detail/id/24 (accessed 2023-01-02).
83. Omnexus. The material selection platform. Technical Datasheet of InStruc FEPGF10 by Americhem. https://omnexus.specialchem.com/product/t-americhem-instruc-fepgf10 (accessed 2023-01-02).
84. Teng, H. Overview of the Development of the Fluoropolymer Industry. *Applied Sciences* **2012**, *2* (2), 496–512. DOI: 10.3390/app2020496.
85. Mitchell, G. D. A review of Permeation Tubes and Permeators. *Separation and Purification Methods* **2000**, *29* (1), 119–128. DOI: 10.1081/SPM-100100005.
86. Craster, B.; Jones, T. G. J. Permeation of a Range of Species through Polymer Layers under Varying Conditions of Temperature and Pressure: In Situ Measurement Methods. *Polymers* **2019**, *11* (6). DOI: 10.3390/polym11061056.
87. McKeen, L. W. Permeability properties of plastics and elastomers, Fourth edition; Plastics design library; *William Andrew*, **2016**.
88. Cussler, E. L. Permeability Properties of Plastics and Elastomers. *Journal of Controlled Release* **2003**, *92* (3), 399. DOI: 10.1016/S0168-3659(03)00333-X.
89. van Leeuwen, P. W. Decomposition pathways of homogeneous catalysts. *Appl Catal A-Gen* **2001**, *212* (1-2), 61–81. DOI: 10.1016/S0926-860X(00)00844-9.
90. Skowerski, K.; Czarnocki, S. J.; Knapkiewicz, P. Tube-in-tube reactor as a useful tool for homo- and heterogeneous olefin metathesis under continuous flow mode. *ChemSusChem* **2014**, *7* (2), 536–542. DOI: 10.1002/cssc.201300829.
91. Li, W.-L.; Wang, J.-H.; Chen, H.; Shao, L.; Chu, G.-W.; Xiang, Y. CFD analysis on the intensified mechanism of gas-liquid mass transfer in a microporous tube-in-tube microchannel reactor. *Int. J. Heat Mass Transf.* **2022**, *182*, 121914. DOI: 10.1016/j.ijheatmasstransfer.2021.121914.
92. Han, S.; Kashfipour, M. A.; Ramezani, M.; Abolhasani, M. Accelerating gas-liquid chemical reactions in flow. *Chemical communications (Cambridge, England)* **2020**, *56* (73), 10593–10606. DOI: 10.1039/d0cc03511d.
93. Buba, A. E.; Koch, S.; Kunz, H.; Löwe, H. Fluorenylmethoxycarbonyl- N -methylamino Acids Synthesized in a Flow Tube-in-Tube Reactor with a Liquid-Liquid Semipermeable Membrane. *Eur. J. Org. Chem.* **2013**, *2013* (21), 4509–4513. DOI: 10.1002/ejoc.201300705.

94. Elvira, K. S.; Wootton, R. C. R.; Reis, N. M.; Mackley, M. R.; deMello, A. J. Through-Wall Mass Transport as a Modality for Safe Generation of Singlet Oxygen in Continuous Flows. *ACS Sustainable Chem. Eng.* **2013**, *1* (2), 209–213. DOI: 10.1021/sc300093j.
95. Aka, E. C.; Wimmer, E.; Barré, E.; Cortés-Borda, D.; Ekou, T.; Ekou, L.; Rodriguez-Zubiri, M.; Felpin, F.-X. Comparing Gas–Liquid Segmented and Tube-in-Tube Setups for the Aerobic Dimerization of Desmethoxycarpacine with an Automated Flow Platform. *Org. Process Res. Dev.* **2020**, *24* (5), 745–751. DOI: 10.1021/acs.oprd.9b00525.
96. Rahman, M. T.; Krishnamurthy, P. G.; Parthiban, P.; Jain, A.; Park, C. P.; Kim, D.-P.; Khan, S. A. Dynamically tunable nanoparticle engineering enabled by short contact-time microfluidic synthesis with a reactive gas. *RSC Adv.* **2013**, *3* (9), 2897. DOI: 10.1039/c2ra23216b.
97. Kouridaki, A.; Huvaere, K. Singlet oxygen oxidations in homogeneous continuous flow using a gas–liquid membrane reactor. *React. Chem. Eng.* **2017**, *2* (4), 590–597. DOI: 10.1039/C7RE00053G.
98. Aslam, R.; Müller, K.; Müller, M.; Koch, M.; Wasserscheid, P.; Arlt, W. Measurement of Hydrogen Solubility in Potential Liquid Organic Hydrogen Carriers. *J. Chem. Eng. Data* **2016**, *61* (1), 643–649. DOI: 10.1021/acs.jced.5b00789.
99. Razzaq, T.; Glasnov, T. N.; Kappe, C. O. Accessing Novel Process Windows in a High-Temperature/Pressure Capillary Flow Reactor. *Chem. Eng. Technol.* **2009**, *32* (11), 1702–1716. DOI: 10.1002/ceat.200900272.
100. Jiang, X.; Sotowa, K.-I.; Tonomura, O. Controlling gas–liquid segment length in microchannels using a high-speed valve. *Chem. Eng. Res. Des.* **2022**, *188*, 868–876. DOI: 10.1016/j.cherd.2022.10.038.
101. Zhang, Y.; Zhang, J.; Tang, Z.; Wu, Q. Regulation of gas-liquid Taylor flow by pulsating gas intake in micro-channel. *Chem. Eng. J.* **2021**, *417*, 129055. DOI: 10.1016/j.cej.2021.129055.
102. Garstecki, P.; Fuerstman, M. J.; Stone, H. A.; Whitesides, G. M. Formation of droplets and bubbles in a microfluidic T-junction-scaling and mechanism of break-up. *Lab chip* **2006**, *6* (3), 437–446. DOI: 10.1039/b510841a.
103. Kurzweil, P.; Scheipers, P. Chemie; *Vieweg+Teubner Verlag*, **2010**. DOI: 10.1007/978-3-8348-9367-3.
104. Grigoriev, S.; Porembsky, V.; Fateev, V. Pure hydrogen production by PEM electrolysis for hydrogen energy. *Int. J. Hydrog. Energy* **2006**, *31* (2), 171–175. DOI: 10.1016/j.ijhydene.2005.04.038.
105. Street, J. R.; Tek, M. R. Dynamics of bullet shaped bubbles encountered in vertical gas liquid slug flow. *AIChE J.* **1965**, *11* (4), 644–650. DOI: 10.1002/aic.690110415.
106. Aussillous, P.; Quéré, D. Quick deposition of a fluid on the wall of a tube. *Phys. Fluids* **2000**, *12* (10), 2367. DOI: 10.1063/1.1289396.
107. Han, Y.; Shikazono, N. Measurement of the liquid film thickness in micro tube slug flow. *Int J Heat Fluid Flow* **2009**, *30* (5), 842–853. DOI: 10.1016/j.ijheatfluidflow.2009.02.019.

108. Cahill, B. P.; Land, R.; Nacke, T.; Min, M.; Beckmann, D. Contactless sensing of the conductivity of aqueous droplets in segmented flow. *Sensors and Actuators B: Chemical* **2011**, *159* (1), 286–293. DOI: 10.1016/j.snb.2011.07.006.
109. Mohd Amin, U. S. B.; Osman, N. B.; Uemura, Y.; Majid, N. M. N. A. Catalytic Transfer Hydrogenation of Castor Oil Using Glycerol-Based Reaction. *Waste Biomass Valor* **2020**, *11* (10), 5591–5597. DOI: 10.1007/s12649-020-01010-8.
110. Yu, D.; Chen, J.; Zhou, Q.; Wang, X.; Chen, Y.; Wang, L.; Yu, B. Catalytic Transfer Hydrogenation of Low-erucic-acid Rapeseed Oil over a Ni-Ag0.15/SBA15 Catalyst. *J oleo sci* **2020**, *69* (10), 1191–1198. DOI: 10.5650/jos.ess20055.
111. Nait Ajjou, A.; Pinet, J.-L. The biphasic transfer hydrogenation of aldehydes and ketones with isopropanol catalyzed by water-soluble rhodium complexes. *J Mol Catal A Chem A* **2004**, *214* (2), 203–206. DOI: 10.1016/j.molcata.2004.01.004.
112. Dipu, A. L.; Ujisawa, Y.; Ryu, J.; Kato, Y. Electrolysis of carbon dioxide for carbon monoxide production in a tubular solid oxide electrolysis cell. *Ann Nucl Energy* **2015**, *81*, 257–262. DOI: 10.1016/j.anucene.2015.02.046.
113. Pardal, T.; Messias, S.; Sousa, M.; Machado, A. S. R.; Rangel, C. M.; Nunes, D.; Pinto, J. V.; Martins, R.; da Ponte, M. N. Syngas production by electrochemical CO 2 reduction in an ionic liquid based-electrolyte. *J CO2 Util* **2017**, *18*, 62–72. DOI: 10.1016/j.jcou.2017.01.007.
114. Mac Giolla Eain, M.; Egan, V.; Punch, J. Film thickness measurements in liquid–liquid slug flow regimes. *Int. J. Heat Mass Transf.* **2013**, *44*, 515–523. DOI: 10.1016/j.ijheatfluidflow.2013.08.009.
115. Xue, T.; Wang, Q.; Li, C. Analysis of horizontal slug translational velocity based on the image processing technique. *In 2019 IEEE International Instrumentation and Measurement Technology Conference (I2MTC); IEEE*, **2019**, pp 1–5. DOI: 10.1109/I2MTC.2019.8827088.
116. Cierpka, C.; Kähler, C. J. Particle imaging techniques for volumetric three-component (3D3C) velocity measurements in microfluidics. *J Vis* **2012**, *15* (1), 1–31. DOI: 10.1007/s12650-011-0107-9.
117. Wang, D.; Jin, N.; Zhai, L.; Ren, Y. Measurement of Liquid Film Thickness Using Distributed Conductance Sensor in Multiphase Slug Flow. *IEEE Trans. Ind. Electron.* **2020**, *67* (10), 8841–8850. DOI: 10.1109/TIE.2019.2950861.
118. Tang, X.-Y.; Huang, J.; Ji, H.; Wang, B.; Huang, Z. New method for bubble/slug velocity measurement in small channels. *The Review of scientific instruments* **2020**, *91* (5), 55001. DOI: 10.1063/1.5134548.
119. Mithran, N.; Venkatesan, M. Volumetric Reconstruction of Taylor Slug Gas Flow Using IR Transceiver in Minichannels. *IEEE Trans. Instrum. Meas.* **2020**, *69* (6), 3818–3825. DOI: 10.1109/TIM.2019.2937426.
120. Harvie, A. J.; deMello, J. C. Optical determination of flow-rate and flow-uniformity in segmented flows. *Chem Eng J* **2020**, *394*, 124908. DOI: 10.1016/j.cej.2020.124908.

121. Vishay Intertechnology Inc. Technical Specifications: Subminiature Dual Channel Transmissive Optical Sensor with Phototransistor Outputs (TCUT1300X01) **2019**.
122. National Center for Biotechnology Information. PubChem. https://pubchem.ncbi.nlm.nih.gov/ (accessed 2020-10-04).
123. Fluorotherm. FEP Properties. https://www.fluorotherm.com/technical-information/materials-overview/fep-properties/ (accessed 2020-10-04).
124. Fresnel, A. J. Oeuvres complètes d'Augustin Fresnel: Volume 1; *Impériale*, **1866**.
125. Sabra, A. I. Theories of light: From Descartes to Newton / *A.I. Sabra* **1981**.
126. Liu, L.; Yang, C.; Tan, W.; Wang, Y. Degradation of Acid Red 73 by Activated Persulfate in a Heat/Fe3O4@AC System with Ultrasound Intensification. *ACS omega* **2020**, *5* (23), 13739–13750. DOI: 10.1021/acsomega.0c00903.
127. Liu, X.; Liu, H.; Zhang, W.; Li, X.; Fang, N.; Wang, X.; Wu, J. Facile synthesis and photocatalytic activity of bi-phase dispersible Cu-ZnO hybrid nanoparticles. *Nanoscale research letters* **2015**, *10*, 195. DOI: 10.1186/s11671-015-0895-2.
128. Pizarro, A. H.; Molina, C. B.; Rodriguez, J. J. Decoloration of azo and triarylmethane dyes in the aqueous phase by catalytic hydrotreatment with Pd supported on pillared clays. *RSC Adv.* **2016**, *6* (115), 113820–113825. DOI: 10.1039/C6RA24542K.
129. Kurtan, U.; Onuş, E.; Amir, M.; Baykal, A. Fe3O4@Hpipe-4@Cu Nanocatalyst for Hydrogenation of Nitro-Aromatics and Azo Dyes. *J Inorg Organomet Polym* **2015**, *25* (5), 1120–1128. DOI: 10.1007/s10904-015-0218-1.
130. Krieger, W.; Bayraktar, E.; Mierka, O.; Kaiser, L.; Dinter, R.; Hennekes, J.; Turek, S.; Kockmann, N. Arduino - based slider setup for gas–liquid mass transfer investigations: Experiments and CFD simulations. *AIChE J.* **2020**, *66* (6). DOI: 10.1002/aic.16953.
131. Krieger, W.; Lamsfuß, J.; Zhang, W.; Kockmann, N. Local Mass Transfer Phenomena and Chemical Selectivity of Gas-Liquid Reactions in Capillaries. *Chem. Eng. Technol.* **2017**, *40* (11), 2134–2143. DOI: 10.1002/ceat.201700420.
132. Dietrich, N.; Loubière, K.; Jimenez, M.; Hébrard, G.; Gourdon, C. A new direct technique for visualizing and measuring gas–liquid mass transfer around bubbles moving in a straight millimetric square channel. *Chem Eng Sci* **2013**, *100*, 172–182. DOI: 10.1016/j.ces.2013.03.041.
133. Höving, S.; Bobers, J.; Kockmann, N. Open-source multi-purpose sensor for measurements in continuous capillary flow. *J Flow Chem* **2022**, *12* (2), 185–196. DOI: 10.1007/s41981-021-00214-w.
134. Villers, D.; Platten, J. K. Temperature dependence of the interfacial tension between water and long-chain alcohols. *J. Phys. Chem.* **1988**, *92* (14), 4023–4024. DOI: 10.1021/j100325a005.
135. Verein Deutscher Ingenieure; VDI-Gesellschaft Verfahrenstechnik und Chemieingenieurwesen. VDI-Wärmeatlas: Mit 320 Tabellen, 11., bearb. und erw. Aufl.; VDI-Buch*; Springer Berlin Heidelberg*, **2013**. DOI: 10.1007/978-3-642-19981-3.

136. Light-Emitting Diodes and Lighting, *Wiley-VCH* **2008**, 1–168. DOI: 10.1002/9783527628445.ch1.
137. Sato, T.; Hamada, Y.; Sumikawa, M.; Araki, S.; Yamamoto, H. Solubility of Oxygen in Organic Solvents and Calculation of the Hansen Solubility Parameters of Oxygen. *Ind. Eng. Chem. Res.* **2014**, *53* (49), 19331–19337. DOI: 10.1021/ie502386t.
138. Richard, R.; Li, Y.; Dubreuil, B.; Thiebaud-Roux, S.; Prat, L. On-line monitoring of the transesterification reaction between triglycerides and ethanol using near infrared spectroscopy combined with gas chromatography. *Bioresource technology* **2011**, *102* (12), 6702–6709. DOI: 10.1016/j.biortech.2011.03.111.
139. Richard, R.; Dubreuil, B.; Thiebaud-Roux, S.; Prat, L. On-line monitoring of the transesterification reaction carried out in microreactors using near infrared spectroscopy. *Fuel* **2013**, *104*, 318–325. DOI: 10.1016/j.fuel.2012.07.054.
140. Albrand, P.; Julcour, C.; Gerbaud, V.; Billet, A.-M. Accurate hydrogenated vegetable oil viscosity predictions for monolith reactor simulations. *Chem Eng Sci* **2020**, *214*, 115388. DOI: 10.1016/j.ces.2019.115388.
141. Souza, R. J. de; Mente, A.; Maroleanu, A.; Cozma, A. I.; Ha, V.; Kishibe, T.; Uleryk, E.; Budylowski, P.; Schünemann, H.; Beyene, J.; Anand, S. S. Intake of saturated and trans unsaturated fatty acids and risk of all cause mortality, cardiovascular disease, and type 2 diabetes: systematic review and meta-analysis of observational studies. *BMJ* **2015**, *351*, h3978. DOI: 10.1136/bmj.h3978.
142. Mozaffarian, D.; Micha, R.; Wallace, S. Effects on coronary heart disease of increasing polyunsaturated fat in place of saturated fat: a systematic review and meta-analysis of randomized controlled trials. *PLOS Medicine* **2010**, *7* (3), e1000252. DOI: 10.1371/journal.pmed.1000252.
143. Schuchardt, U.; Sercheli, R.; Vargas, R. M. Transesterification of vegetable oils: a review. *J. Braz. Chem. Soc.* **1998**, *9* (3). DOI: 10.1590/s0103-50531998000300002.
144. Wagner, H.; Luther, R.; Mang, T. Lubricant base fluids based on renewable raw materials. *Appl Catal A-Gen* **2001**, *221* (1-2), 429–442. DOI: 10.1016/S0926-860X(01)00891-2.
145. Vondran, J.; Benninghoff, T.; Emminghaus, A. I.; Seidensticker, T. Catalytic Synthesis of Methyl 9,10 - dihydroxystearate from Technical Feedstocks in Continuous Flow via Epoxidation and Hydrolysis. *Euro J Lipid Sci & Tech* **2022**, *124* (7), 2200041. DOI: 10.1002/ejlt.202200041.
146. Zaccheria, F.; Psaro, R.; Ravasio, N.; Bondioli, P. Standardization of vegetable oils composition to be used as oleochemistry feedstock through a selective hydrogenation process. *Euro J Lipid Sci & Tech* **2012**, *114* (1), 24–30. DOI: 10.1002/ejlt.201100044.
147. an Philippaerts; Jacobs, P. A.; Sels, B. F. Hat die Hydrierung von Pflanzenölen noch eine Zukunft? *Angew. Chem.* **2013**, *125* (20), 5328–5334. DOI: 10.1002/ange.201209731.
148. Wurster, O. H. Hydrogenation Of Fats. *Ind. Eng. Chem.* **1940**, *32* (9), 1193–1199. DOI: 10.1021/ie50369a029.
149. Lindlar, H. Ein neuer Katalysator für selektive Hydrierungen. *HCA* **1952**, *35* (2), 446–450. DOI: 10.1002/hlca.19520350205.

150. Laverdura, U. P.; Rossi, L.; Ferella, F.; Courson, C.; Zarli, A.; Alhajyoussef, R.; Gallucci, K. Selective Catalytic Hydrogenation of Vegetable Oils on Lindlar Catalyst. *ACS omega* **2020**, *5* (36), 22901–22913. DOI: 10.1021/acsomega.0c02280.
151. Itatani, H.; Bailar, J. C. Homogenous catalysis in the reactions of olefinic substances. V. Hydrogenation of soybean oil methyl ester with triphenylphosphine and triphenylarsine palladium catalysts. *J Am Oil Chem Soc* **1967**, *44* (2), 147–151. DOI: 10.1007/BF02558176.
152. Frankel, E. N. Conversion of polyunsaturates in vegetable oils to cis -monounsaturates by homogeneous hydrogenation catalyzed with chromium carbonyls. *J Am Oil Chem Soc* **1970**, *47* (1), 11–14. DOI: 10.1007/BF02680158.
153. Papadopoulos, C. E.; Lazaridou, A.; Koutsoumba, A.; Kokkinos, N.; Christoforidis, A.; Nikolaou, N. Optimization of cotton seed biodiesel quality (critical properties) through modification of its FAME composition by highly selective homogeneous hydrogenation. *Bioresource technology* **2010**, *101* (6), 1812–1819. DOI: 10.1016/j.biortech.2009.10.016.
154. Bouriazos, A.; Ikonomakou, E.; Papadogianakis, G. Aqueous-phase catalytic hydrogenation of methyl esters of Cynara cardunculus alternative low-cost non-edible oil: A useful concept to resolve the food, fuel and environment issue of sustainable biodiesel. *Industrial Crops and Products* **2014**, *52*, 205–210. DOI: 10.1016/j.indcrop.2013.10.040.
155. Winterbottom, J.; Khan, Z.; Raymahasay, S.; Knight, G.; Roukounakis, N. A comparison of triglyceride oil hydrogenation in a downflow bubble column using slurry and fixed bed catalysts. *J. Chem. Technol. Biotechnol.* **2000**, *75* (11), 1015–1025. DOI: 10.1002/1097-4660(200011)75:11<1015:AID-JCTB304>3.0.CO;2-7.
156. Bansode, A.; Guilera, G.; Cuartero, V.; Simonelli, L.; Avila, M.; Urakawa, A. Performance and characteristics of a high pressure, high temperature capillary cell with facile construction for operando x-ray absorption spectroscopy. *The Review of scientific instruments* **2014**, *85* (8), 84105. DOI: 10.1063/1.4893351.
157. Goor, G.; Glenneberg, J.; Jacobi, S.; Dadabhoy, J.; Candido, E. Hydrogen Peroxide. In Ullmann's encyclopedia of industrial chemistry. Vol. 40, Index volume, 6th, completely rev. ed.; Ullmann, F., Ed.; *Wiley-VCH*, **2003**, pp 1–40. DOI: 10.1002/14356007.a13_443.pub3.
158. Ranganathan, S.; Sieber, V. Recent Advances in the Direct Synthesis of Hydrogen Peroxide Using Chemical Catalysis—A Review. *Catalysts* **2018**, *8* (9), 379. DOI: 10.3390/catal8090379.
159. Termühlen, M.; Etmanski, M. M.; Kryschewski, I.; Kufner, A. C.; Schembecker, G.; Wohlgemuth, K. Continuous slug flow crystallization: Impact of design and operating parameters on product quality. *Chem Eng Res Des* **2021**, *170*, 290–303. DOI: 10.1016/j.cherd.2021.04.006.
160. Termühlen, M.; Strakeljahn, B.; Schembecker, G.; Wohlgemuth, K. Quantification and evaluation of operating parameters' effect on suspension behavior for slug flow crystallization. *Chem Eng Sci* **2021**, *243*, 116771. DOI: 10.1016/j.ces.2021.116771.

161. Jiang, M.; Zhu, Z.; Jimenez, E.; Papageorgiou, C. D.; Waetzig, J.; Hardy, A.; Langston, M.; Braatz, R. D. Continuous-Flow Tubular Crystallization in Slugs Spontaneously Induced by Hydrodynamics. *Crystal Growth & Design* **2014**, *14* (2), 851–860. DOI: 10.1021/cg401715e.
162. Scheiff, F.; Mendorf, M.; Agar, D.; Reis, N.; Mackley, M. The separation of immiscible liquid slugs within plastic microchannels using a metallic hydrophilic sidestream. *Lab on a chip* **2011**, *11* (6), 1022–1029. DOI: 10.1039/c0lc00442a.
163. Gaakeer, W. A.; Croon, M. de; van der Schaaf, J.; Schouten, J. C. Liquid–liquid slug flow separation in a slit shaped micro device. *Chem. Eng. J.* **2012**, *207-208*, 440–444. DOI: 10.1016/j.cej.2012.06.148.
164. Kashid, M. N.; Harshe, Y. M.; Agar, D. W. Liquid−Liquid Slug Flow in a Capillary: An Alternative to Suspended Drop or Film Contactors. *Ind. Eng. Chem. Res.* **2007**, *46* (25), 8420–8430. DOI: 10.1021/ie070077x.
165. Breisig, H.; Schmidt, M.; Wolff, H.; Jupke, A.; Wessling, M. Droplet-based liquid–liquid extraction inside a porous capillary. *Chem. Eng. J.* **2017**, *307*, 143–149. DOI: 10.1016/j.cej.2016.08.024.
166. Adamo, A.; Heider, P. L.; Weeranoppanant, N.; Jensen, K. F. Membrane-Based, Liquid–Liquid Separator with Integrated Pressure Control. *Ind. Eng. Chem. Res.* **2013**, *52* (31), 10802–10808. DOI: 10.1021/ie401180t.
167. Holbach, A.; Kockmann, N. Counter-current arrangement of microfluidic liquid-liquid droplet flow contactors. *Green Process Synth* **2013**, *2* (2). DOI: 10.1515/gps-2013-0006.
168. Langemann, M. Bipolarplattenmaterialien für Polymer-Elektrolyt-Membran Elektrolyse; Schriften des Forschungszentrums Jülich Reihe Energie & Umwelt / Energy & Environment; Vol. 348; Forschungszentrum Jülich, **2017**.
169. Rozendal, R. A.; Hamelers, H. V. M.; Buisman, C. J. N. Effects of membrane cation transport on pH and microbial fuel cell performance. *Environ. Sci. Technol.* **2006**, *40* (17), 5206–5211. DOI: 10.1021/es060387r.
170. Langbein-Pfanhauser-Werke AG, Neuss/Rhein. LPW-Taschenbuch für Galvanotechnik, 12th ed.; *Eigenverl. der Langbein-Pfanhauser-Werke*, **1970**.
171. Schneider, Rosana de Cassia de Souza; Lara, L. R. S.; Martinelli, M. An alternative process for hydrogenation of sunflower oil. *Orbital: Electron. J. Chem.* **2010**, *2* (2), 189–200. DOI: 10.17807/orbital.v2i2.152.
172. Sancheti, S. V.; Gogate, P. R. Ultrasound assisted selective catalytic transfer hydrogenation of soybean oil using 5% Pd/C as catalyst under ambient conditions in water. *Ultrasonics sonochemistry* **2017**, *38*, 161–167. DOI: 10.1016/j.ultsonch.2017.03.004.

A. Details and assumptions for the start-up modeling of a compressible multiphase flow in capillaries

Some assumptions are made for this purpose:

- Liquids are incompressible and behave like Newtonian fluids.
- The flow is assumed to be a block flow (no wall film) whose contact angle θ at the interface equals 90°. Thus, the pressure component generated by the phase interface becomes zero according to Kashid's equation (Eq. A.1). *(70)*

$$\Delta p_{IF} = \frac{2\gamma}{r} cos\theta \tag{A.1}$$

  This reduces the pressure drop of the flow to the hydrodynamic pressure drop, according to Hagen-Poiseuille *(77)*.

$$\Delta p_H = \frac{8\eta_L \bar{u} L}{R^2} \tag{A.2}$$

- Assuming block flow, all liquid phases involved can be combined into one, whose physical properties result from Kaufmann's mixing rule according to the liquid fractions.
- The block flow is always assumed to be the flow pattern independent of the velocity.
- In the liquid phase, a parabolic velocity profile is formed in analogy to the Hagen-Poiseuille law.
- The gas phase does not result in any additional pressure loss due to friction.
- The gas follows the ideal gas law.
- The influence of the gravity force is neglected.
- The inlet unit cell always has the same geometry and volume flow. Only the pressure is variable. This means that the liquid segment (incompressible) always has the same geometries (length, volume).
- It is assumed that there is no sink of gas. Thus, there are no mass transfer processes, permeation flow out of the capillary, or consumption by a reaction.
- The expansion of the FEP capillaries is negligible.

Selection of the time interval δt

If the time discretization is selected too large, the newly calculated volumes from a gas segment may become negative. This happens, for example, if the previous liquid segment has a significantly higher velocity than the following one. With a too large time interval δt, the distances passed by the liquid segments differ too much. In that case, a smaller time discretization has to be chosen to obtain physically reasonable results. Especially for small gas segments, long capillaries, and for the consideration of filled capillaries during the start-up process, small time steps are necessary. Depending on the application, time intervals δt in the order of 0.01-10 ms are sufficient. For significantly smaller time intervals, no improvement of the model was achieved.

Model without inertia force

To compare the model presented in Chapter 2.2, considering the inertia force, a model without inertia force is derived using the same methodology. The consideration of the gas phase, including the gas expansion, remains identical since inertial forces have no influence here. In the liquid phase, only the pressure and frictional forces on the capillary wall are considered in the force balance. This force balance, in turn, results in the Hagen-Poiseuille law, which, converted to the mean velocity ū (Eq. A.3), replaces Equation 2.8 (Chapter 2.2). However, the linking with the preceding and following unit cells remains as described in Chapter 2.2.

$$\bar{u} = \frac{\Delta p_H \cdot R^2}{8\eta_L \cdot L} \tag{A.3}$$

Data logging

Pressure and velocity are used to evaluate the results. The pressure in the first unit cell is followed over time, and the axial pressure is considered in the last time step. On the other hand, velocity is tracked over time in the last unit cell since there the most significant variations are expected (velocity is constant at the inlet of the capillary) and axial velocity in the last time step. For the pressure over time, a pair of values (pressure and elapsed time) are stored every 1000 iterations. A different time is chosen for the outflow velocity in time. Due to the outflow of a liquid segment and the simultaneous relaxation of the following gas bubble, slight pulsations occur at the end of the capillary. A pair of values is stored for the outlet velocity over time when a whole unit cell has left the capillary to prevent misinterpretation. For the axial pressure and velocity profiles, all pressures and velocities of all unit cells are stored together with their axial position for the last time step.

Influence of viscosity

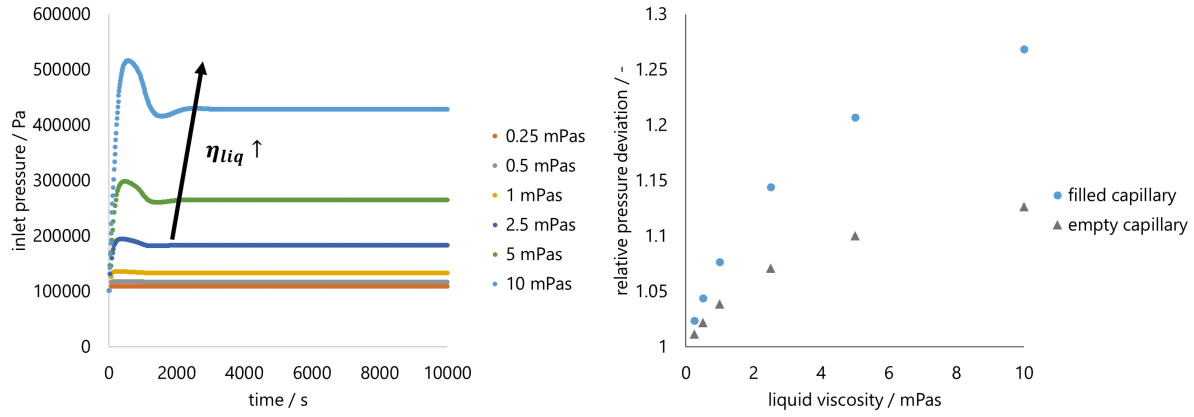

Figure A.1. Left: Time-depending pressure profile at the inlet of the capillary for a start-up of a filled capillary at different liquid viscosities. Right: Relative pressure deviation of filled and empty capillaries during start-up for different liquid viscosities. 40 m capillary length, 1 mm inner diameter, L_{gas}=0.5 mm, L_{liq}=1mm, $\dot{V}_{tot}$=1.8 mL/min, p_{end}=1.013 bar, ρ_{liq}=800 kg/m³, δt=0.0125 ms.

Influence of volume flow rate

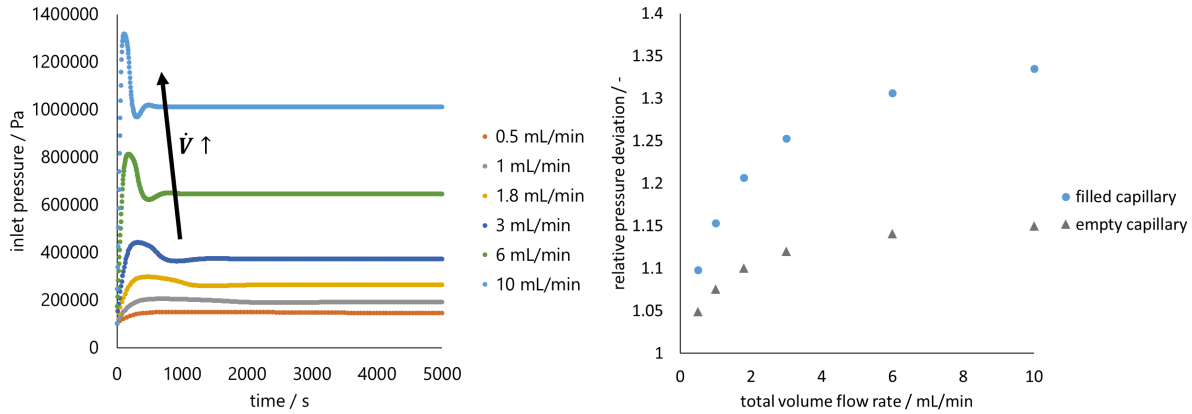

Figure A.2. Left: Time-depending pressure profile at the inlet of the capillary for a start-up of a filled capillary at different inlet volume flow rates. Right: Relative pressure deviation of filled and empty capillaries during start-up for different inlet volume flow rates. 40 m capillary length, 1 mm inner diameter, L_{gas}=0.5 mm, L_{liq}=1mm, p_{end}=1.013 bar, ρ_{liq}=800 kg/m³, $\bar{\eta}_{liq}$=5 mPas, δt=0.0125 ms.

Dynamic viscosities of 1-hexanol and water as a function of the temperature

The dynamic viscosity of water (H_2O) and hexanol (Hex) can be calculated with the temperature T (in K) according to Eq. A.11 and A.12 *(135)*.

$$\eta_{H_2O} = 0.00006896 \cdot \exp\left(0.45047\left(\frac{613.181 - T}{T - 63.697}\right)^{1/3} + 1.39753\left(\frac{613.181 - T}{T - 63.697}\right)^{4/3}\right) \quad \text{(A.11)}$$

$$\eta_{H_2O} = 0.00002196 \cdot \exp\left(2.38169\left(\frac{628.673 - T}{T - 36.282}\right)^{1/3} + 2.01882\left(\frac{628.673 - T}{T - 36.282}\right)^{4/3}\right) \quad \text{(A.12)}$$

B. Experimental procedure, chemicals, and setup details

Experimental procedure

For starting up the capillary reactor, the temperature is set first and controlled to a steady state. Since heating can take up to two hours, the catalyst and solutions can be prepared in the meantime.

In applications with pressure, the pressure is first provided at the end of the capillary, as the flow reaches a steady state more quickly. Then, the fluids are fed into the empty capillary. Finally, 2-3 theoretical mean residence times are awaited until a steady state is reached. During this process, the flow drains into collection vessel B1 at the end of the capillary.

The external pressure in reactor elements R1-4 should always be slightly above the internal capillary pressure (e.g., 1 bar). Samples can be taken according to Chapter 2.4.

For the shut-down, the rinsing solvents are supplied at a high volume flow (approx. 4 mL/min per pump). At the same time, the pressure at the end of the capillary is released, and the heating is switched off. The capillary is then rinsed for one hour with a single-phase flow of isopropanol. The solvent can also be recycled for this purpose. Finally, the capillary is flushed with a high-volume flow of nitrogen until no more liquid is present.

Tank B1 can be drained with back pressure via the upstream three-way valve through the tube to B2.

Coaxial slug flow generator

The coaxial slug generators were designed according to the concept of Arsenjuk et al. *(44)*. However, the slug generator was constructively adapted to be pressure stable up to at least 35 bar. In addition, the height-adjustable inner capillary was used with a 1 mm inner diameter so that the biphasic gas-liquid slug flow from K1 is not unstabilized before the organic phase encloses it. In Figure B.1, the slug flow generator is depicted.

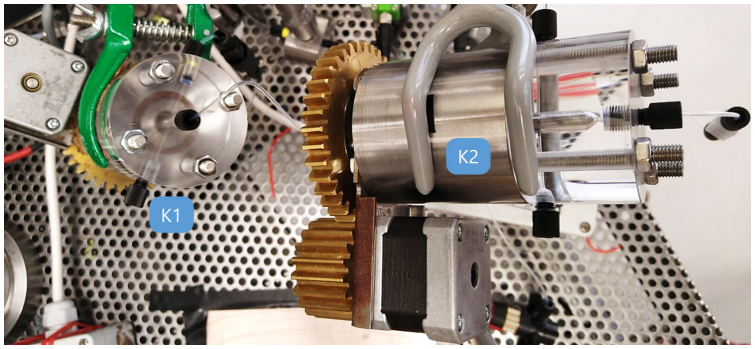

Figure B.1. Slug flow generator in an adjustable coaxial configuration. Left: Slug generator for biphasic gas-liquid flow. Right: Slug generator for triphasic gas-liquid-liquid flow.

List of chemicals

Substance	Purity	Supplier
1-hexanol	99%	Alpha Aesar (Haverhill, MA; USA)
3,3′,3′′-phosphanetriyltris(benzenesulfonic acid) trisodium salt (TPPTS)	saturated in water	Oxea (Monheim, Germany)
Ammonium formate	>95%	Carl Roth (Karlsruhe, Germany)
Argon	99.996%	Messer (Bad Solden, Germany)
Blue Ink (4001)		Pelikan (Hannover, Germany)
Bromothymol blue	ACS, Reag. PhEur	Merck (Darmstadt, Germany)
Chloro-(1,5-cyclooctadiene)-rhodium(I) dimer	98%	abcr (Karlsruhe, Germany)
Crystal violet	ACS, Reag. PhEur	Merck (Darmstadt, Germany)
Helium	99.999%	Messer (Bad Solden, Germany)
Hydrogen	99.999%	Messer (Bad Solden, Germany)
Isopropanol	>99.5	Carl Roth (Karlsruhe, Germany)
Methyl tertiary-butyl ether (MTBE)	>99.5%	Carl Roth (Karlsruhe, Germany)
Nitrogen	99.999%	Messer (Bad Solden, Germany)
Ponceau BS	>85%	Thermo Fischer Scientific (Waltham, MA, USA)
Potassium dicyanoaurate(I)	"pure"	Carl Roth (Karlsruhe, Germany)
Potassium dihydrogen phosphate	>99%	Carl Roth (Karlsruhe, Germany)
Potassium Formate	>98%	Carl Roth (Karlsruhe, Germany)
Potassium hydroxide	>85%	Carl Roth (Karlsruhe, Germany)
Solvent Black 3	>99.99%	Kremer Pigments (Aichstetten, Germany)
Sudan III	88%	Carl Roth (Karlsruhe, Germany)
Sunflower oil	food grade	Aro (Düsseldorf, Germany)
Thermo oil AP 200		Wacker (München, Germany)
Trimethyl sulfonium hydroxide (TMSH)	0.2 mol/L in methanol	tci chemicals (Eschborn, Germany)
Wood's nickel strike		Tifoo (Regensburg, Germany)

List of equipment

Equipment	Typ	Manufacturer
FEP capillary	KAP FEP (1 mm ID, 1/16" OD)	TechLab (Braunschweig, Germany)
Arduino	Arduino Uno Rev 3 SMD	Arduino LLC (Chiasso, Switzerland)
Backpressure valve	CV-3000	IDEX H&S ((Oak Harbor, WA, USA)
Camera	DFK37BUX	Imagingsource (Bremen, Germany)
Data acquisition	TCP 750-891	Wago (Minden, Germany)
Dual optoelectrical sensor	TCUT1300×01	Vishay (Malvern, PA, USA)
Flangeless Ferrule	UP P200	IDEX H&S (Oak Harbor, WA, USA)
Flangeless Male nut	UP P201	IDEX H&S (Oak Harbor, WA, USA)
Flexible heat coils	HAT 22	Horst (Lorsch, Germany)
Gas diffusion layer	E20H GDL	Quintech (Göppingen, Germany)
LabView	2020	NI National Instruments (Austin, TX, USA)
LED	LED-5 white 18 cd	Thomsen (Greifenstein-Nenderoth, Germany)
Light filter	Peacock Blue	Lee Filters (Hamshire, UK)
Liquid flow sensors	SLI-2000	Sensirion (Chicago, IL, USA)
Mantel-Thermoelement	Typ K, L=300mm,d=2mm	TC Direct (Mönchengladbach, Germany)
Mass flow controller	F-200CV	Bronkhorst (Kamen, Germany)
MatLab	2020a	MathWorks (Natick, MA, USA)
Nafion membrane	NM 115	Quintech (Göppingen, Germany)
Phototransistor	BPY 62	Osram (München, Germany)
Power supply	LPS 301	Amrel (Pasadena, CA, USA)
Pressure control valve	C5I	Bronkhorst (Kamen, Germany)
Pressure difference indicator	DRMOD-I2C-PD0B5	B+B Thermo-Technik (Donaueschingen, Germany)
Pressure indicator	D0A-05	AirCom (Ratingen, Germany)
Pressure regulator	R414003373	Aventics (Laatzen, Germany)
Solenoid valve (1)	ATS-V4	Wittko (Riedenburg, Germany)
Solenoid valve (2)	VA204-715 12 V	Staiger (Erligheim, Germany)
Stirred tank reactor	Parr 4560	Parr Instruments (Frankfurt, Germany)
Syringe pumps	SyrDos_CKP	Hitec-Zang (Herzogenrath, Germany)
Teensy	Teensy 4.1	Pjrc (Sherwood, OR, USA)
Thermostat	F25	Julabo (Seelbach, Germany)
Three-way valve	UP V-101T	IDEX H&S (Oak Harbor, WA, USA)
UV-Vis spectrometer	Genesys 10 UV	Thermo Electron (Langensbold, Germany)

Technical drawing reactor module

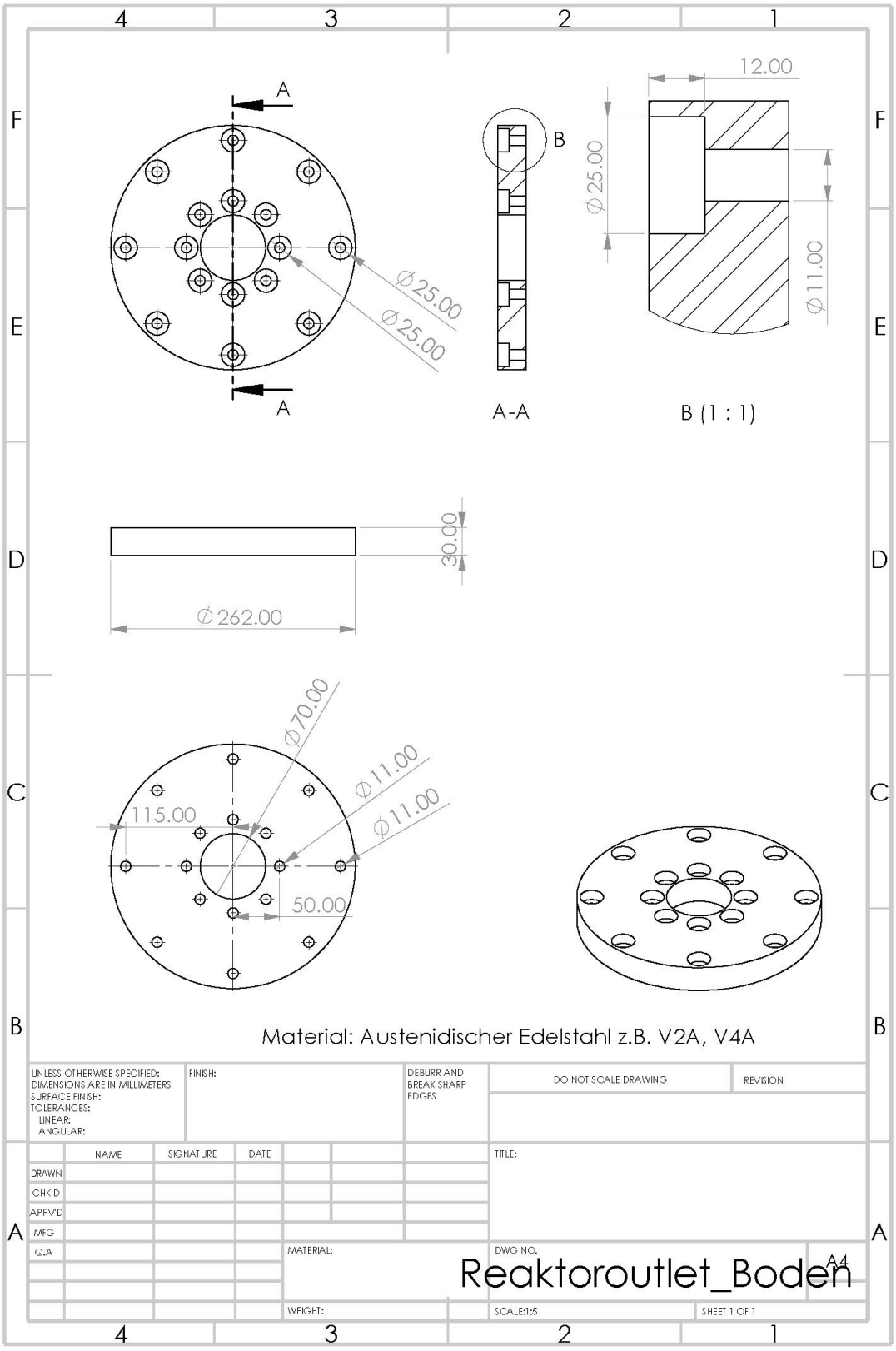

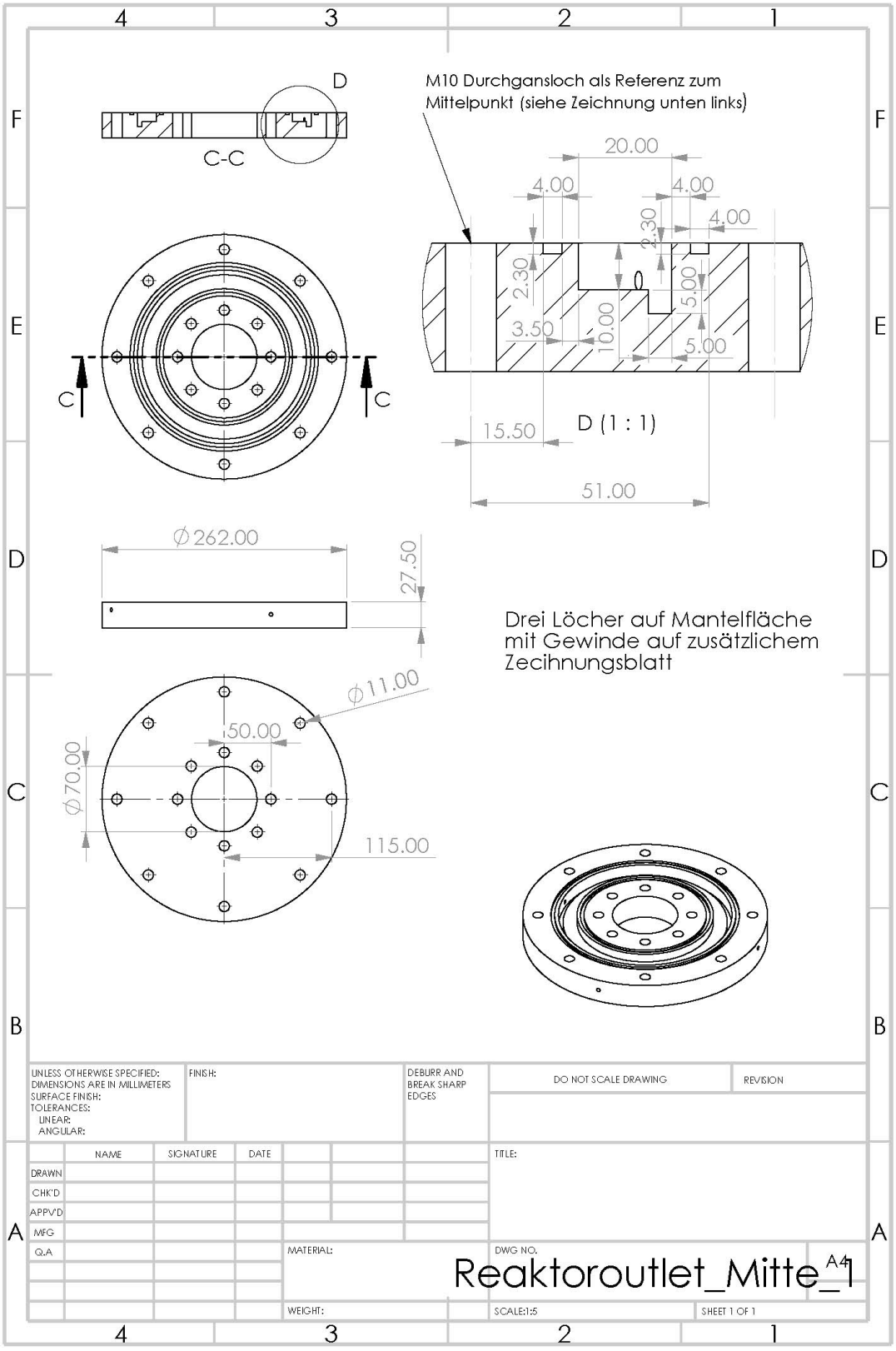
D
C-C
M10 Durchgansloch als Referenz zum Mittelpunkt (siehe Zeichnung unten links)
20.00
4.00
4.00
4.00
2.30
2.30
5.00
3.50
10.00
5.00
15.50
D (1 : 1)
51.00
C
C
⌀262.00
27.50
Drei Löcher auf Mantelfläche mit Gewinde auf zusätzlichem Zecihnungsblatt
⌀11.00
50.00
⌀70.00
115.00
UNLESS OTHERWISE SPECIFIED:
DIMENSIONS ARE IN MILLIMETERS
SURFACE FINISH:
TOLERANCES:
LINEAR:
ANGULAR:
FINISH:
DEBURR AND BREAK SHARP EDGES
DO NOT SCALE DRAWING
REVISION
NAME
SIGNATURE
DATE
DRAWN
CHK'D
APPV'D
MFG
Q.A
TITLE:
MATERIAL:
DWG NO.
Reaktoroutlet_Mitte_1
A4
WEIGHT:
SCALE:1:5
SHEET 1 OF 1

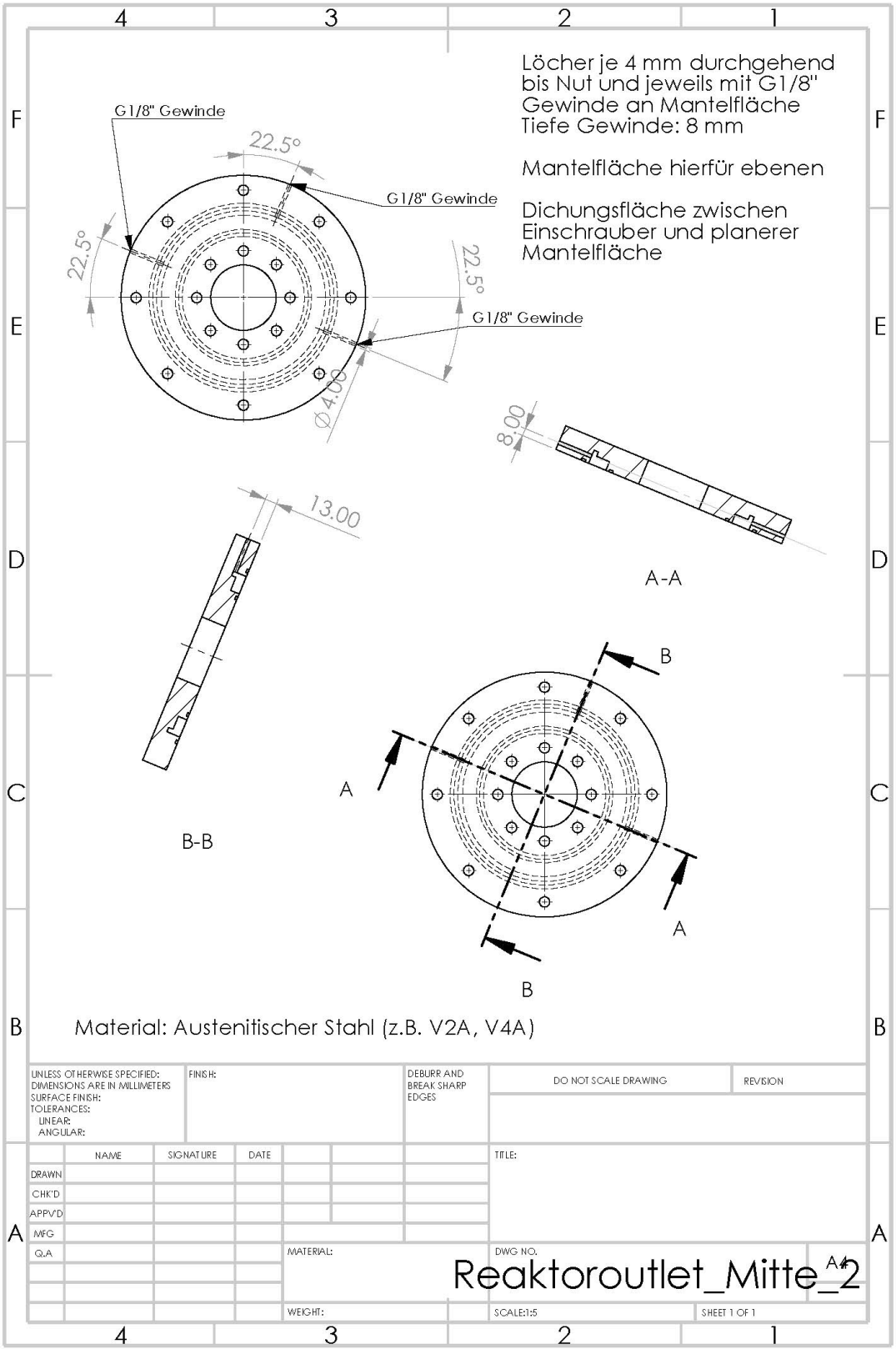
Löcher je 4 mm durchgehend bis Nut und jeweils mit G1/8" Gewinde an Mantelfläche
Tiefe Gewinde: 8 mm
Mantelfläche hierfür ebenen
Dichungsfläche zwischen Einschrauber und planerer Mantelfläche
G1/8" Gewinde
G1/8" Gewinde
G1/8" Gewinde
22.5°
22.5°
22.5°
Ø4.00
8.00
A-A
13.00
B-B
A
B
A
B
Material: Austenitischer Stahl (z.B. V2A, V4A)
UNLESS OTHERWISE SPECIFIED:
DIMENSIONS ARE IN MILLIMETERS
SURFACE FINISH:
TOLERANCES:
LINEAR:
ANGULAR:
FINISH:
DEBURR AND BREAK SHARP EDGES
DO NOT SCALE DRAWING
REVISION
NAME
SIGNATURE
DATE
DRAWN
CHK'D
APPV'D
MFG
Q.A
TITLE:
MATERIAL:
DWG NO.
A4
Reaktoroutlet_Mitte_2
WEIGHT:
SCALE:1:5
SHEET 1 OF 1

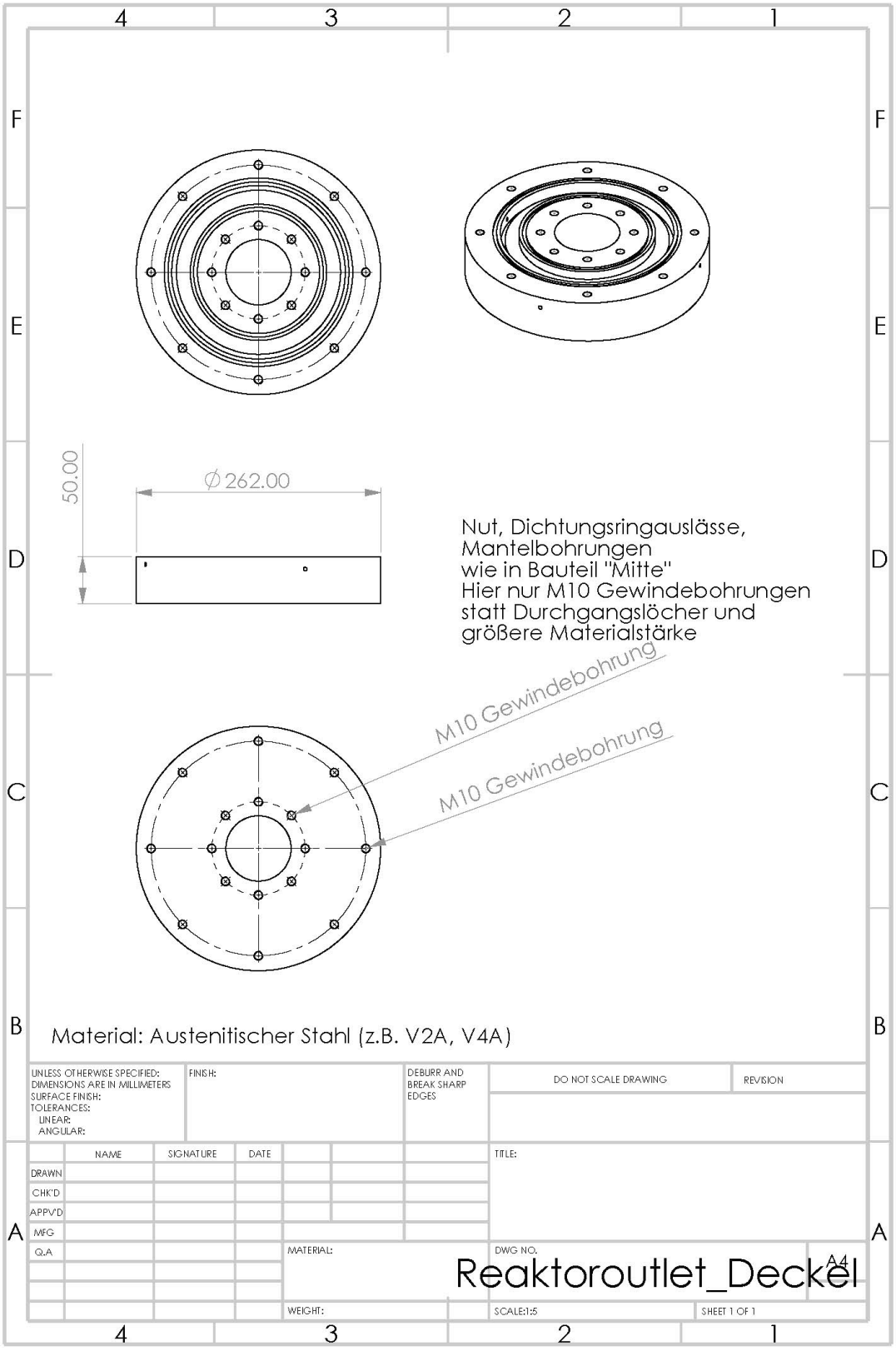
4
3
2
1
F
E
D
C
B
A
50.00
∅262.00
Nut, Dichtungsringauslässe,
Mantelbohrungen
wie in Bauteil "Mitte"
Hier nur M10 Gewindebohrungen
statt Durchgangslöcher und
größere Materialstärke
M10 Gewindebohrung
M10 Gewindebohrung
Material: Austenitischer Stahl (z.B. V2A, V4A)
UNLESS OTHERWISE SPECIFIED:
DIMENSIONS ARE IN MILLIMETERS
SURFACE FINISH:
TOLERANCES:
LINEAR:
ANGULAR:
FINISH:
DEBURR AND
BREAK SHARP
EDGES
DO NOT SCALE DRAWING
REVISION
NAME
SIGNATURE
DATE
DRAWN
CHK'D
APPV'D
MFG
Q.A
TITLE:
MATERIAL:
DWG NO.
A4
Reaktoroutlet_Deckel
WEIGHT:
SCALE:1:5
SHEET 1 OF 1

X

C. Feedback control reactor temperature

Four individually controllable electric heating bands control the temperature of the reactor elements R1-R4. A two-step, two-point controller is used for this purpose. In the first step, the reactor is heated with the full power of the heating bands until the temperature in all reactor elements is higher than the setpoint. Then the heating bands are switched off until the temperature of all elements has fallen below the setpoint temperature. Then, in a second step, the power of the heating bands is reduced to 5-30% and further controlled according to a two-point controller. This reduces the oscillation of the temperature to <0.3 K. The power of the heating bands in the second step can be adjusted according to the setpoint (the higher the temperature, the higher the power). In addition, temperature differences between the reactor elements R1-4 can be compensated by heating, i.e., the lower element more strongly (with more power) than the other elements.

Figure C.1 shows a temperature curve of this control at 75 °C. After about 90 min, the setpoint is reached for the first time. Afterward, a slight temperature oscillation can be seen due to too high power (40%) in the second control step. A reduction of 15% resulted in oscillations of 0.1 °C.

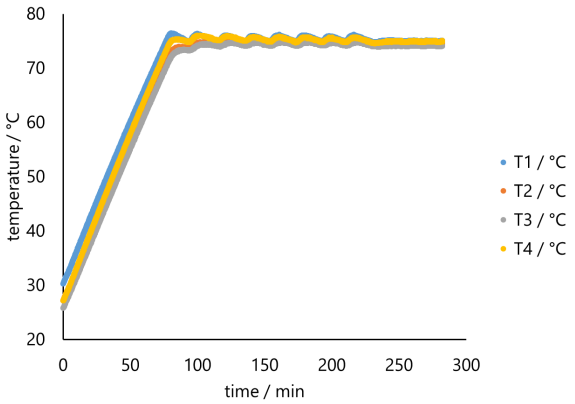

Figure C.1. Temperature curves of the heating process of the reactor for the thermocouples T1-T4 of the corresponding reactor elements.

More complex control of the temperature is possible, but this is not necessary due to the reactor's high mass and heat capacity.

D. Gas injection: solenoid valve performance, gold-plating, and electrolysis cell

Solenoid valve performance

The gas bubble length was measured for different t_{open} at different upstream pressures. On the one hand, gas bubbles of up to 18 mm could be achieved; a linear relationship between the gas bubble and opening time was determined with an accuracy of >99%.

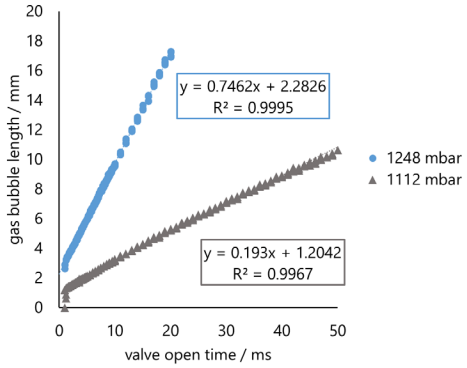

Figure D.1. Resulting gas bubble length by injecting hydrogen in a single-phase capillary flow by varying t_{open} at two upstream pressures provided by the electrolysis cell. Capillary pressure is approximately 1013 mbar.

Gold-Plating

In order to minimize corrosion of the anode, some components were gold-plated. (Based on the results from *(168)*. Since the preferred application by vapor deposition was not possible, electroplating was used. The components were made of V4A steel and could not be gold-plated directly due to a rapid oxide formation on the surface. In order to still be able to gold plate, Woods nickel strike (tifoo) was performed after degreasing using a surfactant solution in an ultrasonic bath. The nickel layer thus deposited was stabilized with classical nickel electrolyte at low current (to minimize gas bubble formation due to overvoltages). Subsequently, gold plating was performed using potassium dicyanoaurate(I) ("pure", Carl Roth) and potassium dihydrogen phosphate (>99%, Carl Roth) to adjust the pH *(169, 170)*. An immersion bath was used for gold plating. A current of 0.1 A was used for 4.5 min, resulting in a gold layer of 1 µm.

Figure D.2. Anode insert. Left: Stainless steel; Right: Gold-plated stainless steel.

Technical drawings

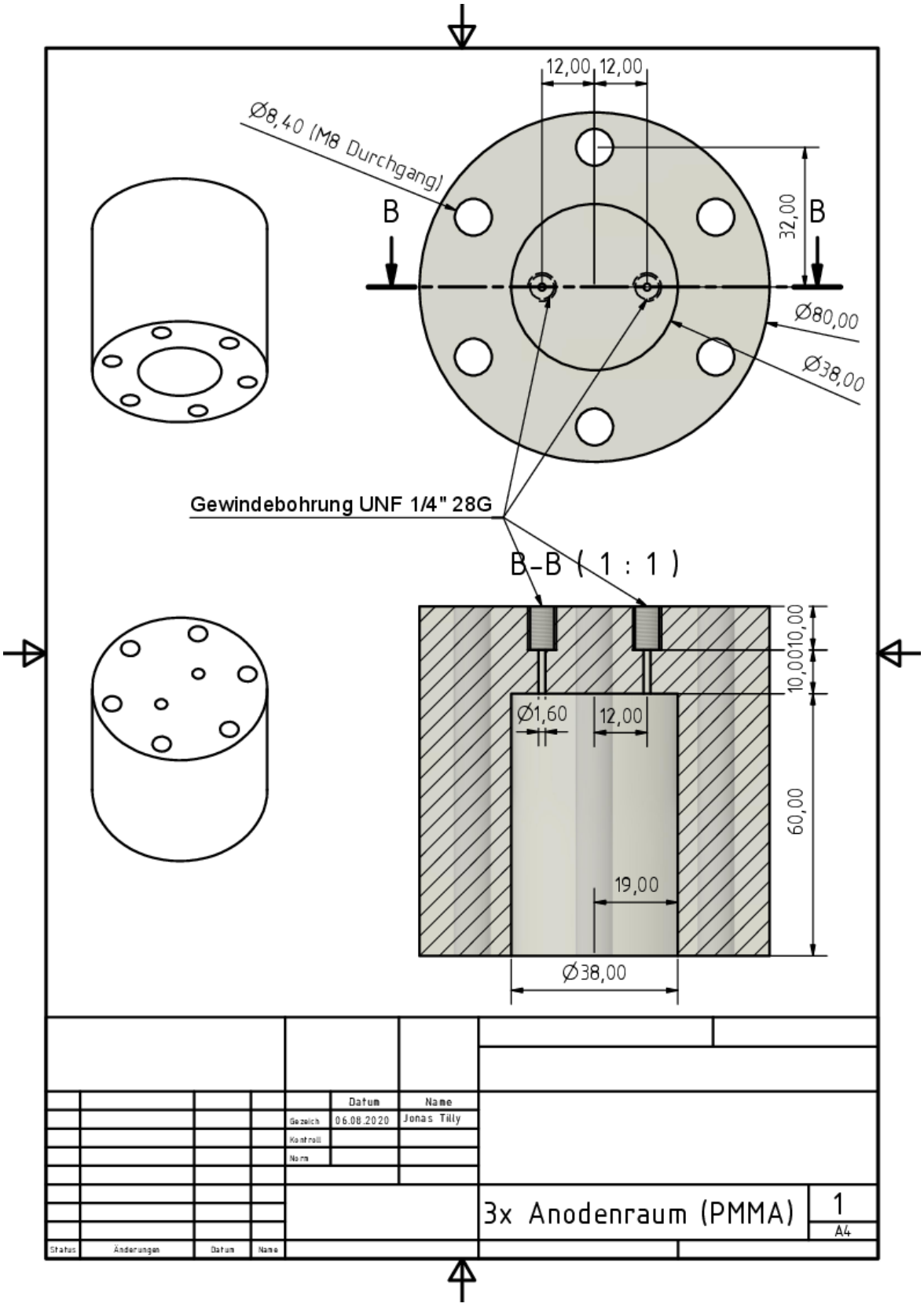

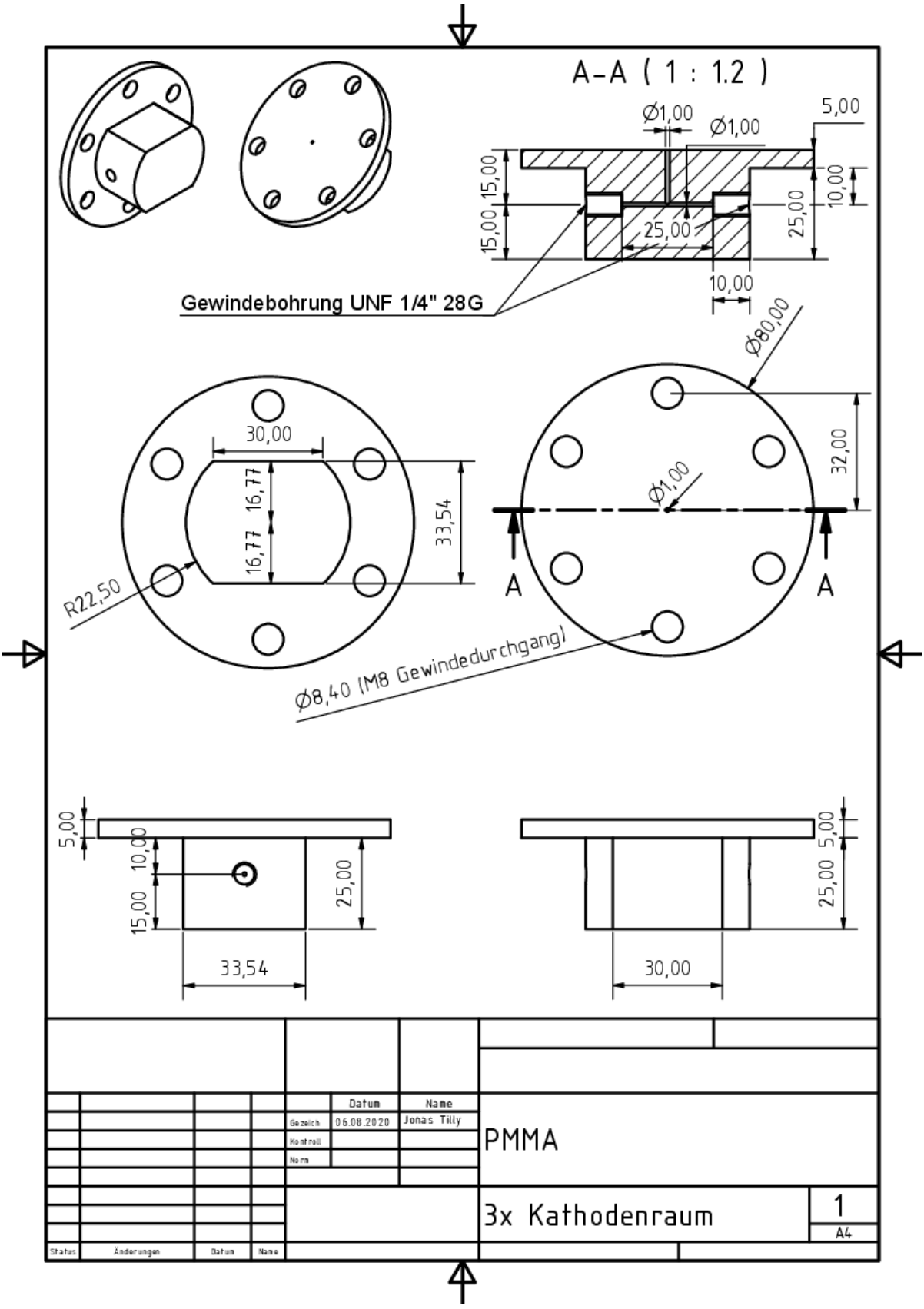
A-A (1 : 1.2)
Ø1,00
Ø1,00
5,00
15,00
15,00
10,00
25,00
25,00
10,00
Gewindebohrung UNF 1/4" 28G
Ø80,00
30,00
16,77
16,77
33,54
R22,50
Ø1,00
32,00
A
A
Ø8,40 (M8 Gewindedurchgang)
5,00
10,00
15,00
25,00
33,54
25,00
5,00
25,00
30,00
Datum
Name
Gezeich
06.08.2020
Jonas Tilly
Kontrolli
Norm
PMMA
3x Kathodenraum
1
A4
Status
Änderungen
Datum
Name

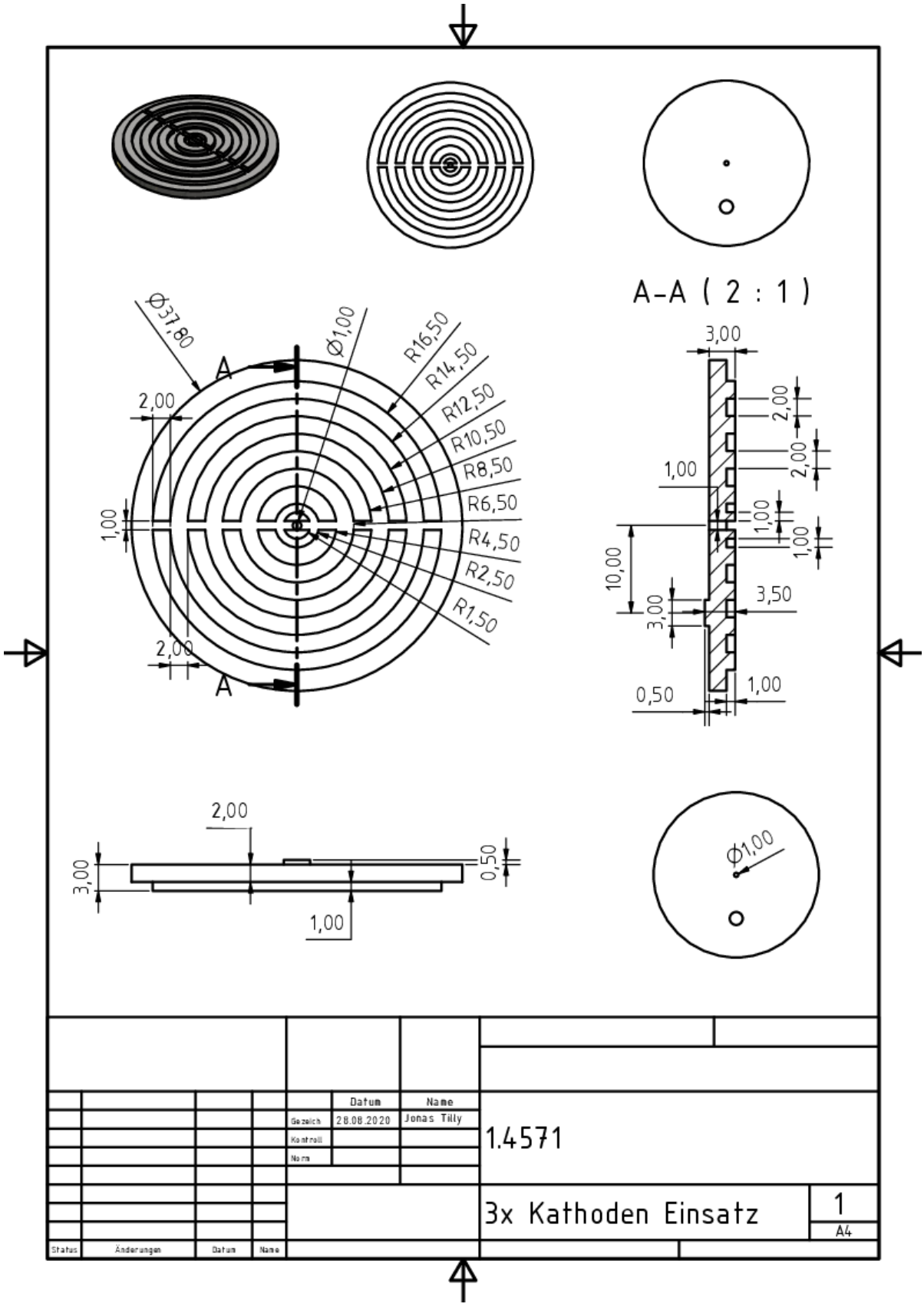
A-A (2 : 1)
Ø37,80
Ø1,00
R16,50
R14,50
R12,50
R10,50
R8,50
R6,50
R4,50
R2,50
R1,50
2,00
1,00
3,00
10,00
3,50
0,50
0,50
Datum
Name
Gezeich
28.08.2020
Jonas Tilly
Kontroll
Norm
1.4571
3x Kathoden Einsatz
1
A4
Status
Änderungen
Datum
Name

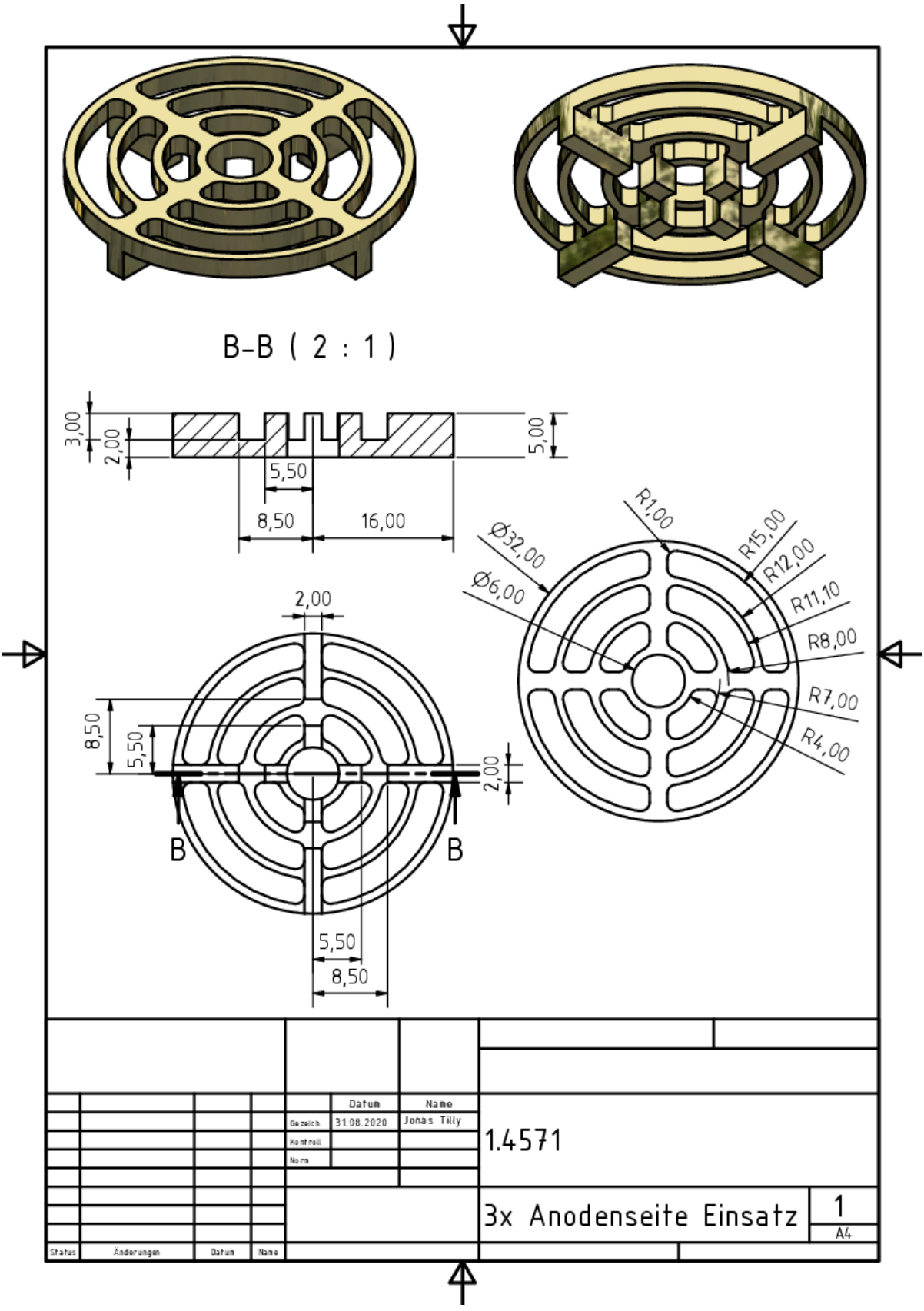
B-B (2 : 1)
3,00
2,00
5,00
5,50
8,50
16,00
2,00
8,50
5,50
2,00
B
B
5,50
8,50
R1,00
R15,00
R12,00
R11,10
R8,00
R7,00
R4,00
Ø32,00
Ø6,00
Datum
Name
Gezeich
31.08.2020
Jonas Tilly
Kontrolli
Norm
1.4571
3x Anodenseite Einsatz
1
A4
Status
Änderungen
Datum
Name

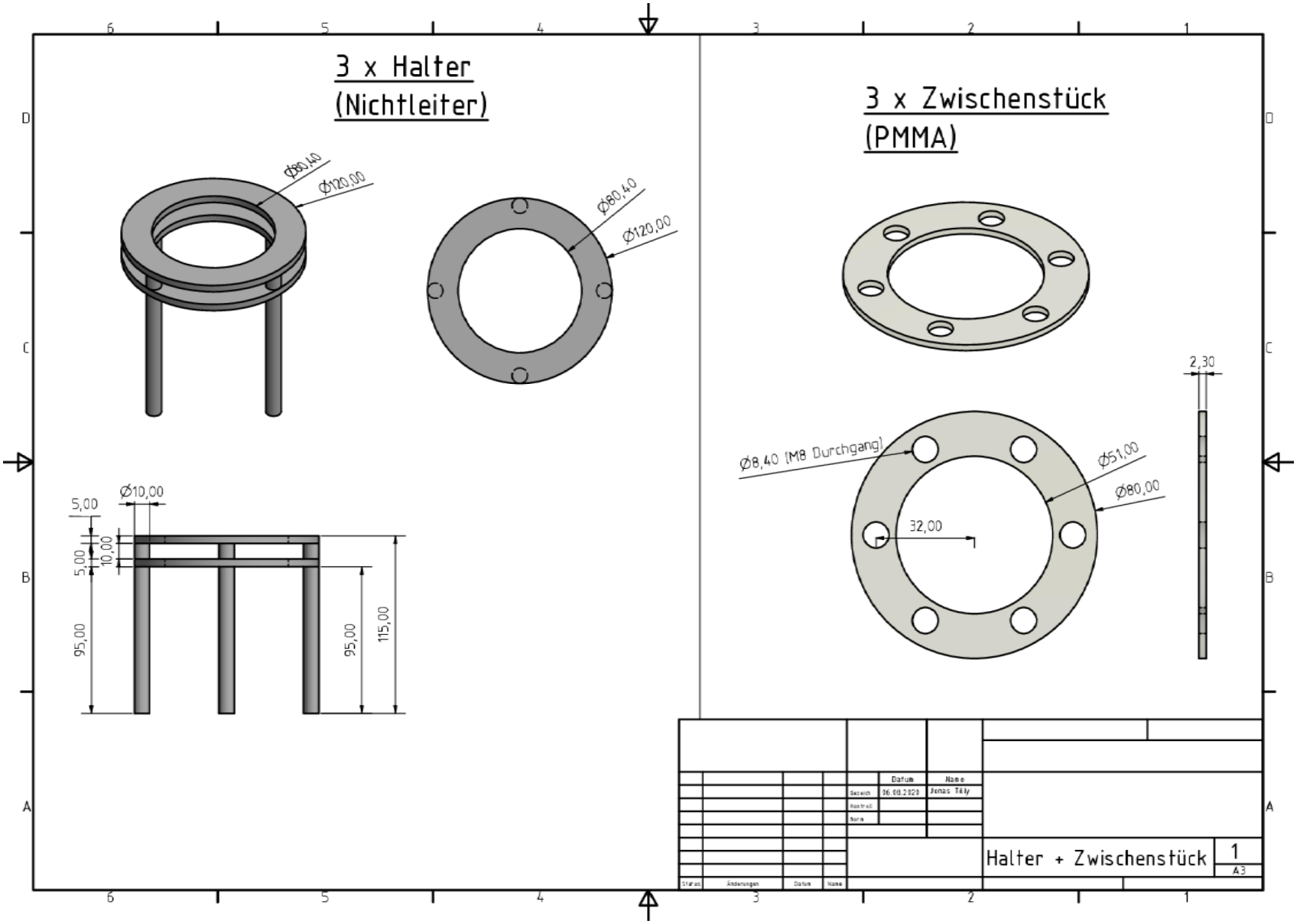
3 x Halter
(Nichtleiter)
Ø80,40
Ø120,00
Ø80,40
Ø120,00
Ø10,00
5,00
5,00
10,00
95,00
95,00
115,00
3 x Zwischenstück
(PMMA)
2,30
Ø8,40 (M8 Durchgang)
Ø51,00
Ø80,00
32,00
Datum
Name
Bezeich
06.08.2020
Jonas Tilly
Kontrolli
Norm
Halter + Zwischenstück
1
A3
Status
Änderungen
Datum
Name

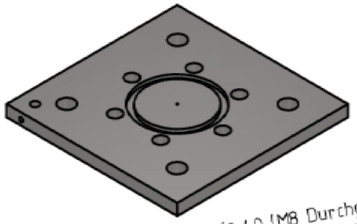

Oberseite

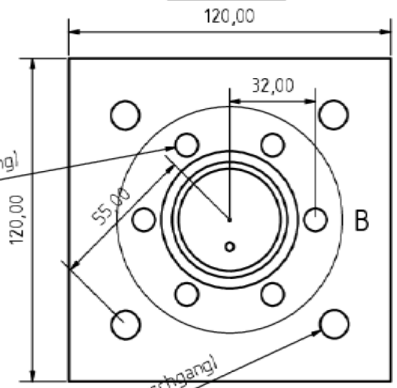

Unterseite

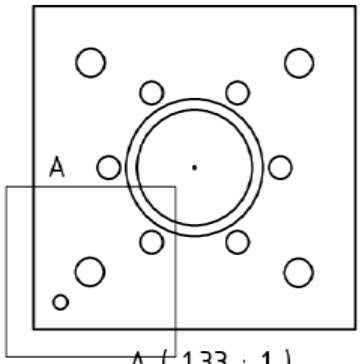

C-C (2 : 1)

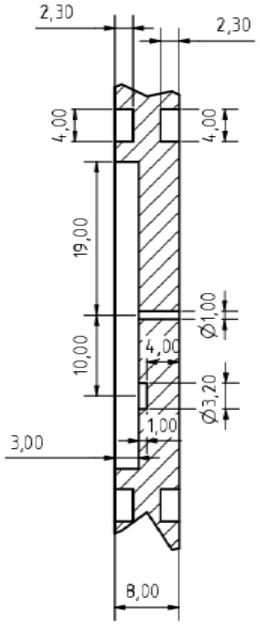

B (1 : 1)

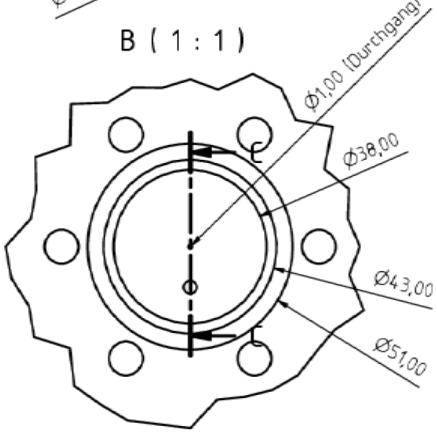

D-D (2 : 1)

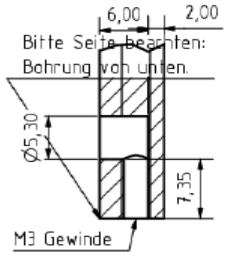

A (1,33 : 1)

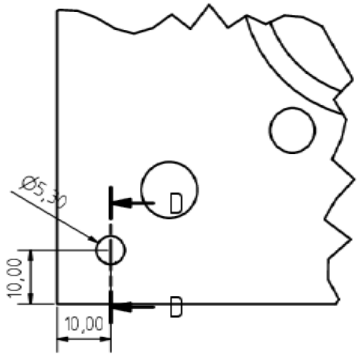

					Datum	Name	
				Gezeich.	07.08.2020	Jonas Tilly	1.4571
				Kontrolli.			
				Norm			
							3x Kath.raum Endplatte 1
Status	Änderungen	Datum	Name				A3

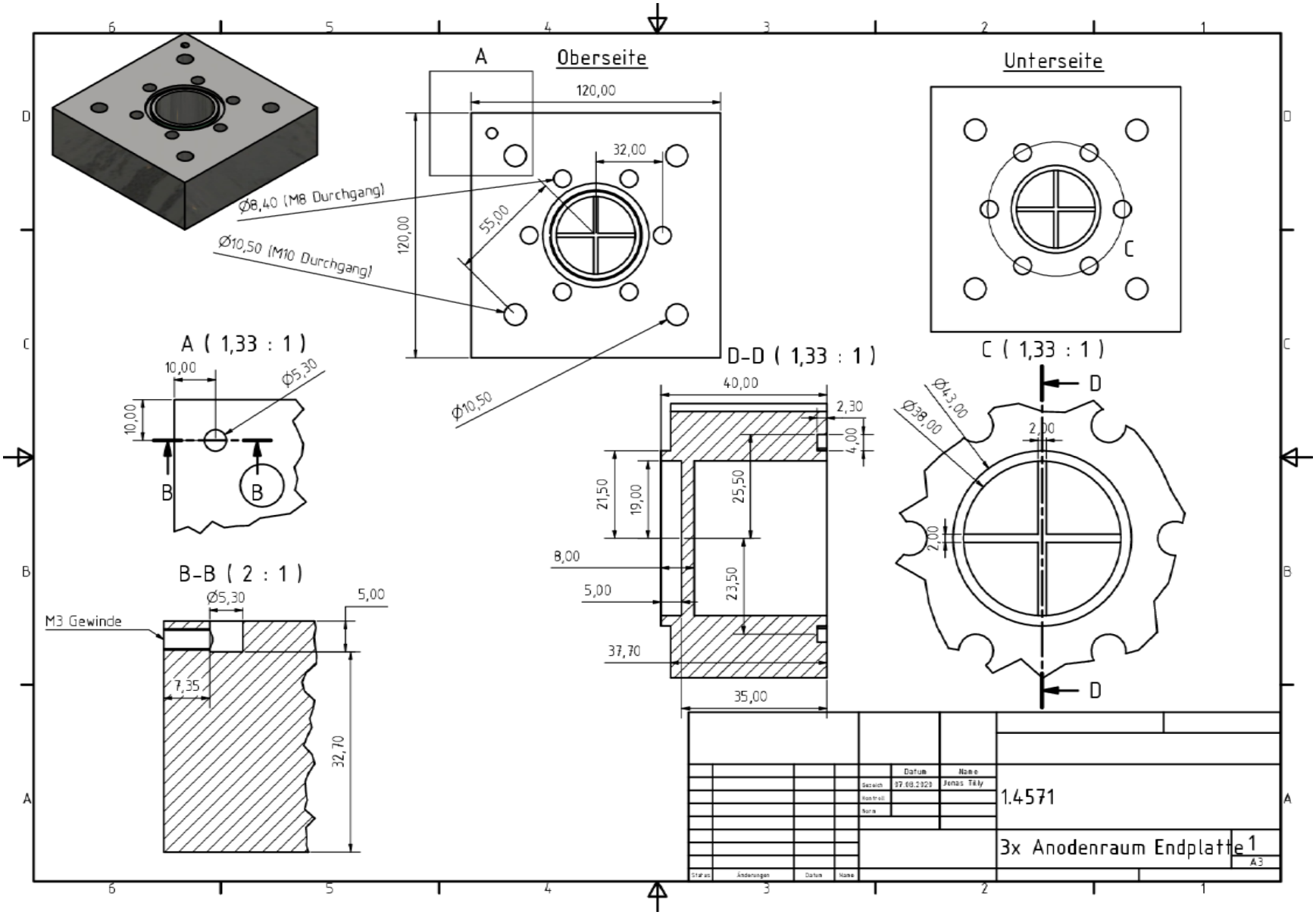
A
Oberseite
120,00
32,00
55,00
120,00
Ø8,40 (M8 Durchgang)
Ø10,50 (M10 Durchgang)
Ø10,50
Unterseite
C
A (1,33 : 1)
10,00
10,00
Ø5,30
B
B
B-B (2 : 1)
Ø5,30
5,00
M3 Gewinde
7,35
32,70
D-D (1,33 : 1)
40,00
2,30
4,00
21,50
19,00
25,50
8,00
5,00
23,50
37,70
35,00
C (1,33 : 1)
D
Ø43,00
Ø38,00
2,00
2,00
D
Datum
Name
Bezeich
27.08.2023
Jonas Tilly
Kontroll
Norm
1.4571
3x Anodenraum Endplatte
1
A3
Status
Änderungen
Datum
Name

E. Transfer hydrogenation in a biphasic slug flow

Transfer reactions are reactions in which a liquid reactant replaces the gaseous reactant of a gas-consuming reaction. This liquid reactant supplies the gaseous reactant as a donor. Thus, the gas-liquid reaction becomes a liquid phase reaction. Studies on donor reactions as an alternative to gas-consuming reactions can be found in the literature, for example, for hydrogenations or hydroformylations. *(109, 110, 171, 172)*.

For example, donors used for transfer hydrogenation are different formates or glycerol *(109, 110)*. In addition, transfer hydrogenation is often carried out at milder temperatures and ambient pressure than classical gas-consuming hydrogenation. Furthermore, de Souza Schneider et al.'s investigations showed a high selectivity regarding monounsaturated fatty acids *(171)*.

Therefore, the transfer hydrogenation of sunflower oil is examined as an alternative to the classical hydrogenation of fatty acids (Chapter 7). The same Rh(TPPTS) catalyst (0.3 mmol/L and 1:5 Rh:ligand) was used for comparison purposes, resulting in a liquid-liquid reaction system. Ammonium (>95%, Carl Roth) and potassium formate (>98%, Carl Roth) were used as donor substrates. The reaction was used in the stirred tank setup from Chapter 6.2.

Figure E.1 shows a conversion-time curve of the transfer hydrogenation of sunflower oil. Besides the low conversion of C18:2 of 25% after four hours of reaction time, a large number of undefined by-products were detected by gas chromatography, so this reaction system is evaluated as unsuitable. Nevertheless, other transfer hydrogenations for selective fat hydrogenation can lead to high conversions and selectivities and is thus an alternative to conventional hydrogenation.

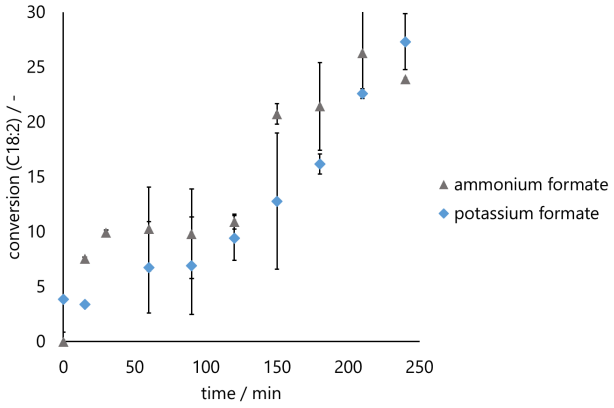

Figure E.1. Conversion of C18:2 in transfer hydrogenation of 5 w% sunflower oil in hexanol with Rh(TPPTS) with formates ($n_{formate}$:n_{oil} ratio: 27:1). T=100 °C, p=1 atm.

F. UV-Vis spectra of water and hexanol

UV-Vis spectra (Figure F.1) for the liquid phases hexanol and water were recorded in order to neglect additional effects of absorption on the recorded signals (Genesys 10 UV, Thermo Electron, Langensbold, Germany). At the wavelength of 940 nm used, only a bit of light is absorbed, so the influence of absorption can be considered negligible.

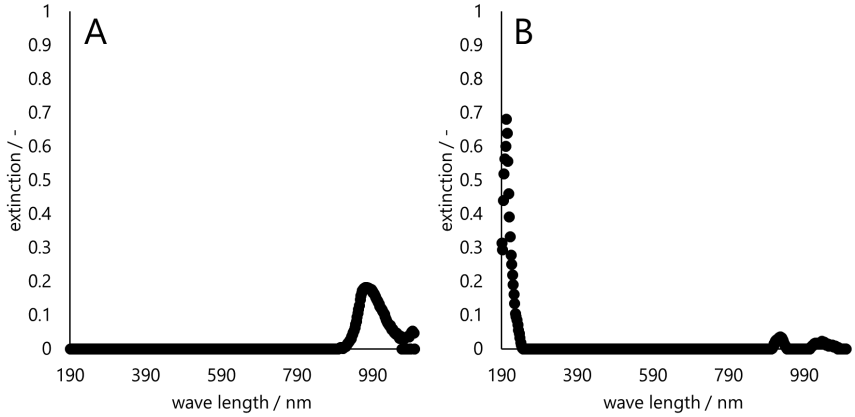

Figure F.1. UV-Vis spectra of water (A) and hexanol (B). Reference medium: air.

G. Phase separation

Some phase separators for biphasic capillary flows already exist in the literature. Due to the small dimensions, surface forces dominate compared to gravity. Hence simple density differences cannot be used for phase separation. Therefore, materials or membranes with different surface affinities (e.g., hydophilic, lipophilic) are used *(162–167)*.

Separation of a triphasic gas-liquid-liquid flow has not been performed in a single-stage concept so far. However, in a modular capillary reactor design, this would simplify the setup.

Due to the significant density differences, separating the gas phase tends to be easier than separating the liquid phases. Hence, additional surface forces were exploited for phase separation in a cylindrical phase separator with inserts made of hydrophilic steel and hydrophobic PMMA. A schematic setup of the designed phase separator is shown in Figure G.1. The internal volume is 0.3 mL, which allows minimal residence times and, thus, low back mixing.

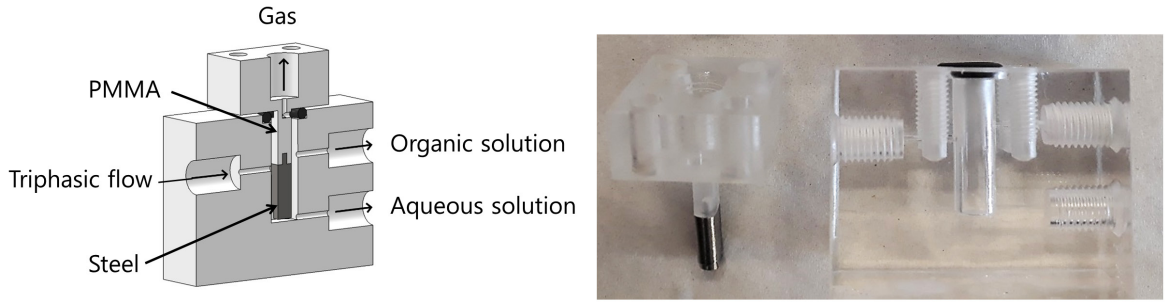

Figure G.1. Left: Sectional view of the phase separator for triphasic flows. Right: Disassembled phase separator with the PMMA/steel inlet on the left.

This phase separator was used to separate a triphasic slug flow with a phase ratio of 1:1:1. Figure G.2 shows an example of the phase fractions of the respective liquid outputs at different total input volume flows for a mixture of hexanol, water, and nitrogen. The gas could be separated entirely and purely at each point. Up to a total volume flow of 6 mL/min, pure liquids were observed at each of the outputs; at higher volume flows, the flows were slightly contaminated with the other liquid.

This separation efficiency is remarkable because of the small volume of the separation apparatus (0.3 mL). However, density and viscosity still greatly influence the separation performance, and the surface forces are not solely dominant. This phase separator can be further optimized in terms of separation performance and surface availability. Transferring to a pressure-stable design would allow direct recycling of a catalyst phase in operation conditions.

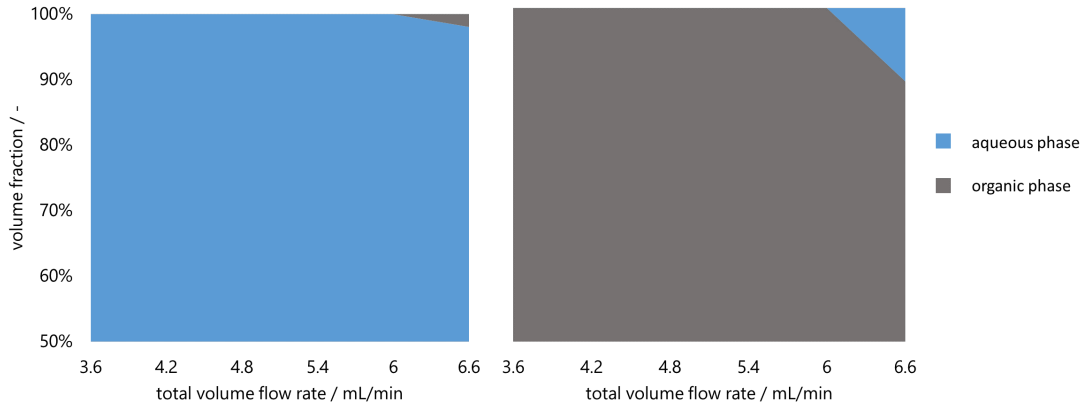

Figure G.2. Phase fractions at the outlet of the aqueous and organic phases plotted versus the total volumetric flow rate of the triphasic system. Substance system: Hexanol, water, and nitrogen in a phase ratio of 1:1:1.